Experimental and Numerical Investigation of Positively and Negatively-buoyant Round Jets in a Stagnant Water Ambient

by

Hassan Alfaifi

Thesis submitted
in partial fulfillment of the requirements for the
Doctorate in Philosophy degree in
Environmental Engineering

Ottawa-Carleton Institute for Environmental Engineering
Department of Civil Engineering
Faculty of Engineering
University of Ottawa

uOttawa

THESIS SUPERVISOR:

Prof. Majid Mohammadian

THESIS EXAMINERS:

Prof. Ram Balachandar (University of Windsor)

Prof. Ioan Nistor (University of Ottawa)

Prof. Ousmane Seidou (University of Ottawa)

Prof. Hamidreza Shirkhani (University of Ottawa)

DATE OF ORAL DEFENCE:

Monday, November 4, 2019

Acknowledgments

It is a challenging and sometimes lonely path to reach the end of this journey; pursuing a Ph.D. can be defined by both the challenges and successes. At the end of this journey, it is my privilege to thank those who helped to make this thesis a reality where such work would not have been possible without their support includes my supervisor, family, friends, thesis committee as well as financial support. First and foremost, I would like to thank "Allah" for blessing me with the strength and knowledge to fulfill my goals and to accomplish this work.

I would like to express my sincere gratitude to my supervisor, Dr. Majid Mohammadian for his continued guidance, support, and encouragement throughout the years of my Ph.D. study. Dr. Mohammadian kindly helped me by leading countless discussions and providing experimental support that also helped shape this thesis into the final product. I will not forget the first day I have met him and the words he said, they still resonate with me to this day. Because of his diverse experience, I was able to successfully reach my goals and completed this stage of my career successfully, I feel indebted to you forever. With the same grateful attitude, I would also like to thank Dr. Hossein Bonakdari for his valuable contributions, support and assistance in all aspects of this thesis.

Special thanks to the committee members, Prof. Ram Balachandar, Prof. Ioan Nistor, Prof. Ousmane Seidou and Prof. Hamidreza Shirkhani for their valuable feedback, helpful suggestions, and serving in my Ph.D. defence.

At the same time, I would like to thank my country, the Kingdom of Saudi Arabia, represented by King Abdulaziz City for Science and Technology (KACST) for the scholarship and financial support during the period of my Ph.D. study.

My special and extreme thanks to the former president of KACST, Prince Turki bin Saud bin Mohammed Al Saud who gave me the opportunity to complete my study and without his generous support and encouragement, this work would not have been completed.

The assistance and support I have received from all my friends and colleagues at the University of Ottawa are highly appreciated, and I will all the success to each of you. At last but not least, I would also like to express my appreciation to all my friends in Ottawa, particularly Dr. Othman Nasir, Dr. Mohammad Abdulla, Dr. Bashar Tahir, Dr. Jacob Stolle, Dr. Abdullah Alharbi, Dr. Abdullah Alfaify, Hassan Amri, Dr. Abdullah Alodah, Ahmad Alzahrany, Mark Lapointe, Laith Alani, Hossein Kheirkhah Gildeh, Amir Gharavi and Xiaohui Yan for their excellent help and support to conquer the obstacles I faced during my study.

To my beloved family,

Finally, to my Dad and Mom, my brothers and sisters, the goal that I have been planning for the past years has been achieved, and I am aware that you have been with me through your hearts and souls, and I will never forget your prayers and support. Your efforts will not be forgotten for the rest of my life. Words can never tell my parents how much I'm grateful for their love, support, and encouragement. *Dad: Thank you for all you've done for me and raised me the way that you have. I hope you're very proud of me, as I am*. My sincere appreciation and thanks also go to my sisters and brothers, especially Mohammad, Ali, Abdullah, Yahia and Majed. I also thank my Father and Mother-in-law (Ali and Afia) for their prayers and love. Special thanks goes to my brother Yahia, for his patience, encouragement and assistance in overcoming the challenges and difficulties I faced during my studies.

To my wonderful and lovely wife Majedah, I'm so thankful and grateful that you're always with me, so patient and always encouraging. *Majedah: I will never forget your patience and support during my study, you were with me during the whole story, moment by moment, we suffered and endured the difficulties together, you never complained, and you've always been motivating and supportive. I couldn't have made it without your unconditional love and support. "This dream would not have come true"*. To my wonderful "gorgeous" kids, Turki, Rema, Rawan, Raeed and Yamen, thank you for your patience and endurance during this journey, and also your unlimited positive support by bringing endless pleasure, and joy to your parent's lives.

IN THE NAME OF 'ALLAH', THE ENTIRELY MERCIFUL, THE ESPECIALLY MERCIFUL

DEDICATED TO

MY PARENTS, BROTHERS AND SISTERS, WONDERFUL WIFE MAJEDAH, AND LOVELY KIDS TURKI, REMA, RWAN, RAEED AND YAMEN

Abstract

Discharge of brine wastewater produced from industrial plants into adjacent coastal water bodies is considered as a preferable and common method currently used in many offshore industrial plants. Therefore, it is important to carefully study the behavior of jets and their environmental impacts on water bodies close to the discharge points, especially when the density is different between the jets and the receiving water. The main goal of this study is to improve the understanding of the mixing behaviour of jet trajectories for positively (offset) and negatively (inclined) buoyant jets when density is considered a significant factor, and also to examine the accuracy of some RANS turbulence models and one type of artificial neural network in predicting jet trajectory behaviours.

In the first part of this study, experiments using a PIV system for offset buoyant jets were conducted in order to study the effect of the density differences (due to salinity [nonthermal] or temperature [thermal]) between the discharge and the receiving water body on the jet behaviour, and the results showed that the nonthermal jets behaved differently as compared to the thermal jets, even though the densimetric Froude numbers (Fr_d) and density differences ($\Delta\rho$) were similar. In addition, a Reynolds-averaged Navier-Stokes (RANS) numerical model was performed using open-source CFD code (OpenFOAM) with a developed solver (modified form of the pisoFoam solver). The realizable k-ε model showed the best prediction among the models.

Secondly, an extensive experimental study of an inclined dense jet for two angles (15°and 52°) was conducted to study the effect of these angles on the jets' geometrical characteristics in the presence of a wide range of densimetric Froude numbers as well as with different discharge densities. More experimental data were obtained for these angles to be added to the previous data for the purpose of calibrating, validating, and comparing the various numerical models for future studies. The results of these experiments are used to evaluate the performance of a type of artificial neural network method called the group method of data handling (GMDH), and the GMDH results are then compared with existing analytical solutions in order to prove the accuracy of the GMDH method in simulating mixing behaviors in water bodies.

Thirdly, a comprehensive study on predicting the geometrical characteristics of inclined negatively-buoyant jests using GMDH approach was conducted. The superiority of this model was demonstrated statistically by comparing to several previous analytical models. The results obtained

from this study confirm that the GMDH model was highly accurate and was the best among others for predicting the geometrical characteristics of inclined negatively-buoyant jests.

Table of Contents

List of Figures

List of Tables

List of Abbreviations and Symbols

List of Abbreviations

AI	Artificial Intelligence
ANN	Artificial Neural Network
ANOVA	Analysis of variance
CFD	Computational Fluid Dynamics
FVM	Finite Volume Method
GAA	Genetic Algorithm Artificial
GEP	Gene Expression Programming
GMDH	Group Method of Data Handling
GP	Genetic Programming
LA	Light Attenuation
LES	Large Eddy Simulation
LIF	Laser-induced Fluorescence
MAE	Mean absolute error
MAPE	Mean absolute percentage error
MED	Multi Effect Distillation
MGGP	Multigene Genetic-Programming
MSF	Multi-Stage Flush
OpenFOAM	Open Field Operation and Manipulation
PIV	Particle Image Velocimetry
PTV	Particle Tracking Velocimetry
RANS	Reynolds-averaged Navier-Stokes
RMSE	Root mean squared error
RO	Reverse Osmosis
SEE	Standard Error of the Estimate
SON	Self-organizing networks
FVM	Finite Volume Method
FDM	Finite Difference Method
MPE	Mean Prediction Error
WUB	Width of Uncertainty Band

List of Abbreviations

B_0	Buoyancy flux [m^4/s^3];
b	Jet half-width, the distance from the point of maximum velocity (centerline) to the point where the velocity decreases to 1/e=0.37u_m [m];
D	Jet diameter [m];
Fr_d	densimetric Froude number;
H	The depth of the receiving water (ambient water) [m];
g	Gravitational acceleration [m/s^2];
g'	Effective gravitational acceleration [m/s^2];
K	A constant, can be obtained experimentally;

L_M	Momentum length scale [m];
L_Q	Source length scale [m];
M_0	Momentum flux [m^4/s^2];
P	Fluid pressure [N/m^2];
Pr	Prandtl number;
Pr_t	Turbulent prandtl number;
Q_0	Discharge volume [m^3/s];
R^2	Coefficient of determination;
Re	Reynolds number;
r	Radial distance [m];
S	Salinity [ppt];
S_A	Absolute salinity [ppt];
s	The streamwise coordinates of the jet;
S_0	Initial salinity [ppt];
S_a	Ambient water salinity [ppt];
T	Temperature [℃];
T_0	Initial temperature [℃];
T_a	Ambient water temperature [℃];
t	Time [s];
U	Jet velocity [m/s];
U_a	Ambient water velocity [m/s];
$U_m = u_m$	Mean velocity of the jet centerline [m/s];
U_0	Initial jet velocity [m/s];
θ	Initial jet angle to the horizontal [°];
ρ_a	Ambient water density [kg/m^3];
ρ_0	Initial jet density [kg/m^3];
$\Delta\rho$	Density differences [kg/m^3];
$\Delta\rho_{thermal}$	Density differences due to temperature [kg/m^3];
$\Delta\rho_{nonthermal}$	Density differences due to salinity [kg/m^3];
C_{x_m}	The constant for the distance of the terminal height rise from the nozzle in x-direction;
C_{x_r}	The constant for the return point;
C_{y_m}	The constant for maximum height of the jet centerline in y-direction;
C_{y_t}	The constant for the jet terminal height rise;
k_e	heat transfer coefficient [W/s℃];
k	turbulent kinetic energy;
u_x, u_y, u_z	Components of the mean velocity in the cartesian coordinates [m/s];
x_m	The distance of the terminal height rise from the nozzle in x-direction [m];
x_r	Return point of the jet centerline, which is the distance between the tip of the nozzle and the location of that point [m];
y_m	Maximum height of the jet centerline in y-direction [m];
y_t	Jet terminal rise height [m];

v_e	effective kinematic viscosity of water ($v_e = v_t + v$) [m^2/s];
v_t	Turbulent kinematic viscosity [m^2/s];
v	Kinematic viscosity [m^2/s];
ε	turbulent dissipation rate
s_d	Standard Deviation;
E_i	prediction error;
$\overline{u_i^{'} u_j^{'}}$	velocity fluctuation [m];
$\hat{B}$	production of turbulence due to the buoyancy effect;
G_k	production of turbulence due to shear;
$\overline{\Omega}_{ij}$	Mean rate of rotation tensor;
ω_k	Angular velocity for rotating reference frame [m/s];
S_{ij}	Strain rate tensor;
$u_i^{'}, u_j^{'}$	Fluctuating part of velocity [m/s];
σ_ε	the turbulent Prandtl number for ε;
Dk_{eff}	Effective diffusivity for k [m^2/s];
$D\varepsilon_{eff}$	Effective diffusely for ε [m^2/s];
G_ε	Generation of turbulent kinetic energy due to the mean velocity gradients;
Co	Courant number;
λ	Damping factor;
S_f	Cell face surface normal vector [m^2].

Chapter 1. Introduction and objectives

1.1. Introduction

Providing safe and clean drinking water for growing populations in arid and semi-arid countries is a major challenge in terms of engineering and management. One of the primary solutions addressing this issue is desalination of seawater using desalination plants. These plants are usually located on the shores of major water bodies (i.e. seas and rivers) for the uptake of source water and discharge of by-products. The desalination process produces the pure water used as drinking water as well as a highly-concentrated brine by-product– which is subsequently discharged into the nearby water body as one of the most common ways of disposing this type of wastewater. Different methods have been used in the seawater desalination process, such as Multi-Stage Flush (MSF), Multi Effect Distillation (MED), and Reverse Osmosis (RO). The MSF technology (which is a mix between hot (higher than the surrounding environment) and high-salinity water, which is referred to as brine) is well-established producing about 60% of all the desalinated water in the world. Figure 1-1 shows one of the largest MSF desalination plants in the world that is located on the east coast of Saudi Arabia (Al-Jubail desalination plant). This plant produces 0.96 million m^3 per day of drinkable water, with approximately 1.4 million m^3 per day of effluents with high temperature and salinity that is constantly discharged back into the aquatic environment (Ahmad, 2002).

Figure 1-1: Brine discharged directly from Al Jubail desalination plant into the Gulf using an open channel method (surface discharge) (Picow, 2009).

On the other hand, with the economic growth of some countries, the RO method is considered the preferred technology, as it reduces the cost of desalination and is considered more efficient and cost-effective compared to other methods (Abessi, 2018; Ahmad and Baddour, 2014). This method still produces large quantities of brine effluent with a high concentration of salinity.

The amount of this effluent is generally larger than the water produced from the plant (freshwater), with approximately 40% (effluents from the total amount of product) for the RO method and up to 90% for MSF (thermal technologies) (Bleninger et al., 2010). Therefore, a large volume of discharge water results from MSF. As mentioned previously, these effluents are discharged back to the nearby waterbody using outfall systems, which can vary depending on the type of effluent and required mixing characteristics with the surrounding waterbody (see Figure 1-1 and 1-2).

Figure 1-2: Brine discharged of the Delray Beach sewage outfall, Florida, USA, using submerged pipe (Prins, 2016).

These outfall systems are among the preferred methods for discharging effluent into the sea when industry is close to the sea. One of the benefits of these systems is to reduce the concentration of the effluent by having rapid mixing with the ambient seawater resulting in more dilution of these effluents before reaching the seabed. However, the use of these systems to discharge effluent into the marine environment can still have negative impacts on the ecosystem, particularly in the near-field zone (Lattemann and Höpner, 2008; Petersen et al., 2018). Therefore, a comprehensive study with key considerations related to surrounding environments must be conducted before making the decision to discharge effluent into the sea. More details regarding discharge methods of outfall systems are discussed in the following section.

The sensitivity of coastal regions to the desalination plant discharges depends on a wide-range of factors. Open sea areas may be less sensitive to the effluents, as they are more capable of diluting and dispersing discharges than enclosed and shallow sites (Hoepner and Windelberg, 1996; Lattemann and Hoepner, 2008). Due to the adverse influence of thermal effluents on the marine ecosystem (Cambridge et al., 2017; Hashim and Hajjaj, 2005; Mabrook, 1994; Milione and Zeng, 2008; Roberts et al., 2010), it is necessary to study the characteristics of the near-field mixing zone in order to prevent adverse impacts and to keep the marine environment clean and usable as a sustainable source of drinking water for future generations, especially for countries with a shortage of clean and safe drinking water resources. Accordingly, it is of paramount importance to consider both the site and discharge methods in the design of effective outfall systems.

1.1.1. *Outfall discharge methods*

Desalination plants usually discharge their effluents into seawater using different outfall methods, either as surface discharge, using open channels, or submerged discharge using submerged pipes, as shown in Figure 1-1 and Figure 1-2, respectively. The concept behind these methods is to find the optimal way to reduce the impact of these effluents on the marine environment by having higher mixing efficiency and achieving maximum dilution of the pollutants contained in the effluent. These pollutants (such as chemically-active and toxic substances) can be substantially increased with the increase in the concentration of desalination brines. These discharges can lead to an increase in the salinity and temperature of the receiving waters as well as the accumulation of hydrocarbons, metals and toxic anti-fouling compounds (Ketsetzi et al., 2008; Roberts et al., 2010). As a result, if the discharge effluent is poorly mixed in the surrounding environment, the potential of ecological impact increases with variable effects on the benthic communities, as well as the community structure of seagrass, coral reef, and soft-sediment ecosystems (Roberts et al., 2010).

Discharging an effluent with a high concentration of brine using the surface method results in a negatively-buoyant discharge stream – which does not efficiently mix with the ambient seawater in the near field as compared to submerged discharges. Therefore, the dense effluent accumulates near the bottom in the receiving water and can negatively impact the coastal environment, as shown in Figure 1-3a. In the case where the effluent in positively-buoyant (thermal effluent), marine organisms that live on the water surface can be influenced by the high concentration of the effluent, which can float on the surface of the receiving water (see Figure 1-3b).

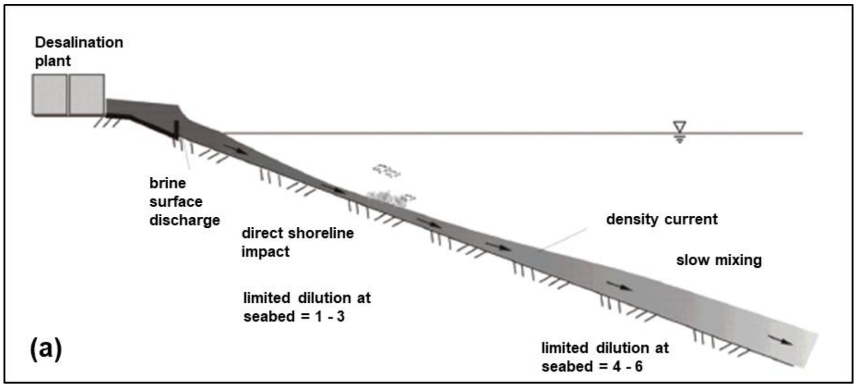

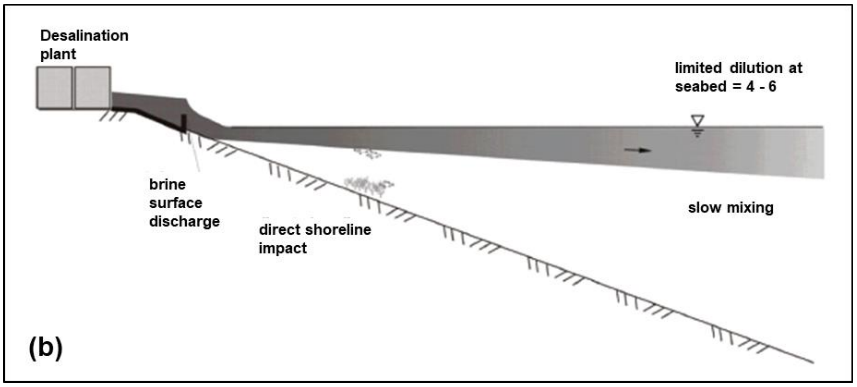

Figure 1-3: Schematic view of surface jet discharged on a shoreline: a) dense effluent; b) thermal effluent (mixed between dense and cooling water). Source: Bleninger et al. (2010).

In contrast, the submerged method has the advantage of obtaining higher mixing and dilution rates and, as a result, this method has recently become widely used for effluent discharge (Figure 1-4). The main reason for the higher dilution is the water entrainment in the discharge from the surrounding water body for both positively or negatively buoyant jets. Therefore, the most common method used in the vast majority of countries is submerged pipes. These pipes (outfalls) are located on the coast near the plants, and thus create plumes of pollutants, behaving as jets. In engineering practice, especially in mixing flow at coastal area, the word “jet” refers to the effluent (brine or thermal) the discharged from industrial facility using submerged pipe which is, ultimately, created jets either directed upward to the water surface (as a buoyant jet) or inclined at an angle (as a dense jet), see Figure 1-4. While these outfall systems have improved dilution rates, the entrained pollutants still have an impact on the marine environment. Therefore, understanding the properties of both the effluents and the receiving environments (near-field) is required in order to evaluate the potential impacts of the discharge on the marine environment.

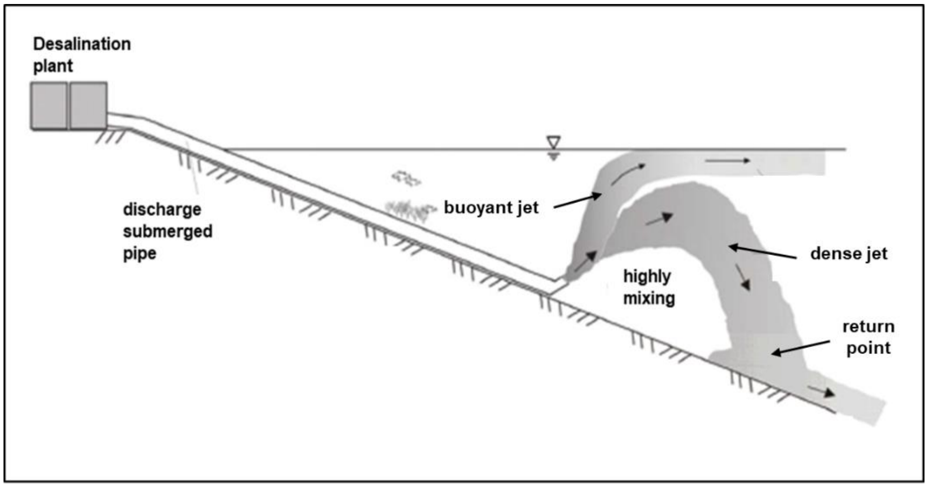

Figure 1-4: Schematic view of submerged discharges for positive and negative buoyant jets. Source: Bleninger et al. (2010)

1.1.2. *Outfall design guidelines*

The position of the submerged pipes that discharge effluent is one of the most critical parameters dictating the influence of the discharge on the marine environment. The proper position of these pipes can help reduce the impact of effluents, particularly in the case of desalination effluents. Another important factor that can influence the effect on the marine environment is the level of effluent brine concentration. This also depends on the environmental and hydrogeological characteristics of the sea: bathymetry, waves, currents, water column depth, etc. Such factors will determine the extent of brine mixing and thus the regional impact distance (Einav et al., 2003). To ensure that the negative impact of these effluent is minimized, an appropriate design guideline should be adopted to mitigate this effect. For example, World Bank Group (2007b) proposed a new Guidelines for Environment, Health and Safety (EHS) consisting of General EHS Guidelines containing cross-cutting information potentially applicable to all sectors of industry and specific guidelines for the sector. The General EHS Guidelines (World Bank Group, 2007b) specified that discharges from desalination plants to surface water should not result in pollutants exceeding local water quality standards or other sources of ambient water quality in the absence of local criteria. It also recommends decreasing the temperature of heated water before discharge to ensure that the temperature of the discharge of water does not result in an increase of more than 3˚C compared to ambient temperature at the edge of a scientifically established mixing area. The Pollution

Prevention and Abatement Handbook states that if the effluent is discharged from thermal power plants, it is recommended that there should be no vulnerable marine habitats within 100 m of the discharge point (World Bank Group, 1998). Another example, under Omani regulations on the disposal of liquid waste into the marine environment, the temperature of liquid waste at the discharge point should not exceed 10˚C above the receiving water temperature. The discharge should not result in an increase of more than 1˚C (weekly average) in seawater temperature in a circular area around the point of discharge of 300 m diameter (Sultanate of Oman, 2005).

On the other hand, similar to temperature, increased salinity can also be harmful for the marine life. The Western Australian guidelines stated that the salinity of the fresh and marine waters should not exceed 5% of that of the source water. Their regulation requires that the salinity in the 50 m of the discharge point should be within 1.2 units of ambient levels, while within 0.8 units of the levels of the source water within 1,000 m of the discharge point (Wec, 2002). The US Environmental Protection Agency (EPA) guidelines state that salinity variations from natural levels should not exceed 4 units, which leads to an increase in salinity from background levels between 11% and 39% (US EPA, 2006). In Sultanate of Oman, the regulations for the discharge of liquid waste into the marine environment stated that, in a circular area of 300 m diameter around the point of discharge, salinity should not be above the local average for more than 2 units (Sultanate of Oman, 2005).

Therefore, there are general guidelines for designing the outfall structure of the discharge from desalination plants, which can be suitable for: offshore, submerged, and multiport diffusers. These guidelines/principles are summarized by Bleninger and Jirka (2010), as following:

Site of discharge:

1. The location of the discharge should be selected in less-sensitive coastal regions. The effluent should not directly discharge onshore or close to any environmentally sensitive or protected sites. For example, places near coral reefs, lagoons, enclosed bays, etc.
2. To prevent aggregation and allow for further mixing, the location of the discharge should be chosen in coastal regions with good transport and flushing characteristics. The effluent should not be discharged into stagnant flows or a very shallow waters that have low current velocities.

Discharge design

1. The structure of the outfall discharge should be designed properly to protect the nearby boundaries from any direct or immediate impacts. Therefore, the outfall should be oriented into the open water body and should not make any direct interactions to the sea bed or the water surface. Also, it should not be oriented or concentrated at a single point.
2. The structure should be designed to enhance the mixing of the effluents to make sure that the discharge has more dilution. Also, the discharge design should be generally perpendicular or parallel to the ambient water current. Moreover, the discharge water should be optimally and equally distributed within the water body to ensure the enhanced dilution.

1.2. Positively and negatively-buoyant jets

1.2.1. *Positively-buoyant jets*

The effluent from industrial plants can be denser or lighter than the receiving water. Thus, if the effluent density is less than the ambient water density, the effluent (i.e., the jet) behaves like a positively buoyant jet (e.g., thermal jet), as it rises towards the water surface. As mentioned previously, a submerged outfall (inclined, offset, or wall jets) is typically designed to achieve a higher dilution of the effluents. A positively buoyant offset jet is considered in this study, where the "offset" refers to the source of the flow that is discharged at a certain distance above the seabed, as shown in Figure 1-5. Although outfalls with offset jets are currently used in many offshore industrial plants (e.g., desalination plants), minimal research has been conducted on understanding their mixing characteristics, especially for buoyant offset jets with both salinity and temperature variations. Differences between the characteristics of the jet and those of the receiving water body (e.g., density differences due to salinity or temperature) may also affect the jet and its mixing characteristics. Therefore, the relative density of the two fluids can impact the trajectory of the discharge.

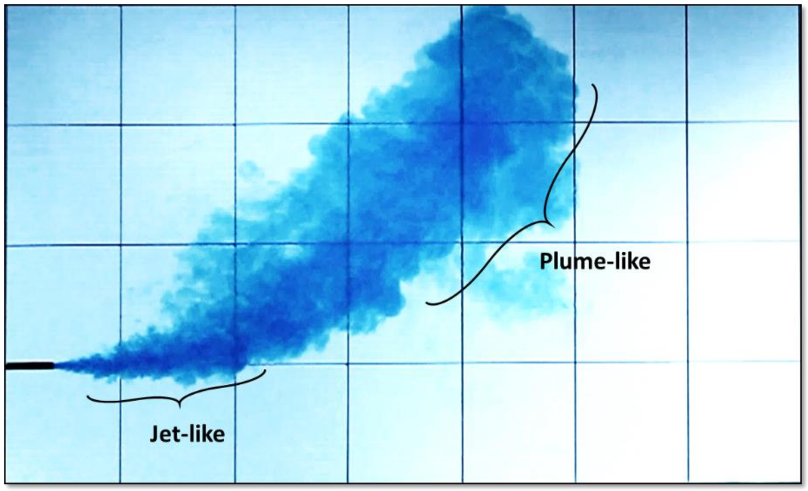

Figure 1-5: A submerged outfall discharge for offset buoyant jet.

The first study (to the author's knowledge) on positively buoyant offset jets was by Rawn and Palmer (1930), who investigated the mixing characteristics of horizontal offset jets discharged into seawater. Their study included 388 experimental observations of dilution at the surface for offset freshwater jets injected into water of higher density. Only recently, Michas and Papanicolaou (2009) revived the research in this area, investigating horizontal round turbulent jets discharged into calm ambient water. Their study looked at both jet-like (where the jet is driven by the momentum force) and plume-like (where the jet is dominated by the buoyancy force) cases for the purpose of covering a wide range of applications (Figure 1-5). The mixing and geometric characteristics, such as jet trajectories, were obtained with video imaging. They found that the flows exhibited jet-like behavior in the horizontal regime, and that the mean and turbulent temperature profiles became asymmetrical in the transition and vertical regimes.

Recently, the effect of density differences between two liquids was studied by Eleuch et al. (2018), who conducted laboratory experiments to evaluate the evolution of a pure water jet injected vertically downwards into water of higher density. Their study focused on the effects of flow rate and difference in density between the jet and the surrounding water, and the results showed that jet penetration depth was affected by the flow rate – increasing with increasing flow rate. Moreover, the jet penetration depth increased significantly when the density difference between the two liquids was decreased.

The previously mentioned studies were conducted experimentally. However, numerical simulations of buoyant offset jets are ongoing and require further investigation. A numerical investigation of a sediment-laden round jet discharged horizontally was carried out by Liu and Lam (2015), who applied large eddy simulation (LES) for the fluid-phase comparison with Lagrangian particle tracking to calculate the motion of the sediment particles.

Therefore, most of the previous studies that related to this topic have focused on the mixing characteristics of effluent discharge into freshwater; however, to the author's knowledge, the effects of the properties of the receiving water, particularly water of high salinity, on the mixing and trajectory characteristics of jets have not been previously studied. Thus, efforts in this aspect are needed and require further investigation, both experimentally and numerically.

Thus, in the first part of the present study, experimental and numerical investigations of the behaviors of thermal and nonthermal buoyant offset jets discharged into fresh and saline stagnant water have been conducted and are discussed in detail in Chapter 2. In this study, fourteen thermal and nonthermal experiments were conducted using the PIV technique. In addition, the performance of various turbulence models was then tested using the open-source CFD code Open Field Operation and Manipulation (OpenFOAM). Three Reynolds-averaged Navier-Stokes (RANS) turbulence models were examined in this study (i.e., the standard k-ε, realizable k-ε, and buoyancy-modified k-ε models), and the results were compared with the experimental data.

1.2.2. *Negatively-buoyant dense jets*

This section introduces the other type of industrial effluent dispersal method, which is negatively-buoyant dense jets. The negatively-buoyant dense jet phenomenon can be seen when the density of the effluent is higher than that of the ambient water, and thus the effluent behaves as a negatively-buoyant jet (e.g., inclined dense jets), where it rises for a distance and then falls towards the seabed. This type of effluent dispersal method is often seen in near-field coastal areas adjacent to desalination plants that use the RO technology. The effluent (brine) resulting from the RO method usually has a concentration 1.3-1.7 times higher than that of the seawater (Einav et al., 2002). The negatively-buoyant dense jets have also been shown to have significant negative impacts on the surrounding marine environment (Petersen et al., 2018). Minimizing these effects has been achieved by using inclined discharge angles. This method propels the effluent vertically for a certain distance towards the water surface, and afterwards the jet starts falling toward the seabed, thus forming a negatively buoyant jet. At present, this is considered as one of the best ways for ensuring rapid mixing of the discharged brine and thus high dilution before reaching the seabed.

Different inclinations have been applied and tested by several researchers to obtain the highest possible efficiency in increasing the effluent dilution. All these experimental studies were performed to measure the main geometry and dilution characteristics of the jets using various techniques, such as laser-induced fluorescence (LIF), light attenuation (LA), and particle tracking velocimetry (PTV), or by using high-resolution digital cameras (Bashitialshaaer et al., 2012; Oliver, 2012; Cipollina et al., 2005; Crowe, 2013; Kikkert, 2006; Lai and Lee, 2012; Oliver et al., 2013; Papakonstantis et al., 2011; and Shao and Law, 2010; Abessi and Roberts, 2015a; and Papakonstantis and Tsatsara, 2018).

In addition to the experiments, other studies employed analytical solutions using different methods to predict the geometrical characteristics of jet flow. For example, Kikkert (2006) and Kikkert et al. (2007) used the LA and LIF techniques to study the geometrical characteristics and dilution of inclined dense jets for angles ranging from 0 to 75°, with different Froude numbers ranging from 14 to 99. In addition to the obtained data, they developed an analytical solution that can predict the behavior of an inclined dense jet. Later, Lai (2010) used the VISJET model (a virtual reality visualization computer software enclosed with the Lagrangian jet model JETLAG, first introduced by Lee and Cheung (1990) to interpret the results obtained from his experiments. The results of this model showed underestimation in relation to the jet dilution. Oliver (2012) carried out experiments to study dense jets with source inclinations of between 15° and 75°, and also developed a new model called “forced jet” that can reduce the buoyancy flux of the jet when the flow rises to the maximum height. The prediction results of this model were reasonable for source inclinations of less than 60°.

More efforts with regard to predicting and modeling the behavior of the mixing characteristics of inclined dense jets are required, and in order to achieve this goal, more laboratory experiments with a wide range of angles and densimetric Froude numbers are needed to fill the gaps in the existing data. Since most of the existing studies on negatively buoyant jets have dealt with specific angles (e.g., 30°, 40°, and 60°), other angles need more investigation, especially in ranges close to 60°, as this angle has been the preferred and recommended angle for inclined dense jets discharged into deep stationary water (Zeitoun et al., 1970; Abessi and Roberts, 2015a). Therefore, in addition to the need to increase research efforts for prediction, more data are also needed to improve the understanding of the behaviors and geometric characteristics of inclined dense jets as well as for use in calibrating, validating, and comparing various numerical models for future studies.

Moreover, predictions for inclined dense jets using different analytical methods have received little research effort and need more investigation.

1.3. Artificial neural network

An artificial neural network (ANN) method is considered to be an Artificial Intelligence (AI) method whose foundation is derived from the functions of the neural network of the human brain. An efficient and proven category of ANN for prediction and modeling is known as self-organizing networks (SONs), of which one type is the polynomial network. Neural networks and linear regression methods are combined in these types of networks, and one SON training algorithm – important to this thesis – involves the group method of data handling (GMDH) (Ivakhnenko 1982). Several researchers in various engineering fields have used artificial neural network methods to address a wide-range of applications, such as multigene genetic-programming (MGGP) technique, genetic algorithm artificial neural network (GAA), the genetic programming (GP), Gene Expression Programming (GEP), and the GMDH. These approaches were used for solving nonlinear engineering problems while providing an explicit equation for predicting and modeling each phenomenon. Their studies have shown accurate results compared to those of other methods (Alitaleshi and Daghbandan, 2019; Azimi et al., 2017; Bonakdari and Mohammadian, 2019; Daghbandan et al., 2019; Ebtehaj et al., 2017, 2015; Gholami et al., 2017; Madandoust et al., 2012; Mehri et al., 2019; Naeini et al., 2018; Najafzadeh et al., 2013; Parsaie et al., 2018; Parsaie and Haghiabi, 2017; Rostami et al., 2019; Yan and Mohammadian, 2019; Zaji and Bonakdari, 2019). Therefore, regarding the outcomes obtained from previous studies, it is worth implementing some of those methods to predict the geometrical characteristics of inclined buoyant jets.

Accordingly, in the second part of the present study, a series of laboratory experiments on inclined dense jets has been conducted to determine the main geometrical characteristics of two nozzle inclinations, 15° and 52°, with a wide range of densimetric Froude numbers. These angles were chosen because few studies have been conducted on them and more data are needed, especially for the 52° angle, since there is only one study relating to this in the literature. Moreover, an artificial neural network method (GMDH) has been employed in this study to establish a model for estimating the geometrical characteristics of inclined buoyant jets, and this is its first use in this area (i.e., outfall systems). This part is a step towards a more comprehensive study that compares the GMDH with the other most common technical tools used in this field, which has been done in the third part of this thesis.

In the third part, a comprehensive study was conducted using same method of the artificial neural network (GMDH) described in the second part. The different thing in this part was the wide range of angles that employed in order to present a comprehensive model that can predict the geometrical characteristics of inclined buoyant jets for any angles located between 15° to 85°. To the best of the authors’ knowledge, this study with use of the GMDH method has not been used before for predictions for inclined negatively buoyant jets.

1.4. Thesis objectives and contributions

1.4.1. *Objectives*

The primary objective of this study is to improve the understanding of jet flow behavior in the near-field zone of coastal regions for discharged water and mixing for both positively and negatively buoyant jets, and to assist engineers to better understand the factors that may contribute to enhancing outfall system designs. Thus, the present study is divided into four major objectives, as follows, along with the secondary objectives of each:

1) **Experimental investigation of the effect of receiving water conditions on offset buoyant jet behavior:**
    - Experimentally evaluate the effect of receiving water conditions on offset buoyant jet behavior.
    - Determine the jet velocity distribution by Implementing the PIV system as an advanced technology.
    - Experimentally assess the behaviors of thermal and nonthermal buoyant offset jets discharged into fresh and saline stagnant water.
    - Provide some insights in order to understand the effect of different receiving water conditions on offset jet behavior.
2) **Numerical modeling investigation of the effect of receiving water conditions on offset buoyant jet behavior:**

- Assess and compare the performance of various numerical models (RANS) in simulating the behavior of offset buoyant jets injected into receiving water with different properties.
- Evaluate the potential of the OpenFOAM solver (pisoFoam) in simulating the behavior of offset buoyant jets.
- Examine the performance and capability of various turbulence models such as the realizable $\boldsymbol{k}$-$\boldsymbol{\varepsilon}$ and standard $\boldsymbol{k}$-$\boldsymbol{\varepsilon}$ as RANS turbulence models to better understand the nature of offset jet flows in receiving water with different properties.

3) **Experimental study of geometrical characteristics of the inclined negatively buoyant jets for angles 15° and 52°:**
   - Experimentally evaluate the effect of the different angles of inclined dense jets on the mixing characteristics.
   - Measure the main geometrical parameters of inclined dense jets for both angles
   - Identify and evaluate the most significant parameters affecting the jet behavior.
   - Provide more data by using a wide range of densimetric Froude numbers in order to better understand the effect of angles on the rate of the dilution as well as for use in prediction methods.

4) **Apply an artificial neural network called GMDH on the inclined negatively buoyant jets to predict the geometrical characteristics of the jet trajectory:**
   - Apply a non-linear method (GMDH) to develop explicit equations for predicting the geometrical characteristic.
   - Evaluate the performance of the GMDH model in assessing the mixing of inclined dense jets in outfall systems
   - Assess the accuracy of the GMDH predictions of the geometrical characteristics of the jet trajectory in inclined dense jets statistically
   - Compare the outcome of this method to the previous analytical solution models reported in the literature
   - Evaluate the potential output of the GMDH model as compared with the results of other models available in the literature

1.4.2. *Contributions*

The outcomes of this thesis are either published, accepted with revision, or under review, as several journal articles. The first three articles are included as chapters in this thesis.

1. Alfaifi[1], H., Mohammadian, A., Gildeh, H.K. and Gharavi, A., 2019. Experimental and numerical study of the characteristics of thermal and nonthermal offset buoyant jets discharged into stagnant water. *Desalination and Water Treatment*, 141, pp.171-186. https://doi.org/10.5004/dwt.2019.23477
2. Alfaifi[1], H., Mohammadian, A. and Bonakdari, H. Experimental investigation and model development of geometrical characteristics of 15° and 52° inclined negatively buoyant jets using GMDH neural network. Submitted to the *Journal of Coastal Research*. Accepted.
3. Alfaifi[1], H., Mohammadian, A. and Bonakdari, H. A comprehensive study for predicting the geometrical characteristics of an inclined negatively buoyant jet using GMDH neural network. Submitted to the Journal of *Desalination and Water Treatment*. Under review.

The following papers have been presented and published at various conferences, and not included in this thesis.

1. Alfaifi[1], H., Mohammadian, A. and Kheirkhah Gildeh, H. Experimental and numerical study of thermal buoyant wall jet in calm ambient water. Conference proceedings. *22nd Canadian Hydrotechnical*. 29 April-2 May, 2015, Montreal, Canada.
2. Alfaifi[1], H., Mohammadian, A. and Kheirkhah Gildeh, H. Comparison of Salinity and Temperature Mixing: Experimental and Numerical Study. *International Symposium on Outfall Systems* (ISOS 2016), 10-13 May, 2016, Ottawa, Canada.
3. Alfaifi[1], H., Mohammadian, A. Experimental study of the characteristics of a horizontal offset buoyant jet discharged into different conditions of stagnant water.

[1] The author was responsible for the experimental designed, setup, and execution experimentally and numerically, as well as analysis the data and writing of the manuscripts.

E-proceedings of the *8th International Symposium on Environmental Hydraulics* (ISEH 2018) 4 - 7 June, 2018, University of Notre Dame, Indiana, USA.

4. Alfaifi[1], H., Mohammadian, A. Experimental and Numerical Study of thermal buoyant offset jet Discharged into stagnant water. Conference proceedings, CSCE 2018, 13 - 16 June, 2018. Fredericton, Canada.

1.5.Novelty

The experimental results obtained in this study are of importance in practical applications for avoiding the environmental impacts of outfall systems. In addition, it can be useful for developing models for predictive purposes and validating numerical models, as well as being useful in helping in the decision-making for future outfall systems. Moreover, the numerical results can also provide methods for predicting these phenomena to limit the impact of the effluent discharged from desalination plants. Therefore, the novelty of this thesis is summarized in the following points:

- The effects of receiving water conditions on jet behavior are investigated and presented using experimental analysis from a PIV system. The effect of the source of the density difference (temperature versus salinity) on jet behaviors is determined and can be considered as a control parameter.
- A numerical simulation of positively offset buoyant jets was also performed using the finite volume open-source code OpenFOAM with a structured grid. The performance of three different Reynolds-averaged Navier-Stokes (RANS) turbulence models, i.e., the standard $\boldsymbol{k}$-$\boldsymbol{\varepsilon}$, realizable $\boldsymbol{k}$-$\boldsymbol{\varepsilon}$, and buoyancy-modified $\boldsymbol{k}$-$\boldsymbol{\varepsilon}$, was evaluated. The results of the numerical models confirmed the ability of the realizable $\boldsymbol{k}$-$\boldsymbol{\varepsilon}$ in predicting the jet trajectory better than other models.
- More than forty laboratory experiments were performed using a high-resolution digital camera to determine the main geometrical characteristics of inclined negatively-buoyant jets for two angles (15° and 52°), with a wide range of densimetric Froude numbers ($\boldsymbol{Fr_d}$) ranging from 11 to 75. The obtained results are useful for filling in the gaps in the data reported in the literature and for developing an analytical model for predictive purposes and validating numerical models, as well as being useful in helping in the decision-making for future outfall systems.

- A novel set of equations using a non-linear method (artificial neural network, ANN) called the group method of data handling (GMDH) was established and developed in this study to estimate the geometrical characteristics of the inclined negatively-buoyant jets for any angles located within the range of 15° to 85°.

1.6.Scope of work

Studying jet behaviors and their mixing in the near-field zone for either positively or negatively-buoyant jet can be performed experimentally and numerically using different techniques and different models for predicting. The scope of this thesis is limited to the following:

- In the positively-buoyant jet section, the results obtained in this study deal with the case of offset discharges whether multi-port diffuser or single port. Also, the results of this research were considered the difference between the densimetric Froude numbers and density differences ($\boldsymbol{Fr_d}$, ranging from 9.9 to 29.8) and density differences ($\Delta\boldsymbol{\rho}$, ranging from 5.1 to 17.41).
- The performance of the realizable $\boldsymbol{k}$-$\boldsymbol{\varepsilon}$ numerical model is limited to the $\boldsymbol{Fr_d}$ values, ranging from 9.9 to 29.8.
- As for the second part (the negatively-buoyant jet), the experimental results of angles 15° to 52° and the explicit equations obtained from GMDH model can be applied when jet reaches the fully-turbulent stage (i.e., the Reynolds number ($\boldsymbol{Re}$) is greater than 2000).
- The prediction results obtained for the proposed model (i.e., GMDH approach) can be used for any angles of the inclined dense jets located between 15° to 85° with the limitation in $\boldsymbol{Fr_d}$ not exceeding 100.

1.7.Thesis organization

This thesis is divided into five chapters and is organized as a series of technical papers, as follows:

Chapter 2 presents the first technical paper, entitled "Experimental and numerical study of the characteristics of thermal and nonthermal offset buoyant jets discharged into stagnant water". This chapter includes an extensive literature review on positively offset buoyant jets and describes the experimental setup and procedures along with the PIV system. The theoretical of the numerical model, as well as the governing equations and boundary conditions are also discussed in detail. The experimental and numerical results are also provided. This chapter was published in the Journal of Desalination and Water Treatment, 141 (2019) 171-186. Also, some results of this work were published and presented at three different conferences: the International Symposium on Outfall Systems (ISOS) organized by the IAHR-IWA Joint Committee on Marine Outfall Systems 2016, Ottawa, Canada; the 8th International Symposium on Environmental Hydraulics (ISEH 2018), Indiana, USA; and The Canadian Society for Civil Engineering (CSCE) 2018 Fredericton Annual Conference, Fredericton, Canada.

Chapter 3 describes the second technical paper, “Experimental and analytical study of geometrical characteristics of 15° and 52° inclined negatively-buoyant jets”. A general introduction to negatively inclined dense jets is provided at the beginning of this chapter, followed by a detailed description of the previous efforts of the researchers. Theoretical information regarding dimensional analysis and experimental procedures is also presented. The results of the laboratory experiments for the main geometrical characteristics of the jet trajectory obtained for both angles are presented. An introduction to the artificial neural network (group method of data handling, GMDH) is also provided, followed by the predicted results obtained from this method, as well as the comparison results for some previous analytical solutions. This chapter is accepted with revision in the Journal of Coastal Research.

Chapter 4 presents the third technical paper, “a comprehensive study for predicting the geometrical characteristics of an inclined negatively-buoyant jet using GMDH neural network”. As previous chapters, this part starts with a general introduction for the negatively buoyant jet with the previous conducted efforts in the experiments and modeling, focusing on the analytical and numerical approach. Then, the dimensional analysis and the methodology used in this chapter regarding to the GMDH approach are also presented. The predicted results of the GMDH method are provided along with the evaluation results obtained from statistical indices as well as the comparison with the previous analytical models. This chapter has been submitted to the Journal of Desalination and Water Treatment.

Chapter 5 summarizes and concludes efforts that have been drawn based on the work from the previous chapters. Furthermore, it provides information in relation to how the work could progress further, with recommendations for future studies.

Chapter 2. Experimental and numerical study of the characteristics of thermal and nonthermal offset buoyant jets discharged into stagnant water[2]

Abstract

This paper evaluates the effect of receiving water conditions on offset buoyant jet behavior. Several experiments on the discharge of thermal and nonthermal horizontal buoyant offset jets into stagnant ambient water are conducted. Particle Image Velocimetry (PIV) is used to measure the time history of the jet velocity distribution. Various characteristics of the jet flow, such as the centerline jet trajectory, jet growth rate and jet velocity decay, are discussed. All comparative experiments are conducted with the same densimetric Froude numbers (Fr_{d}, ranging from 9.9 to 29.8) and density differences ($\Delta\rho$, ranging from 5.1 to 17.41). The results show that the trajectories of thermal jets are not the same as those of nonthermal jets, which suggests that thermal jets travel farther than nonthermal jets. The experimental results were then compared to predictions of three Reynolds-averaged Navier-Stokes (RANS) turbulence models: the standard k-ε, realizable k-ε, and buoyancy-modified k-ε. The best prediction of the centerline jet trajectory was found to be obtained from realizable k-ε. The study results revealed that the source of buoyancy (salinity versus temperature for the same values of Fr_{d} and same $\Delta\rho$) affects the trajectory and mixing properties of the jet.

Keywords: Offset jet; buoyancy; salinity; Particle Image Velocimetry (PIV); densimetric Froude number, realizable $\boldsymbol{k}$-$\boldsymbol{\varepsilon}$

---

[2] This chapter has been published as Alfaifi, H., Mohammadian, A., Gildeh, H.K. and Gharavi, A., 2019. Experimental and numerical study of the characteristics of thermal and nonthermal offset buoyant jets discharged into stagnant water. Desalination and Water Treatment, 141, pp.171-186. https://doi.org/10.5004/dwt.2019.23477

2.1. Introduction

In recent decades, seawater desalination systems have been considered the best option for providing drinkable water to the public in arid and semiarid countries. This method has created an increased demand for the planning and execution of new desalination plant projects. The largest Multistage Flash (MSF) desalination plant in the world is located in Saudi Arabia, which is producing 0.96 million m^3/day of the drinkable water and approximately 1.4 million m^3/day of the effluents that is usually discharged back, with high temperature and salinity, to the aquatic environments (Ahmad, 2002). These effluents are usually disposed using submerged pipes. These pipes (outfalls) are located on the coast near the plants and thus creates a plume of pollutants (i.e., jet) that may affect the marine environment.

It is important to carefully study a jet's behavior and its environmental impact on water bodies close to the discharge point. Several studies have revealed that discharging these effluents has an adverse influence on the marine ecosystem, particularly in the near-field zone of the discharge (Cambridge et al., 2017; Hashim and Hajjaj, 2005; Lattemann and Höpner, 2008; Mabrook, 1994; Milione and Zeng, 2008; Roberts et al., 2010). Therefore, it is necessary to study the characteristics of the near-field mixing zone to prevent any adverse impacts caused by the outfall systems and to maintain the marine environment such that it remains clean and suitable for its inhabitants and usable as a sustainable source of drinking water for future generations.

Although outfalls with offset jets are currently used in many offshore industrial plants (e.g., desalination plants), little research has been conducted on their mixing characteristics, especially for buoyant offset jets with both salinity and temperature variations. Differences between the characteristics of the jet and those of the receiving water body (e.g., density differences due to salinity or temperature) may also affect the jet and its mixing characteristics.

Most previous experimental and numerical studies dealing with single-port horizontal offset jets have focused on dense jets discharged into fresh water (Agelin-Chaab and Tachie, 2011; Assoudi et al., 2016, 2015; Bosanquet et al., 1961; Gu, 1996; Hoch and Jiji, 1981; Kanna and Das, 2005; Nasr and Lai, 1998; Shao and Law, 2009, 2011). Some of these studies were performed using the PIV system, either alone or in combination with laser-induced fluorescence (LIF). As mentioned above, most existing experimental studies have focused on offset dense jets; On the other hand, offset buoyant jets have rarely been studied and require further investigation.

Rawn and Palmer (1930) were the first researchers to attempt to investigate the mixing characteristics of horizontal offset jets discharged into seawater, and their study included 388 experimental observations of dilution at the surface for offset freshwater jets injected into water of higher density. Later, Michas and Papanicolaou (2009) investigated horizontal round turbulent buoyant jets discharged into a homogeneous and calm ambient fluid and studied both jet-like and plume-like cases to cover a wide range of applications. The mixing and geometric characteristics, such as trajectories, were obtained with video imaging; the turbulence properties were measured with fast response thermistors, and the dilution factors were evaluated. They found that the flow exhibited jet-like behavior in the horizontal regime; moreover, the mean and turbulent temperature profiles became asymmetrical in the transition and the vertical regime.

Recently, the effect of density differences between two liquids was studied by Eleuch et al. (2018), who conducted some laboratory experiments to evaluate the evolution of a pure water jet injected vertically downwards into water of higher density. The researchers' study focused on the effect of the flow rate and the difference in density between the jet and the surrounding salt water. The results showed that jet penetration depth was affected by the flow rate and was increased by increasing the flow rate. Moreover, the jet penetration depth increased significantly when the density difference between the two liquids was decreased.

All the previously mentioned studies were conducted experimentally. However, numerical simulations of buoyant offset jets are ongoing and require further investigation. A numerical investigation of a round jet discharged horizontally and continuing with sediment particles was carried out by Liu and Lam (2015). The authors applied large eddy simulation (LES) for the fluid phase comparison, while Lagrangian particle tracking was used to calculate the motion of the sediment particles.

As a result, recent experimental and analytical investigations of outfall systems have indicated that Fr_{d} is correlated to many flow characteristics and can therefore be considered an influential parameter as a function of density (Kheirkhah Gildeh et al., 2015a; Zhang et al., 2016). Therefore, the mixing characteristics of buoyant jets can be controlled and affected by changing this important parameter.

To the best of the authors' knowledge, most of the existing literature on turbulent (positively) buoyant jets focuses either on flow kinematic behavior or on the mixing characteristics of effluent discharge into freshwater (as a dense or buoyant jet). However, the effects of the properties of the receiving water, particularly water of high salinity, on the mixing and trajectory characteristics of jets have rarely been studied. Thus, this paper reports experimental and numerical investigations of the behaviors of thermal and nonthermal buoyant offset jets discharged into fresh and saline stagnant water. Fourteen thermal and nonthermal experiments were conducted using the PIV technique. The performance of various turbulence models was then tested using the open-source CFD code, Open Field Operation and Manipulation (OpenFOAM). Three Reynolds-averaged Navier-Stokes (RANS) turbulence models were examined in this study (i.e., the standard k-ε, realizable k-ε and buoyancy-modified k-ε models), and the results were compared with the experimental data.

This paper is organized as follows. Theoretical concepts such as dimensionless groups and density calculation are presented in Section 2.2. In Section 2.3, the experimental setup and procedures are described. The results of some experimental cases are shown and discussed in Section 2.4. Computational approach such as governing equations, numerical methods and boundary conditions are presented in Section 2.5, as well as the preliminary results of numerical simulations compared with the experimental results. Finally, some concluding remarks complete the study.

2.2. Theory

2.2.1. *Dimensionless groups*

Figure 2-1 shows a schematic sketch of an offset positive round buoyant jet discharging horizontally into a stagnant water body (ambient velocity, $U_a = 0$). The discharge port (jet) has diameter D and is placed above a horizontal solid surface at a specific distance. The receiving water (ambient water) is an unstratified fluid with a constant density ρ_a. The jet has a discharge velocity of U_0 and density of ρ_0 (where $\rho_0 < \rho_a$). The streamwise coordinates of the jet and the centerline of mean velocity are denoted by s and U_m, respectively, and b denotes the jet half-width.

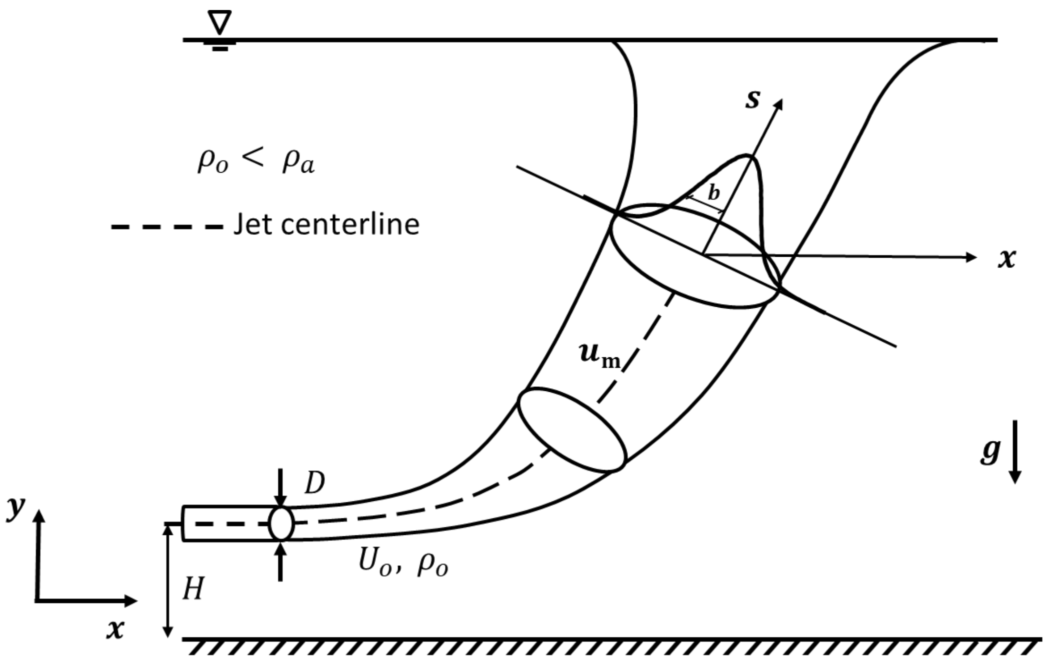

Figure 2-1: Schematic sketch of a positive round buoyant jet in stagnant ambient water.

When a horizontal round buoyant jet is discharged into a stagnant fluid, the jet in the regions closer to the nozzle is dominated by momentum flux M_0 (i.e., within a short distance of the discharge port). The buoyancy flux effect B_0 then increases and dominates the jet, forcing it to rise to the water surface. Jet behavior is characterized by various fluxes: discharge volume flux $Q_0 = U_0 \pi D^2/4$, momentum flux $M_0 = U_0\, Q_0$, and buoyancy flux $B_0 = Q_0\, g'_0$, where $g' = g(\rho_0 - \rho_a)/\rho_a$ is the effective gravitational acceleration and g is the gravitational acceleration (Fischer et al., 1979). L_M (the momentum length scale) is a measure of the distance over which the jet's momentum is more important than its buoyancy, and L_Q (the source length scale) indicates the length over which the source discharge is important. The axes are normalized using L_M where $L_M = M_0^{0.75}/B_0^{0.5}$ (the ratio of the momentum and buoyancy fluxes) and where $L_Q = Q_0/M_0^{0.5}$ (the ratio of the volume and momentum fluxes). To determine the geometric and mixing characteristics of the turbulent buoyant jet, these two length scales are used. The jet densimetric Froude number Fr_d, the ratio of inertia to buoyancy, can be derived for turbulent buoyant jets and is proportional to the ratio of length scales: $Fr_d = L_M/L_Q = U_0/(g'D)^{0.5}$. The mean velocity U_m of the jet centerline, which decreases with longitudinal distance s from the discharge point, can also be calculated using the formula as following (Cuthbertson and Davies, 2008):

$$U_m = K\sqrt{M_0}/s \tag{2-1}$$

2.2.2. *Density calculation*

The density can be calculated based on the equation of state. Millero and Poisson's equation (Millero and Poisson, 1981) is one of the most widely used formulas for calculating density as a function of temperature and salinity. This formula is referred to as the equation of state of seawater and is used in this paper for calculating the density. The limits of temperature and salinity in this equation are $0 < T < 40$, $0.5 < S < 43$. Later, Millero and Huang (Millero and Huang, 2009) conducted new seawater density measurements to modify Millero and Poisson's equation of state with the aim of expanding its limits to a wider range of temperature (0-90 ℃) and absolute salinity S_A (0-70 kg/m^3) values and found that the results obtained were consistent: the standard error was 0.0063 kg/m^3.

2.3. Experimental setup and procedures

The scaled model experiments were conducted in the Water Resources Laboratory at the University of Ottawa, Canada. The experiments were performed in a rectangular transparent glass tank 1.2 m long, 0.5 m wide, and 0.5 m deep, as shown in Figure 2-2. The bottom and sidewalls of the tank were made of glass panels. A circular nozzle with an internal diameter of 5.18 mm was placed horizontally at one end of the tank (centered), far enough (10 cm) from both the bed and back walls to avoid any influences and to ensure a fully developed velocity profile. All experiments were performed using water from the same source (i.e., tap water). A buoyant jet (with a density less than that of the receiving water) was generated by discharging water (heated into cold water for thermal jets and unheated freshwater into dense water for nonthermal jets) into the tank through this nozzle.

The nozzle was connected to a pipe equipped with: (1) a flow meter (Rotameter, FL-3840ST, up to ±2% FS accuracy, OMEGA) to determine the flow rate of the discharged water; (2) valves to control the discharge water. The pipe was connected to a constant-head tank with dimensions of 0.75 m length, 0.3 m width, and 0.3 m depth. This tank (containing the discharge water, which was fed by gravity into the large tank) was located approximately 1.5 m above the discharge nozzle.

The constant-head tank had two separate storage tanks, one of which was used to store surplus discharged water, as shown in Figure 2-2. The water was then returned from the storage tank using a pump to maintain a constant water level. The storage tank was equipped with an instrument that enabled precise temperature control (Corio CD Heating Immersion & Bridge Mounted Circulator) with an accuracy of approximately ±0.03 ℃. This device was used to ensure that the temperature in the discharge tank remained constant during the experiments. To ensure that the water temperature in the pipe was equal to that of the heated water in the elevated tank, the pipe was covered with insulating material. Another outlet was located at the end of the discharged pipe, outside of the experimental tank, at a distance of 20 cm upstream of the nozzle tip to test the temperature of the discharged water before running the experiments. Moreover, the nozzle outlet was equipped with a very thin sensor, which was connected to a thermometer, to measure the flow temperature during the experiments.

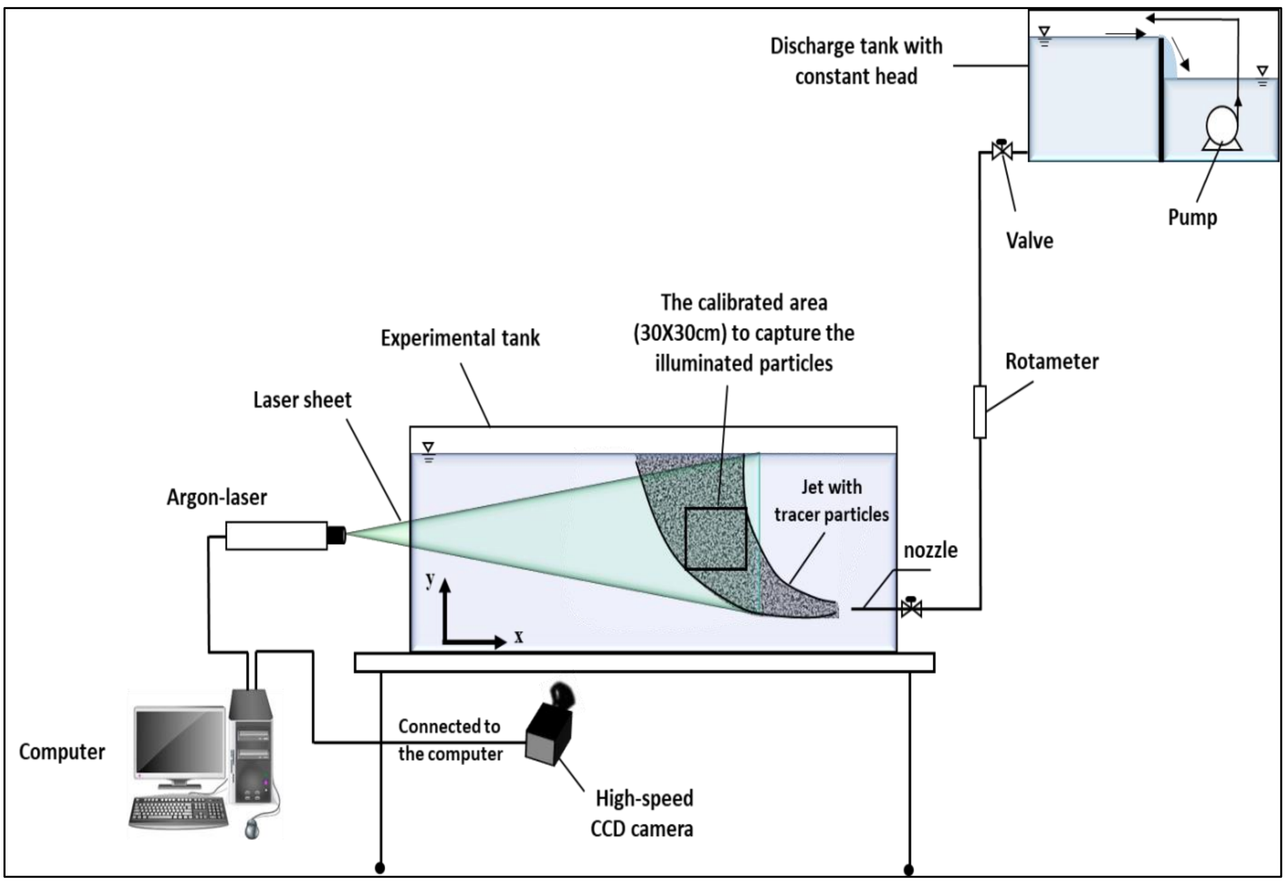

Figure 2-2: Schematic view of the experimental setup with the PIV system

2.3.1. *Particle image velocimetry (PIV)*

In the present study, a PIV system was used to measure the time history of the velocity distribution. PIV system is an experimental technique which has four main components: a laser box unit (an Nd:YAG laser with a frequency of 100 mJ per pulse at a wavelength of 532nm), a high-speed camera (sCMOS) that achieves a 40Hz frame rate at full resolution, a computer with the Davis software, and a synchronizer/timing box.. The main function of the PIV system is to photographically record the movement of tracer particles in fluid. Thereafter, the motion of the particles is determined using image processing methods, and the flow velocity is obtained from the photographic recordings. In most applications, small tracer particles are added to the discharge flow to follow the fluid path. Two green laser beams were emitted from the laser box at a wavelength of 532 nm and were designed to overlap to ensure the correct velocity field calculation. The beams were then passed through the optical system to generate planar laser sheets. The high-resolution sCMOS camera (2560 x 1026 pixels) was placed at a cross-section of the tank that was illuminated by a laser sheet to capture the illuminated tracer particles in the fluid flow. An optical filter was placed in front of the camera lens to allow wavelengths of less than 532 nm, which were scattered by the particles, to pass. Images were recorded in the double-frame (image) mode; from these images, the instantaneous velocity field was calculated by cross-correlation calculations between the two frames. During laser illumination, the camera captured two frames (one frame for each pulse of the pulse pair) separated by a very small time interval. The obtained images were then transferred to the processor for the cross-correlation computations (Raffel et al., 2007).

2.3.2. *Experimental procedure*

Two sets of experiments were conducted using a high-resolution camera to determine the jet behavior under two sets of conditions. The jet velocity was captured using the PIV system. The capture zone was a 30 cm x 30 cm square area of the jet trajectory, as shown in Figure 2-2. In the first set of experiments, a thermal buoyant offset jet of hot water was discharged into cold water. The second set of experiments utilized a different concept to generate a buoyant jet without the presence of a temperature differential, in which a high concentration of salt (sodium chloride; NaCl; high purity (99.99%)) was dissolved in the ambient water to increase its density, while the discharged water was fresh (i.e., not saline). The temperatures of the jet and the ambient water were identical. The density was highly dependent on changes in salinity due to the similarity of the temperature in both fluids. For each comparison experiment, the values of Fr_d and $\Delta\rho$ were constant. The amount of salt required to achieve the target density difference was calculated using the Millero and Poisson (Millero and Poisson, 1981) formula. The experimental parameters are summarized in Table 2-1.

Table 2-1: Experimental parameters

Case	D (mm)	U_0 (m/s)	T_0 (°C)	S_0 (ppt)	ρ_0 (kg/m³)	T_a (°C)	S_a (ppt)	ρ_a (kg/m³)	Fr_d	$\Delta\rho$ (kg/m³)
Thermal jet experiments										
T1	5.18	0.16	38.60	0.00	992.75	21.5	0.00	997.89	9.90	5.10
T2	5.18	0.32	39.60	0.00	992.37	21.5	0.00	997.89	19.10	5.50
T3	5.18	0.23	50.50	0.00	988.06	21.5	0.00	997.89	10.30	9.80
T4	5.18	0.45	50.70	0.00	987.75	21.5	0.00	997.89	19.80	10.10
T5	5.18	0.48	39.55	0.00	992.39	22.2	0.00	997.73	29.10	5.30
T6	5.18	0.67	50.65	0.00	987.77	22.2	0.00	997.73	29.80	10.00
T7	5.18	0.60	66.40	0.00	980.24	23.3	0.00	997.47	20.25	17.23
Nonthermal jet experiments										
S1	5.18	0.16	21.5	0.00	997.89	21.5	6.79	1003.00	9.90	5.10
S2	5.18	0.32	21.5	0.00	997.91	21.4	7.33	1003.50	19.10	5.60
S3	5.18	0.23	21.3	0.00	997.93	21.3	13.00	1007.80	10.30	9.80
S4	5.18	0.45	21.3	0.00	997.95	21.2	13.52	1008.20	19.80	10.20
S5	5.18	0.48	21.3	0.00	997.91	21.4	6.80	1003.10	29.80	5.10
S6	5.18	0.67	21.2	0.00	997.97	21.1	13.30	1008.00	29.70	10.10
S7	5.18	0.60	34.5	0.00	994.21	34.5	23.60	1011.62	20.29	17.41

In this study, two different concepts have been used in the two sets of experiments (fourteen experiments), which are divided into two groups. Each group has seven cases with the following features: In the first group (the first set of experiments, thermal experiments, i.e., T1 to T7), the density gradient is caused only by the difference in temperature, and the salinity is zero. In the second group (the second set of experiments,-nonthermal experiments, i.e., S1 to S7), the density gradient arises from differences in salinity, and the domain temperature is constant. Two parameters were maintained at similar levels in all comparisons: the Fr_d and $\Delta\rho$ between the jet and ambient water.

To determine whether the source of the density difference (temperature versus salinity) affects jet behavior, as controlling parameter, the density differences due to temperature ($\Delta\rho_{thermal} = \rho_a - \rho_0$) and salinity ($\Delta\rho_{nonthermal} = \rho_a - \rho_0$) were also set as equal ($\Delta\rho_{thermal} = \Delta\rho_{nonthermal}$) in the two groups of experiments. In these experiments, the development of the jet was recorded using a PIV system. For brevity, only the results of three comparison cases (T1 and S1, T3 and S3, and T7 and S7) are shown in most of the figures.

2.4.Experimental results and discussion

2.4.1. *Experimental observations*

Finding the parameter with the most influence over jet flow characteristics and behavior is complicated since each parameter is influenced by others. For example, many flows are characterized by and correlated with a densimetric Froude number, which is considered a function of density. Moreover, the density of effluents can be changed by altering their temperature or concentration (here, salinity). Therefore, changing the density of the discharge water can also control the jet characteristics. Thus, it is logical to assume that jets with different temperatures and salinity values but with the same densimetric Froude number can behave similarly provided they are discharged into the same ambient water conditions. However, if the ambient water conditions are changed, the effect of these parameters may be expected to change, and the jet behavior would not be the same.

To further clarify this point, Figure 2-3 shows the results for two cases of offset buoyant jets with the same densimetric Froude number and density difference ($\Delta\rho_{thermal} = \Delta\rho_{nonthermal}$). One can clearly see the difference in the jet trajectories; one (nonthermal) jet reaches the water surface at a point closer to the source of discharge than the other. Therefore, to visualize the effects of the receiving water conditions on the jet trajectory of any discharged flow, numerous experiments have been conducted. In experiments in which salt was used in the ambient water (i.e., nonthermal experiments), all jets reached the water surface at shorter distance from the source than those reached in the thermal experiments. Moreover, the time to reach the surface was also shorter. More details are presented in the next section. In addition, the nonthermal jets reached the water surface with a higher velocity than was the case for the thermal jets. This result is evidence that a mechanism is making the jet rise faster toward the water surface. This raises an important point about this mechanism and its interaction with the momentum force: It is anticipated that nonthermal jets decay faster than thermal jets.

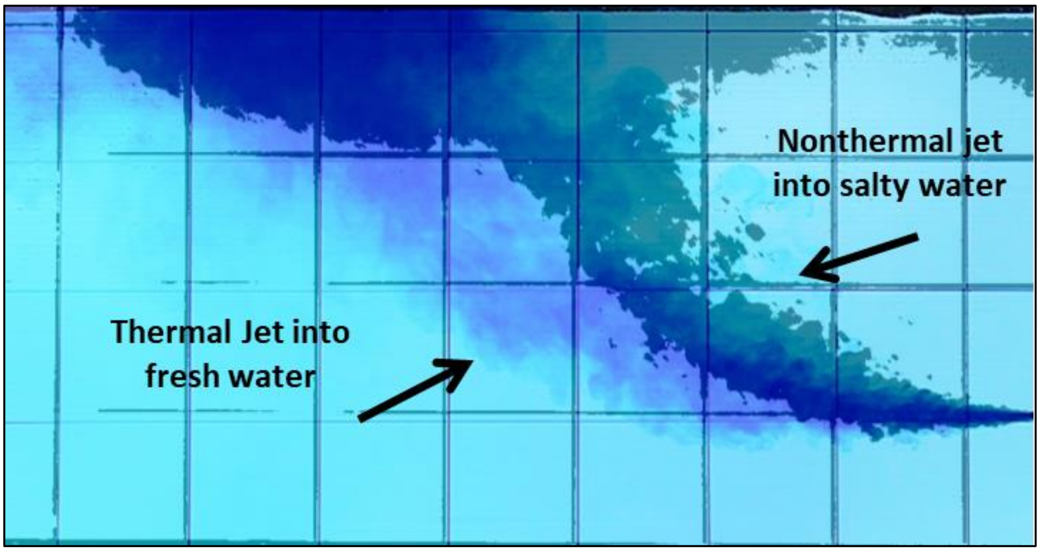

Figure 2-3: Comparison between the jet trajectory patterns of thermal and nonthermal jets.

2.4.2. *Jet evolution and propagation speed*

When buoyant jets are discharged into two stagnant water bodies with different properties, the evolution and propagation of the jets may differ. To verify this notion, an experiment was conducted to compare thermal and nonthermal jets with similar densimetric Froude number and density differences as they discharged into tanks with different ambient water conditions: freshwater (zero salinity) and denser, saline water. A blue dye was used to visualize the jet trajectories. It was observed that the penetration of the thermal jet was very slow; thus, it reached the surface more slowly than the nonthermal jet, which penetrated faster and reached the surface in less time and over a smaller distance. These phenomena and the scaled time for both jets can be seen in Figure 2-4.

From the thermal jet experimental results, it was observed that the jet penetrates the ambient water horizontally and progressively slows down. During this transient phase, a large head is formed in front of the jet. At a certain distance from the nozzle, the jet reaches a maximal depth of penetration, the buoyancy flux becomes larger, and the jet begins to slowly rise toward the water surface. Gradual expansion was observed from both sides of the thermal jet (inner and outer) from the nozzle to the extreme point of the jet prior to reaching the water surface. It is clear from the figures that the thermal jet propagates more slowly than the nonthermal jet. It can also be seen that the thermal jet reached the stationary depth (the point at which the effective force on the jet transforms from momentum to buoyancy flux) at t = 10 s, started to slowly rise to the top at t = 15 s, and reached the surface at t = 30 s. However, in the nonthermal case, the jet reached the stationary depth of penetration at less than 5 s and reached the surface at t = 15 s; that is, the thermal jet took two times longer to reach the water surface than the nonthermal jet.

Although the flow rate, Fr_d and $\Delta\rho$ were the same in both experiments, the jet penetration depths were different. The results were consistent with those obtained by Eleuch et al. (2018), who demonstrated that jet penetration depth and head spread decrease as the difference in density between the jet and ambient water increases.

In contrast, in the nonthermal experiments, the jets were progressively faster, and no head development was seen. As clearly shown in the figures for the nonthermal jet (Figures 2-4a-e), the jet reached the water surface at a distance of 50 cm in an axial direction from the nozzle tip; in contrast, the thermal jet took longer and reached the water surface at a distance of more than 70 cm. It was also noted that the effect of buoyancy on the nonthermal jet may have started earlier and at a shorter distance from the nozzle and then forced the jet to rise toward the water surface more rapidly. This distance is shorter than that in the case of the thermal jet. Moreover, to compare the propagation, considering Figure 2-4b at the scaled time 0.4 for both jets, it can be seen that the thermal jet is clearly wider.

This result may lead to the conclusion that if the jet remains longer within the water before reaching the surface, the jet propagation increases, thus increasing the dilution. These

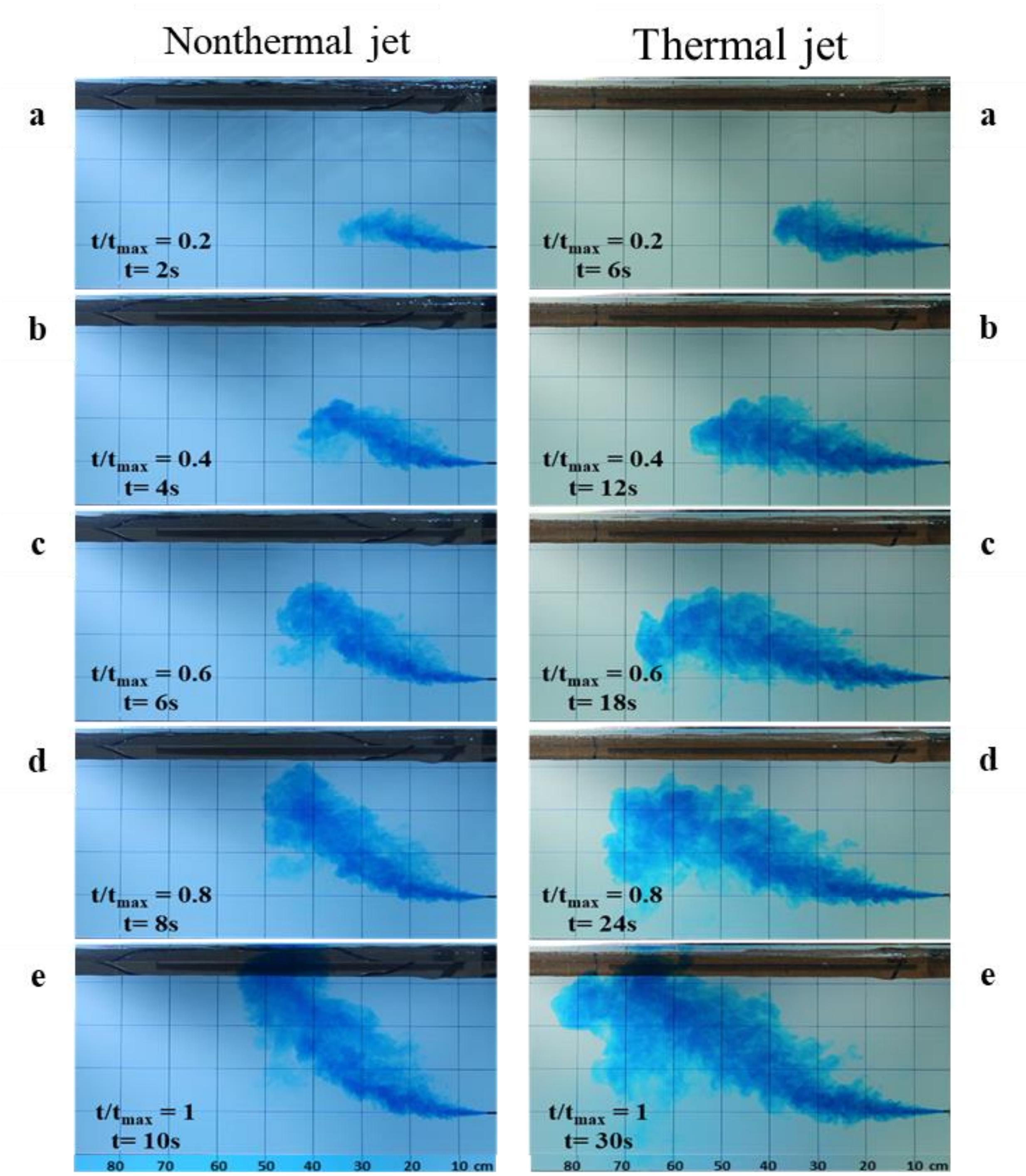

Figure 2-4: Comparison between the times to reach the water surface for the thermal and nonthermal jets (cases T7 and S7).

figures were chosen for comparison due to the similarity of the locations and distances from the nozzle. In addition, it was seen that the jet tends to be flatter before reaching the water surface for all thermal experiments than for the nonthermal cases, which are mostly steeper.

An explanation of these phenomena is as follows. The difference between the two cases might be attributed to the difference in the content of the ambient water, which can be considered a solution with physical properties for the thermal experiment and a solution with chemical properties for the nonthermal experiment. Indeed, in the thermal experiment, the jet can be affected by the surrounding cold water. Thus, the thermal energy of the jet is mainly lost in the surrounding water; hence, the jet's velocity decays more rapidly (Rathore and Das, 2015). However, for the nonthermal experiment, it is known that if the water molecules are totally saturated with salt, it becomes a highly concentrated solution, such that there is less opportunity for any solution to move between the water molecules. Therefore, due to its low density, the solution rises up, after a distance, from the nozzle to the surface of the water.
As a result, when comparing the jet trajectories of the thermal and nonthermal cases, the divergence between the jets was noted to increase. Therefore, the density difference due to different salinity can be considered an influential parameter that can affect and change the jet trajectory. Thus, based on the results obtained in this study, it could be argued that salinity can also be considered a significant parameter for characterizing jet flow in a fluid.

2.4.3. *Jet flow pattern*

Dispersion of the fluid discharged within a water body can be affected by the characteristics and conditions of the receiving fluid. In this study, it was observed that the jet pattern required less time and distance to rise to the surface in the nonthermal experiments (retracted backward) than in the thermal experiments, in which the salinity in both the discharged and receiving water was zero. Figure 2-5 presents superimposed time-averaged velocity vectors and contour maps of the velocity obtained from the PIV results for two comparison cases (T1 compared with S1, and T3 compared with S3); Fr_d was 9.9 for the first comparison and 19.8 for the second.

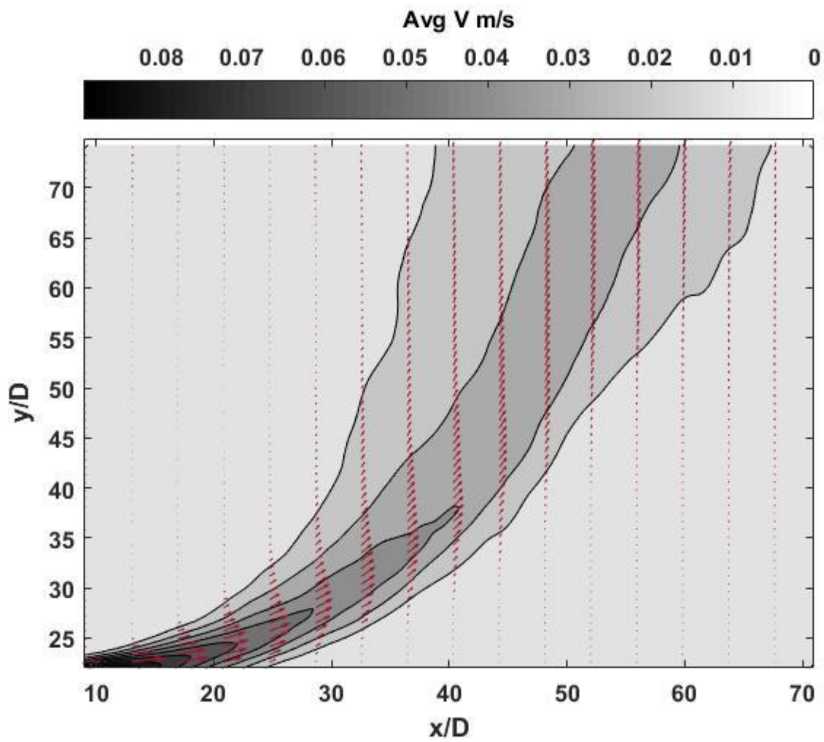
Avg V m/s
0.08 0.07 0.06 0.05 0.04 0.03 0.02 0.01 0
y/D
x/D

(a)

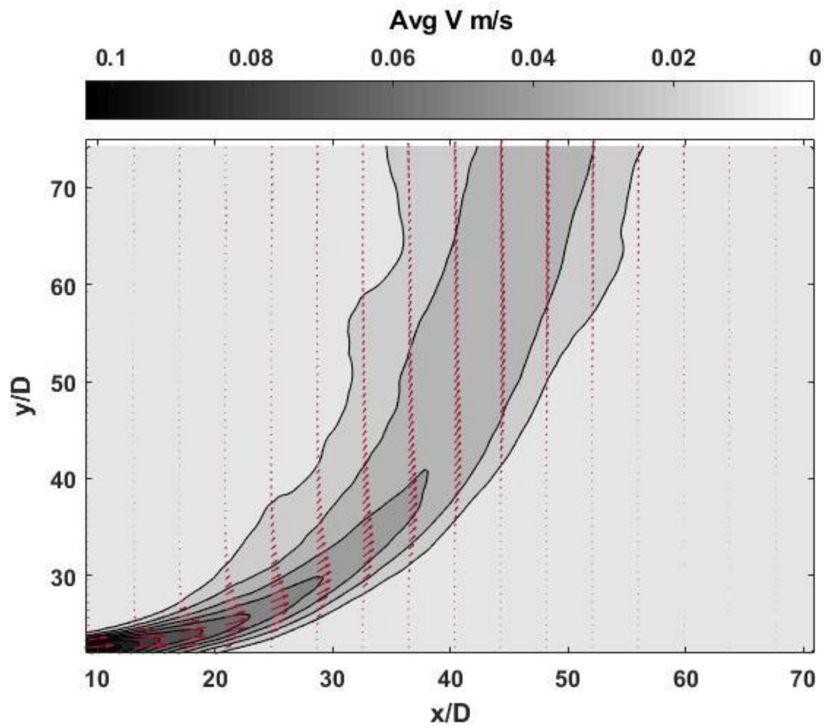
Avg V m/s
0.1 0.08 0.06 0.04 0.02 0
y/D
x/D

(b)

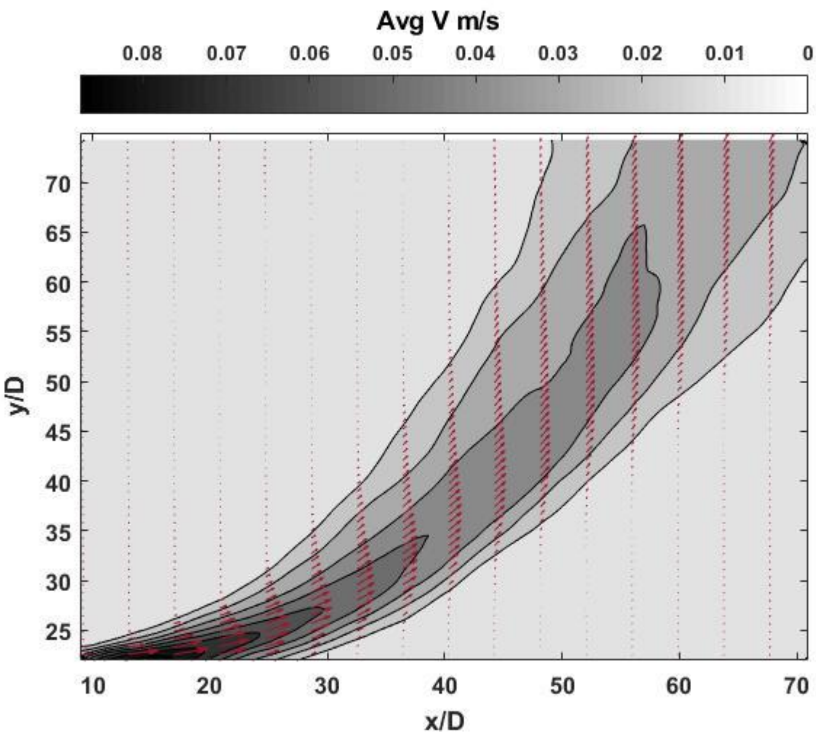

(c)

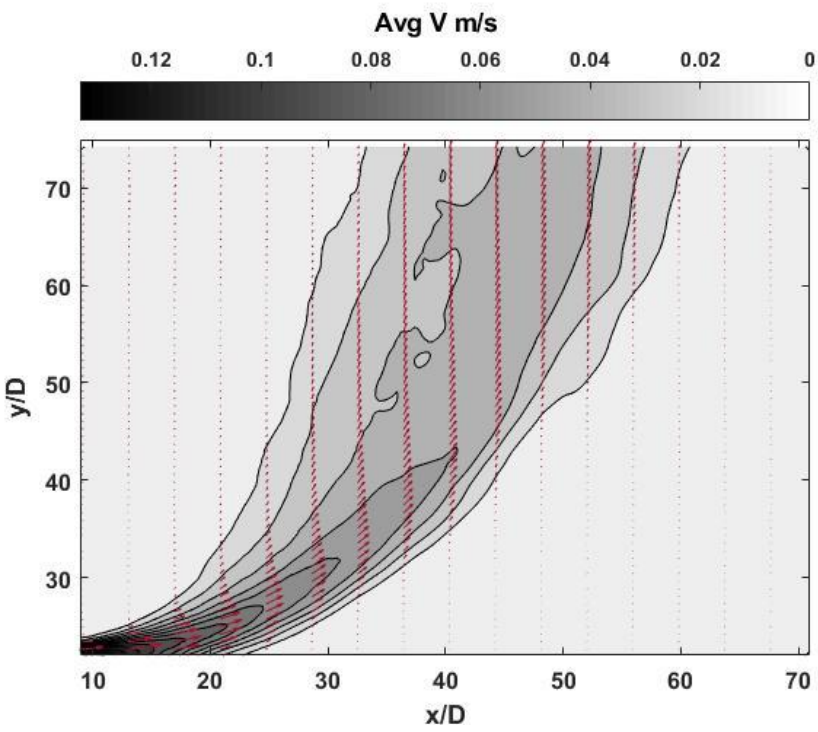

(d)

Figure 2-5: Dimensionless mean velocity vectors with contour maps for: (a) case T1- thermal jet; (b) case S1- nonthermal jet; (c) case T3- thermal jet; and (d) case S3- nonthermal jet.

The PIV experimental results showed that all the nonthermal jets reached the water surface within a shorter distance than the thermal jets. In the thermal cases, the ambient water conditions (zero salinity) seem to allow the jet to spread more easily when compared with the nonthermal cases; this causes the jet to travel farther from the nozzle and reach the surface at a point farther than that reached by the nonthermal jet. As a result, the jet spread is greater for the thermal jet and increases gradually as the distance from the source increases, indicating greater dilution. This process was previously reported for a negatively-buoyant jet (i.e., a dense jet) (Roberts and Toms, 1987; Zeitoun et al., 1970). These authors mentioned that when the jet trajectory is longer, the dense jet can achieve a higher dilution; as a result, if the jet remains in the water body for a longer time before reaching the surface, the discharged water will become more diluted. Therefore, and based on the present study, it can be argued that if a thermal jet is discharged into stagnant and unstratified water, the level of dilution will be higher than for a nonthermal jet.

An industrial plant discharging cold freshwater that reaches the water surface at a point closer to the source is an example of a nonthermal jet. Therefore, this result is likely to be of importance in practical applications for avoiding the environmental impacts of outfall systems, as it relates to determining how far the intake pipe (feed pipe) should be placed from desalination plants.

2.4.4. *Jet trajectory*

Jet trajectory, also known as jet centerline, is a very important parameter in outfall system design because it identifies the path followed by the jet and the location where the jet reaches the water surface (in the case of a positive jet) or the seabed (in the case of a negative jet). The jet trajectory passes through three regions: 1) an initial region, 2) a transitional region, and 3) a buoyant or free-jet region. In this study, the results of both experiments were obtained at the transition region and at the beginning of the buoyant region. The centerlines of the mean velocities obtained from the experimental measurements of the thermal and nonthermal jets are shown in Figure 2-6. The centerline values are obtained from the maximum velocity at various cross-sections of the jets. Three different experimental results obtained with different values of Fr_d and $\Delta\rho$ are shown for comparison. The Fr_d values were ≈ 10 for the first and second comparisons and ≈ 20 for the third comparison. The $\Delta\rho$ values were ≈ 5 for the first comparison and ≈ 10 for the second and the third comparisons. The results clearly indicate a difference in the behavior of the jet trajectory between the two sets of experiments. As shown in these figures, all nonthermal jets were above the thermal jets, indicating that in the dense water, the nonthermal jets rose toward the water surface more rapidly and within a shorter distance from the nozzle than did the thermal jets. Although the values of $\Delta\rho$ and Fr_d were equal between the experiments in all comparisons, it can be seen that the nonthermal jets behaved differently than the thermal jets.

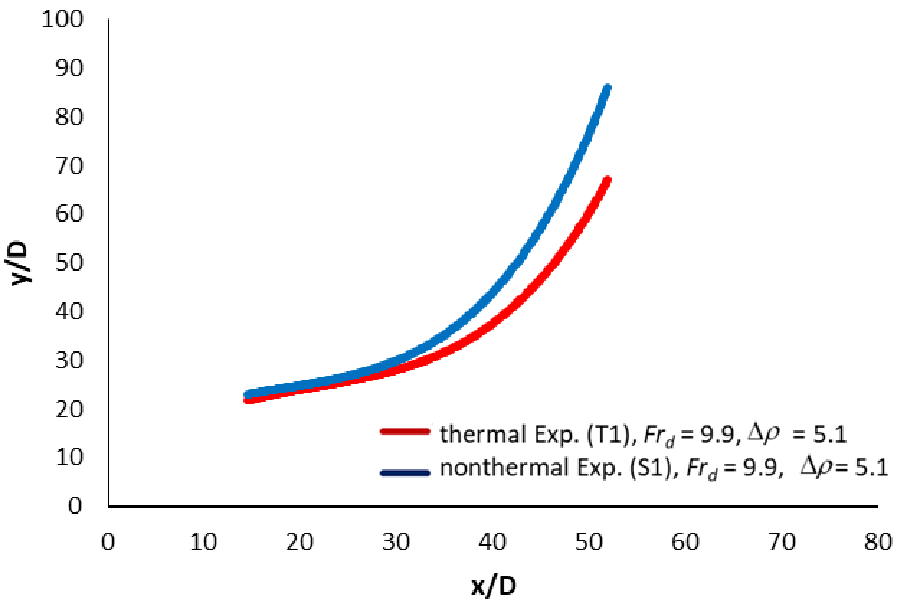

(a)

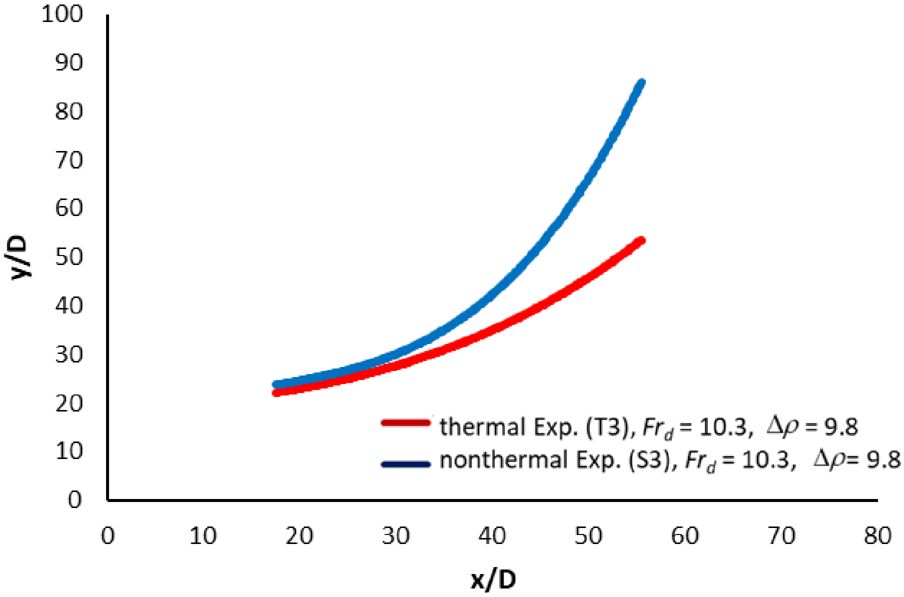

(b)

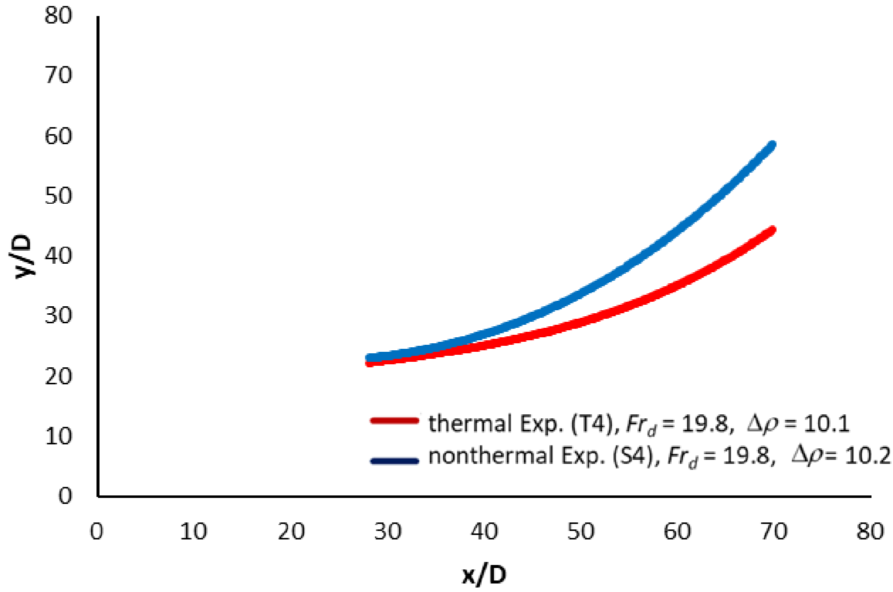

(c)

Figure 2-6: Centerline trajectory of the velocity profile for both experiments: (a) comparison of T1 with S1; (b) comparison of T3 with S3; and (c) comparison of T4 with S4.

In addition, an effect of $\Delta\rho$ was clearly observed on jet trajectory behavior. The deviation between the thermal and nonthermal jet centerlines due to $\Delta\rho$ increased even though the values of Fr_d were equal (Figure 2-6a and b). Moreover, Fr_d had an almost nonexistent effect, although the value was changed, while $\Delta\rho$ values remained almost the same (Figure 2-6b and c). As a result, one can conclude that differences in density can affect jet trajectory behavior; therefore, salinity can play an important role in jet flow. In other words, the reason underlying the density difference (i.e., of thermal or nonthermal origin) could be a significant factor in the way in which the jet mixes with the ambient water.

2.4.5. *Cross-sectional velocity profile*

When studying buoyant jets, the velocity and concentration distributions at the cross-sections are often compared with the Gaussian profile. This comparison is valid when the jet has entered a region known as the zone of established flow (ZEF) (Shao and Law, 2010). In the present study, various cross-sectional profiles were selected along the axial centerline velocity of the jet for each experiment.

Figure 2-7 illustrates the normalized cross-sectional profiles of U/U_m against r/b at various downstream locations, where r is the radial distance, and b is the distance from the point of maximum velocity (centerline) to the point where the velocity decreases and is equal to $1/e = 0.37$. As mentioned previously, for brevity, only the results of two comparative experiments (T1 with S1 and T3 with S3) are shown (Figure 2-7). The extracted cross-sectional profiles were recorded at the same distance from the source of the jet (nozzle) for T1 and S1 (s/D = 6, 10, 14, 23, 31, 37 and 47) and for T3 and S3 (s/D = 3, 7, 11, 16, 22, 27 and 50). These profiles were then compared with a typical Gaussian profile to evaluate the distribution and evolution of the jet pattern. In general, the selected profiles for all experiments follow a Gaussian distribution and show a well-developed axisymmetric profile.

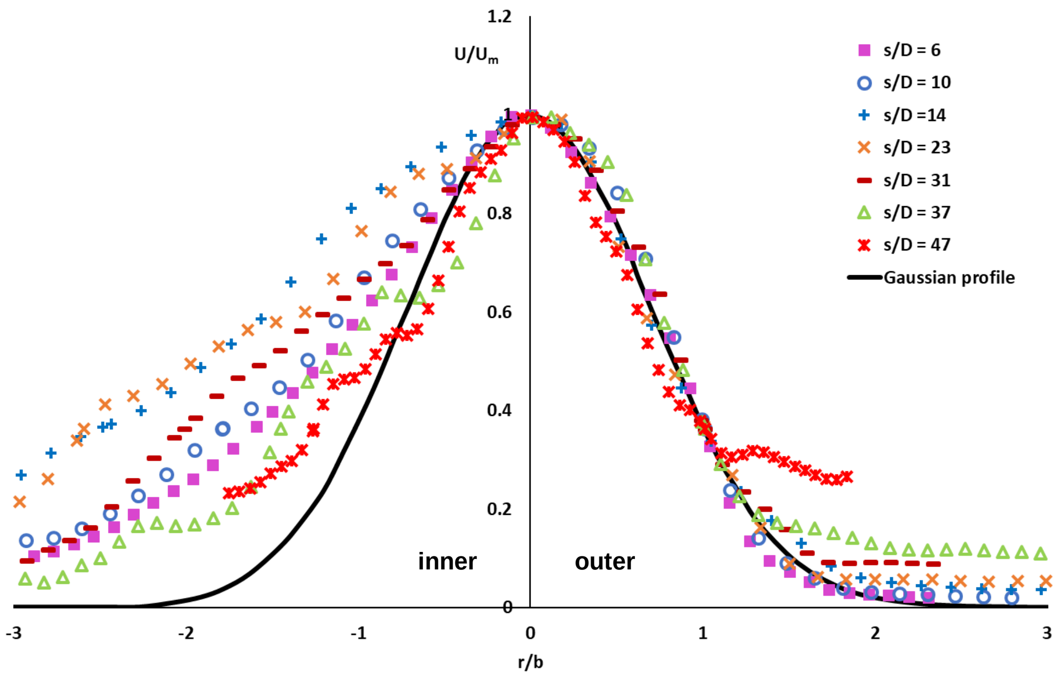

(a)

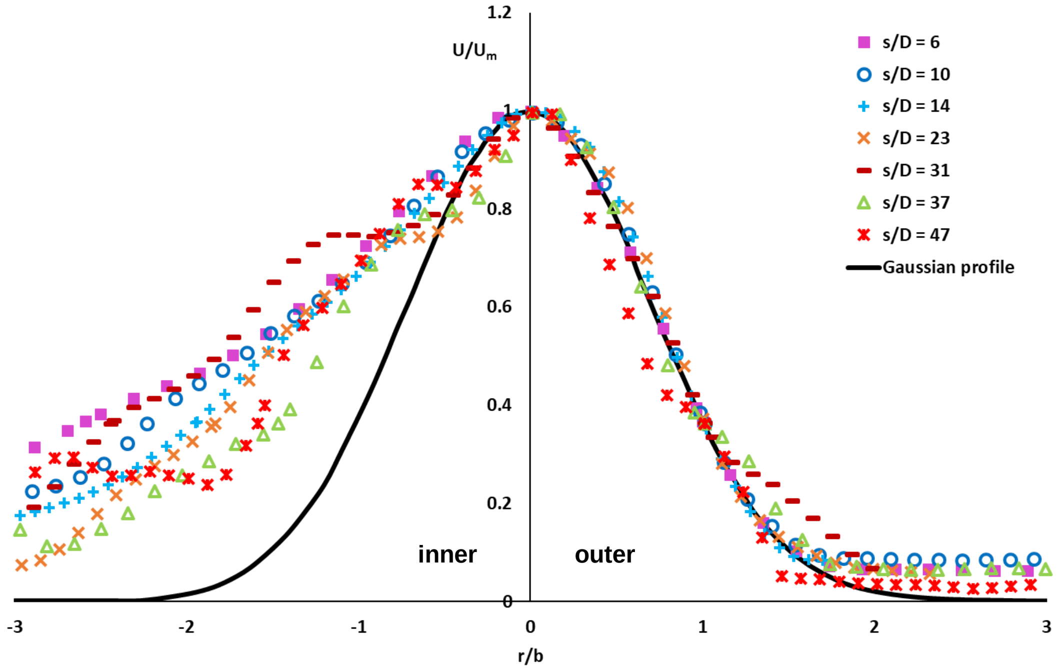
1.2
U/U$_m$
1
0.8
0.6
0.4
0.2
0
-3
-2
-1
0
1
2
3
r/b
inner
outer
s/D = 6
s/D = 10
s/D = 14
s/D = 23
s/D = 31
s/D = 37
s/D = 47
Gaussian profile

(b)

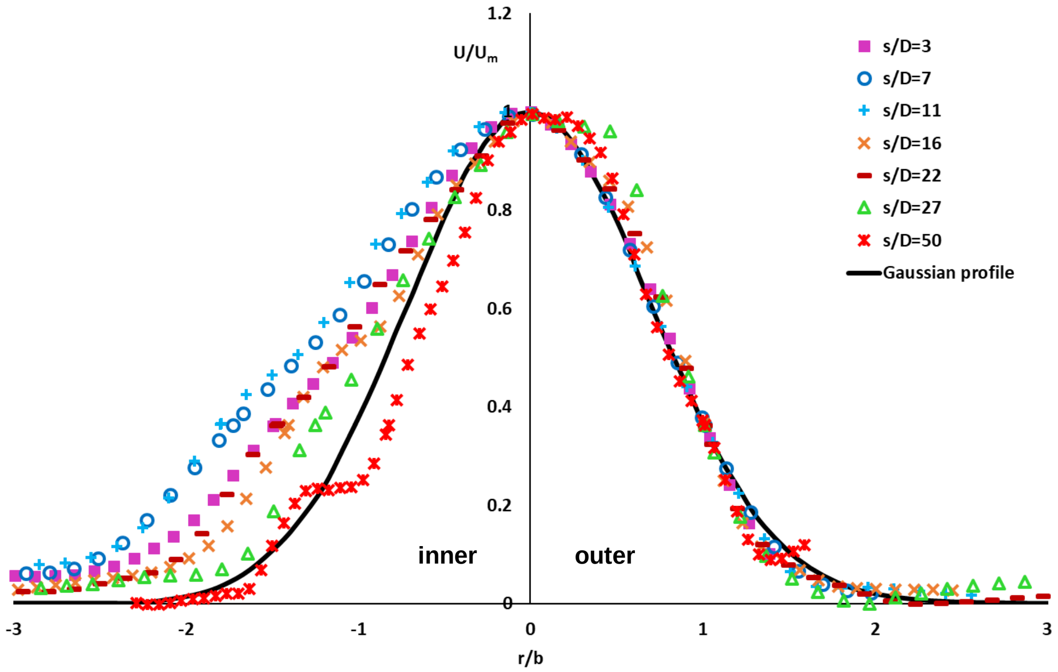
1.2
U/U$_m$
1
0.8
0.6
0.4
0.2
0
-3
-2
-1
0
1
2
3
r/b
inner
outer
s/D=3
s/D=7
s/D=11
s/D=16
s/D=22
s/D=27
s/D=50
Gaussian profile

(c)

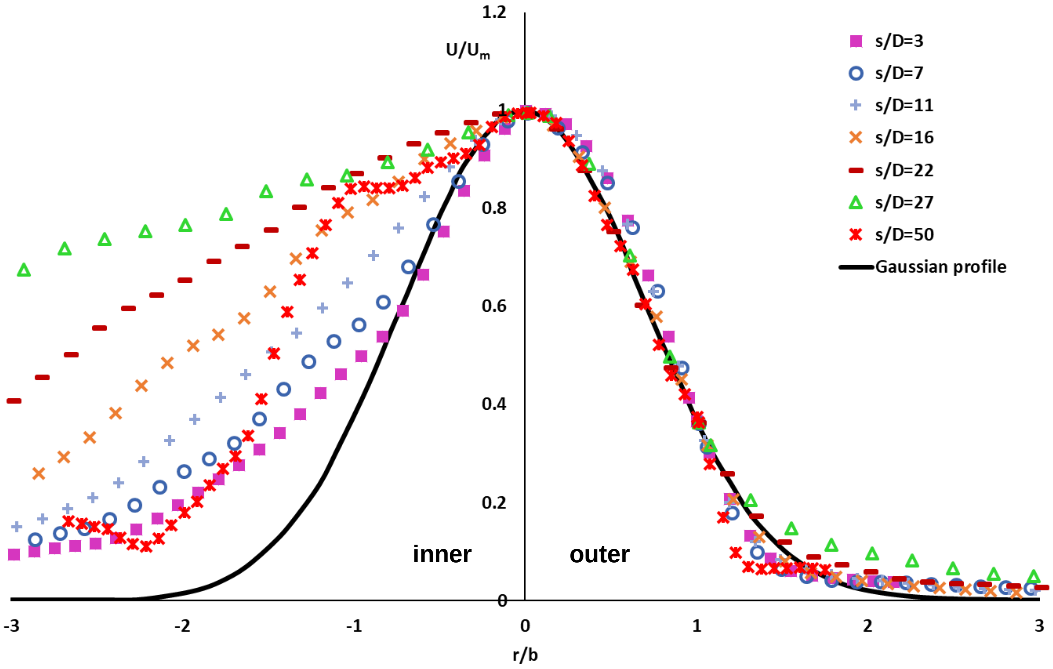

(d)

Figure 2-7: Nondimensional velocity distribution profile at various downstream cross-sections along the jet centerline for: (a) thermal jet for case T1; (b) nonthermal jet for case S1; (c) thermal jet for case T3; and (d) nonthermal jet for case S3.

A reasonable Gaussian distribution is seen for the outer (lower) half of the various cross-sections for both experiments. However, it was observed that the comparison of T3 and S3 (Figure 2-7c and d) better fitted a Gaussian distribution. Additionally, in both comparison cases, it can be seen that as the jet gets farther from the source (the nozzle), the inner (upper) half spreads out more widely and gradually diverges from the jet centerline. This phenomenon is observed clearly in the nonthermal cases and is mainly attributed to buoyancy-induced distortions, which can be seen in the inner (lower) half of the dense jet (Kheirkhah Gildeh et al., 2014). This distortion appears to increase with increased distance from the source to the water surface. When comparing the distributions of the thermal and nonthermal jets, the results reveal that the inner half distribution spreads farther for the nonthermal jets than for the thermal jets. As a result, nonthermal jets can decay and rise toward the water surface more rapidly than thermal jets; this result is consistent with the findings of Rathore and Das (2015), in which the thermal energy of the jet is lost in the surrounding fluid due to the latter's coldness.

2.4.6. *Jet growth rate*

Jet width is commonly used to characterize jet growth rate. This is based on the Gaussian profile for various cross-sections of axial velocity distribution along the jet centerline. The growth rates of the velocity half-widths are calculated by plotting the nondimensionless values of b/D against the distances of the streamwise cross-section (s/D) along the jet centerline from the nozzle tip. The outer and inner half-widths of both jets are combined in the same figure to clearly show the difference in the spread widths, as seen in Figure 2-8. The upper spread widths show more scatter than the lower spread widths, especially for the thermal jet. As shown in the figure, the tendency of both jets to spread is revealed when moving downstream and away from the nozzle, along the jet trajectory. After a short distance from the nozzle, the inner (upper) width of the thermal jet deviates and spread more than of the nonthermal jet. As mentioned previously, this result offers further evidence that thermal jets tend to be flatter and spread more, while nonthermal jets tend to rise more steeply. As a result, the jet width profiles provide good evidence that the nonthermal jets decrease in intensity more rapidly as the flow turns toward the water surface over a shorter distance, and thus a shorter time exists for spreading and dilution.

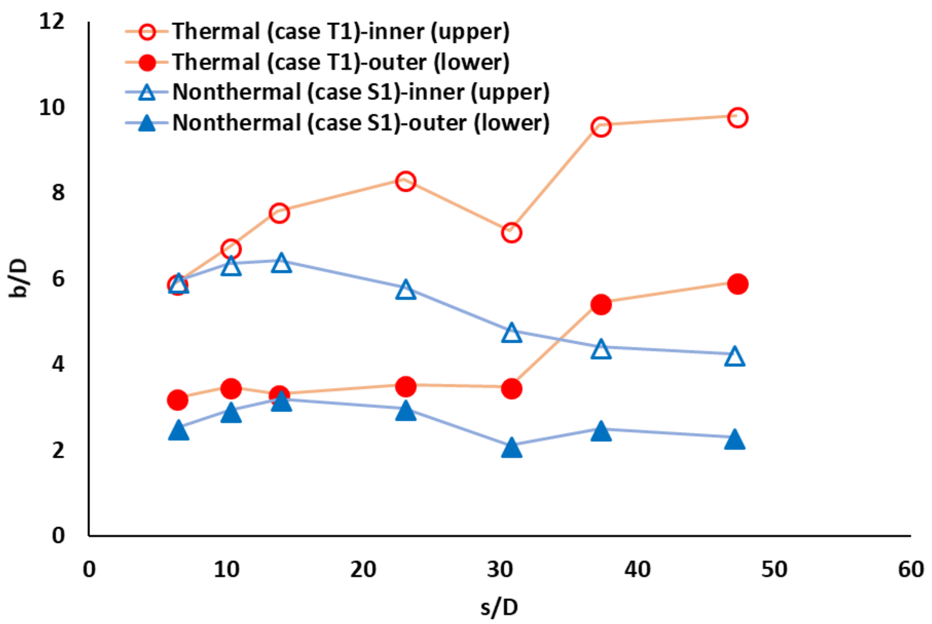

Figure 2-8: Comparison between the velocity spread widths along the jet trajectory for thermal and nonthermal jets for cases T1 and S1.

2.4.7. *Streamwise velocity decay*

To further illustrate the effect of the receiving water conditions on the two buoyant offset jet flows (thermal and nonthermal) having similar properties, the results for the jet streamwise velocity decay are also presented. The U_m at several cross-sections of the jet centerline are extracted and plotted against the s downstream of the jet source for four selected cases (comparing T1 with S1 and T3 with S3), as shown in Figure 2-9.

Figure 2-9a compares the velocity decays for T1 and S1 at a difference in density of approximately 5 kg/m^3. Both the thermal and nonthermal velocity decays closely follow those of the pure jet with a value of 7 for the constant K from Equation (2-1), which is consistent with results reported in the literature (Fischer et al., 1979; Lee and Chu, 2003). Another comparison of decays having a higher difference in density of approximately 10 kg/m^3 is shown in Figure 2-9b. In this figure, both the thermal and nonthermal maximum velocities decayed faster than those of the pure jet, and the divergence between the velocity values for both cases and those of the pure jet is obvious. In this case, the value of K was found to be 6.55 and 6.62 for the thermal and nonthermal jets, respectively. Although these values are almost identical, it is noted that a difference in density can affect a jet by accelerating its decay. In the case of a dense jet, two factors can affect the velocity decay: jet spreading and negative buoyancy (Lai and Lee, 2012). Accordingly, an offset buoyant jet can also be affected by jet spreading and positive buoyancy. However, based on the present results, we find that a difference in density between a jet and the receiving water represents another significant factor that can accelerate jet decay.

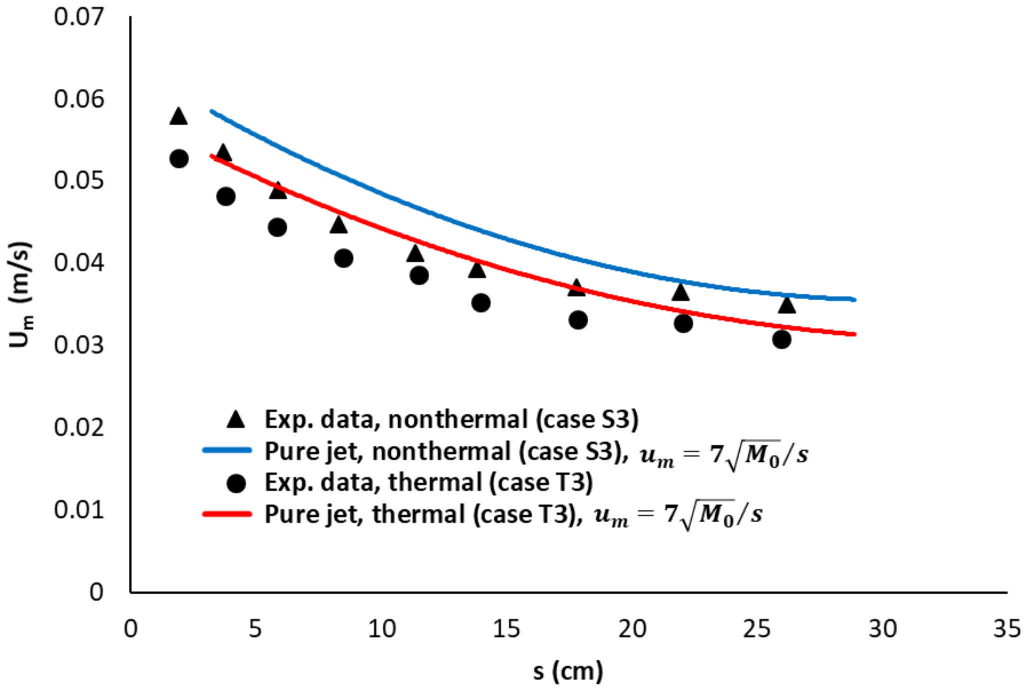

(a)

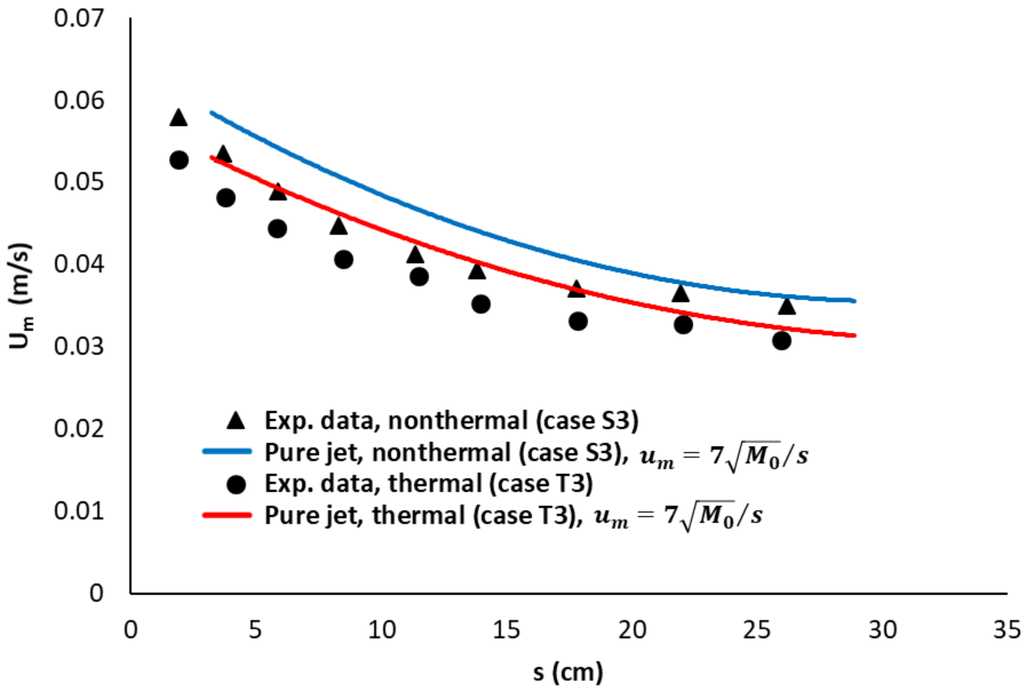

(b)

Figure 2-9: Streamwise velocity decay of thermal and nonthermal jets compared with a pure jet: (a) cases T1 and S1, and (b) cases T3 and S3.

2.5.Computational approach

2.5.1. *Governing Equations*

Three-dimensional turbulent flow of the RANS equations are used as the governing equations for incompressible fluids as follows:

Continuity Equations:

$$\frac{\partial u_x}{\partial x}+\frac{\partial u_y}{\partial y}+\frac{\partial u_z}{\partial z}=0 \tag{2-2}$$

Momentum Equations:

$$\frac{\partial u_x}{\partial t}+\frac{u_x\partial u_x}{\partial x}+\frac{u_y\partial u_x}{\partial y}+\frac{u_z\partial u_x}{\partial z}=\frac{\partial}{\partial x}\left[v_e\left(\frac{\partial u_x}{\partial x}\right)\right]+\frac{\partial}{\partial y}\left[v_e\left(\frac{\partial u_x}{\partial y}\right)\right]+\frac{\partial}{\partial z}\left[v_e\left(\frac{\partial u_x}{\partial z}\right)\right]-\frac{1}{\rho_0}\frac{\partial P}{\partial x} \tag{2-3}$$

$$\frac{\partial u_y}{\partial t}+\frac{u_x\partial u_y}{\partial x}+\frac{u_y\partial u_y}{\partial y}+\frac{u_z\partial u_y}{\partial z}=\frac{\partial}{\partial x}\left[v_e\left(\frac{\partial u_y}{\partial x}\right)\right]+\frac{\partial}{\partial y}\left[v_e\left(\frac{\partial u_y}{\partial y}\right)\right]+\frac{\partial}{\partial z}\left[v_e\left(\frac{\partial u_y}{\partial z}\right)\right]-\frac{1}{\rho_0}\frac{\partial P}{\partial y}-g' \tag{2-4}$$

$$\frac{\partial u_z}{\partial t}+\frac{u_x\partial u_z}{\partial x}+\frac{u_y\partial u_z}{\partial y}+\frac{u_z\partial u_z}{\partial z}=\frac{\partial}{\partial x}\left[v_e\left(\frac{\partial u_z}{\partial x}\right)\right]+\frac{\partial}{\partial y}\left[v_e\left(\frac{\partial u_z}{\partial y}\right)\right]+\frac{\partial}{\partial z}\left[v_e\left(\frac{\partial u_z}{\partial z}\right)\right]-\frac{1}{\rho_0}\frac{\partial P}{\partial z} \tag{2-5}$$

where u_x, u_y and u_z are the components of the mean velocity in the Cartesian coordinates; P is the fluid pressure; t is the time; v_e is the effective kinematic viscosity of water ($v_e = v_t + v$); v_t is the turbulent kinematic viscosity; and v is the kinematic viscosity. The effect of variable density (buoyancy) in the vertical direction (y-coordinate) is considered and added in Equation (2-4)

Temperature and Salinity Equations:

$$\frac{\partial T}{\partial t}+\frac{u_x\partial T}{\partial x}+\frac{u_y T}{\partial y}+\frac{u_z T}{\partial z}=k_e\frac{\partial}{\partial x}\left[\frac{\partial T}{\partial x}\right]+\frac{\partial}{\partial y}\left[\frac{\partial T}{\partial y}\right]+\frac{\partial}{\partial z}\left[\frac{\partial T}{\partial z}\right] \tag{2-6}$$

$$\frac{\partial S}{\partial t}+\frac{u_x\partial S}{\partial x}+\frac{u_y S}{\partial y}+\frac{u_z S}{\partial z}=k_e\frac{\partial}{\partial x}\left[\frac{\partial S}{\partial x}\right]+\frac{\partial}{\partial y}\left[\frac{\partial S}{\partial y}\right]+\frac{\partial}{\partial z}\left[\frac{\partial S}{\partial z}\right] \tag{2-7}$$

where:

$$k_e=\frac{v_t}{Pr_t}+\frac{v}{Pr} \tag{2-8}$$

where k_e is the heat transfer coefficient, Pr is the Prandtl number, and Pr_t is the turbulent Prandtl number. The common ranges of both Pr and Pr_t are 0.6-1.0; both parameters are chosen as 1.0 based on Kheirkhah Gildeh et al. (2015a, 2015b and 2014). The details of the buoyancy-modified k-ε turbulence model are not described here for brevity but can be found in Yan and Mohammadian (2017).

2.5.2. *Boundary conditions*

In the present study, only half of the buoyant offset jet domain is considered because of the symmetrical nature of the problem. Figure 2-10a and b illustrates the computational domain with the mesh system. The dimensions of the computational domain (Figure 2-10a) were chosen to simulate the present experiments. A refined mesh is considered in the near-field area of the offset jet for all simulations to better capture the velocity and temperature characteristics, as shown in Figure 2-10b. The parameters used herein are similar to those used in the experiments (see Table 2-1). The nozzle boundary conditions are chosen based on Kheirkhah Gildeh et al. (2015a and 2015b) as follows: $u_x = U_0$, $u_y = u_z = 0$, $T = T_0$, $k = 0.06u^2$,$\varepsilon = 0.06u^3/D$. A zero gradient boundary condition perpendicular to the outlet plane is defined for u_x, u_y, u_z, k, ε, T, and S for the flow at the outlet boundary section. For the walls, boundary conditions defined as z and $u_z = 0$ and a no-slip condition were applied in this study. Thus, k and ε are assumed to follow standard wall functions at the wall for both thermal and nonthermal buoyant jets. Finally, the symmetry boundary was modeled using a symmetry plane condition.

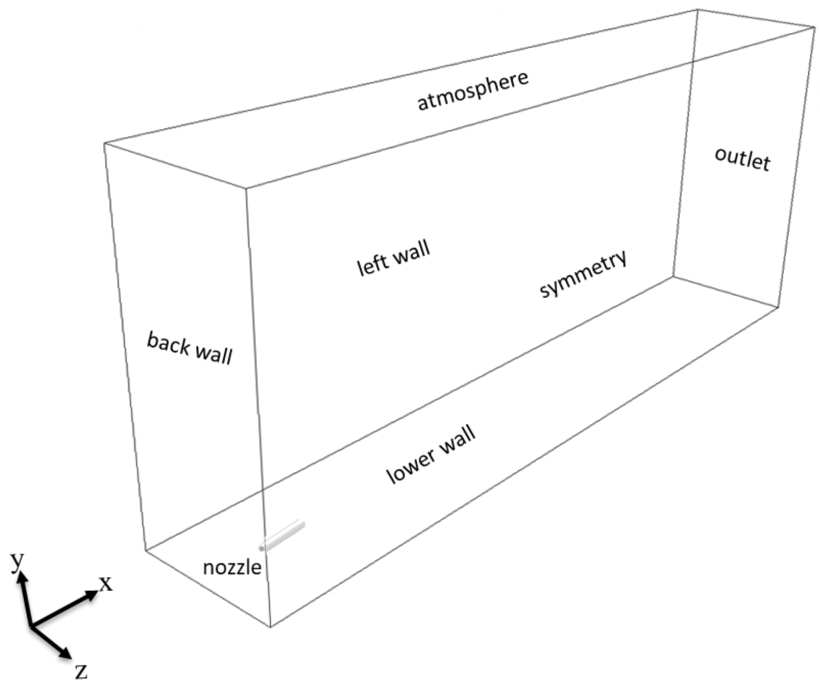

(a)

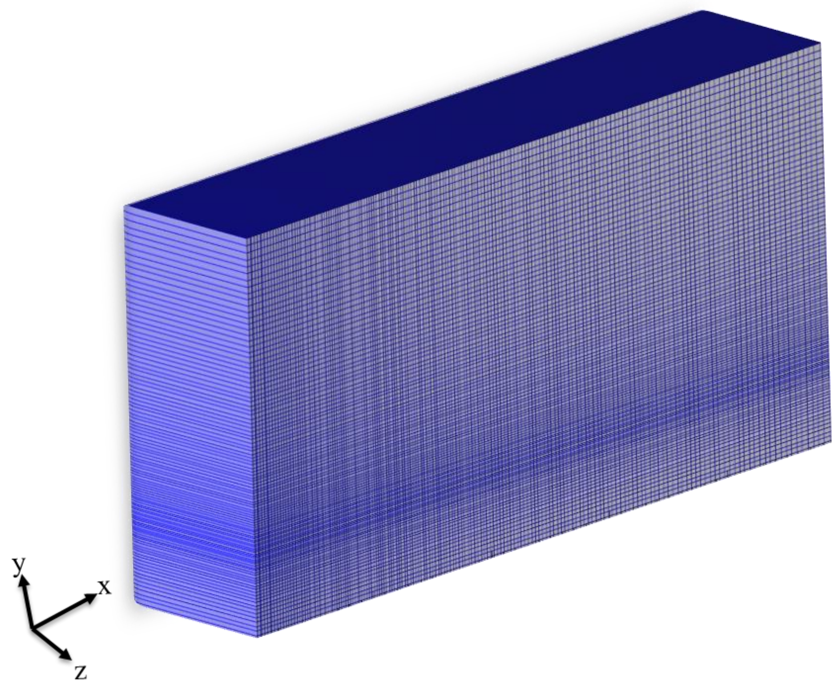

(b)

Figure 2-10: Computational domain: (a) The numerical model domain and boundary definitions; and (b) the structured grid of the domain with a refined mesh near the nozzle.

2.5.3. *Numerical simulation*

In this study, the finite volume open source code OpenFOAM with a structured grid was used to simulate buoyant offset jet discharge. The OpenFOAM (a free open-source package) is widely used for modeling and solving scientific problems, including positively and negatively-buoyant jets (Kheirkhah Gildeh et al., 2015a, 2015b; Zhang et al., 2016). The model solves a set of partial differential equations (PDEs) using the finite volume method (FVM). The base pisoFoam solver for incompressible fluids was modified for use in this study. The advection-diffusion equation for salinity and temperature was added to calculate the transport and dispersion of these parameters. Three RANS turbulence models were chosen for this study due to their better accuracy compared with other RANS turbulence models, as reported in recent studies by Kheirkhah Gildeh et al. (2015a, 2015b and 2014) and Yan and Mohammadian (2017). These models are the standard k-ε, realizable k-ε and buoyancy-modified k-ε models.

2.5.4. *Numerical results*

2.5.4.1. *Comparison with experimental results*

In this section, the preliminary results of the numerical simulation are compared with various experimental data presented in this study. The experimental results of six thermal and nonthermal cases (T1, T3, T4 and S1, S3, S4) were selected to examine the performance of three turbulence models (the standard k-ε, realizable k-ε, and buoyancy-modified k-ε models) under the same conditions. The general behavior of the jets according to the numerical results for all models and the disparities between the results (cases 1, 2 and T3) can be observed in Figure 2-11.

Figure 2-12 shows the numerical results of the centerline trajectory for all models and compares them with the experimental results. The comparison shows that the numerical results obtained for all models were in good agreement with cases T4 and S4. More comparison between the data extracted from the PIV measurements and the models tested here can be shown in Figure 2-13. In this figure, the velocity field contours of the numerical results are compared with experimental results (cases T1 and S1). As shown in this figure, the realizable k-ε model predicts better, but thinner when compared to the experimental contours. This was clearly seen in all results of the numerical models. This could be due to the isotropic assumption of these turbulence models, as a Linear Eddy Viscosity Models (LEVMs), where the jet predicted by these models is usually thinner (Kheirkhah Gildeh et al., 2015b).

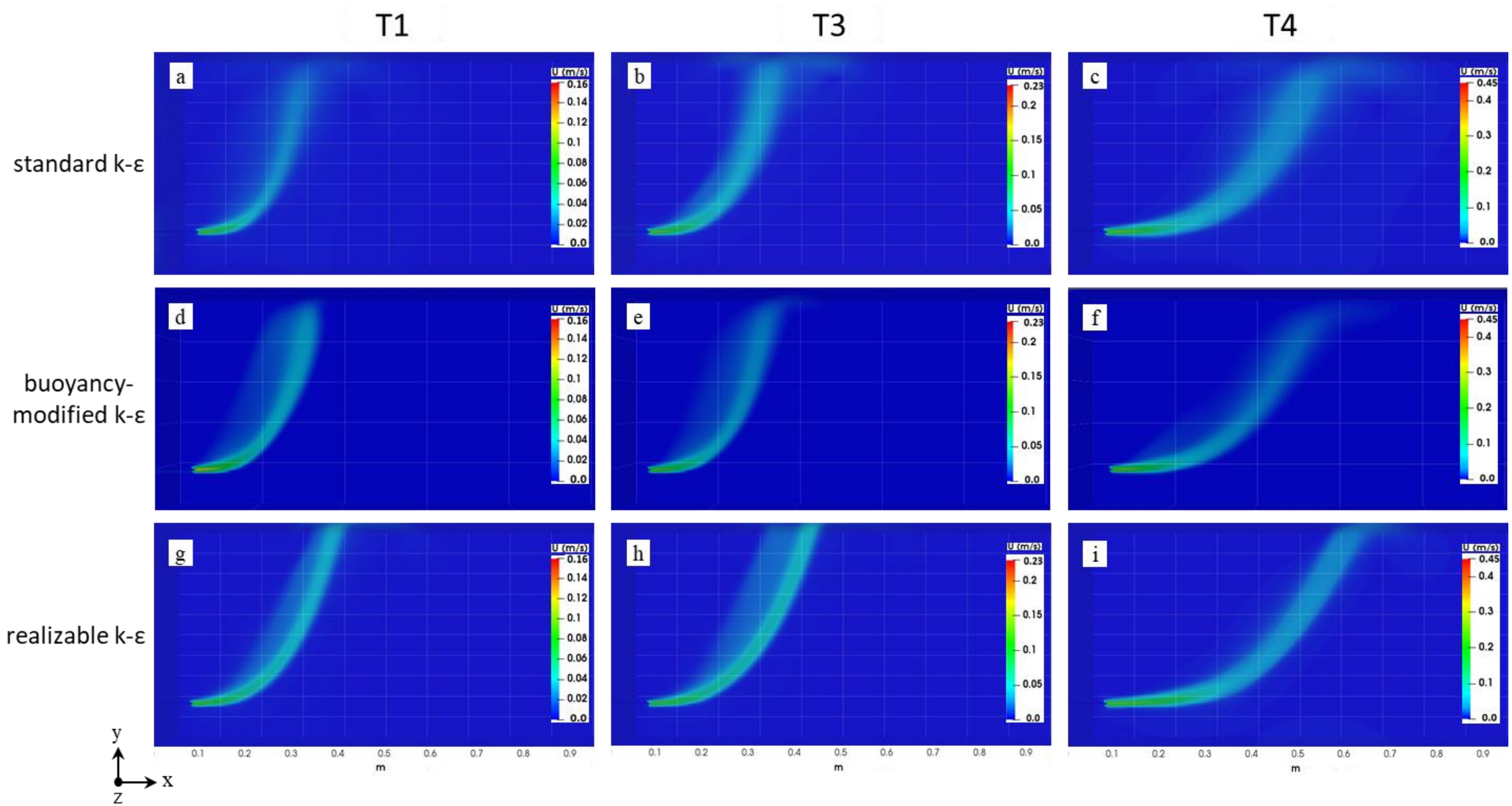

Figure 2-11: Jet behavior according to the numerical simulation results: (a, b and c) the standard k-ε model; (d, e and f) the buoyancy-modified k-ε model; and (g, h and i) the realizable k-ε model.

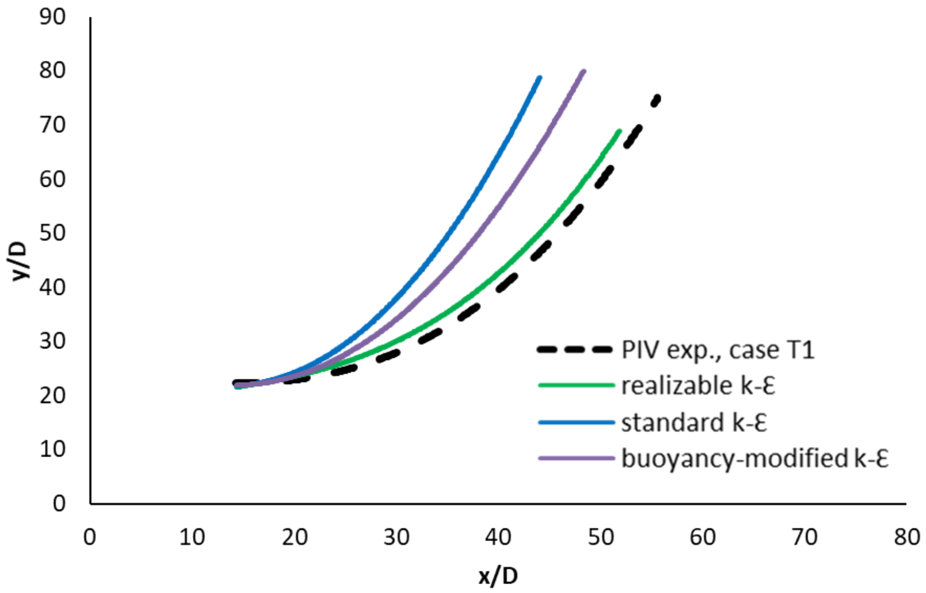
PIV exp., case T1
realizable k-Ɛ
standard k-Ɛ
buoyancy-modified k-Ɛ
y/D
x/D

(a)

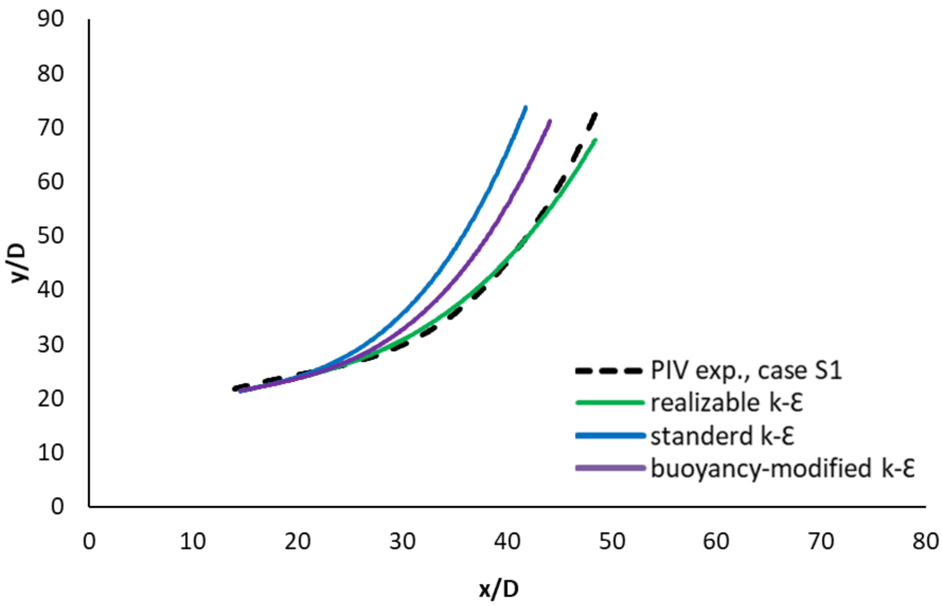
PIV exp., case S1
realizable k-Ɛ
standerd k-Ɛ
buoyancy-modified k-Ɛ
y/D
x/D

(b)

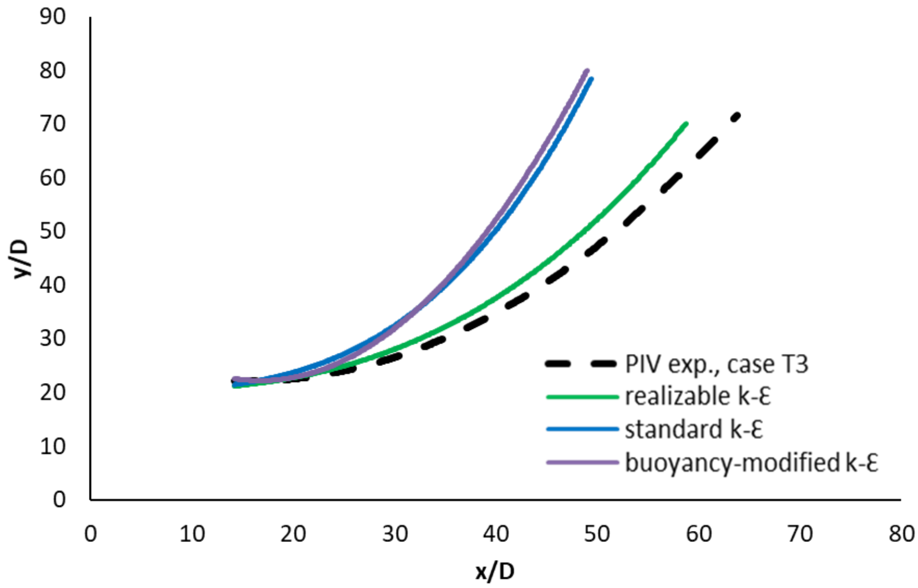
90
80
70
60
50
40
30
20
10
0
y/D
0
10
20
30
40
50
60
70
80
x/D
PIV exp., case T3
realizable k-Ɛ
standard k-Ɛ
buoyancy-modified k-Ɛ

(c)

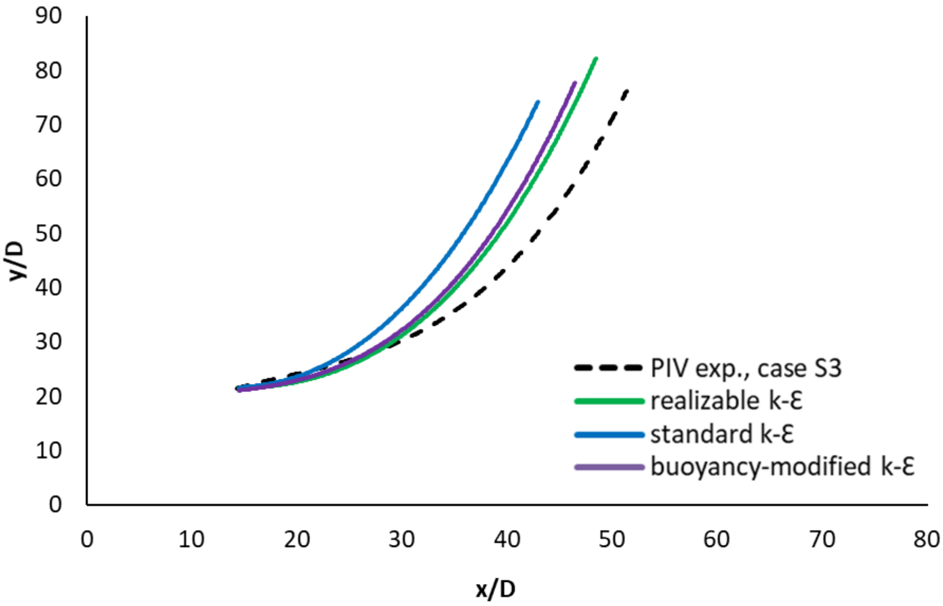
90
80
70
60
50
40
30
20
10
0
y/D
0
10
20
30
40
50
60
70
80
x/D
PIV exp., case S3
realizable k-Ɛ
standard k-Ɛ
buoyancy-modified k-Ɛ

(d)

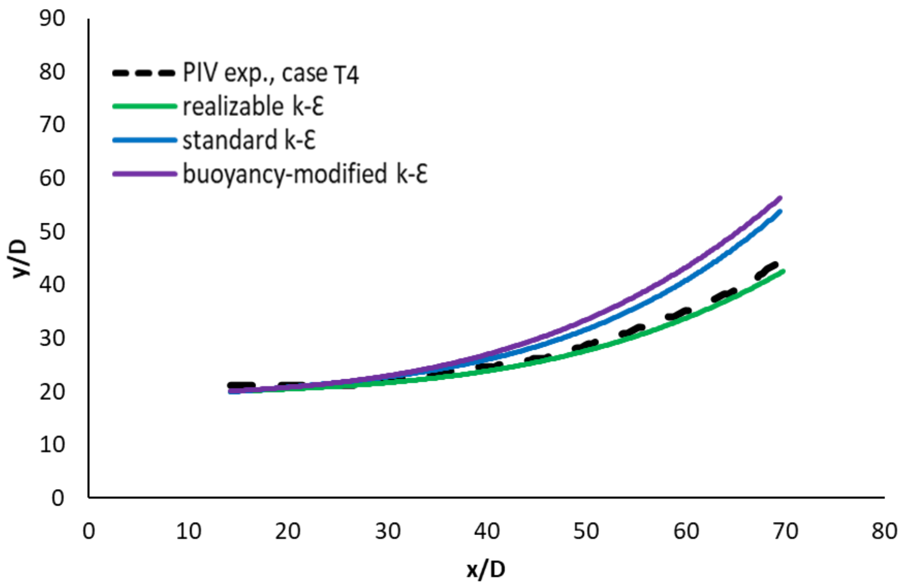

(e)

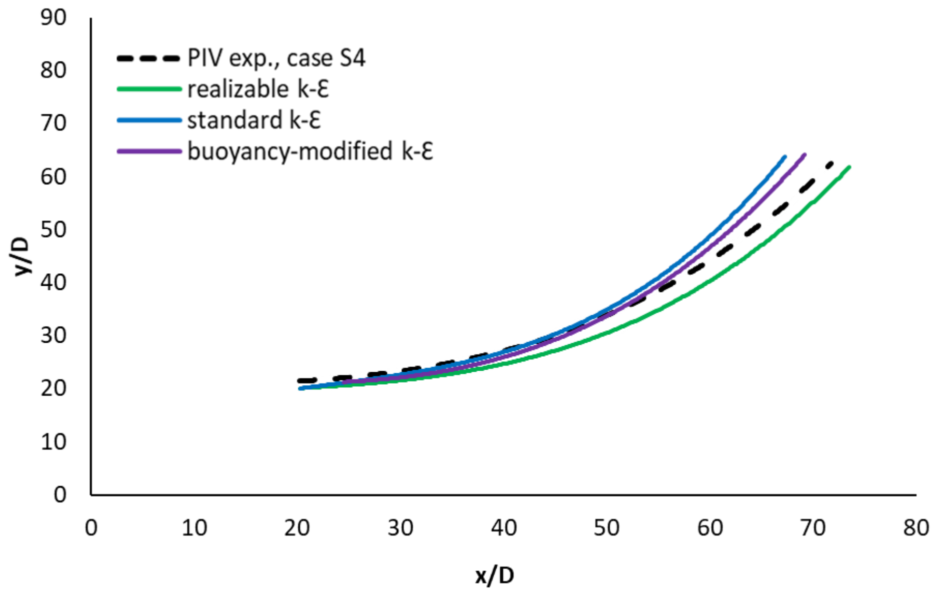

(f)

Figure 2-12: Numerical results for the centerline trajectory: (a,b) u = 0.16 m/s , Fr_d= 10, Δρ = 5.1; (c,d) u= 0.23 m/s, Fr_d= 9.8, Δρ =10.3; and (e,f) u= 0.45 m/s, Fr_d = 19.8, Δρ =10.1.

In addition, a good match was observed between the numerical results obtained using the realizable k-ε model and all other experimental cases, except S3. As mentioned, one can see clearly from the figures that the realizable k-ε model better predicts the results than the standard k-ε and buoyancy-modified k-ε turbulence models. This can be attributed to the different calculations of eddy viscosity (v_t) in the k-ε turbulence models which make the results different. This is due to the difference in the calculation of the C_μ for these models, which is non-constant value in the realizable k-ε while a constant value for others (0.09). Thus, the outcome from the v_t will change and give a different result comparing to standard k-ε and buoyancy-modified k-ε models. As a result, the realizable k-ε provides a more accurate prediction.

Moreover, the standard k-ε and buoyancy-modified k-ε models better predict the results for cases T4 and S4 than for other cases in which the value of Fr_d is increased. Accordingly, the standard k-ε and the buoyancy-modified k-ε models can good predictions in cases where the value of the Fr_d is high.

Consequently, the numerical results of the realizable k-ε model are in good agreement with all experimental cases presented in this study. More results and details of various numerical models compared with the present experimental data are currently being by the authors.

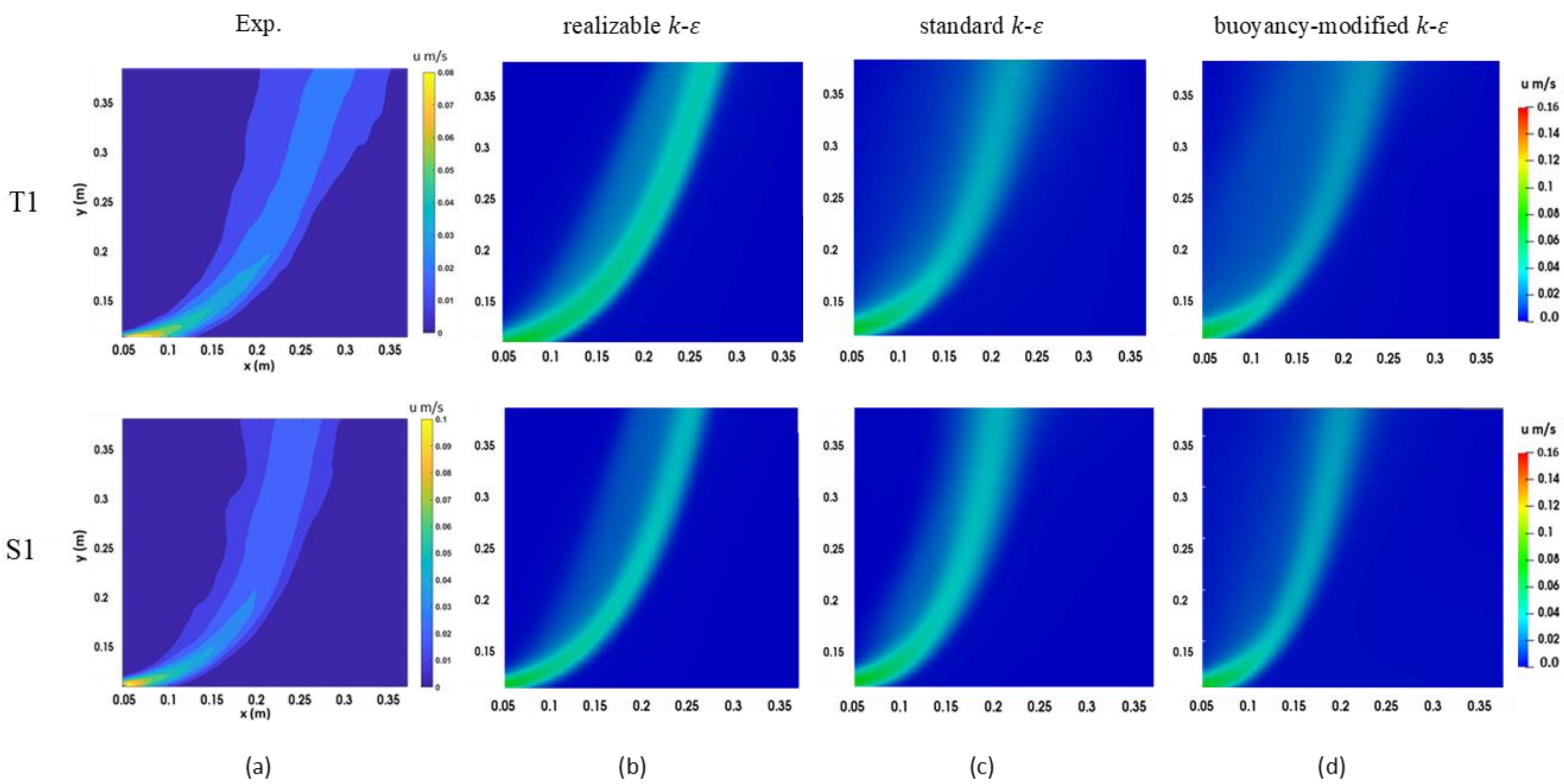

Figure 2-13: Comparison of the velocity field contours: (a) the experimental result of the case T1 and S1; (b) the realizable k-ε model; (c) the standard k-ε model; and (d) the buoyancy-modified k-ε model.

To quantify the variations in the centerlines of the turbulence models with the centerlines of the experimental cases, values of the Standard Error of the Estimate (SEE) were calculated for all turbulence models using the following equation:

$$SEE = \sqrt{\sum (\hat{y} - y)^2 / n} \tag{2-9}$$

where $\hat{y}$ is the estimated (numerical) value, y is the experimental value, and n is the number of observations. The results for all turbulence models are summarized in Table 2-2. The values of the standard error of the estimate show that the realizable k-ε model is the most preferred model. In addition, the results show that the buoyancy-modified k-ε provided better prediction than the standard k-ε in all nonthermal cases, and was the best for the case S4.

Table 2-2: Values of the standard error of the estimate for the comparison of the centerline trajectories of the tested turbulence models with the experimental results

Case	Turbulence model		
	Standard k-ε	Realizable k-ε	Buoyancy-modified k-ε
T1	17.27	2.99	12.64
T3	13.85	2.60	15.20
T4	3.84	0.96	5.25
S1	6.58	0.77	4.15
S3	6.15	3.91	4.38
S4	1.10	1.51	0.82

2.6. Conclusion

This paper presents the results of an experimental study of thermal and nonthermal buoyant offset jets discharged into fresh and saline ambient waters. The influence of the ambient water conditions on jet behavior was the focus of this study. Therefore, the characteristics of a jet affected by changes in the properties of the ambient water have been investigated in detail, including jet propagation, patterns, centerline trajectory, and jet width and decay. Fourteen cases (7 thermal and 7 nonthermal) have been considered in this study. In the first set of cases (thermal experiments), a density gradient was caused by difference in temperature only, whereas salinity was assumed to be constant (i.e., zero). In the second set of experiments (nonthermal cases), the density gradient was caused by salinity and the domain temperature was constant. The Fr_d and Δρ were kept similar for all comparative experiments. As a controlling parameter, this consideration was applied in the present study to determine whether the source of the density difference (temperature versus salinity) can affect jet behavior. In general, the results show that jet flows behave differently if discharged into ambient water with different conditions. It was also observed that the jets rose in the saline ambient (i.e., nonthermal) cases faster than in the fresh ambient (thermal) cases. The propagation speed was shown to be slower, and the time taken to reach the surface was longer for the thermal jets, while the nonthermal jets propagated more rapidly and reached the surface in less time and over shorter distances. The results showed that thermal jets had different patterns due to their slower motion and longer distance to reach the water surface when compared with the nonthermal jets. Differences in the trajectories between the thermal and nonthermal jets were clearly noted, even though the Fr_d and the Δρ remained the same. Therefore, it is concluded that the Fr_d and the Δρ cannot be the only controlling factors in jet evolution. In addition, based on the jet growth and velocity decay rates, the nonthermal jets decayed faster than the thermal jets in all the experiments.

Moreover, three RANS turbulence models, (the standard k-ε, realizable k-ε and buoyancy-modified k-ε models) were applied to predict the behavior of these jets. The numerical results for the jet trajectory obtained using the realizable k-ε model was in good agreement with all experimental data. Finally, the buoyancy-modified k-ε model better predicted jet trajectory than the standard k-ε turbulence model, especially in the nonthermal cases. Further investigations into buoyant offset jets with higher Froude numbers and various numerical models is currently in progress by the authors. In conclusion, this study demonstrates that ambient water conditions can significantly affect jet characteristics and behaviors.

Chapter 3. Experimental investigation and model development of geometrical characteristics of 15° and 52° inclined negatively-buoyant jets using GMDH neural network[3]

Abstract

The goal of this study is to provide more experimental data on the main geometrical characteristics of an inclined negatively-buoyant jet discharged into deep stagnant water, as well as to use the data for developing and evaluating the performance of the proposed model. A series of laboratory experiments were performed using a high-resolution digital camera to determine the main geometrical characteristics of two jet discharge angles, 15° and 52°. A wide range of densimetric Froude numbers (Fr_d) were used in this study, ranging from 11 to 75. The results showed that the behavior of the jet is significantly affected by the Fr_d and the initial discharge angle (θ). A comparison of the present results for the geometrical characteristics with previously reported data was also presented. The present results also showed good agreement with previously reported data for all geometrical parameters, especially for the angle of 15°, while the 52° values differed slightly. A non-linear method (artificial neural network, ANN) called the group method of data handling (GMDH) was employed in this study to develop explicit equations for the geometrical characteristic of the two studied inclined jets. This method has not previously been used in the prediction of mixing of inclined dense jets. Moreover, different statistical indices are utilized to evaluate the accuracy of the proposed equations. The statistical results of the R-squared (R^2) and

[3] This chapter is submitted to the Journal of Coastal Research as Hassan Alfaifi, Abdolmajid Mohammadian and Hossein Bonakdari. It has been Accepted and is Pending Revisions.

the mean absolute percentage error (MAPE) for the geometrical characteristic were ranged between 0.964 to 0.995 and 2.6 to 8.4% respectively, which indicates that the GMDH model performed very well. The GMDH results provided good predictions for both angles for the provided data used within this study. Finally, a comparison of the predicted results obtained using GMDH with the analytical solutions from previous studies was presented. The results showed accurate and satisfactory predictions for the GMDH method for both angles, compared with those of analytical solutions for all geometrical characteristics, where the scattered of the experimental data are closely located around the GMDH fitting lines showing better prediction than those of analytical solutions.

Keywords: Desalination plants, near-field zone; discharge angle; geometrical characteristics; densimetric Froude number; GMDH

3.1.Introduction

Seawater desalination plants produce potable water as a solution for countries that have a shortage of freshwater resources, such as arid and semiarid countries. Therefore, research into desalination technology has increased in the last decade, and desalination has become especially popular in coastal areas (Ahmad and Baddour, 2014).

Two major types of desalination technologies have been widely used around the world for producing freshwater: multistage flash (MSF) and reverse osmosis (RO). In these technologies, there is a byproduct that is usually discharged back into the sea and contains a higher salt concentration than that of seawater. This brine usually has a concentration 1.3-1.7 times higher than that of seawater for RO and 1.1-1.5 for MSF (Einav et al., 2003). The RO method is considered the preferred technology, and it is currently widely used in many countries, especially in the Middle East, as it reduces the cost of desalination and is considered more efficient and cost-effective compared to other methods (Abessi, 2018; Ahmad and Baddour, 2014). This method still produces large quantities of brine effluent with a high concentration of salinity as a byproduct, and this effluent is usually discharged back into the coastal waterbody through different types of outfall systems (e.g., submerged pipe). Such wastewater can affect the marine environment and cause negative impacts on the ecosystem, particularly in the near-field zone of discharge (Lattemann and Höpner, 2008; Petersen et al., 2018). To minimize these impacts, the use of the inclination discharge jet method, which propels the effluent upward toward the water surface, is one of the best ways to ensure rapid mixing of the discharged brine and thus high dilution before reaching the seabed. Therefore, different inclinations have been applied and tested to obtain the highest possible efficiency in increasing effluent dilution. Most previous studies were performed experimentally, either alone or in combination with theoretical efforts. These studies have been utilized with different concepts to predict the geometrical characteristics of inclined dense jets using various methods and therefore still require further investigation.

Numerous experimental studies have been conducted to measure the geometrical and dilution characteristics of inclined dense jets, and these studies have been performed using different techniques for various angles ranging from 0° to 90°. The first experimental study was carried out by Zeitoun and McIlhenny (1971), who pioneered the studies on inclined dense jets discharged into stagnant ambient water for three different angles (30°, 45°, and 60°). Further details on this angle were reported by Roberts et al. (1997), who performed experiments to measure the geometry and dilution characteristics using laser-induced fluorescence (LIF) and a micro-conductivity probe and reported the experimental constant values of various parameters. Other experiments regarding jet geometrical parameters have been conducted, including Bashitialshaaer et al. (2012), Cipollina et al. (2005), Crowe (2013), Kikkert (2006), Lai (2010), Lai and Lee (2012), Oliver (2012), Oliver et al. (2013), Papakonstantis et al. (2011), Shao and Law (2010) and more recently Abessi and Roberts (2015a, b) and Papakonstantis and Tsatsara (2018, 2019).

Kikkert (2006) and Kikkert et al. (2007) used the light attenuation (LA) and LIF techniques to study the geometrical characteristics and dilution of inclined dense jets for angles ranging from 0 to 75° and with different Froude numbers ranging from 14 to 99. In addition to the obtained data, they also used the data reported from previous studies to develop an analytical solution that can predict the jet behavior of an inclined dense jet. The results showed that the analytical solutions provide reasonable predictions of two geometrical points, the maximum centerline height and return point, while the maximum height of the outer edge was predicted with reasonable accuracy. They also tested the performance of the CORJET and VISJET numerical models, and their results were lower than the results obtained from the analytical solutions.

Another experimental study was conducted by Lai (2010) to study the mixing behavior of an inclined dense jet for six angles of 15°, 30°, 38°, 45°, 52° and 60° with two different cases of receiving water (i.e., stagnant and crossflow). The results included geometrical properties, concentration distributions, dilution and velocity. The obtained results were then interpreted using a validated Lagrangian jet model (VISJET). The results of VISJET revealed a reasonable prediction for the jet trajectory and dilution, although the predicted result of the maximum jet rise was underestimated by 10-15% and 30%, respectively, for the associated dilutions.

Later, Oliver (2012) carried out experiments to study dense jets for source inclinations 15° to 75°. The LIF technique was employed to measure the rate of dilution at the centerline of negatively-buoyant jets. The reported results included the geometrical characteristics of the jet trajectory, concentration distributions and dilution. He found that the maximum rates of dilution at the return point (i.e., the horizontal distance from the nozzle tip to the location of the jet centerline as the jet returns to the bed) occurred with source inclination angles of 60° and 75°. He also developed a new model named “forced jet” that can reduce the buoyancy flux of the jet where the flow rises to the maximum height. The prediction results of this model were reasonable for source inclinations of less than 60°.

Near-field velocities and geometric parameters were experimentally measured for inclined negatively-buoyant jets by Crowe (2013), who used the particle tracking velocimetry (PTV) technique. Forty-nine experiments were conducted for discharge angles of 15°, 30°, 45°, 60°, 65°, 70°, and 75°, with Froude numbers ranging between 10.1 and 81. The obtained experimental results and the empirical coefficients were compared to previous experimental studies and integral model predictions.

Another study, applying the LIF technique to single dense jets with various angles from 15° to 85°, was conducted by Abessi and Roberts (2015b), and the geometrical properties of the maximum rise height, impact point, and dilution at the end of the near field were measured. They concluded that the dilution at the near field was highly sensitive to the nozzle orientation, and the dilution was highest for an angle of 60°.

Recently, an extensive experimental study was carried out by Papakonstantis and Tsatsara (2018) to investigate the effect of discharge angle on the characteristics of inclined buoyant jets for angles of 15°, 30°, 35°, 50°, and 70°. A high-resolution digital camera was used in their study. They reported correlations between the geometrical characteristics and the discharge angle. The most recent work on inclined dense jets was conducted by the same authors, Papakonstantis and Tsatsara (2019), for angles 35°, 50°, and 70° to measure the concentration and geometric characteristics of inclined dense jets. They determined the vertical distributions of mean and RMS concentration at the horizontal location of terminal rise height using micro-scale conductivity probes.

Overall, most previous studies have been conducted on negatively-buoyant jets and focused on specific angles (e.g., 30°, 45°, and 60°), while other angles need more investigation, especially in ranges close to 60°, as this angle has been the normally recommended angle for inclined dense jets discharged into deep stationary water (e.g., Abessi and Roberts, 2015a; Bashitialshaaer et al., 2012; Zeitoun and McIlhenny, 1971). Therefore, more data are needed to further improve the understanding of the behaviors and geometric characteristics of inclined dense jets as well as for use in calibrating, validating, and comparing the various numerical models for future studies. Moreover, predictions of inclined dense jets using different analytical methods have received little research effort and need more investigation.

On the other hand, several researchers in different hydraulic subjects and various fields of engineering science have focused their efforts on the use of artificial neural network methods, such as the group method of data handling (GMDH), for solving nonlinear engineering problems and providing an explicit equation. Their studies have shown accurate results compared to those of other methods (Gholami et al. 2017; Naeini et al. 2018; Sadi and Shahrabadi 2018; Rostami et al. 2019). For example, Gholami et al. (2017) studied the ability of the GMDH model to predict the geometric variables of stable channels (width, depth and slope). The results showed that the GMDH model performed well. Moreover, they compared the results obtained from the GMDH with those from previous theoretical equations (based on regression analysis), and this comparison showed the ability of the GMDH model to predict the geometric variables of channels better than other theoretical equations. Naeini et al. (2018) developed a model using GMDH to estimate the Elasticity modulus (E_s) of clayey deposits that is used to predict the elastic settlement of foundations. The results obtained were compared with the previous empirical equations. They found that the GMDH model showed higher performance (32 to 42% improvement) with respect to the other correlations. Another study was conducted by Rostami et al. (2019) to establish a model for predicting the heat capacity of Ionic Liquids (ILs) using a hybrid group method of data handling (GMDH). The model results showed best performance in comparison with literature correlations. Therefore, based on the outcomes of their study, they strongly recommend using the model obtained from GMDH in the research or industrial operations that dealing with heat transfer studies by ILs. Therefore, regarding the outcomes obtained from previous studies, it is worth implementing this method (GMDH) to predict the geometrical characteristics of inclined buoyant jets.

In the present study, more than seventy laboratory experiments on inclined dense jets were performed by using a digital camera to determine the main geometrical characteristics of two nozzle inclinations, 15° and 52°. A wide range of densimetric Froude numbers was used in this study, ranging from 5 to 75. The angle of 52° was selected as it is within the recommended angle range of 45° to 60°, which needs further investigation since there is only one study in the literature. In addition, a new artificial neural network method (GMDH) has been employed, for the first time within the field of outfall systems, in this study to establish empirical equations for estimating the geometrical characteristics of inclined buoyant jets. To the best of the authors' knowledge, the GMDH method has not been used to predict the geometrical characteristics of the inclined negatively-buoyant jets prior to this study. Also, there is no literature that applies GMDH modeling to the subject at hand.

Therefore, the objective of this study is to provide more experimental laboratory data on the main geometrical characteristics of inclined buoyant jets at angles of 15° and 52° in order to complete the existing studies. Also, the results of this study can be useful for developing an analytical model for predictive purposes and for validating numerical models. Furthermore, the performance of the GMDH method in predicting the jet geometrical parameters is evaluated. Finally, the results of the GMDH method are assessed by comparison with some of those obtained previously using analytical solutions.

3.2. Methodology

In this section, details of the dimensional analysis used in this study are presented. The concept of the group method of data handling (GMDH) is also discussed, followed by the statistical indices, experimental setup, and procedures and methodology.

3.2.1. *Dimensional analysis*

Figure 3-1 shows a schematic sketch of an inclined turbulent round dense jet discharging into a stagnant water body (ambient velocity, $U_a = 0$). The discharge port (jet) has diameter D and is placed with an angle (θ) to the horizontal. The receiving water (ambient water) is an unstratified fluid with a constant density ρ_a, and has enough water depth (H) to allow the jet to be developed without reaching the water surface. The jet has an initial discharge velocity of U_0 and density of ρ_0 (where $\rho_a < \rho_0$).

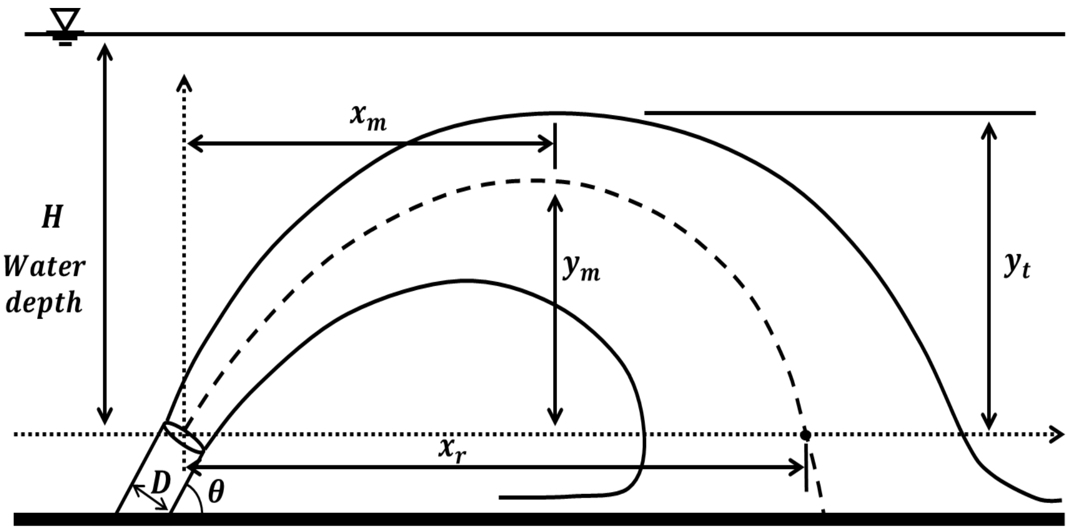

Figure 3-1: Schematic sketch of inclined round dense jet in stagnant ambient water.

When a negatively turbulent round dense jet is discharged upward, with a known angle, into a stagnant fluid, the jet rises upward until a maximum elevation height and then, the jet begins to decelerate and falls down as a negatively-buoyant jet due to the density of the discharged water is higher. The most important geometrical characteristics of the jet mixing characteristics are: the terminal rise height (y_t), the horizontal distance from the nozzle to the point of a maximum height of the centerline (x_m), the height of the centerline (y_m), and the return point (x_r), which is known as the horizontal distance from the nozzle tip to where the centerline of the jet returns to the nozzle elevation (Figure 3-1).

The distribution of the jet flow that is discharged into a homogeneous and calm ambient fluid can be affected by various parameters known as the source angle θ, D, U_0 and the initial density difference ($\Delta\rho = \rho_0 - \rho_a$) between the ambient fluid and the discharge fluid. In addition, the inclined dense jets can be characterized by its discharge volume flux $Q_0 = U_0 \pi D^2/4$, momentum flux $M_0 = U_0\, Q_0 = U_0^2 D^2\, \pi/4$, and buoyancy flux $B_0 = Q_0\, g_0' = g_0'\, U_0 \pi D^2/4$, where $g' = g(\rho_0 - \rho_a)/\rho_a$, is the effective gravitational acceleration and g is the gravitational acceleration.

From these fluxes one can form two length scales, the momentum length scale $L_M = M_0^{0.75}/B_0^{0.5}$, which is a measure of the number Fr_d, the ratio of inertia to buoyancy, can be derived for turbulent buoyant jets and is proportional to the ratio of length scales: $Fr_d = L_M/L_Q = U_0/(g'D)^{0.5}$, which means that the L_M and L_Q can be related to the densimetric Froude number and the jet diameter as:

$$L_M = Fr_d D \left(\frac{\pi}{4}\right)^{0.25} \quad (3\text{-}1)$$

$$L_Q = D \left(\frac{\pi}{4}\right)^{0.5} \quad (3\text{-}2)$$

For inclined dense jet, the M_0 is an important parameter where the jet is originally moving upward, because the vertical component of M_0 and B_0 are not acting in the same direction. Therefore, any dependent variable will be a function of M_0, B_0, Q_0 and θ as (Robert et al, 1997):

$$y_t = f(M_0, B_0, Q_0, \theta) \quad (3\text{-}3)$$

Based on the above equation, the jet terminal rise height edge y_t, for example, can be expressed in terms of the length scales as reported by Roberts et al. (1997):

$$\frac{y_t}{L_M} = f\left(\frac{L_M}{L_Q}, \theta\right) \quad (3\text{-}4)$$

In case of $L_M \gg L_Q$, the effect of Q_0 becomes negligible, thus, L_Q will be negligible as well. Therefore, the Equation (3-4) becomes:

$$\frac{y_t}{L_M} = C_{y_t}(\theta) \quad (3\text{-}5)$$

where C_{y_t} is a constant for the jet terminal rise height, which is a function of the initial angle of the fluid discharged θ. This constant can be determined from experiments.

The terminal rise height can also be expressed alternatively in terms of the nozzle diameter and jet densimetric Froude number instead of the length scales and the Equation (3-5) can be rewritten as:

$$\frac{y_t}{Fr_{\mathrm{d}}D} = C_{y_t}(\theta) \tag{3-6}$$

Likewise, the other geometric jet parameters (x_m, y_m and x_r) can also be derived in an analogous form where they are all proportional to $Fr_{\mathrm{d}}D$, but the coefficient value (C) will be different, i.e.

$$\frac{x_m}{Fr_{\mathrm{d}}D} = C_{x_m}(\theta) \tag{3-7}$$

$$\frac{y_m}{Fr_{\mathrm{d}}D} = C_{y_m}(\theta) \tag{3-8}$$

$$\frac{x_r}{Fr_{\mathrm{d}}D} = C_{x_r}(\theta) \tag{3-9}$$

where C_{x_m}, C_{y_m}, C_{x_r} are constants and as mentioned previously, they can also be determined from experiments. Note that, all these constants are also functioning of the discharge angle θ.

3.2.2. *Group method of data handling (GMDH)*

An artificial neural network (ANN) method is considered an artificial intelligence method whose function is derived from the functions of the neural network of the human brain. An efficient and proven category of ANN for prediction and modeling is known as self-organizing networks (SONs), of which one type is the polynomial network. Neural networks and linear regression methods are combined in these types of networks, and one SON training algorithm involves the GMDH (Ivakhnenko 1982). This type of algorithm is often used to model problems that involve data series for multi-input-single-output systems. Second-order polynomials are used in the GMDH as network functions, and the main advantage of the GMDH, as opposed to traditional neural networks, is its use in establishing mathematical models for a given procedure. Generally, when establishing a model for a multi-input-single-output system, Volterra-Kolmogorov-Gabor (VKG) polynomials are useful, and one such use is as expressed in Equation (3-10) (Ebtehaj et al., 2015; Gholami et al., 2017) as follows:

$$y = a_0 + \sum_{i=1}^{n} a_i x_i + \sum_{i=1}^{n}\sum_{j=1}^{n} a_{ij} x_i x_j + \sum_{i=1}^{n}\sum_{j=1}^{n}\sum_{k=1}^{n} a_{ijk} x_i x_j x_k + \cdots \quad (3\text{-}10)$$

where $x = (x_1, x_2, \dots, x_n)$ is the vector for input, y is the output, and a_i, a_{ij}, and a_{ijk} are coefficients for the polynomial (weight vectors). VKG polynomials are approached by using quadratic polynomials, and the second-order polynomials are themselves determined by using different input pairs. Therefore, the GMDH can be used as a way to "teach" a given system. A neural network established on the GMDH will have a multilayer, feed-forward network and will combine the "neurons" from the input pairs via a quadratic polynomial, i.e., if the input variable number is m, the first-layer neuron number is $L_1 = \binom{2}{m} = m(m-1)/2$.

All the network layers have one or multiple units for processing, and all of these units have one port for output and two for inputs. The processing units are assumed to be second-order polynomials. Undetermined parameters for the GMDH are sometimes the coefficients for the polynomials, however. A schematic of the GMDH approach with the structure of each neuron (N-Adaline) is given in Figure 3-2.

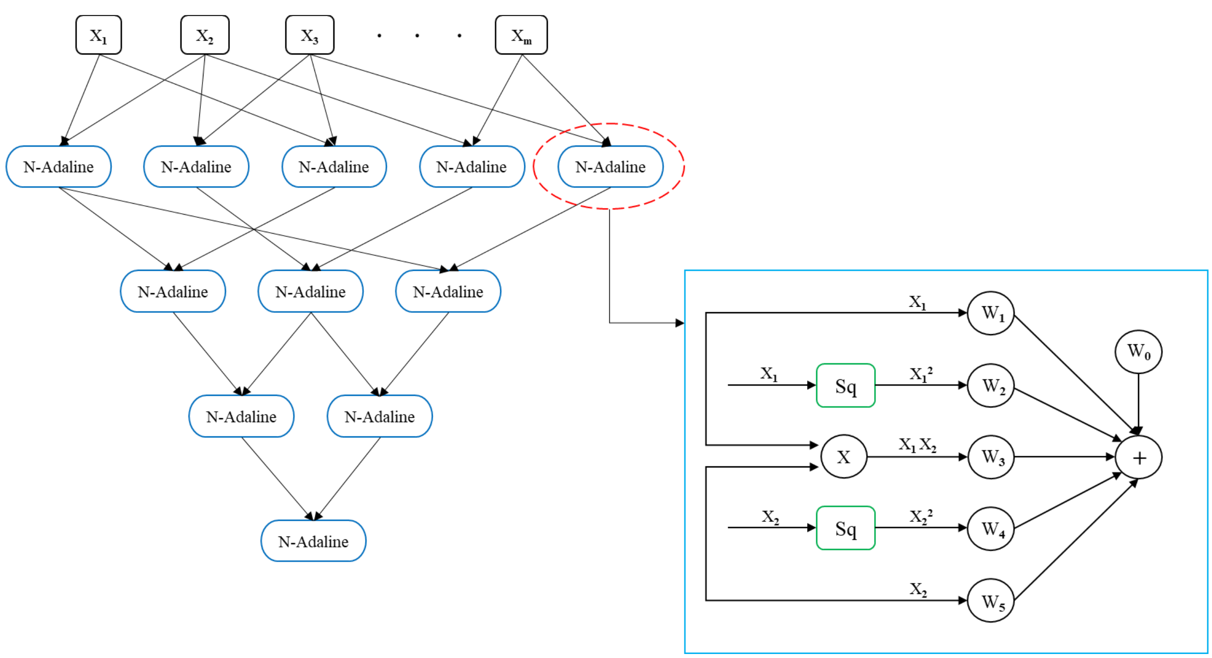

Figure 3-2: Schematic of a classic GMDH.

Based on the target function, the target value is minimized to establish the structure of the network and the value of the output of the input vectors $x = (x_{i1}, x_{i2}, \dots, x_{in})$. The objective function used here is intended to reduce any errors in estimating the modeling coefficients of the GMDH algorithm, i.e., (Ebtehaj et al., 2014):

$$AIC = n\log(MSE) + 2(N+1) \tag{3-11}$$

where N is the number of neurons in the model, n is the sample number, and MSE is the mean square error. Accordingly, six unknown coefficients are in each equation in the following:

$$\begin{cases} y_1 = a_0 + a_1x_{1p} + a_2x_{1q} + a_3x_{1p}x_{1q} + a_4{x_{1p}}^2 + a_5{x_{1q}}^2 \\ y_1 = a_0 + a_1x_{2p} + a_2x_{2q} + a_3x_{2p}x_{2q} + a_4{x_{2p}}^2 + a_5{x_{2q}}^2 \\ ------------------------- \\ ------------------------- \\ y_N = a_0 + a_1x_{Np} + a_2x_{Nq} + a_3x_{Np}x_{Nq} + a_4{x_{Np}}^2 + a_5{x_{Nq}}^2 \end{cases} \tag{3-12}$$

The matrix form of Equation (3-12) is as follows:

$$Aa = Y \tag{3-13}$$

where

$$A = \begin{bmatrix} 1 & x_{1p} & x_{1q} & x_{1p}x_{1q} & {x_{1p}}^2 & {x_{1q}}^2 \\ 1 & x_{2p} & x_{2q} & x_{2p}x_{2q} & {x_{2p}}^2 & {x_{2q}}^2 \\ . & . & . & .. & . & . \\ . & . & . & .. & . & . \\ 1 & x_{Np} & x_{Nq} & x_{Np}x_{Nq} & {x_{Np}}^2 & {x_{Nq}}^2 \end{bmatrix} \tag{3-14}$$

$$a = \{a_0, a_1, a_2, a_3, a_4, a_5\}^T \tag{3-15}$$

$$Y = \{y_1, y_2, y_3, \dots \dots, y_N\} \tag{3-16}$$

Through multiple regression analysis, the least squares method is used to solve the values for each coefficient as follows:

$$a = (A^TA)^{-1}A^TY \tag{3-17}$$

Significant drawbacks with the GMDH involve (i) the necessity for second-order polynomials; (ii) each neuron's inputs only come from adjacent layers; and (iii) each neuron's inputs have only two parameters.

3.2.2.1. *Statistical Indices*

This section presents the statistical indices applied in this study to evaluate the accuracy of the proposed artificial intelligence model (GMDH). Various error measures are commonly used in the literature as statistical parameters that can clearly show the accuracy of a proposed model. Some of the most commonly used measures for absolute errors are selected along with the coefficient of determination (R^2) in the present study, namely, mean absolute error (MAE), root mean squared error (RMSE), and mean absolute percentage error (MAPE). The calculation of these absolute errors is as follows:

$$R^2 = \frac{\sum(\hat{y} - \bar{y})^2}{\sum(y_i - \bar{y})^2} \tag{3-18}$$

$$MAE = \frac{1}{n}\sum_{i=1}^{n}|Actual - Prediction| \tag{3-19}$$

$$RMSE = \sqrt{\frac{1}{n}\sum_{i=1}^{n}(Actual - Prediction)^2} \tag{3-20}$$

$$MAPE\ \% = \left(\frac{1}{n}\sum_{i=1}^{n}\frac{|Actual - Prediction|}{Actual}\right) * 100 \tag{3-21}$$

where $\hat{y}$ is the estimated values of the regression line, $\bar{y}$ is the mean of the actual values, and y_i is the actual values, while *Actual* represents the actual values of the observed experimental data and *Prediction* is the values predicted by the GMDH model. R^2 illustrates how well the predicted data of the GMDH model fit the observed experimental data, where the closer the value is to 1, the more accurate the model is. Low values of the other statistical parameters, *i.e.*, MAE, RMSE, and MAPE, indicate a high model prediction accuracy.

3.3.Experiments

3.3.1. *Setup*

The experiments were performed in a rectangular transparent glass tank at the Water Resources Laboratory at the University of Ottawa, Canada. The tank is 120 cm long, 50 cm wide, and 50 cm deep as shown in Figure 3-3. The bottom and sidewalls of the tank were made of glass panels. Two circular nozzles with different internal diameters of 3 and 6 mm were used. The nozzles inclination angles were 15° and 52° to the horizontal. For all experiments, the nozzles were placed to one end of the tank (centered), far enough (10 cm) from the back walls to avoid any influences and to ensure a fully developed velocity profile. The height of the nozzle tip was set at about 5.4 cm for both angles of inclination, above the bottom of the tank to avoid any influences from the bottom boundary layers.

The nozzle was connected to a pipe equipped with: (1) a flow meter (Rotameter, Omega-FL-3840ST, up to ±2% FS (full-scale accuracy)) to determine the flow rate of the discharged water; (2) valves to control the discharge water. The depth of water above the nozzle ranged from 5 to 25 cm, with enough distance to allow the jets to be fully developed. In this study, the effect of the water depth (or the water surface influence) on the jet was avoided by keeping 10% of the water depth above the maximum rise height of the dense jets.

The pipe was connected to a constant-head tank with dimensions of 75 cm length, 30 cm width, and 30 cm depth. This tank (containing the discharge water - brine water - flown by gravity into the large tank) was located approximately 180 cm above the discharge nozzle. In the present study, the density of the discharged water (ρ_0) was ranged from 1011 to 1030.8 kg/m^3 for each angle to make sure a wide range of the brine discharged from the industrial plants has been covered. The constant-head tank had two separate storage tanks, one of which was used to store the surplus of the discharged water, as shown in Figure 3-3. The water was then returned from the storage tank using a pump to maintain a constant water level. The storage tank was equipped with an instrument that enabled precise temperature control (Corio CD Heating Immersion & Bridge Mounted Circulator) with temperature stability ±0.03 °C. This device was used to ensure that the temperature in the discharge tank remained constant during the experiments.

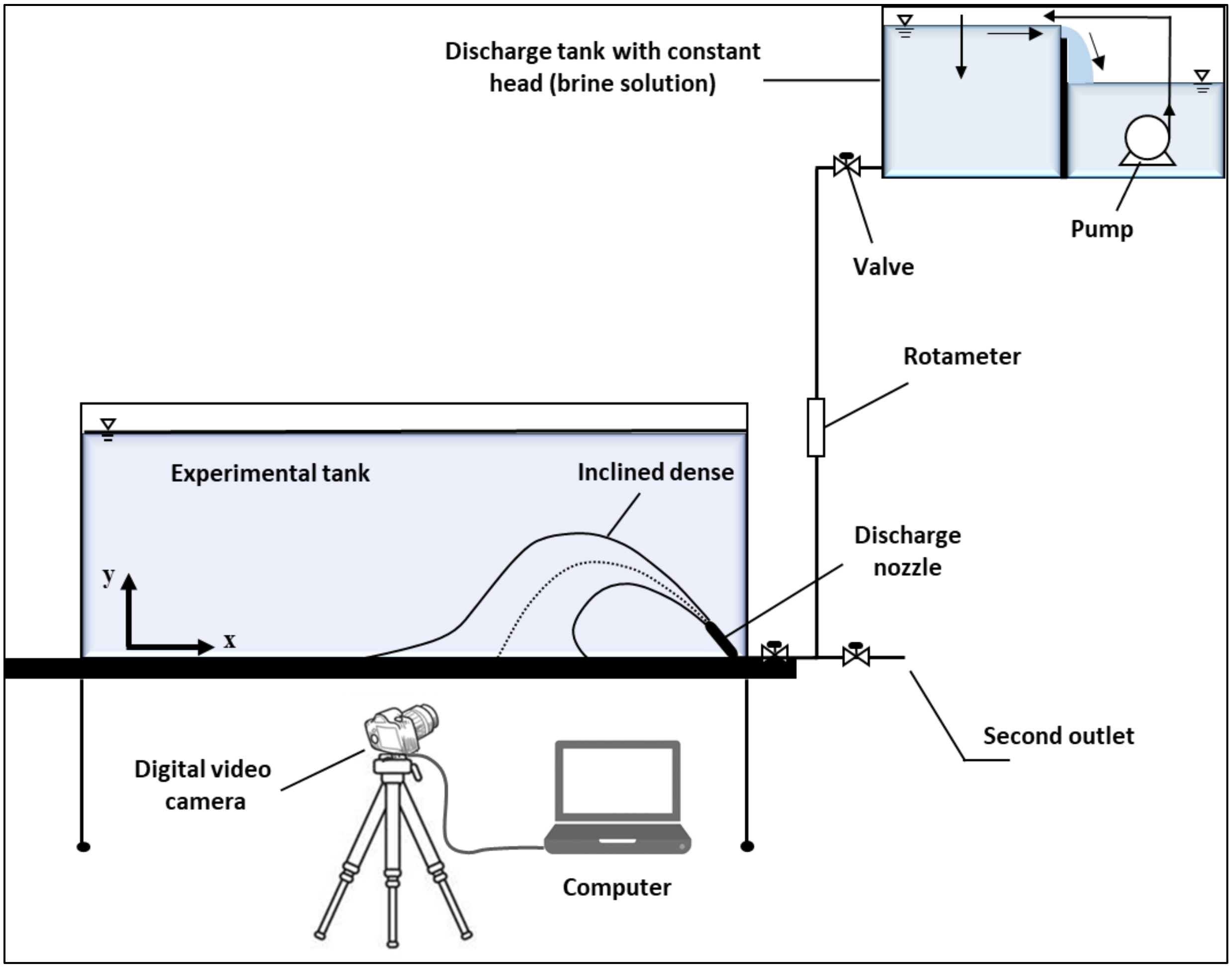

Figure 3-3: Schematic view of the experimental setup of the inclined dense jet.

To ensure that the water temperature in the pipe was equal to that of the heated water in the elevated tank, the pipe was covered with insulating material. Another outlet was located at the end of the discharged pipe, outside of the experimental tank, at a distance of 20 cm upstream of the nozzle tip to test the temperature of the discharged water before running the experiments. Moreover, the nozzle outlet was equipped with a very thin sensor, which was connected to a thermometer, to measure the flow temperature during the experiments.

In each experiment, the density and temperature for brine discharged water and receiving water were measured before starting the experiment using VWR® sympHony™ Handheld Meters and HH12B Handheld Thermometers (OMEGA), respectively. The density was calculated based on the measured conductivity. Also, random samples from discharged and ambient water were taken to calculate the density using weight and volume (measured by weighing the known volume of the sample) to ensure that the density values are correct.

All experiments were performed using water from the same source (tap water). After filling the experimental tank by tap water, it was allowed to settle in the tank for about 20-30 mins prior to performing any test. The temperatures of the ambient and discharged water were approximately similar (± 1.5 °C), for all experiments. The brine water was generated by dissolving sodium chloride (NaCl) with high purity (99.99%) in tap water and discharged into the test tank with various concentration. The amount of salt required to achieve the target density was calculated using the Millero and Poisson (1981) formula. This equation is one of the most widely used formulas for calculating density as a function of temperature and salinity. This formula is referred to as the equation of state of seawater. A blue dye color was used to observe the jet trajectory. The initial jet velocity U_0 was 0.38-1.9 m/s and the densimetric Froude numbers and the Reynolds number *Re* were 11.5-75.59 and 2023-5486, respectively. Details of all experimental parameters are summarized in Table 3-1.

3.3.2. *Image Processing Procedure*

In this study, a total of 43 experiments were performed to determine the inclined dense jets' geometrical characteristics, and for each experiment, a video recording using a digital camera with an image resolution of 1280 × 720 pixels was made. A similar technique has been used in other studies (Abessi *et al.*, 2012; Papakonstantis *et al.*, 2011; Roberts and Toms, 1987). Video sequences with a frequency of 30 fps were recorded using a Canon EOS Rebel T5 camera. The camera was installed on a tripod perpendicular to the main flow direction of the jet. The distance from the camera to the experimental tank was about 200 cm. A gridded whiteboard with known measurements (*i.e.*, 10 cm between each line, vertically and horizontally) was installed and attached to two sides (back and bottom) inside the tank to help in the post-processing analyses. The experimental tank was placed in a dark room to easily control the lighting and avoid any unwanted light that could affect the captured videos.

During each experiment, the video was run for enough time (not less than 2 minutes) for the jet flow to become established and reach the steady-state condition. The flow centerline trajectory of the mean velocity profile was defined based on the maximum intensity of the colored flow by using the intensity tools in MATLAB. To analyze the captured image, a coded program in

MATLAB/Simulink was used to extract the appropriate frames in which the points with the highest intensity of the jet flow were observed. These points were then connected to draw the centerline of the jet trajectory. After determining this line, other geometrical parameters of the jet were calculated for each experiment. As the distance between the lines in the experimental tank was known (10 cm), the same code was used to obtain the dimensions for each frame by calculating the number of pixels in each square (Figure 3-4), where the number of pixels for each square was approximately 245*245. Therefore, the value of each point can be calculated by dividing the number of pixels on the known distance, which is 10 cm. To reduce any errors when obtaining the geometrical parameters, five frames were chosen for each five-second period after the jet reached a steady-state for each experiment. Then, the average was calculated to obtain these parameters. The parallax errors were minimized and taken into account in this study by identifying the nozzle position and reference lines before running each video. The pixel distance between each line was then calculated to determine the points of critical geometric parameters. Figure 3-4 shows the method used to reduce parallax errors in determining the geometrical parameters.

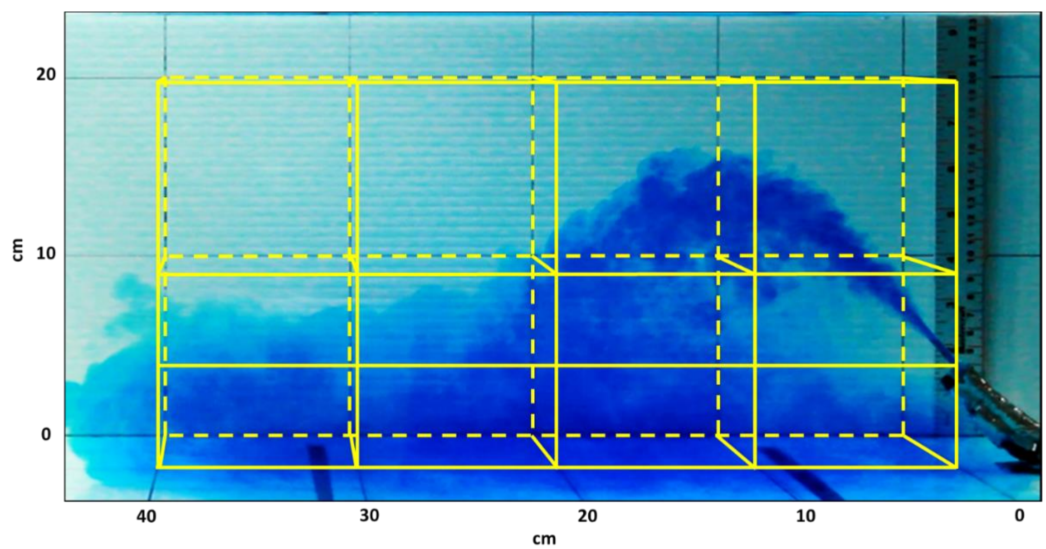

Figure 3-4: Method of determining the geometrical parameters.

Table 3-1: Experimental parameters along with the results of the geometrical characteristics.

Case	θ (°)	D (cm)	U_0 (m/s)	$\Delta\rho/\rho_a$	Fr_d	Re	x_m (cm)	x_r (cm)	y_m (cm)	y_t (cm)
1	15	0.6	0.6	1.353	21.32	3543	15.53	31.07	3.60	6.55
2	15	0.6	0.5	1.365	17.69	2953	12.39	25.95	3.02	5.99
3	15	0.6	0.38	1.370	13.42	2244	9.96	18.93	2.40	4.43
4	15	0.3	0.8	1.343	40.39	2395	14.20	26.22	4.34	7.56
5	15	0.3	1	1.346	50.45	2994	17.29	34.89	4.98	8.93
6	15	0.3	1.5	1.348	75.59	4482	27.51	49.65	6.92	12.50
7	15	0.3	0.75	2.117	30.17	2180	9.93	18.74	2.92	4.91
8	15	0.6	0.46	2.096	13.15	2674	10.00	17.87	2.44	4.60
9	15	0.6	0.56	2.115	15.94	3256	11.65	22.53	3.00	5.31
10	15	0.3	0.7	3.224	22.84	2023	8.92	15.83	2.42	4.18
11	15	0.3	0.75	3.223	24.47	2172	8.88	17.07	2.59	4.32
12	15	0.3	0.8	3.221	26.11	2323	9.66	18.70	2.90	4.62
13	15	0.3	0.85	3.217	27.76	2478	10.01	19.53	2.96	4.61
14	15	0.3	0.9	3.214	29.41	2632	10.47	19.92	3.03	4.85
15	15	0.3	0.95	3.212	31.06	2783	10.43	20.16	3.07	4.92
16	15	0.3	1	3.222	32.63	2885	11.56	21.12	3.26	5.33
17	15	0.3	1.2	3.222	39.16	3468	14.49	24.67	3.73	6.41
18	15	0.3	1.5	3.221	48.96	4344	18.17	30.98	4.83	7.96
19	15	0.3	1.8	3.223	58.73	5212	21.39	40.49	5.64	8.79
20	15	0.6	0.5	3.210	11.56	2857	9.03	16.99	2.02	4.06
21	15	0.6	0.62	3.236	14.27	3543	10.88	20.72	2.71	4.92

Table 3-1: (*continued*).

Case	θ (°)	D (cm)	U_0 (m/s)	$\Delta\rho/\rho_a$	Fr_d	Re	x_m (cm)	x_r (cm)	y_m (cm)	y_t (cm)
22	52	0.3	0.78	3.283	25.20	2161	10.25	18.91	8.69	10.73
23	52	0.3	0.8	3.272	25.90	2243	11.62	19.58	8.68	10.63
24	52	0.3	0.85	3.267	27.54	2388	12.27	20.38	9.15	11.37
25	52	0.3	0.9	3.250	29.24	2576	12.98	21.78	9.26	12.23
26	52	0.3	0.95	3.254	30.85	2725	13.38	23.88	9.96	13.54
27	52	0.3	1	3.256	32.46	2868	15.23	26.89	10.88	13.26
28	52	0.3	1.2	3.253	38.97	3452	20.03	31.64	13.54	16.53
29	52	0.3	1.4	3.248	45.50	4035	22.86	37.45	15.33	19.96
30	52	0.3	1.6	3.245	52.03	4620	24.85	41.05	17.25	23.09
31	52	0.3	1.9	3.245	61.78	5486	29.20	50.22	20.66	26.43
32	52	0.6	0.5	3.243	11.50	2887	12.19	19.74	7.43	10.07
33	52	0.6	0.6	3.243	13.80	3465	14.21	26.20	9.60	12.66
34	52	0.6	0.46	2.130	13.05	2717	12.82	23.86	8.35	11.38
35	52	0.6	0.6	2.136	17.00	3561	16.89	31.33	11.83	15.04
36	52	0.3	0.7	2.126	28.13	2096	13.47	21.72	9.36	12.29
37	52	0.3	0.75	2.126	30.14	2246	14.43	23.99	9.97	13.11
38	52	0.3	0.85	2.126	34.16	2545	15.49	26.10	10.52	14.55
39	52	0.3	0.95	2.126	38.17	2844	17.11	30.41	12.06	15.94
40	52	0.3	0.7	1.342	35.39	2130	16.88	29.14	10.86	14.48
41	52	0.6	0.38	1.350	13.54	2291	14.97	24.72	9.29	12.18
42	52	0.6	0.5	1.352	17.80	3015	18.30	33.38	12.51	16.29

3.4. Results and discussion

In this section, the results of the geometrical characteristics obtained from the experimental measurements are presented. A general observation during the running of the experiments is presented first, followed by the results of the geometrical parameters of the terminal rise height and the return point of the jet trajectory.

3.4.1. *General observations*

The highest point that the jet reaches (y_t) (the maximum rise height) and the return point (x_r) are controlled by several parameters. Bashitialshaaer et al. (2012) reported that the most important parameter is the densimetric Froude number (Fr_d). Therefore, the effects of this parameter in addition to other parameters such as Reynolds number ($Re = U_0D/\nu$, where ν is the kinematic viscosity) and the initial of the jet angle (θ), were taken into account in this study to thoroughly investigate the most significant parameters that play an important role in the jet characteristics.

The experimental results showed that the jet behavior is highly dependent on Fr_d and θ. Regardless of the Re, with similar Fr_d, the jet's geometrical characteristics remained consistent, as shown in Table 3-1. For example, the Fr_d for cases 26 and 37 were 30.85 and 30.14, and the values of x_r and y_t for the same cases were 23.88, 23.99 and 13.54, 13.11, respectively. Therefore, the results of these geometrical characteristics were almost the same, although case 26 had a higher Re and velocity, 2725 and 0.95 m/s, respectively. Thus, the results obtained from this study confirm the importance of Fr_d on the jet behavior as a significant parameter, along with the jet angle θ.

Also, as a general observation, the results indicated that the density of the jet (due to salinity) affected the distribution of the jet, where the penetration of the low-density jet (1011 kg/m^3) was very slow. This jet reached the bottom within 12 s, which was slower than the jet with higher density (1030.6 kg/m^3), which reached the bottom within 8.7 s. The divergence between the velocities for those jets is obvious. Lai and Lee (2012) reported that the velocity decay of a dense jet can be affected by two factors: jet spreading and negative buoyancy. However, Alfaifi et al., (2019a) found that a source of density difference can also be important (salinity versus temperature).

The parameters that influence the distances along the *x*- and *y*-directions were further investigated statistically using regression analysis (Minitab 18). For brevity, only the results of dimensionless of x_r/D and y_t/D are shown in this section.

To explain the most sensitive parameter that can affect the geometrical characteristics of the jet behavior, a sensitivity analysis was applied for Fr_d, θ, and Re. The results for the P and F-values are the indicators that statistically highlight the most significant parameters that affect the jet geometry/shape. When the P-value is less than 0.05, the null hypothesis should be rejected, and the parameter is considered significant. The P-value is calculated from the F distribution table. When the F-value is large, it results in a smaller P-value at the same degree of freedom. Therefore, based on the analysis of variance (ANOVA) table obtained from the regression analysis (Table 3-2), the effect of the considered parameters (*i.e.*, Fr_d, Re, and θ) varied depending on the direction of the jet considered (*i.e.*, along the x-axis or the y-axis). The results of the analysis showed that the jet was dominated by Fr_d and θ for both directions (*i.e.*, x and y) with a statistically insignificant effect from *Re* in the y-direction. However, the jet was affected by all parameters, but with less effect from *Re*, along the x-direction (x_r and x_m). Table 3-2 shows a summary of the ANOVA table of the regression analysis for x_r/D and y_t/D. The statistical results are in agreement with the observed experimental jet shapes. Based on the *F*-values, Fr_d and θ were the most significant parameters influencing geometrical characteristics x_r and y_t. Thus, Fr_d was still the most significant parameter in controlling the distance on both axes, followed by the jet angle θ (Table 3-2).

Table 3-2: ANOVA results from the regression analysis studying the effect of Fr_d, θ, and Re on geometrical characteristics x_r/D and y_t/D.

Geometrical characteristic	Parameter	*F*-value	*P*-value
x_r/D	Fr_d	1499.25	0.000
	θ	100.95	0.000
	Re	9.21	0.004
y_t/D	Fr_d	97.73	0.000
	θ	166.36	0.000
	Re	0.29	0.596

3.4.2. *Geometrical characteristics*

3.4.2.1. *Terminal rise height of the jet trajectory*

Figures 3-5a and b show the behavior of the jet trajectories at the terminal rise heights of the inclined jets. The data obtained for the maximum height rise of the jet are normalized by the nozzle diameter and are plotted versus the initial densimetric Froude number (Fr_d) for the discharge angles of 15° and 25°, along with some data reported by others. A wide range of Fr_d values is covered in the experiments in order to obtain more data for both angles and provide more details about the behavior of the inclined dense jets. The data for the discharge angles of 15° (Figure 3-5a) and 52° (Figure 3-5b) are presented for the maximum rise height in the horizontal direction

(x_m), while the maximum centerline heights (y_m) are presented in Figures 3-6a and b. Then, the edges of the maximum heights of the jets (y_t) are shown in Figure 3-7a and b. A linear data fit is obtained for both angles and compared with previous studies. Notably, for the angle of 52°, only one previous study was found by Lai (2010), which implies that this angle has rarely been studied. Therefore, the comparison can be enhanced by using results for closer angles (*i.e.*, 50° and 55°) that reported previously by Abessi and Roberts (2015b), Papakonstantis and Tsatsara (2018 and 2019). These angles will be shown in all related figures of the angle 52° in this section.

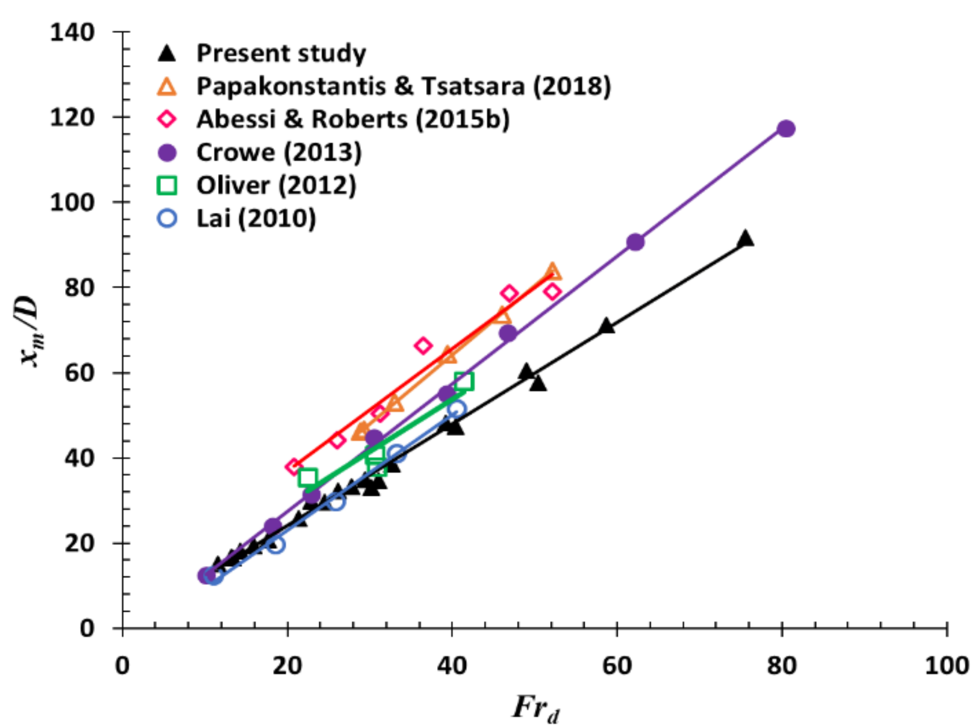

(a)

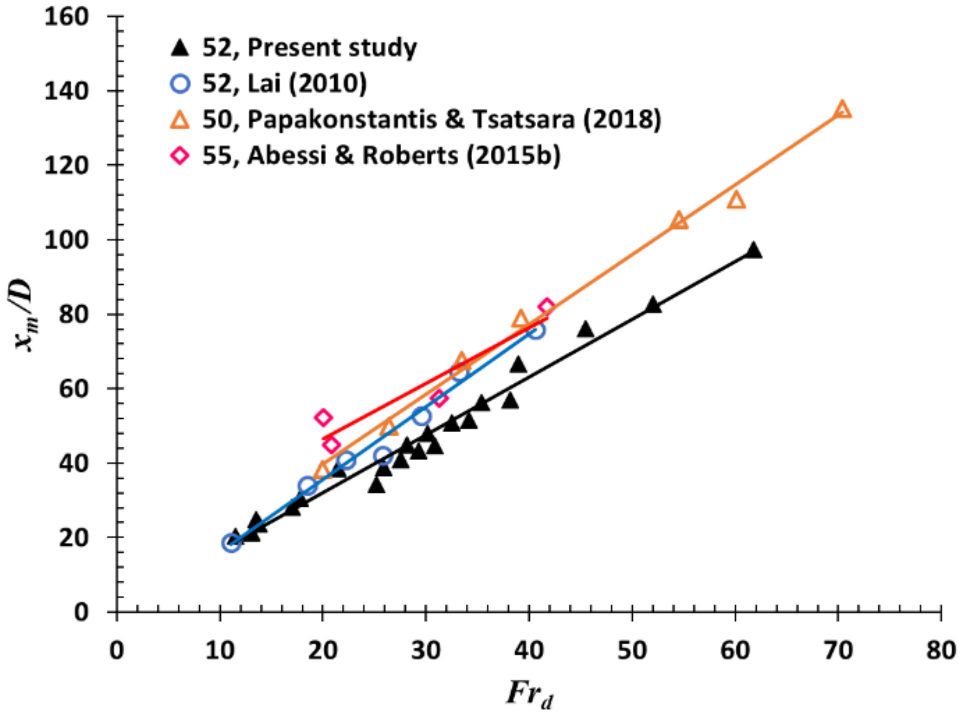

(b)

Figure 3-5: Normalized horizontal distance location of the maximum terminal height (x_m) versus the densimetric Froude number for angles: (a) 15° and (b) 52°.

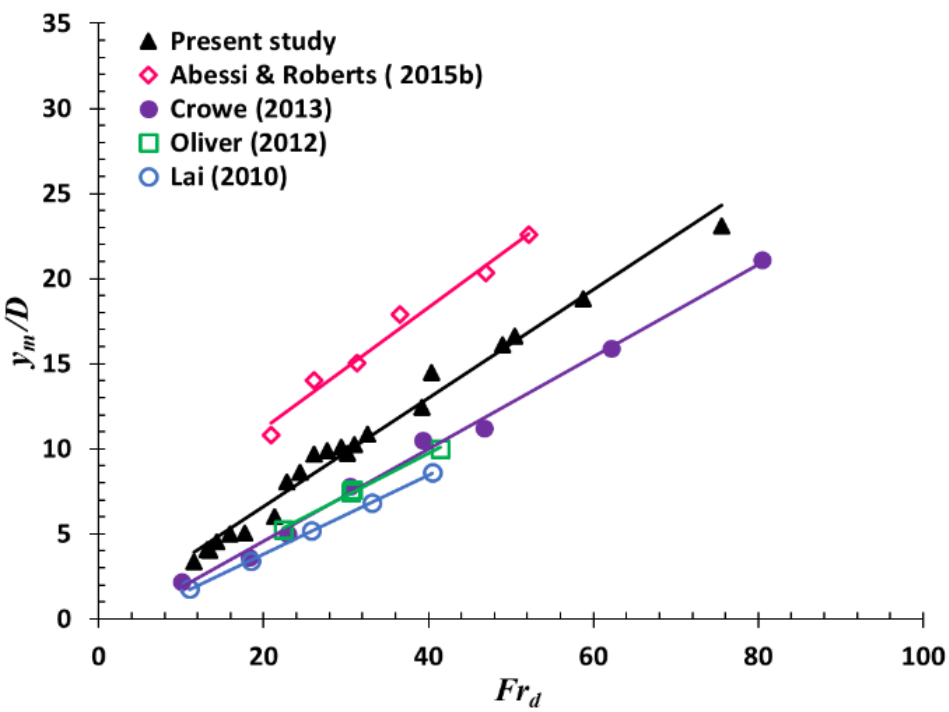

(a)

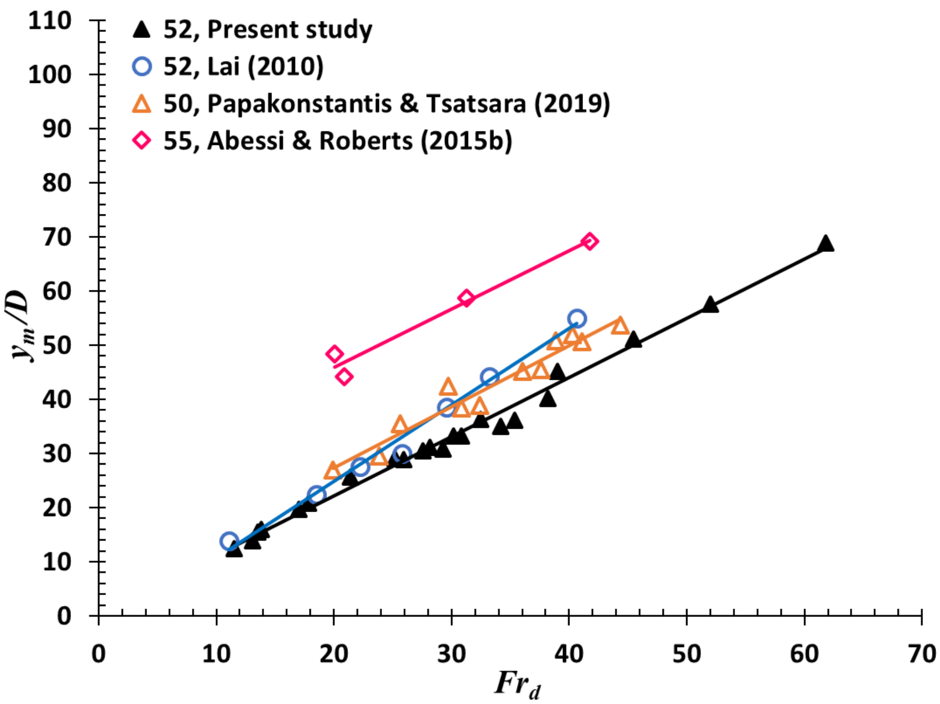

(b)

Figure 3-6: Normalized vertical distance location of the maximum centerline height (y_m) versus the densimetric Froude number with previously reported data for discharge angles: (a) 15° and (b) 52°.

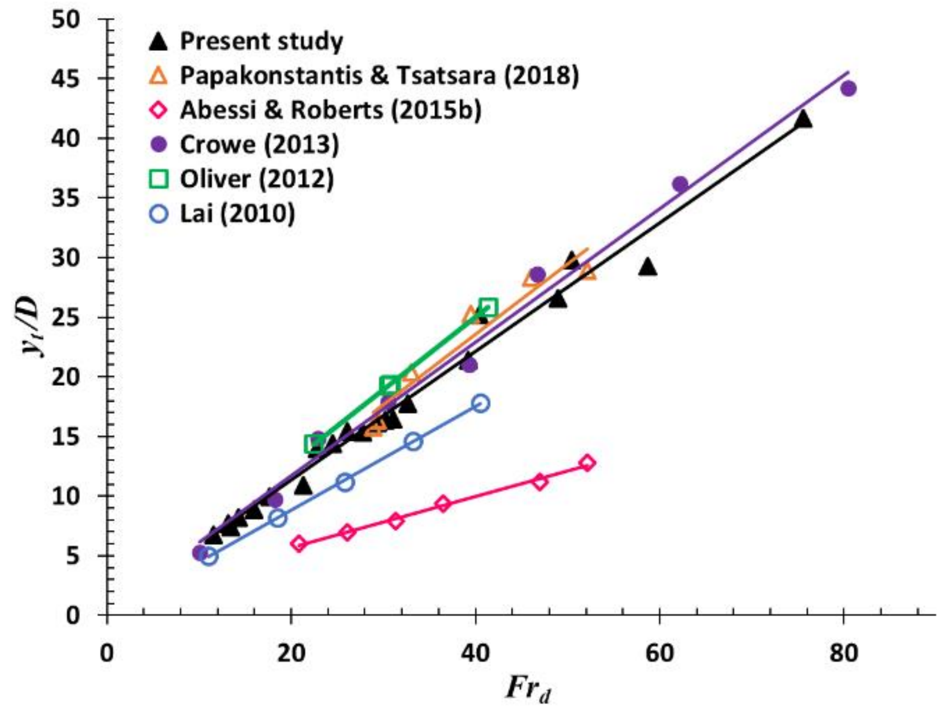

(a)

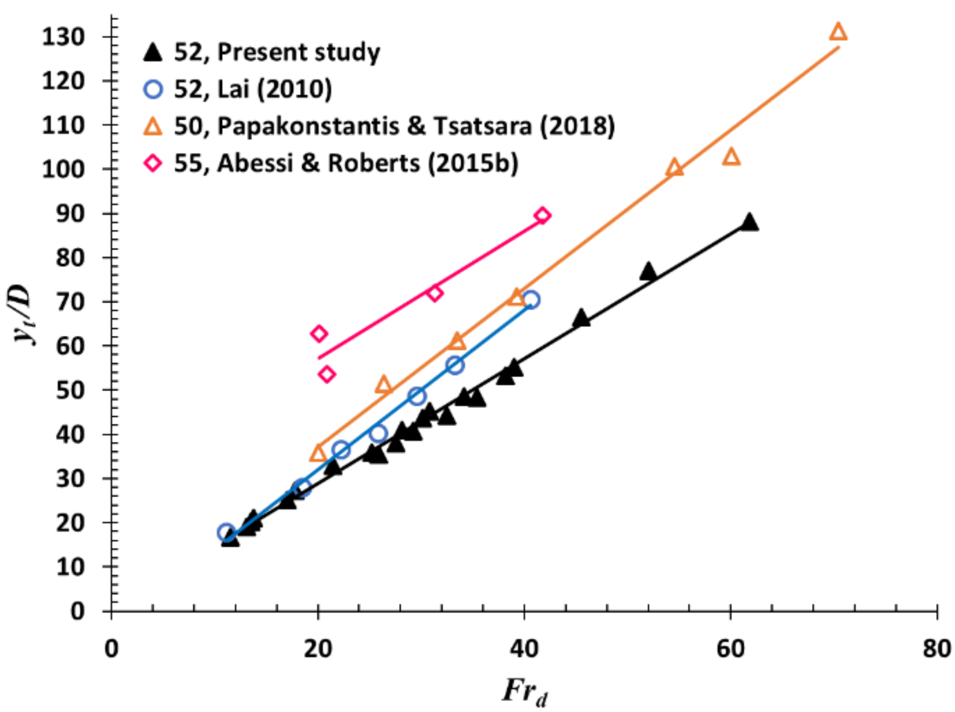

(b)

Figure 3-7: Normalized vertical distance location of the jet edge at the maximum rise height (y_t) versus the densimetric Froude number with previously reported data for discharge angles: (a) 15° and (b) 52°.

The data obtained in the present study are consistent with previously published data, especially for the angle of 15°. In addition, good agreement is also shown for all geometric parameters with most of the previous data, especially for the angle of 15°, while the 52° angle results are slightly different from the compared data. In all the comparison figures (i.e., 3-5, 3-6 and 3-7), the increases in the normalized parameter values (x_m, y_m, and y_t) in the present study are consistent with all previously obtained values for an angle of 15°. On the other hand, for an angle of 52°, these values are slightly higher in the previous study (i.e., Lai, 2010) than in the present study. Figure 3-6b shows the data obtained for an angle of 52° for y_m, which shows better alignment with the previous data than for the other parameters. Figure 3-7a shows that the data obtained in this study for an angle of 15° are consistent with other reported data, especially Crowe (2013), Oliver (2012), and Papakonstantis and Tsatsara (2018), although the methods used in measuring the geometrical dimensions were different. As shown in Figure 3-7b, the results also show good agreement with the existing data, despite their limitations (i.e., 52°).

It can be observed that the data from the present study for the angle of 52° are slightly divergent than the similar angle reported by Lai (2010), and the parameter values are lower than those in other studies. This divergent was observe when the jet inclination angle increased, where was less and/or not existing in the lower angle (*i.e.*, angle 15°). On the other hand, this variation was not observed when compared the present study with the data of angles 50° and 55°.

It was also observed that the smaller values of Fr_d *(i.e., <26)* are more consistent with those in the study by Lai (2010). Moreover, when the Fr_d increases (*i.e.*, *>26*), all normalized values (x_m, y_m and y_t) increase but are still lower than those in the previous study.

The normalized horizontal distances for the terminal height $x_m/(DFr_d)$ of the present results for angles of 15° and 52° versus Fr_d are presented in Figures 3-8a and b and compared with those for similar and closer angles in previous studies. The results in the present study are within the range of the previous data. More specifically, for the angle of 15°, there is good agreement with the data reported by Crowe (2013), Lai (2010), Oliver (2012). Good agreement is also shown for the same angle for normalized y_t (Figure 3-10a) in this study with all previous data except Abessi and Roberts (2015b).

The results for other normalized parameters (*i.e.*, y_m and y_t) are shown in Figures 3-9 and 3-10. Similarly, the data obtained in the present study for both angles are within the range of the previous data.

In contrast, for the angle of 52° in all figures, the results of the presented study are relatively smaller and lower than other reported data, but still in a good agreement and reasonably satisfactory. This may be due to the lack of studies on this angle, as there is only one previous study available for this angle (*i.e.*, 52°) by Lai (2010), which did not cover a wide range of Fr_d.

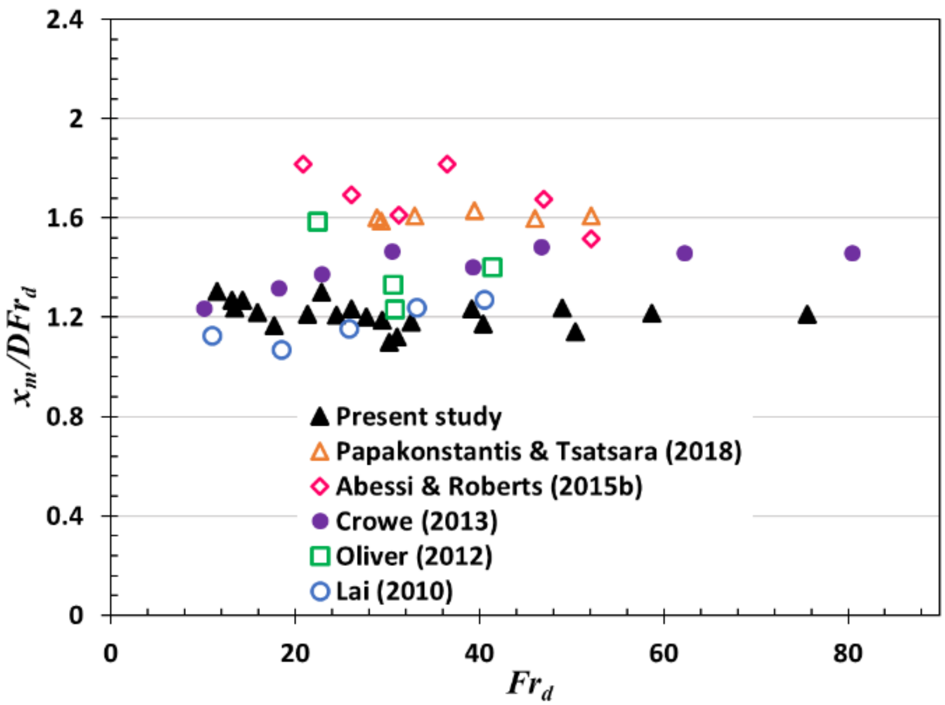

(a)

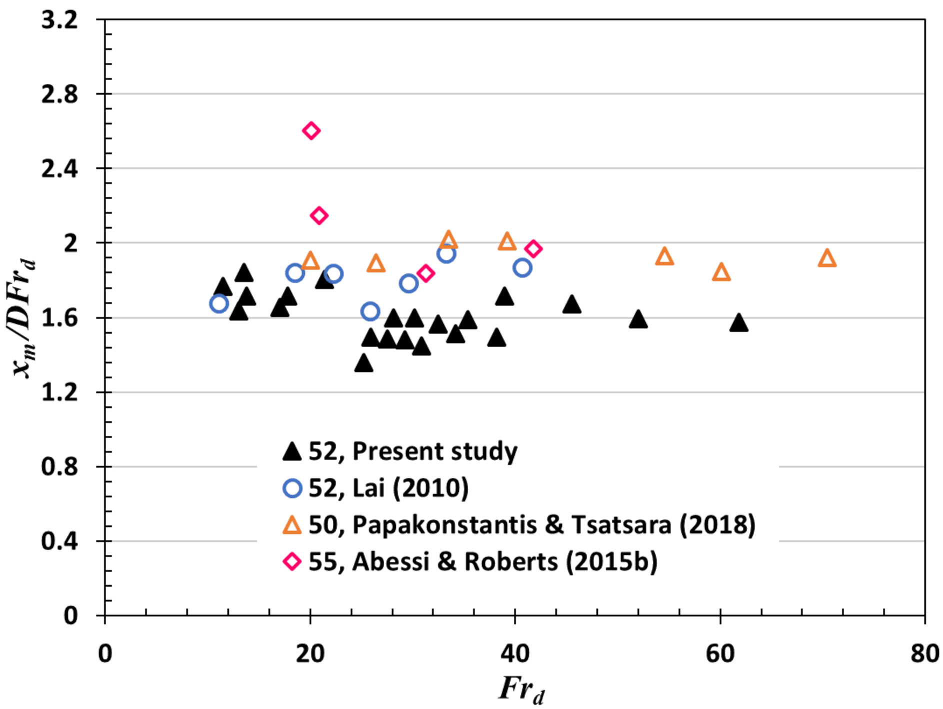

(b)

Figure 3-8: Comparison of the present study with previous studies for dimensionless x_m versus Fr_d for: (a) 15° and (b) 52°.

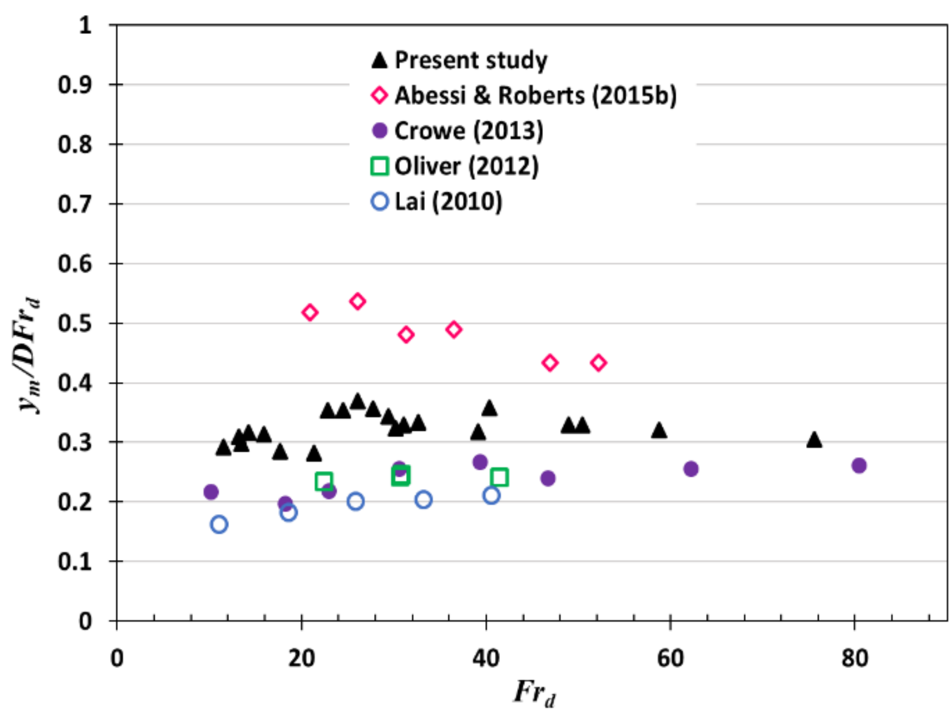

(a)

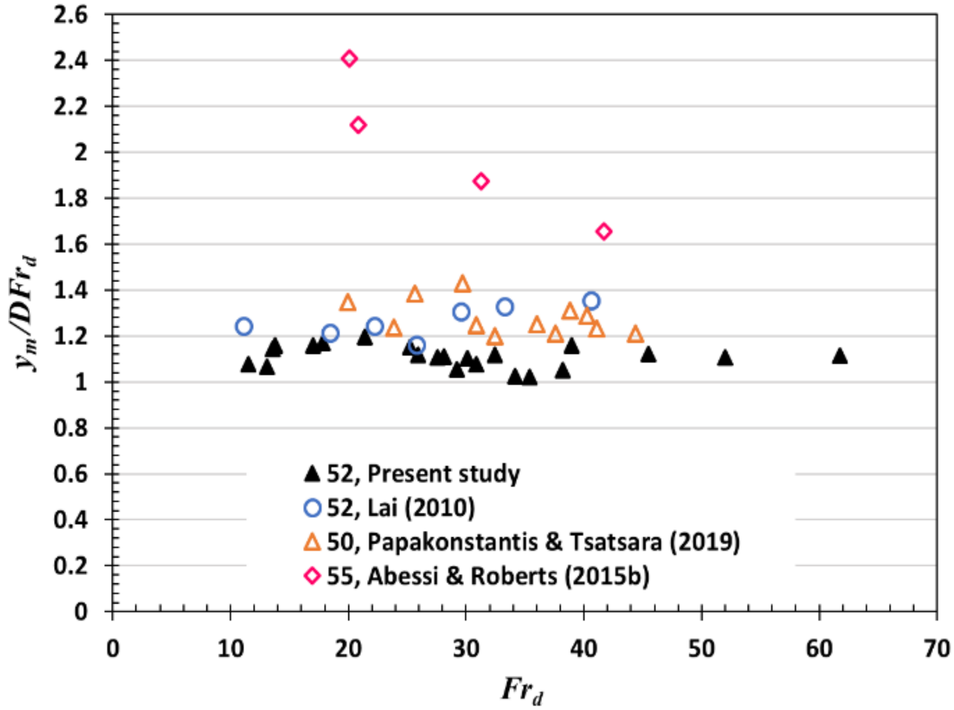

(b)

Figure 3-9: Comparison of the present study with previous studies for dimensionless y_m versus Fr_d for: (a) 15° and (b) 52°.

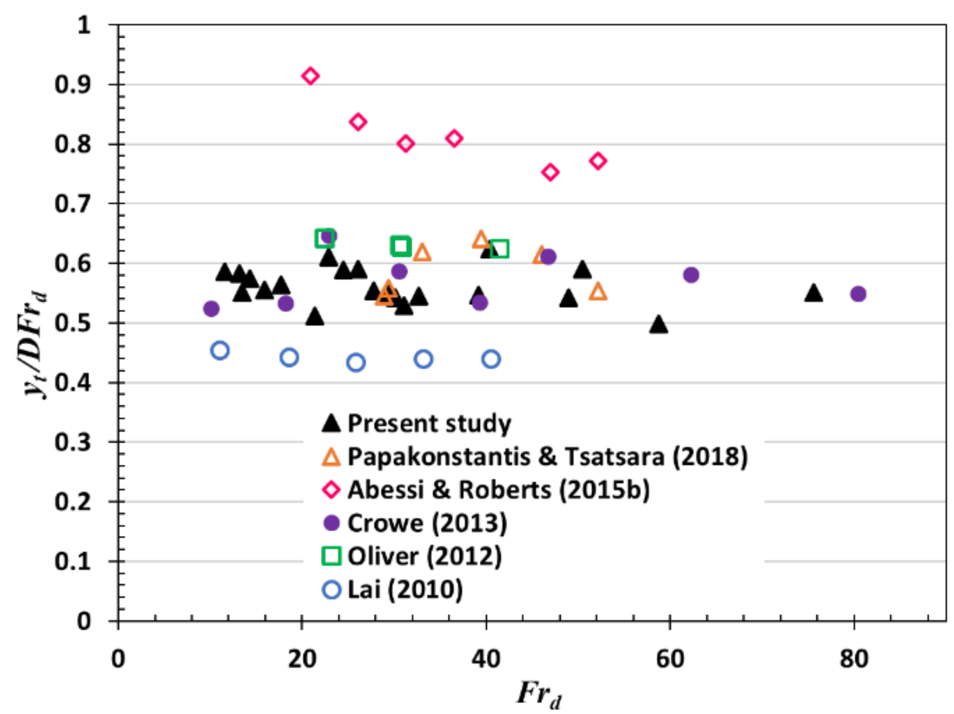

(a)

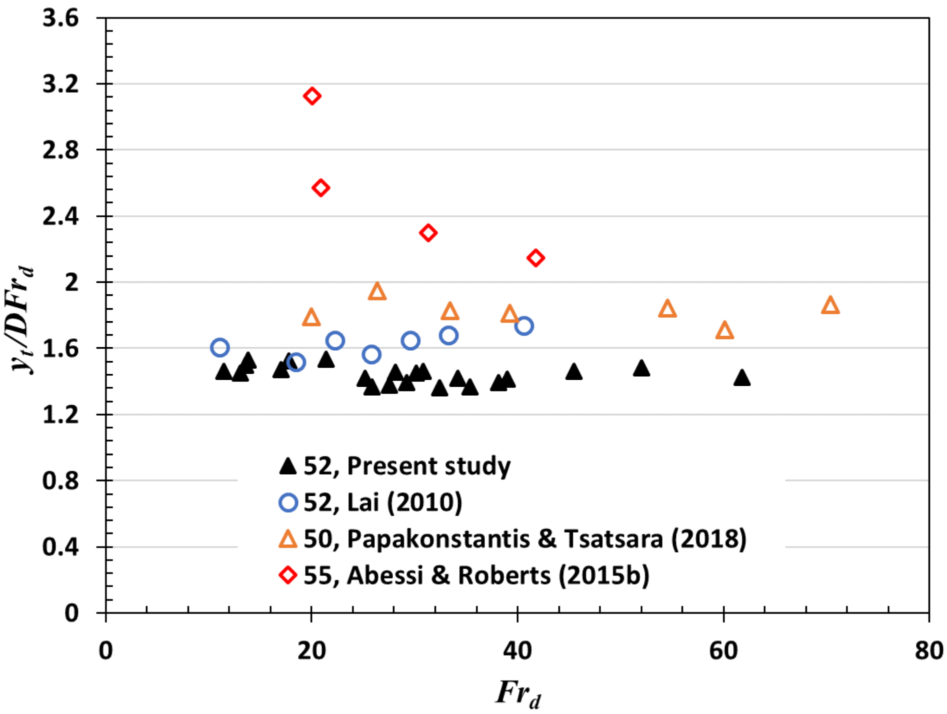

(b)

Figure 3-10: Comparison of the present study with previous studies for dimensionless y_t versus Fr_d for: (a) 15° and (b) 52°

3.4.2.2. *Return point of the jet trajectory*

The experimental results for the return point location (x_r) are shown in Figures 3-11a and b for angles 15° and 52°, respectively. In these figures, the results for the return point are normalized by the diameter of the inner nozzle (D) and plotted against the Fr_d. A linear fit is obtained for each study to clearly show the comparison.

These points were estimated for each experiment based on the distances observed during the experimental record when the jet reached the steady state, and then the specific frame was defined to determine the return point. As shown in Figure 3-11a, good agreement is seen between the results in the present study and those of previous studies. Additionally, Figure 3-11b shows consistency and reasonable agreement between the present study and the previous studies (Lai, 2010; Papakonstantis and Tsatsara, 2019). For the geometrical parameter x_r, for the angle of 52° (see Figure 3-11b), the present study shows a better match with the previous studies than for the other parameters.

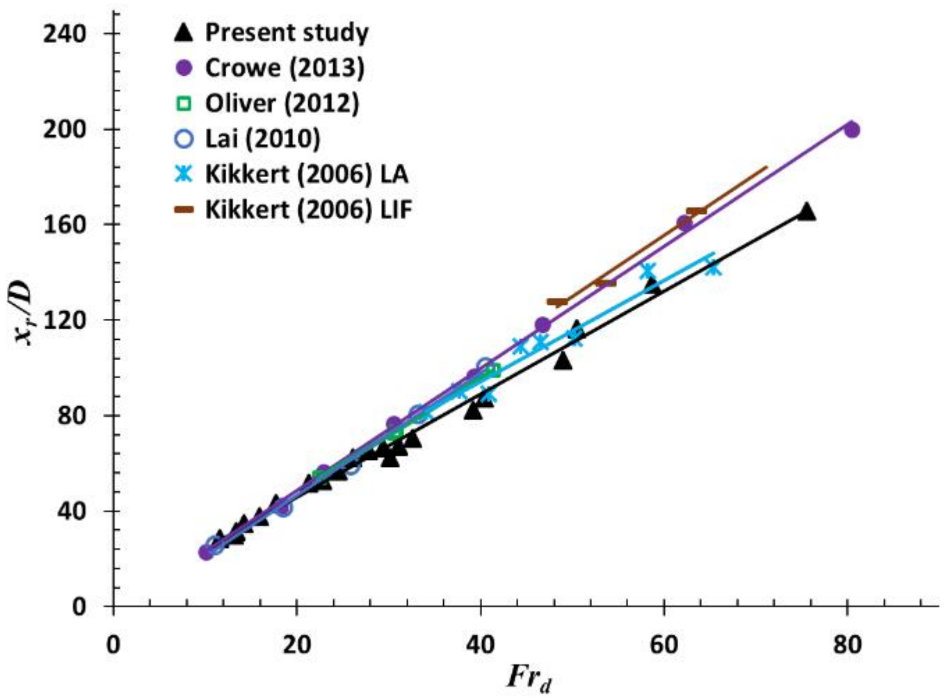

(a)

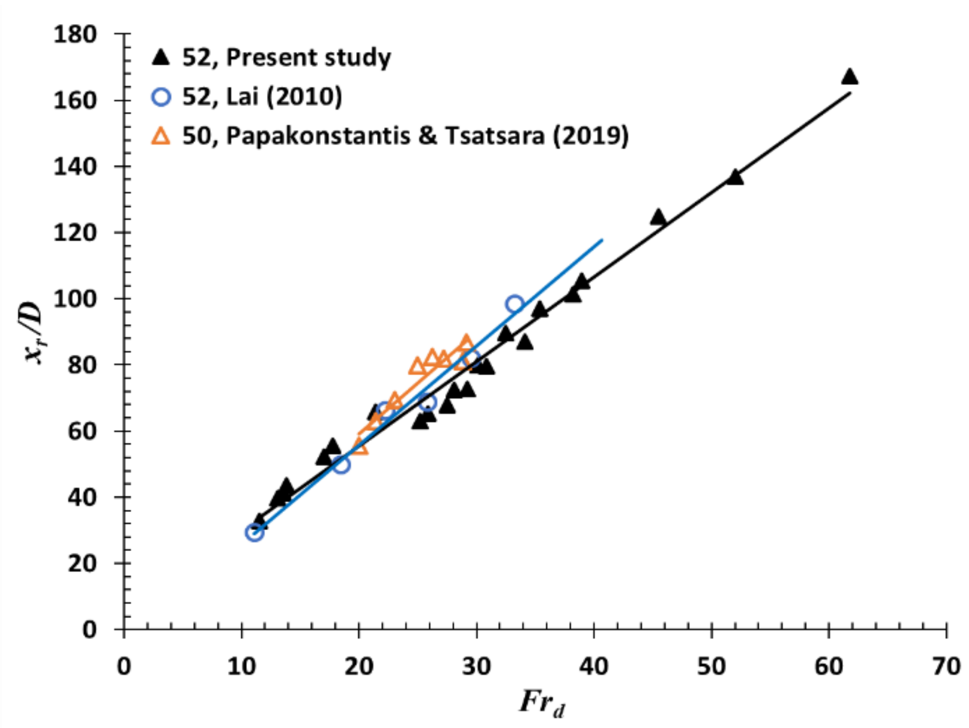

(b)

Figure 3-11: Results for return point x_r versus Fr_d compared with those of previous studies for: (a) angle 15° and (b) angle 52°.

Figures 3-12a and b illustrates the normalized horizontal distances obtained in this study for x_r/DFr_d versus various Fr_d, compared with data reported in previous studies.

The results for all angles in the present study are within the range of the previous data and are in good agreement with those data. The constant value of C_{x_r} obtained in this study for the angle 15° is 2.26, which is considered within the range of values from 2.13 to 2.53 reported in the literature (Crowe, 2013; Lai, 2010; Oliver, 2012).

The results for the angle 52° in the present study are shown in Figure 3-12b. The values of C_{x_r} are somewhat lower than the values from the previous study (Lai, 2010; Papakonstantis and Tsatsara, 2019), especially for Fr_d higher than 25; however, the constant value of C_{x_r} obtained in this study (2.68) is still in good agreement with that of a previous study, which was 2.84 (Lai, 2010).

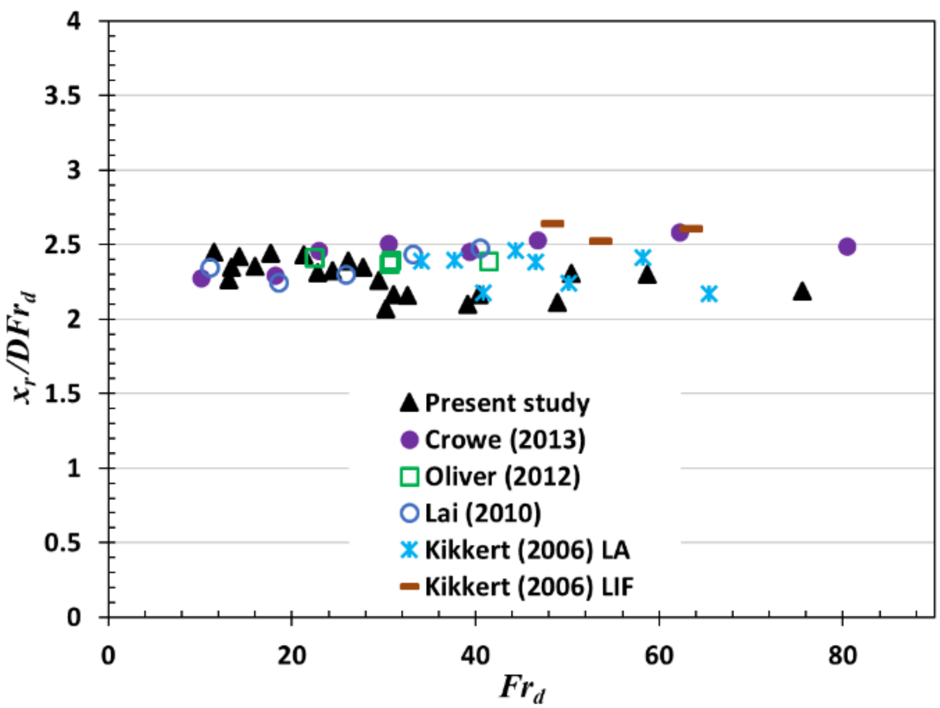

(a)

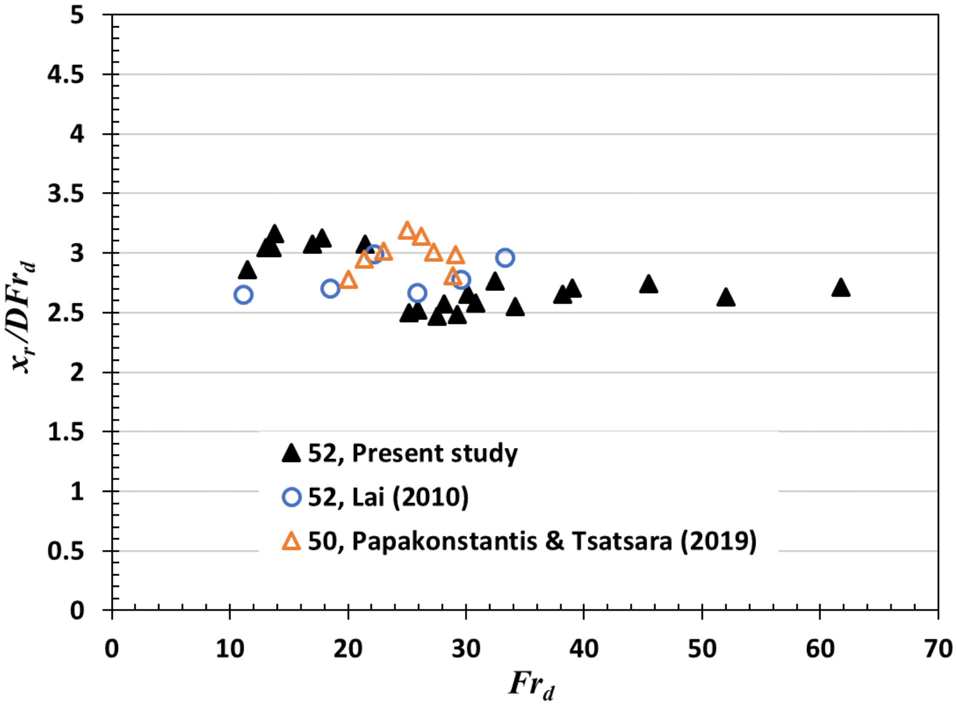

(b)

Figure 3-12: Return point locations compared with those of previous studies for: (a) angle 15° and (b) angle 52°.

The constant values of the horizontal distance of the terminal height, C_{x_m}, and the return point, C_{x_r}, are plotted in normalized form against the nozzle discharge angle in Figures 3-13a and b along with data from previous studies. In both figures, the data were extracted from where the maximum tracer concentration of the jet centerline trajectories was observed. As shown in Figures 3-13a and b, second-order polynomial fittings were obtained for the present study to show the difference in the maximum distance that occurs for each angle. Good agreement was observed between the present and previous experiments for the angles of 15° and 52°, with a marked lower in both values for both angles. Generally, the fitting curve is close to most of the reported data.

It is clearly shown that the horizontal distance of the terminal height and return point (i.e. x_m/DFr_d and x_r/DFr_d) increases with increasing angle up to approximately 40°, and then the distance begins to decrease. Accordingly, it can be estimated from Figures 3-13a and b that the maximum distance for these parameters occur for an angle ≈ 40. For the angle of 52°, the values in the present study are considered lower than the data reported previously (Lai, 2010).

Similarly, the results in the present study for the normalized forms (y_t/DFr_d) and (y_m/DFr_d) are also plotted versus the nozzle angle, as shown in Figures 3-13c and d, along with data from previous studies. The results show that the terminal rise height gradually increases as the angle of the jet increases, and which is consistent with previous data for small angles (i.e., 15°) while slightly diverging for the angle of 52°. Similar behavior was observed in the results for most of the present study; i.e., the obtained results for the angle of 15° are in good agreement with those of previous studies, while the results for the angle of 52° are slightly lower than the values from other studies (e.g., Lai, 2010).

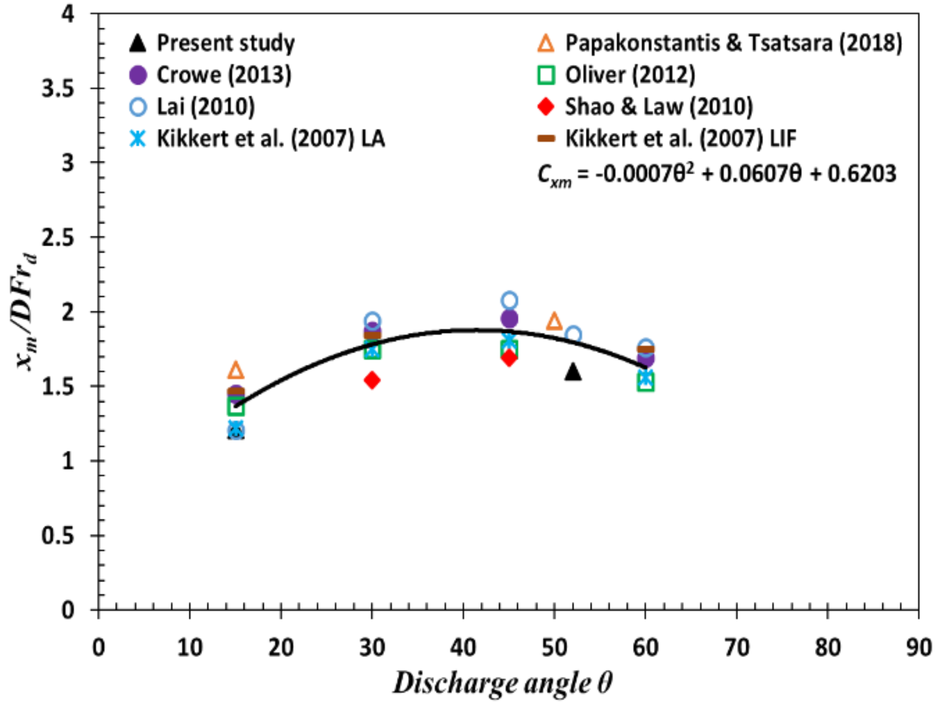

(a)

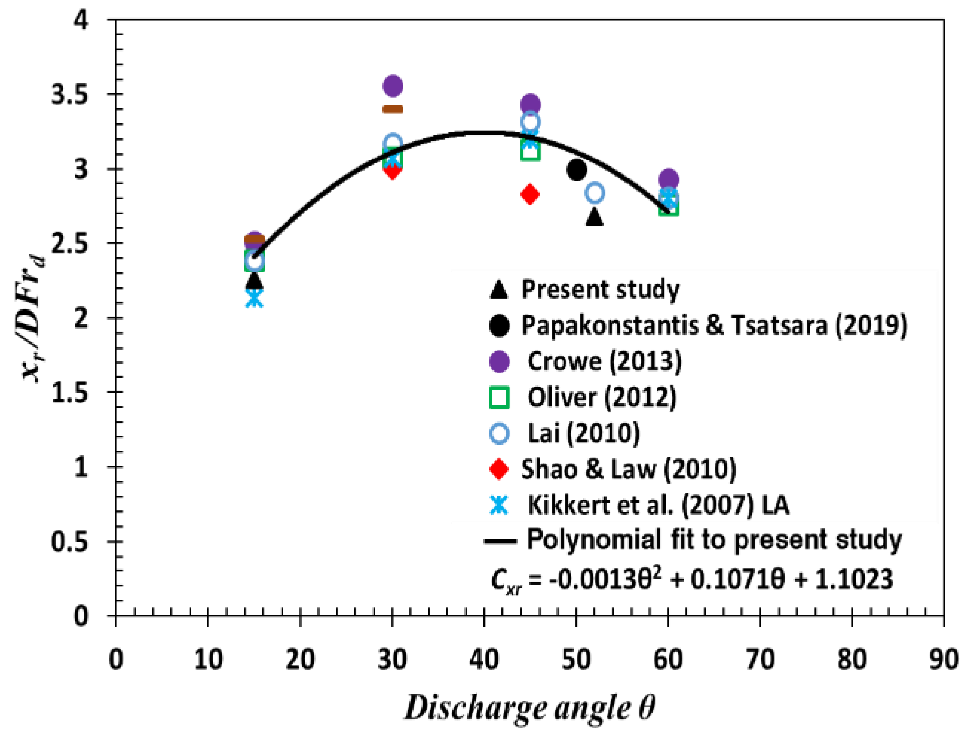

Present study
Papakonstantis & Tsatsara (2019)
Crowe (2013)
Oliver (2012)
Lai (2010)
Shao & Law (2010)
Kikkert et al. (2007) LA
Polynomial fit to present study
$C_{xr} = -0.0013\theta^2 + 0.1071\theta + 1.1023$
x_r/DFr_d
Discharge angle θ

(b)

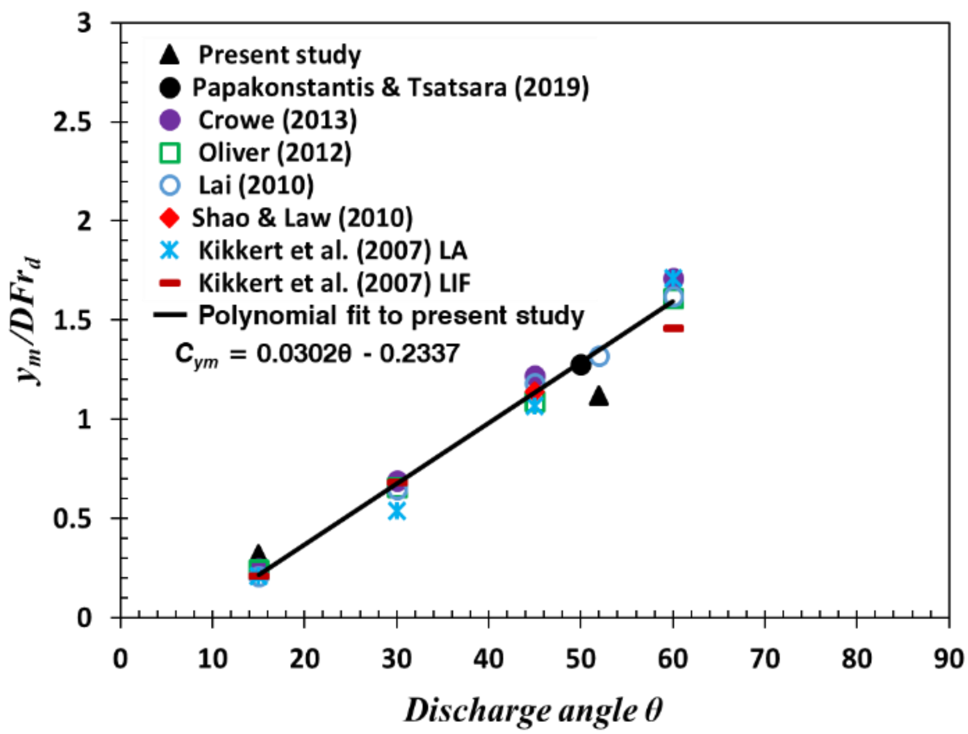

Present study
Papakonstantis & Tsatsara (2019)
Crowe (2013)
Oliver (2012)
Lai (2010)
Shao & Law (2010)
Kikkert et al. (2007) LA
Kikkert et al. (2007) LIF
Polynomial fit to present study
$C_{ym} = 0.0302\theta - 0.2337$
y_m/DFr_d
Discharge angle θ

(c)

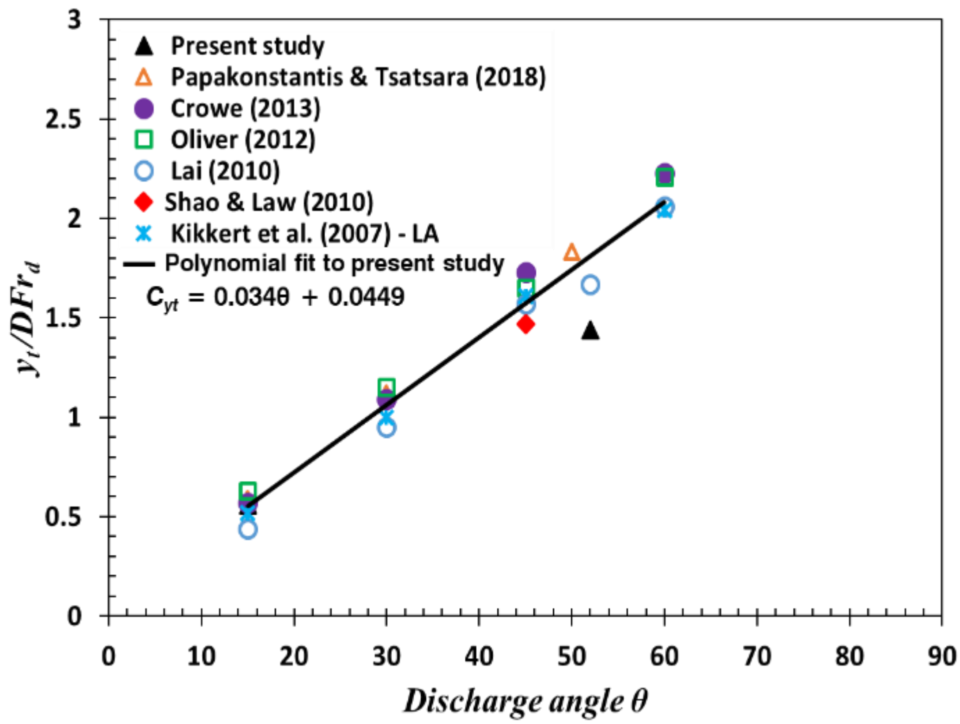

(d)

Figure 3-13: Results for angles 15° and 52° compared with those of previous studies for various nozzle angles for: (a) location of horizontal distance of terminal rise height; (b) location of horizontal distance of return point; (c) location of centerline on the vertical rise, and (d) location of the outer edge of the jet at the maximum rise height.

Table 3-3 summarizes a comparison of the constant values of C_{x_m}, C_{x_r}, C_{y_m} and C_{y_t} in the present results with those from previous studies. The constants in this study were estimated by using the formula in Equations (3-6) to (3-9) and then taking the average value of the constant for each angle. The results in the present study for the angle of 15° for C_{x_m} agree very well to those obtained by Kikkert (2006) LIF and Lai (2010), as the value in the present study is 1.21, compared with the values of 1.21 for Lai (2010), and 1.22 for Kikkert (2006) LA. There is also excellent agreement between the value obtained in this study for the terminal rise height, C_{y_t} (0.56) for angle 15° with the data reported by Crowe (2013), Kikkert (2006) LA and LIF, Papakonstantis and Tsatsara (2018), which were 0.57, 0.52, 0.52, and 0.59, respectively. For the other normalized trajectory characteristics (*i.e.*, C_{x_r} and C_{y_m}), the results show reasonable agreement with most of those values from previous studies. In general, the present study's values for all normalized trajectory characteristics are within the data ranges that were previously reported in the literature. All previous comparisons are specific to the angle of 15°; however, for the angle of 52°, the present values are slightly different than the values obtained by Lai (2010).

Table 3-3: Comparison of present and previous experimental coefficients.

	C_{x_m}						
	15°	**30°**	**45°**	**50°**	**55°**	**52°**	**60°**
Present study	1.21	-	-	-	-	1.60	-
Papakonstantis and Tsatsara (2018)	1.61	1.83	-	1.94	-	-	-
Abessi and Roberts (2015)	1.69	2.13	2.20	2.08	2.14	-	1.88
Crowe (2013)	1.45	1.87	1.96	-	-	-	1.69
Oliver (2012)	1.37	1.75	1.75	-	-	-	1.53
Papakostantis et al. (2011a)	-	-	2.10	-	-	-	1.84
Shao and Law (2010)	-	1.54	1.69	-	-	-	-
Lai (2010)	1.21	1.94	2.08	-	-	1.85	1.76
Kikkert (2006), LA	1.22	1.75	1.81	-	-	-	1.56
Kikkert (2006), LIF	1.47	1.84	-	-	-	-	1.75
	C_{x_r}						
Present study	2.26	-	-	-	-	2.68	-
Papakonstantis and Tsatsara (2019)	-	-	-	3.00		-	-
Crowe (2013)	2.51	3.56	3.43	-	-	-	2.93
Oliver (2012)	2.39	3.08	3.13	-	-	-	2.76
Shao and Law (2010)		3.00	2.83	-	-	-	-
Lai (2010)	2.39	3.17	3.32	-	-	2.84	2.81
Kikkert (2006), LA	2.13	3.07	3.20	-	-	-	2.80
Kikkert (2006), LIF	2.53	3.40	-	-	-	-	-
	C_{y_m}						
Present study	0.32	-	-	-	-	1.12	-
Papakonstantis and Tsatsara (2019)	-	-	-	1.28	-	-	-
Abessi and Roberts (2015)	0.48	0.79	1.63	1.71	2.01	-	1.89
Crowe (2013)	0.25	0.69	1.22	-	-	-	1.71
Oliver (2012)	0.24	0.66	1.09	-	-	-	1.61
Shao and Law (2010)	-	-	1.14	-	-	-	-
Lai (2010)	0.21	0.65	1.18	-	-	1.32	1.62
Kikkert (2006), LA	0.21	0.54	1.07	-	-	-	1.71
Kikkert (2006), LIF	0.21	0.68	-	-	-	-	1.46
	C_{y_t}						
Present study	0.56	-	-	-	-	1.44	-
Papakonstantis and Tsatsara (2018)	0.59	1.12	-	1.83	-	-	-
Abessi and Roberts (2015)	0.81	1.18	2.09	2.19	2.54	-	2.39
Crowe (2013)	0.57	1.09	1.73	-	-	-	2.23
Oliver (2012)	0.63	1.15	1.65			-	2.21
Papakostantis et al. (2011a)	-	-	1.58	-	-	-	2.13
Shao and Law (2010)	-	-	1.47	-	-	-	
Lai (2010)	0.44	0.95	1.57	-	-	1.67	2.06
Papakostantis and Christodoulou (2008)			1.59				2.16
Kikkert (2006), LA	0.52	1	1.61	-	-	-	2.04
Kikkert (2006), LIF	0.52	1.17	-	-	-	-	2.43

3.4.3. *GMDH model results*

The result of statistical indices obtained from Equations (3-18 to 3-21) for the GMDH model's predictions for the two angles are presented in this section. The performance of the predicted model along with comparison with the experimental data obtained from the present study and from previous analytical solutions is discussed in detail.

3.4.3.1. *Evaluating model performance statistically*

Table 3-4 presents the results of the statistical indices obtained from Equations (3-18 to 3-21) for the GMDH model's predictions for the two angles. As mentioned previously, the lower the value, the more accurate the model is, and this applies to all statistical indices (except the coefficient of determintation). The lowest MAE value was shown for the y_m (0.724) for the angle 15°, while the highest value for the same indices was for x_r (4.278) for the angle 52°. The same was found for the RMSE for same parameters (*i.e.*, y_m and x_r) and angles. For the mean absolute percentage error (MAPE), the best value was found for the y_t (2.637) for the angle 52°, while the largest one was for y_m (8.438) for the angle 15°. In general, all the statistical results showed that the prediction results of the GMDH for all geometrical characteristics for both angles were in a good agreement overall.

Table 3-4: Evaluation of the GMDH model predictions using statistical indices.

Geometrical characteristic	R^2	MAE	RMSE	MAPE %
		15°		
x_m/D	0.990	1.113	1.554	2.959
x_r/D	0.992	2.710	3.317	4.142
y_m/D	0.976	0.724	0.862	8.438
y_t/D	0.968	0.946	1.355	4.617
		52°		
x_m/D	0.964	2.677	3.206	6.266
x_r/D	0.966	4.278	4.978	6.968
y_m/D	0.994	1.024	1.145	3.509
y_t/D	0.995	1.126	1.404	2.637

3.4.3.2. *Comparison with data obtained from experimental results*

In this study, more than 60% of the data obtained from present study was used for training the GMDH model, while the rest was used for validation. In this section, the prediction results of the GMDH method are compared with the obtained experimental data presented in this study for the angles 15° and 52°. The results for angles of 15° and 52° were selected in order to examine the performance of the GMDH model under the same conditions. For brevity, only the result of x_r/D is shown in this section.

Figure 3-14 shows the results for the dimensionless geometrical parameters x_r/D for the observed data in the present study for angles 15° and 52° plotted against the values predicted by the GMDH model. The linear fit of the predicted results has also been added to each figure to illustrate how accurate the GMDH method is, compared to the actual data. The R^2 results for each comparison are also presented in Table 3-4. The figures show that the proposed model (GMDH) has high accuracy and gives excellent predictions for all comparisons, and the R^2 values range between 0.964 and 0.995. Figure 3-14 also shows that all fitting lines for the GMDH model performed very well for all geometrical parameter predictions, as the scattered data are closely located around the fitting lines with error ranged from 2.6 to 8.4% for y_t/D and y_m/D, respectively, around the lines. The lowest R^2 result was for x_m (0. 964), while the highest coefficient of determination was for y_t (0.995), both for the angle of 52°. The lowest result of the determination coefficient R^2 was 0.964, which can be considered as reasonably satisfactory.

The equations used for calculating each geometrical parameter for the inclined dense jets with inclination angles of 15° and 52° are provided in Table 3-5. All these equations are presented as dimensionless which depend on the same input variables: Fr_d. In these equations, the geometrical characteristics are mainly affected solely by Fr_d for all angles. Accordingly, this is an indication that the effect of the Fr_d on the geometrical characteristics of the jet trajectory is highly significant.

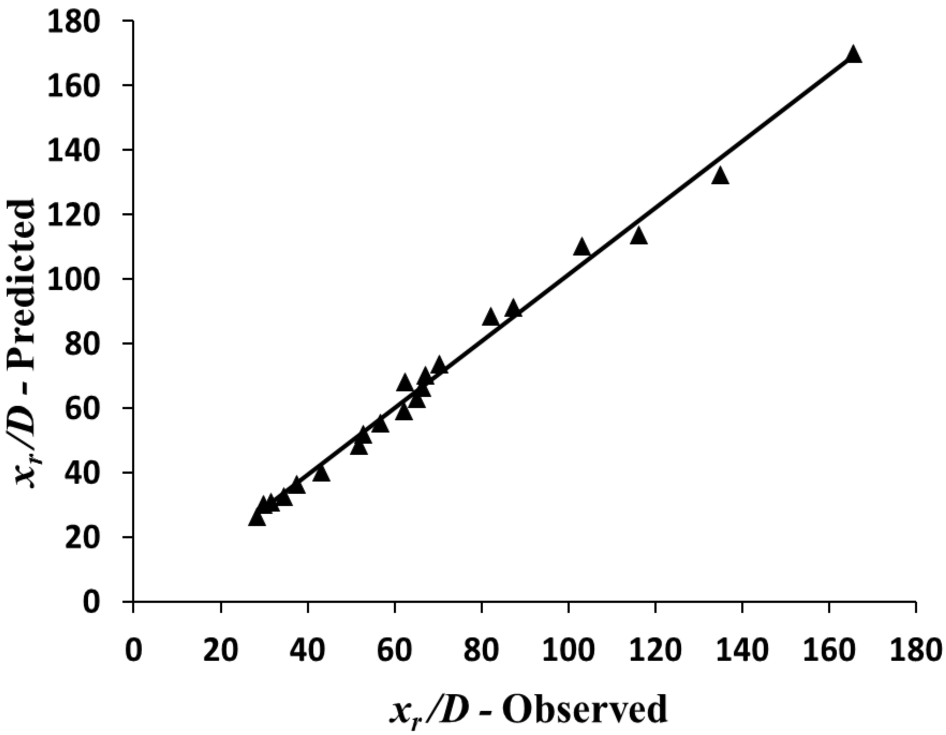

(a)

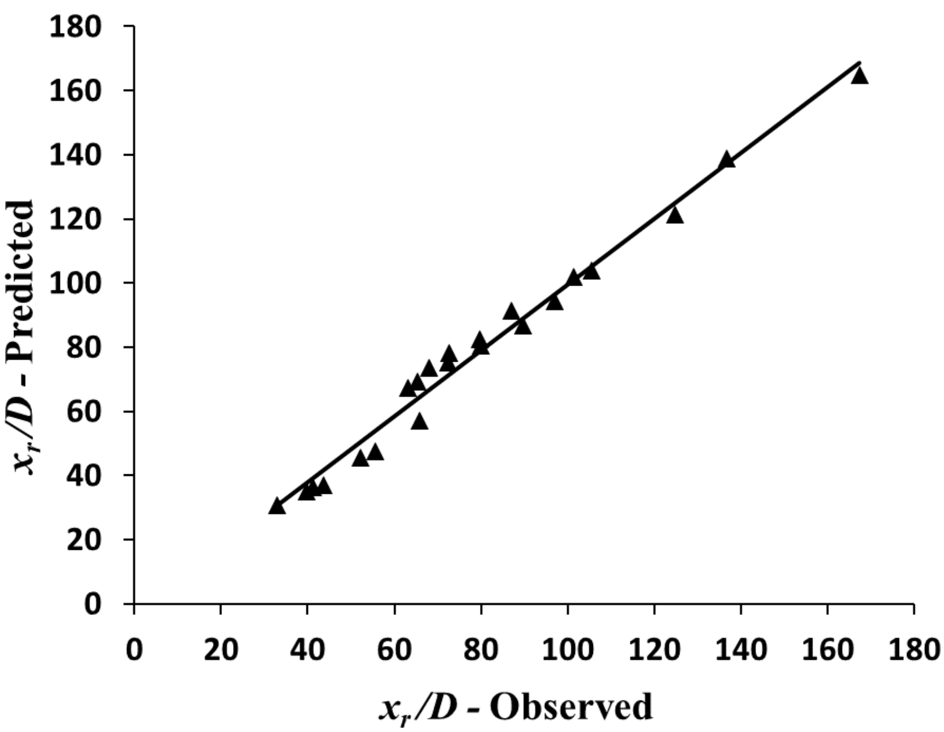

(b)

Figure 3-14: Dimensionless values of geometrical parameters (x_r) of the GMDH predicted results versus observed data for angles: (a) 15° and (b) 52°.

Table 3-5: Equations obtained from the GMDH for dimensionless geometrical parameters.

Geometrical characteristic	Equations	
	15°	
x_m/D	$=-0.0656022 +1.20525\ Fr_d$	(3-22)
x_r/D	$=0.600193 + 2.24027\ Fr_d$	(3-23)
y_m/D	$=0.236+0.31887\ Fr_d$	(3-24)
y_t/D	$= 0.197634 + 0.552475\ Fr_d$	(3-25)
	52°	
x_m/D	$=0.697519 +1.54599\ Fr_d$	(3-26)
x_r/D	$= 0.0713321+2.66735\ Fr_d$	(3-27)
y_m/D	$= 0.122158 + 1.09204\ Fr_d$	(3-28)
y_t/D	$=0.146392 + 1.4332\ Fr_d$	(3-29)

3.4.3.3. *Comparison of the GMDH with previous analytical solutions*

In the previous section, the GMDH model was generated for each angle based on the present study while in this section, a GMDH comprehensive nonlinear model (Equations 3-30 to 3-33) are obtained from present and previous experimental results for both angles, which are presented in Table 3-6.

Table 3-6: Equations obtained from the GMDH for dimensionless geometrical parameters.

Geometrical characteristic	Equations	
x_m/D	$=0.275641+0.00887533\ \theta\ Fr_d+1.13423\ Fr_d$	(3-30)
x_r/D	$=1.45228+0.0102542\ \theta\ Fr_d+2.15477\ Fr_d -0.000395941 Fr_d^2$	(3-31)
y_m/D	$=-0.257905+0.022039\ \theta\ Fr_d+0.000466511\ \theta^2-0.0412161\ Fr_d$	(3-32)
y_t/D	$=0.198959+0.0239452\ \theta Fr_d + 0.214252\ Fr_d-0.000415333\ Fr_d^2$	(3-33)

The performance of the proposed model was then tested by comparison with two previous analytical solutions reported by Kikkert et al. (2007) and Oliver et al. (2013). The results of these comparisons can be seen in Figure 3-15, where all these figures present the dimensionless geometrical parameters versus the initial densimetric Froude numbers (Fr_d) for the discharge angles of 15° and 52° for present and previous study. The predicted results of the GMDH model are presented in black lines and generally, demonstrate better predictions, for most of the geometrical parameters, compared to the observed data obtained from the experiments than those of other analytical models. All figures show the best matches for the GMDH model and all provided data except Figure 3-15b. In general, all 15° figures showed better matches between the GMDH model and the other analytical models and were in good agreement with the observed data. Therefore, based on all the comparison results, it can be concluded that the GMDH model can give good predictions of the observed data obtained from the experiments of the inclined dense jet, particularly for the angle of 15°. However, the performance of the GMDH model for predicting the geometrical characteristics of the angle of 52° is considered satisfactory, although there is a lack of existing data for this angle. Herein, the prediction line of the GMDH method closely fit the obtained data, while the results of the analytical solutions were slightly different, especially for Figures 3-15d and h.

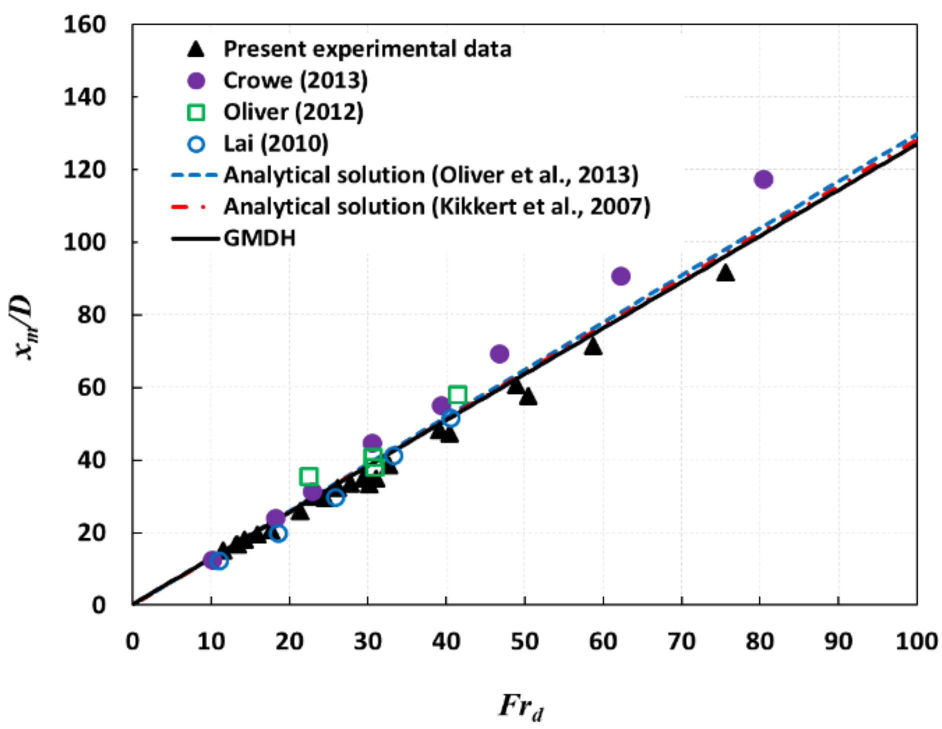

(a)

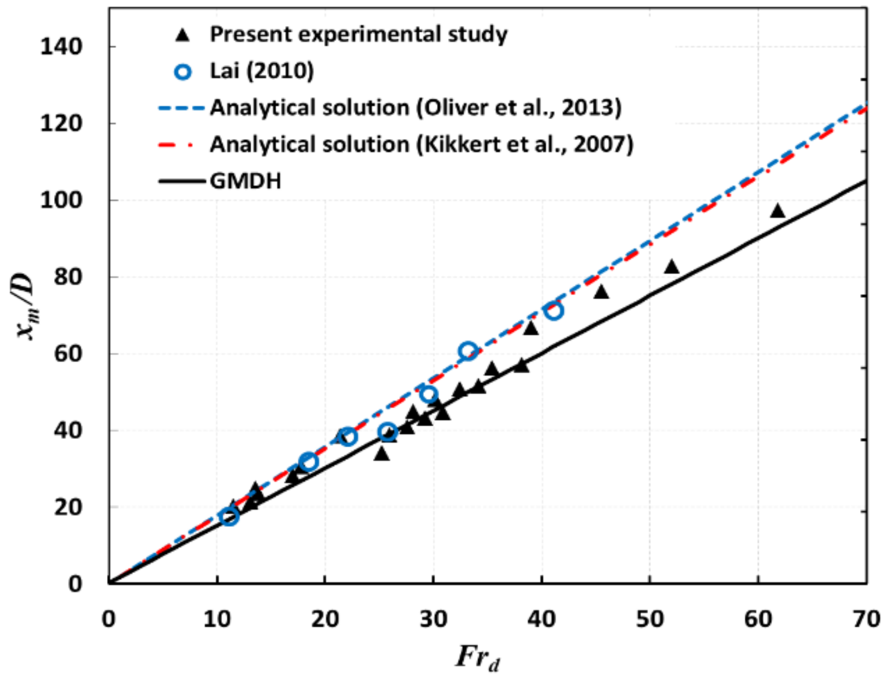
Present experimental study
Lai (2010)
Analytical solution (Oliver et al., 2013)
Analytical solution (Kikkert et al., 2007)
GMDH
x_m/D
Fr_d
0
20
40
60
80
100
120
140
0
10
20
30
40
50
60
70

(b)

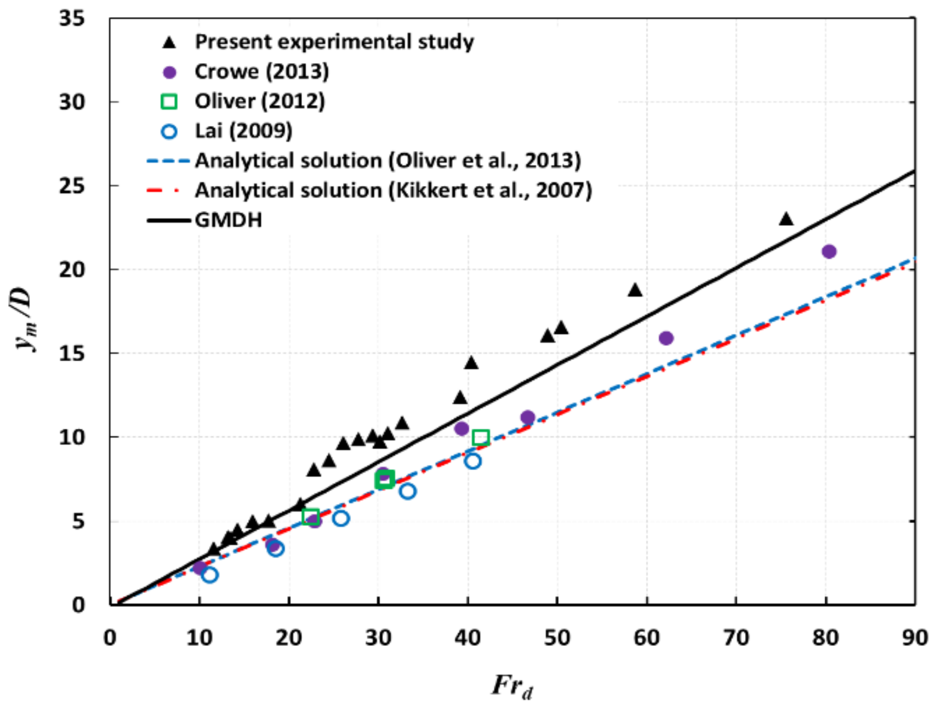
Present experimental study
Crowe (2013)
Oliver (2012)
Lai (2009)
Analytical solution (Oliver et al., 2013)
Analytical solution (Kikkert et al., 2007)
GMDH
y_m/D
Fr_d
0
5
10
15
20
25
30
35
0
10
20
30
40
50
60
70
80
90

(c)

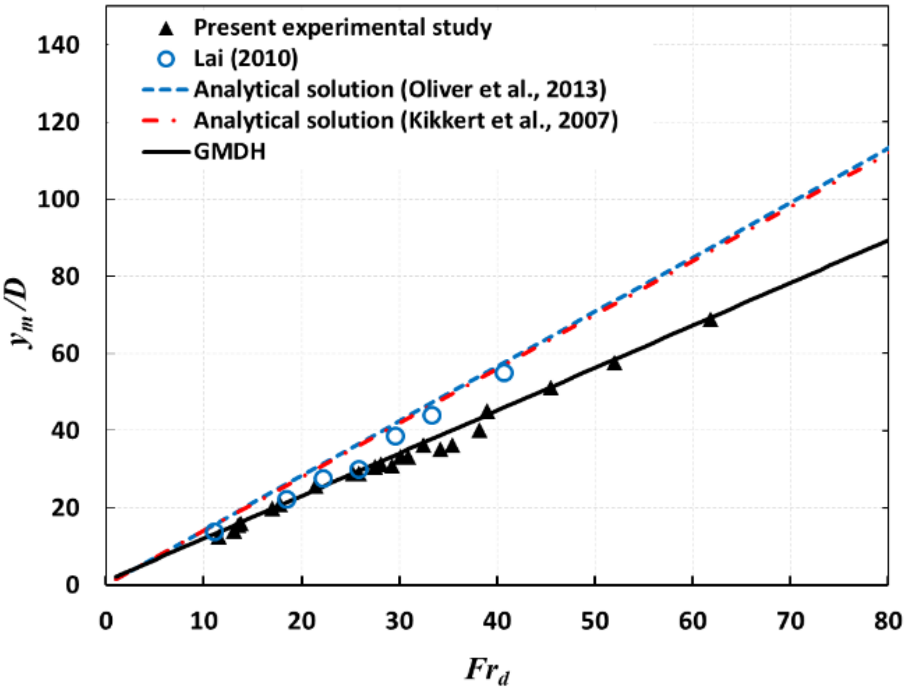
Present experimental study
Lai (2010)
Analytical solution (Oliver et al., 2013)
Analytical solution (Kikkert et al., 2007)
GMDH
y_m/D
Fr_d
0
20
40
60
80
100
120
140
0
10
20
30
40
50
60
70
80

(d)

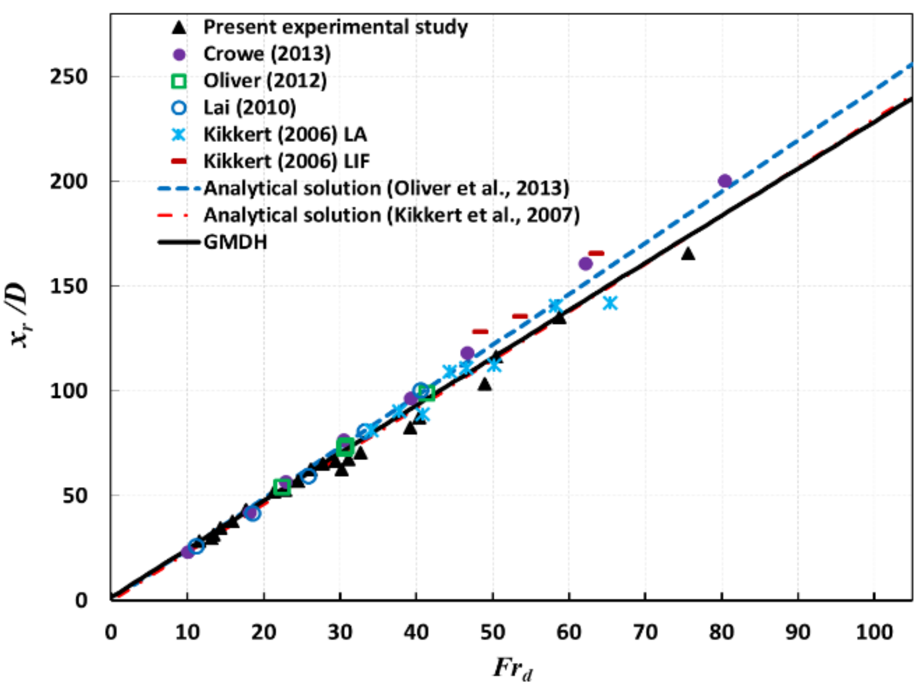
Present experimental study
Crowe (2013)
Oliver (2012)
Lai (2010)
Kikkert (2006) LA
Kikkert (2006) LIF
Analytical solution (Oliver et al., 2013)
Analytical solution (Kikkert et al., 2007)
GMDH
x_r/D
Fr_d
0
50
100
150
200
250
0
10
20
30
40
50
60
70
80
90
100

(e)

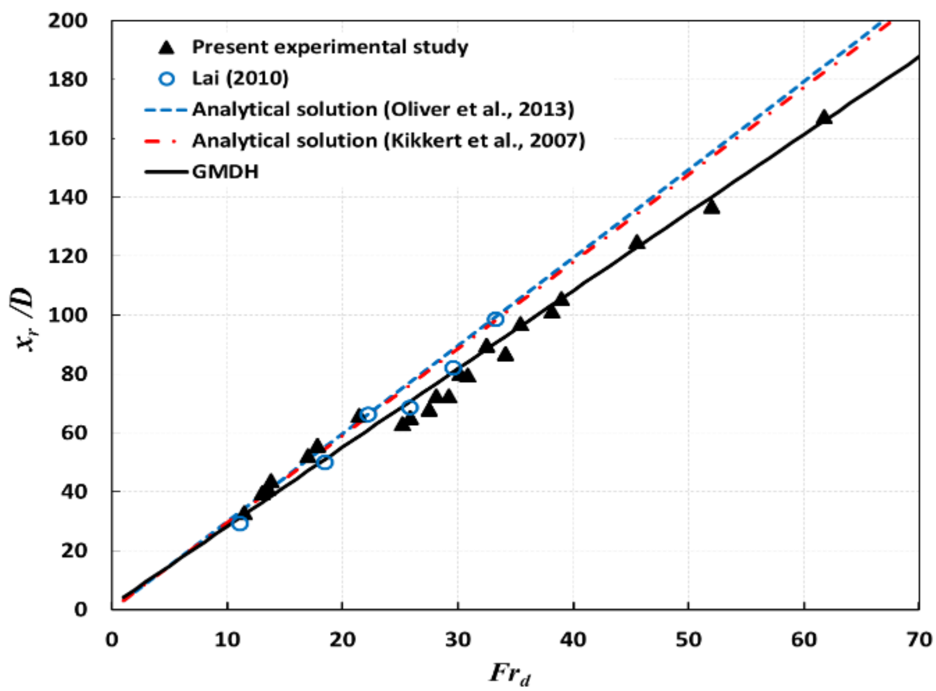

Present experimental study
Lai (2010)
Analytical solution (Oliver et al., 2013)
Analytical solution (Kikkert et al., 2007)
GMDH
x_r/D
Fr_d

(f)

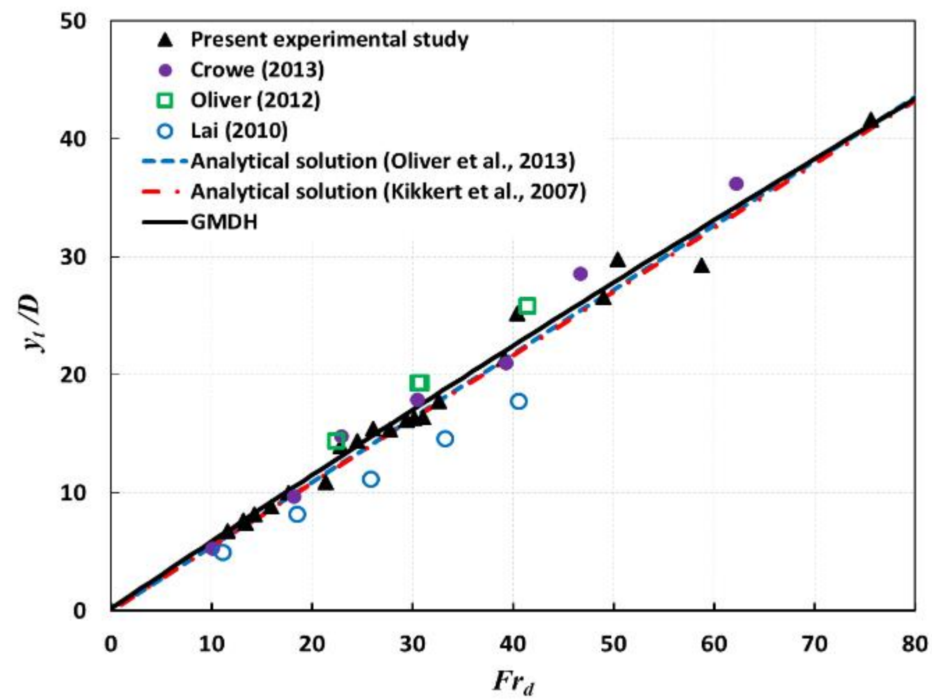

Present experimental study
Crowe (2013)
Oliver (2012)
Lai (2010)
Analytical solution (Oliver et al., 2013)
Analytical solution (Kikkert et al., 2007)
GMDH
y_t/D
Fr_d

(g)

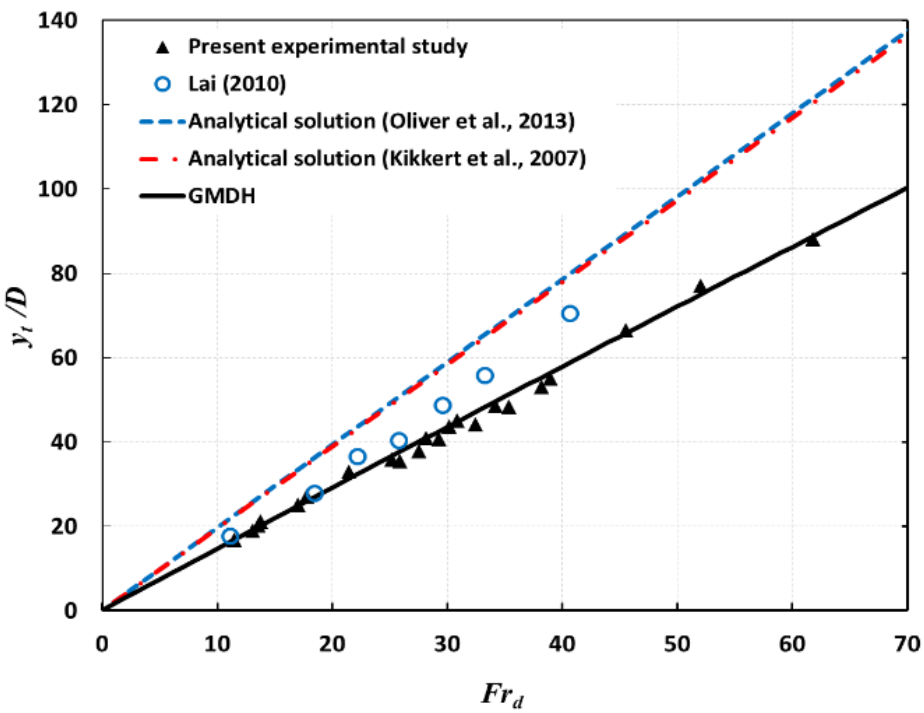

(h)

Figure 3-15: A comparison of the GMDH results with previous analytical solutions for angles: 15° (a, c, e and g) and 52° (b, d, f and h).

3.5.Discussion

In this study, the results obtained from the experiments were compatible with the results of statistical analysis of variance (ANOVA). Among the tested parameters, both results (experimental and statistical) confirmed the importance of the Fr_d as a significant parameter in controlling the mixing behavior of the discharged effluent. Moreover, the inclination of the jet angle θ was also noted as a significant parameter that can affect the geometrical characteristics of the jet trajectory. According to the findings of this study, if the jet has not reached the turbulent stage (*i.e.*, Re<2000), the *Re* and salinity can also be considered as affected parameters on the jet behaviors.

It is noted in the present study that the results of the angle 52° for all parameters (*i.e.*, x_m, x_r, y_m, and y_t) were slightly divergent from the similar angle results reported previously by Lai (2010). This divergence may be due to the lack of studies on this angle, as only one previous study (Lai, 2010) has examined this angle, and that study did not cover a wide range of Fr_d. Also, the divergence may be due to the different testing techniques and methods employed for estimating the trajectory characteristics. Accordingly, more investigation is required due to the absence of existing studies for this angle. However, the observed deviations can be considered in a good agreement and reasonably satisfactory, as there are always some experimental errors, and so no exact results can be obtained from different studies.

In general, it is worth noting that the quality of any geometrical characteristics obtained from experiments is dependent on the number of experiments conducted and the range of Fr_d used. Therefore, the large number of experiments conducted in this study, as well as the wide range of Fr_d, will help on obtaining more data, which can enhance the understanding of the effect of these angles (*i.e.*, 15° and 52°) on jet behavior. The results obtained in this study closely follow those of previously reported data, especially for the angle of 15°.

In the GMDH statistical section, the present study concluded that the predicted equations for geometrical characteristics for both angles showed a good agreement overall, and the R^2 for the fitting lines give high values. Moreover, the results of these equations are consistent with the results obtained from ANOVA, which are mainly affected by Fr_d for all angles.

In conclusion, the GMDH results obtained in this study give encouragement for more study on other angles (*e.g.*, 30° - 80°) using this approach for predicting the geometrical characteristics of inclined dense jets. Therefore, more investigation using more experimental data with various angles is highly recommended in order to obtain the best performance when using the GMDH neural network method.

3.6. Conclusions

This paper presented the results of an experimental study of inclined buoyant dense jets for two different inclinations of 15° and 52°. The important geometrical characteristics of the jet flow, namely, the horizontal direction (x_m) to the point of the maximum centerline height (y_m), the edge of the maximum terminal height of the jet (y_t), and the horizontal direction of the return point (x_r), have been investigated in detail. Forty-three experiments (21 for the angle of 15° and 22 for the angle of 52°) were conducted in this study. At both angles, three different densities ranging from 1011 to 1030.7 kg/m^3 were used to obtain more diversity in the source of the discharged water and thus to investigate how the geometrical characteristics of the jet were affected by changes in density. A wide range of densimetric Froude numbers (Fr_d) was used, ranging from 11.50 to 75.59, with Reynolds numbers (Re) ranging from 2023 to 5486. The effect of the discharge angle on the jet characteristics was investigated, and Equations were presented for predicting the dimensionless values of the geometrical characteristics using the GMDH neural network. The results of this study can be summarized in the following points:

- The results showed that jet flows behave similarly if the Fr_d are the same even if Re are different. The results also showed that the Fr_d is the most significant parameter effecting the jet trajectories in the mixing of the inclined dense jets.
- Comparisons of the present results for the geometrical characteristics of both angles with previous reported data were also presented. The present results showed good agreement for all geometrical parameters with most of the previous data, especially for the angle of 15°, while the 52° angle results were slightly different from the compared data, and this variation may be attributed to the limitations of the existing data for the same angle (*i.e.*, 52°).
- The results for the constant values of C_{x_m}, C_{x_r}, C_{y_m} and C_{y_t} obtained in the present study for the angle of 15° were consistent with the previous data reported in the literature, while for the angle of 52°, the present values were slightly different than the values obtained by Lai (2010).
- An ANN method named the GMDH was employed to predict the observed data of the behavior of dense jets. The obtained results showed, based on the R^2 results, that the GMDH model can predict with high accuracy and has excellent agreement with all observed experimental data.
- The performance of the GMDH model was also tested by a comparison with two analytical solutions reported in previous studies. The results showed accurate and satisfactory predictions for the GMDH method for both angles, compared with those of analytical solutions for all geometrical characteristics, where the scattered of the experimental data are closely located around the GMDH fitting lines showing better prediction than those of analytical solutions.
- In conclusion, this study demonstrates that artificial intelligence methods such as the GMDH model can be significantly useful for giving good predictions. To the authors' knowledge, the present paper is the first to use the GMDH method in the prediction of mixing of inclined negatively-buoyant jets and demonstrate the performance of this method.
- This paper is a step towards a more comprehensive study that compares the GMDH with the other most common technical tools used in this field.

Chapter 4. A comprehensive study for predicting the geometrical characteristics of an inclined negatively-buoyant jet using GMDH neural network[4]

Abstract

A new approach for predicting the geometrical characteristics of the mixing behavior of an inclined dense jet for angles ranging from 15° to 85° is proposed in this study. This approach is called group method of data handling (GMDH) which is based on the artificial neural network (ANN) technique. The proposed model was trained and tested using existing experimental data reported in literature. The model was then evaluated using statistical indices as well as compared with analytical models from previous studies. The results of the coefficient of determination (R^2) indicate a high accuracy of the proposed model with values of 0.9719 and 0.9513 for training and testing for the x_r/D parameter, and 0.9454 and 0.9565 for training and testing for y_t/D. Moreover, four previous analytical models were used to evaluate the GMDH model. The results showed the superiority of the proposed model in predicting the geometrical characteristics of the inclined dense jet for all tested angles. Finally, the standard error of estimate (SEE) was applied to demonstrate which model performed the best in terms of getting closer to the actual data. The results illustrate that all fitting lines of the GMDH model performed very well for all geometrical parameter predictions and was the best model with approximately 10% error, which was the lowest value of error among the models. Therefore, this study confirms that the GMDH model can be used to predict the geometrical properties of the inclined negatively-buoyant jet with high performance and accuracy.

[4] This chapter is submitted to the Journal of Desalination and Water Treatment as Hassan Alfaifi, Abdolmajid Mohammadian and Hossein Bonakdari. Under Review.

Keywords: Inclined negatively-buoyant jet, analytical model, GMDH, statistical indices, densimetric Froude number.

4.1. Introduction

The unwanted wastewater produced from seawater desalination plants is normally discharged back into the coastal water body adjacent to the plants. This is done with a submerged pipe creating a buoyant effluent jet. This effluent (brine) has a high concentration of salinity which causes negative impacts on the marine ecosystem, particularly in the near-field zone of the discharge point (Bombar et al., 2016; Petersen et al., 2019). The discharged effluent is either a positively-buoyant jet (lighter than the receiving water) or a negatively-buoyant jet (denser than the receiving water), depending on the method used in the desalination plant. The dense jet (negatively-buoyant jet) has highly adverse effects on the marine environment. Commonly, desalination plants that use a Reverse Osmosis (RO) system use submerged discharges, which formed a negatively-buoyant jet, to ensure a high dilution of this effluent in order to minimize the adverse impacts on the marine environment.

A large body of previous research has focused on laboratory studies of the mixing of the negatively-buoyant jet either alone or in combination with modeling efforts (Abessi and Roberts, 2015b, 2015a, 2014; Bashitialshaaer et al., 2012; Bloomfield and Kerr, 2002; Cipollina et al., 2005; Crowe, 2013; Jiang et al., 2014; Kikkert, 2006; Lai, 2010; Lai and Lee, 2012; Lindberg, 1994; Nemlioglu and Roberts, 2006; Oliver, 2012; Papakonstantis et al., 2011b, 2011a; Papakonstantis and Christodoulou, 2008; Papakonstantis and Tsatsara, 2019, 2018; Papanicolaou and Kokkalis, 2008; Roberts et al., 1997; Roberts and Toms, 1987; Shao and Law, 2010; Zeitoun and McIlhenny, 1971). Less effort, however, has been given to numerical modeling and developing an analytical solution and to predict the behaviors and geometric characteristics of inclined dense jets (Alfaifi et al., 2019b; Jirka, 2006; Kikkert et al., 2007; Lee and Chu, 2003; Oliver et al., 2013), which still requires further investigation. Therefore, more studies using numerical modeling as an efficient tool can be useful for predicting the behaviors of brine discharges into seawater.

As known, there are two hypotheses for developing models either based on the entrainment or jet spreading, which are being developed and studied previously. In 2003, Lee and Chu developed a model called JETLAG/VISJET in order to predict the mixing of the near-field zone of an inclined round buoyant jet. This model is a combination of two approaches, i.e., entrainment and jet spreading, and presents empirical correlations for the dilution of the geometrical characteristics. In 2004, Jirka developed an integrated numerical model (CORJET) that can predict negatively-buoyant jets for a wide range of angles (0° to 90°) discharged into ambient water with slop or flat bottom. A few years later, Kikkert et al. (2007) presented an analytical method to predict the behavior of an inclined dense jet using experimental data reported from previous studies to validate their model. Their model has limitations as it can be valid for angles ranging from 0° to 75° and for densimetric Froude numbers (Fr_d), the ratio of inertia to buoyancy, ranging from 14 to 99. In the same manner as of Kikkert et al. (2007), Oliver et al. (2013) developed a modified integral model called the Reduced Buoyancy Flux (RBF) model to predict the behavior of negatively-buoyant jets in near-fields. One of the advantages of this modified model is its ability to predict the effects of the additional mixing noted in previous studies.

In recent years, efforts in different areas of the engineering science field have focused on the use of Artificial Neural Network (ANN) methods. One of these methods is the group method of data handling (GMDH), which is used for solving nonlinear engineering problems and providing explicit equations for modeling the hydraulic and hydrological phenomena. Using this method has shown accurate results compared to those of other methods (Alitaleshi and Daghbandan, 2019; Daghbandan et al., 2019; Ebtehaj et al., 2017, 2015; Gholami et al., 2017; Madandoust et al., 2012; Mehri et al., 2019; Naeini et al., 2018; Najafzadeh et al., 2013; Parsaie et al., 2018; Parsaie and Haghiabi, 2017; Zaji and Bonakdari, 2019) For example, Najafzadeh et al. (2013) used GMDH to predict scour depth around a vertical pile exposed regular waves and compared their results with the result of different previous methods. They concluded that the use of GMDH model provided the most accurate prediction of scour depth compared to other models. Another study was conducted by Gholami et al. (2017) to study the ability of the GMDH model for predicting the geometric variables of stable channels (width, depth, and slope). The results showed that the GMDH model performed well. Moreover, they compared the result obtained from GMDH with those from previous theoretical equations (based on regression analysis), and this comparison showed the ability of GMDH model to predict the geometric variables of channels better than other theoretical equations. Naeini et al. (2018) developed a model using GMDH to estimate the Elasticity modulus (E_s) of clayey deposits that is used to predict the elastic settlement of foundations. The results obtained were compared with the previous empirical equations. They found that the GMDH model showed higher performance (32 to 42% improvement) with respect to the other correlations. Alitaleshi and Daghbandan (2019) conducted a study to evaluate the quality of treated water in a water treatment plant using GMDH-type neural network. The results showed the success of the model used (GMDH) for prediction as the results of the determination coefficient were higer than 0.97.

Recently, Alfaifi et al. (2019b) have used a GMDH model to predict the geometrical characteristics of inclined dense jets for angles 15° and 52°. It is believed that this is the first time this new approach has been used in the field of mixing jet behavior. These researchers have established empirical equations for estimating the geometrical characteristics of inclined buoyant jets. The GMDH results gave an accurate prediction for the parameters tested compared to the other analytical models.

Therefore, the goal of the present study is to examine the superiority of the GMDH model in predicting the main geometrical characteristics of inclined negatively-buoyant jets by performing a comprehensive study for a wide range of angles ranging from 15° up to 85°. Moreover, the performance of the GMDH model is assessed by comparing its results to those of other analytical and numerical methods.

4.2. Methodology

4.2.1. *Analysis of an inclined negatively-buoyant Jet*

In Figure 4-1, an inclined turbulent round dense jet being discharge into a body of stagnant water body is illustrated (the ambient velocity is, $U_a = 0$). The port (jet) for the discharge has a diameter D and is positioned at an angle (θ) compared to the horizontal plane. The ambient water into which the jet is being expelled is an unstratified and has a constant density ρ_a. This water is deep enough to allow the jet to fully develop below the water surface. The initial discharge velocity of the jet is U_0 and it has a density ρ_0 ($\rho_a < \rho_0$).

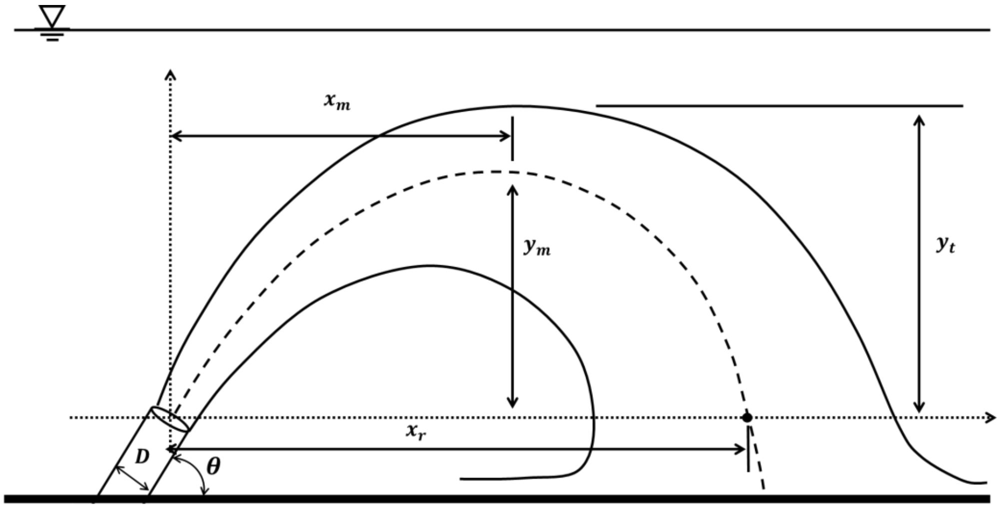

Figure 4-1: Dimensional parameters of the inclined round dense jet in stagnant ambient water.

The four crucial characteristics of the mixing of the jet with regard to geometry are: its terminal rise height (y_t); the horizontal distance from the point of maximum height of the centerline to the nozzle (x_m); its centerline height (y_m), and its return point (x_r), i.e., the distance horizontally from where the jet's centerline returns to the same elevation as the tip of the nozzle (Figure 4-1). The distribution pattern of a jet being discharged into a homogeneous and stagnant ambient fluid can be affected by various parameters known as the source angle θ, D, U_0 and the initial density difference ($\Delta\rho = \rho_0 - \rho_a$) between the ambient fluid and the discharge fluid. In addition, the inclined dense jets can be characterized by its discharge volume flux $Q_0 = U_0 \pi D^2/4$, momentum flux $M_0 = U_0^2 D^2 \pi/4$, and buoyancy flux $B_0 = g'_0\, U_0 \pi D^2/4$, where $g' = g(\rho_0 - \rho_a)/\rho_a$, which defined as the effective gravitational acceleration and g is the gravitational acceleration. Two length scales can be formed from these fluxes: the momentum length scale $L_M = M_0^{3/4}/B_0^{1/2}$, which determines the distance over which the buoyancy of the jet is less important than its momentum, and the source length scale $L_Q = Q_0/M_0^{1/2}$, which determines the distance over which the source discharge is important. These two length scales are employed to determine the mixing and geometric characteristics of a turbulent buoyant jet. The equation defining the jet densimetric Froude number (Fr_d) is as follows:

$$Fr_d = U_0/\sqrt{g'D} \tag{4-1}$$

The terminal rise height of an inclined dense jet can be written in terms of the length scales as:

$$\frac{y_t}{L_M} = f\left(\frac{L_M}{L_Q}, \theta\right) \tag{4-2}$$

Instead of the length scales, y_t can also be alternatively expressed by using the jet's densimetric Froude number and nozzle diameter as:

$$\frac{y_t}{Fr_d D} = C_{y_t}(\theta), \tag{4-3}$$

Similarly, the other geometric parameters of the jet (i.e. x_r, x_m, and y_m) can be derived by using the coefficient values (C_{x_r}, C_{x_m}, and C_{y_m}), which can be established through experiments.

4.2.2. *The GMDH method*

The group method of data handling (GMDH) was first proposed by Ivakhnenko (1971), and is a computer program based algorithm. This type of algorithm is often used to model problems that involve data series for multi-input-single-output systems. Second-order polynomials are used in the GMDH as network functions, and the main advantage of the GMDH, as opposed to traditional neural networks, is its use in establishing mathematical models for a given procedure.

The concept of the GMDH of selection and hybridization corresponds to the genetic algorithm. Like other types of neural networks, the GMDH can have one or more hidden layers. More information regarding GMDH processing is provided in a recently published article by the same authors in Alfaifi et al. (2019b).

4.2.3. *GMDH modeling setup*

To use the GMDH method for prediction of the geometrical characteristics of a negatively-buoyant dense jet, the output variables were set to be the dimensionless of jet characteristics (i.e., x_m/D, y_m/D, x_r/D, and y_t/D) by using one output variable for each run. For all cases, the Fr_d and θ parameters were used as input variables. The explicit equations for the GMDH were developed using the GMDH Shell software (GMDH LLC, 2019). The dataset used covered all discharge angles presented in previous studies ranging from 15° to 85°. Obtaining a good prediction from the GMDH model is based on the preparation of the dataset, and therefore the observed dataset used in this study was randomly divided into two groups one for training and one for testing. For each case, the GMDH model was trained using 70% to 80% of the dataset, while the remaining data were used for testing the model. In this study, the layers were limited to a maximum of two layers in order to ensure the simplicity of the model. The developed models were used to calculate the dimensionality of the jet geometrics as a function of Fr_d and θ for the training dataset. The optimal models were then selected and used to perform additional calculations for the testing dataset. Finally, the performances of these models were evaluated.

For the training dataset, the models developed were used to determine the dimensionless of the jet geometrics as a function of Fr_d and θ, with the optimal models being selected. After that, the models selected were used to perform additional calculations for the testing dataset, and then their performance was evaluated.

4.3.Results and discussion

In this section, the results of the proposed model (GMDH) are presented. The predicted results of the GMDH are compared with the observed data obtained from previous studies for angles ranging from 15° to 85°. For brevity, only the results of x_r/D and y_t/D are shown in this section. The results of the dimensionless geometrical parameters x_r/D and y_t/D for the actual data for training and testing are plotted versus the predicted values of the GMDH model, as shown in Figures 4-2a and b. In order to evaluate the performance of the GMDH model, a linear fit with the coefficient of determination (R^2) was added to each figure to show the accuracy of the proposed model in predicting and fitting the actual data. From these figures, it can be seen that the R^2 values show an excellent prediction for the proposed model (GMDH) where 0.9719 and 0.9513 were for training and testing for x_r/D and 0.9454 and 0.9565 were for training and testing for y_t/D. The testing results for both parameters show a good prediction of the model. Although there was a decrease in the value of the R^2 for x_r/D for the testing model compared to the training model, the accuracy remains high and acceptable. This indicates that all fitting lines pass through most of the data and the proposed model is highly accurate and satisfactory.

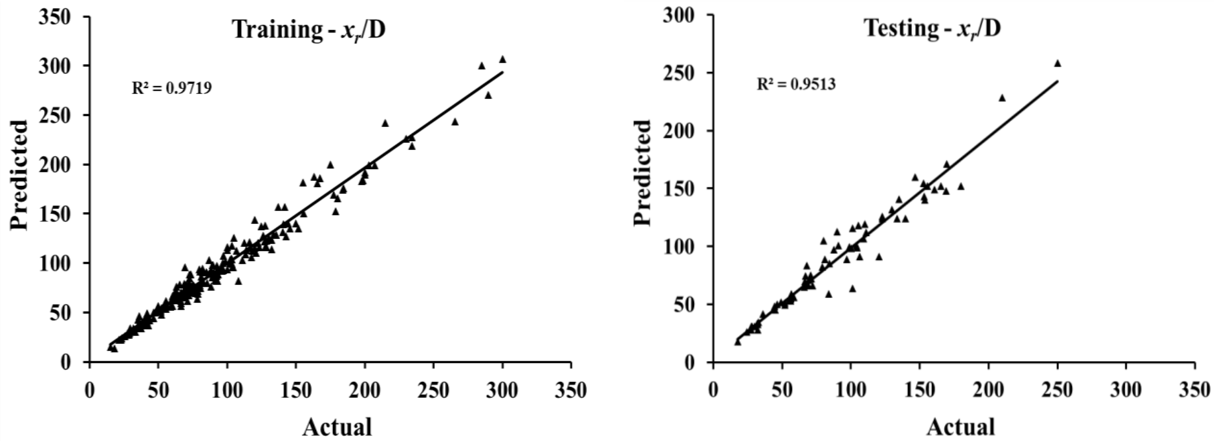

(a)

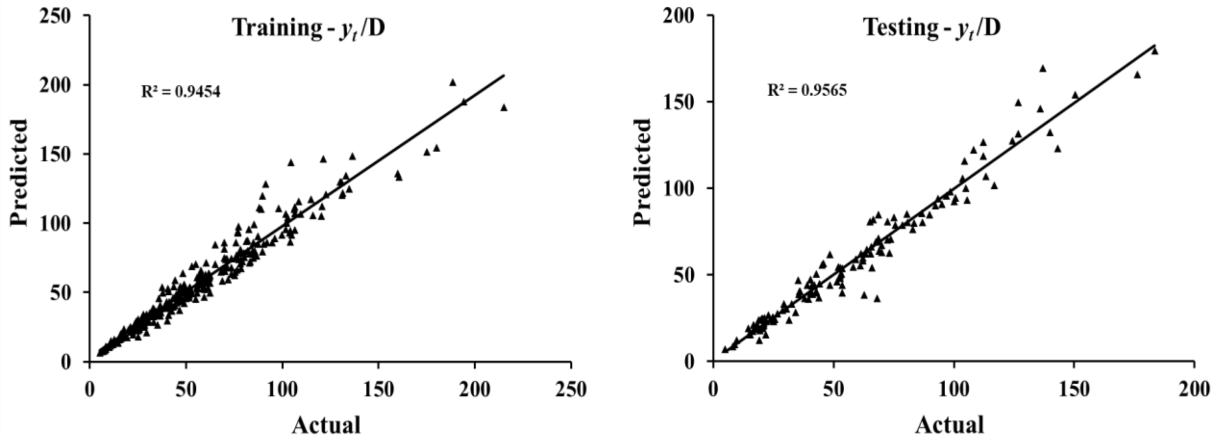

(b)

Figure 4-2: The scatter plot with fitting lines of the actual and GMDH predicted results for angles from 15° to 85°: (a) x_r/D and (b) y_t/D.

Figures 4-3a and b shows a detailed depiction of the performance of the GMDH model for x_r/D (Figure 4-3a) and y_t/D (Figure 4-3b) as well as how the model was trained and tested by the data index. In Figure 4-3a, the model was trained by 75% of the data, while in Figure 4-3b, it was trained by 70% of the data. As mentioned previously, the model was trained by between 70% and 80% of the data. Therefore, the key to influencing the change of training ratio is to obtain a simple model with high accuracy.

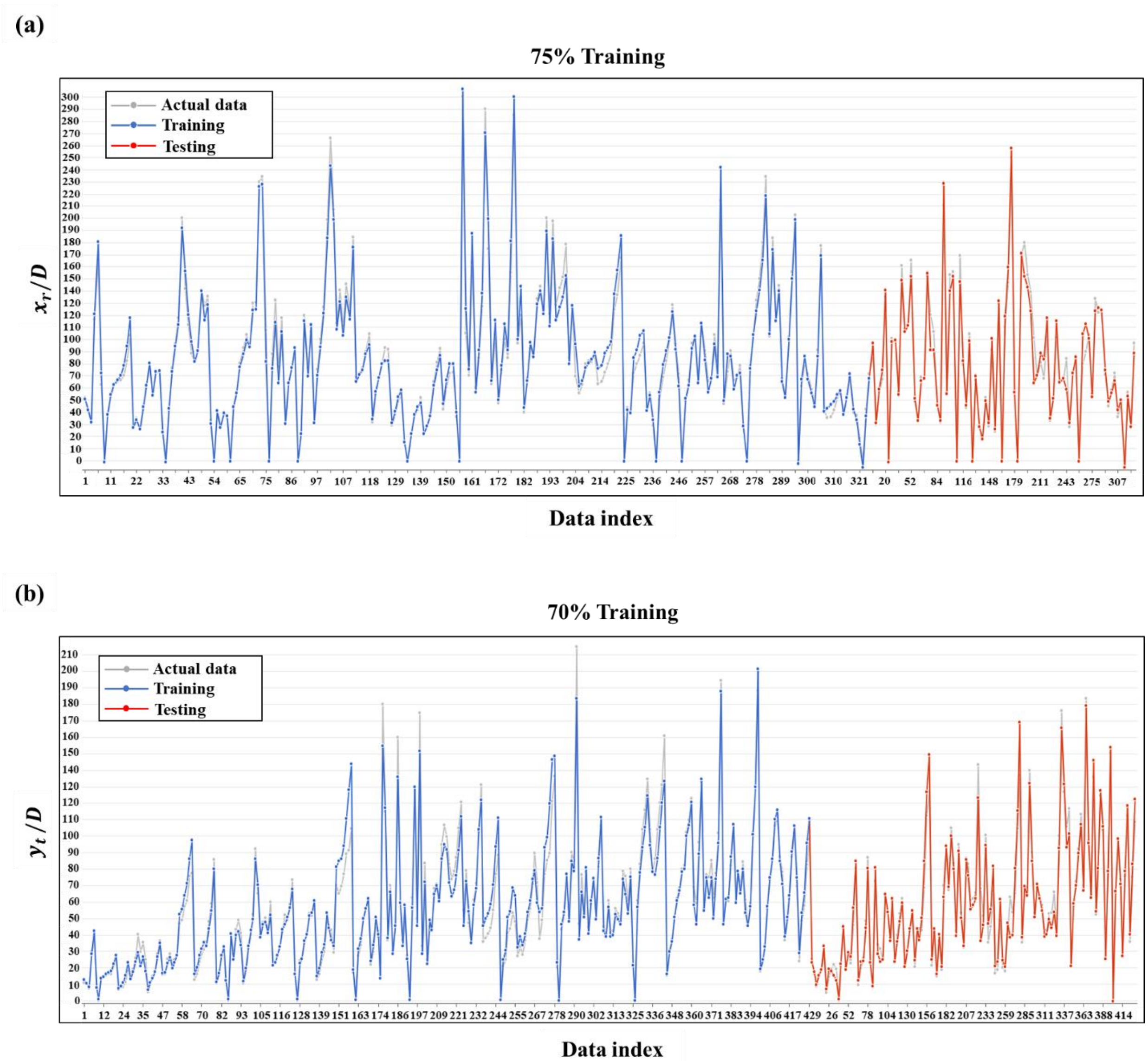

Figure 4-3: The performance of GMDH model in the training and testing stage.

The equations extracted from the GMDH method for all geometrical parameters are presented in Table 4-1. These equations were used to predict the geometrical parameters in this study. As can be seen, all of the equations in Table 4-1 are functions of the Fr_d and the θ. These equations are valid for Fr_d ranging from 10 to 100. All of the equations presented in Table 4-1 can be used for predicting the geometrical parameters for the inclined dense jet for any angles located between 15° and 85°. All of these equations are presented in dimensionless geometric parameters, which depend on the same input variables: $\mathrm{Fr_d}$ and θ.

Table 4-1: Nonlinear equations extracted from GMDH for dimensionless geometrical parameters.

Geometrical parameter	GMDH proposed equations	
x_m/D	$= -31.538 + 1.948873\theta - 0.0234242\theta^2 + 1.63203Fr_d$	(4-4)
x_r/D	$= -0.35311 + 2.9030Fr_d + 0.065091Fr_d N3 - 0.13909\ {Fr_d}^2 - 0.005735\ N3^2$ $N3\ = -47.2107 + 2.77506\ \theta - 0.0340387\theta^2 + 2.82939\ Fr_d$	(4-5)
y_m/D	$= 2.37956 - 0.139279\ \theta + 0.0263993\theta Fr_d + 0.0026574\ \theta^2 + 0.113531\ Fr_d$	(4-6)
y_t/D	$= 1.00174 + 0.0336764\ \theta Fr_d - 0.000250209\ \theta^2 + 0.0418149\ Fr_d$	(4-7)

4.3.1. *Assessment of the model performance statistically*

Some of the most commonly used statistical indices are presented in this study to evaluate the performance of the GMDH model. These indices can clearly show the accuracy of the proposed model as it is commonly used in literature. In the present study, the three most important types of statistical indices were used: the coefficient of determination (R^2), Root Mean Squared Error (*RMSE*), and Mean Absolute Error (*MAE*), which are defined as follows:

$$R^2 = 1 - \frac{\sum(\hat{y} - \bar{y})^2}{\sum(y - \bar{y})^2} \tag{4-8}$$

$$MAE = \frac{\sum_{i=1}^{n}|\hat{y} - y|}{n} \tag{4-9}$$

$$RMSE = \sqrt{\frac{\sum_{i=1}^{n}(\hat{y} - y)^2}{n}} \tag{4-10}$$

where $\hat{y}$ is the predicted values of the GMDH model, $\bar{y}$ is the mean of the actual data, y is the actual data, and n is the number of actual data. As known, the low values of these parameters (except R^2) indicate the high accuracy of the model. The statistical results obtained for the GMDH model from these Equations (i.e., 4-8 to 4-10) are presented in Table 4-2. The results of the GMDH model used for predicting the geometrical characteristics of the inclined jet show a high accuracy of the prediction, as shown from the R^2 results. All geometrical results are higher than 0.94, which means that the model proposed produced excellent predicting results. The highest value of the R^2 was 0.967 for x_r/D, while the lowest value for the same index was for x_m/D, which was 0.948. The most interesting finding from Table 4-2 are the testing results, which are the results that evaluate the accuracy of the proposed model. For *MAE*, the lowest value was noted for the y_m/D (4.458), while the lowest value for the *RMSE* was found for the x_m/D (6.861). On the other hand, the highest value for *MAE* was shown for x_m/D (6.809), while for the *RMSE*, the highest value was found for x_r/D (10.143). Generally, all the results obtained for the statistical indices in Table 4-2 show excellent agreement between the dataset observed and the proposed model (GMDH) which can be used for predicting the geometrical parameters of the inclined dense jets with highly accurate results.

Table 4-2: Results of statistical indices for training and testing of the GMDH model.

Geometrical parameter	R^2	MAE	RMSE	R^2	MAE	RMSE
		training			testing	
x_r/D	0.971	6.052	8.556	0.951	6.499	10.143
y_t/D	0.945	5.471	8.298	0.956	5.236	7.804
x_m/D	0.948	5.911	8.239	0.936	6.809	9.192
y_m/D	0.962	4.009	5.711	0.947	4.458	6.861

4.3.2. *Comparing GMDH results with previous models*

In this study, another evaluation for the performance of the GMDH model has been done by comparing it with several analytical and numerical models reported on in previous studies. Four analytical models explained in the literature were selected. These models were CORJET (Jirka, 2008), Kikkert et al. (2007) analytical solution, VISJET (Lee and Chu, 2003), and Oliver et al. (2013) analytical solution. The results of the GMDH model for dimensionless geometrical characteristics of x_r/D and y_t/D versus the Fr_d are shown in Figures 4-4 and 4-5, along with the previous analytical models. For brevity, the results of four angles (i.e., 15°, 45°, 60°, and 75°) for x_r/D, and five angles (i.e., 15°, 45°, 60°, 75°, and 85°) for y_t/D, are presented in this study. The existing dataset found that the highest angle in the literature was 75° for x_r/D, while 85° was the highest for y_t/D. Due to a lack of previous data for some of the geometrical parameters, results of only two analytical models (CORJET and VESJET) were shown in several pictures. As shown in Figure 4-4, the GMDH model predicted results are presented in black lines and more effectively demonstrate predictions compared to the observed data obtained from the previous experiments compared to other analytical models (see Figures 4-4a and c). It is clear that the GMDH model shows accurate predictions and its results are almost identical and overlap with the previous analytical model for some angles (i.e., 45° and 60°), see Figures 4-4b and c.

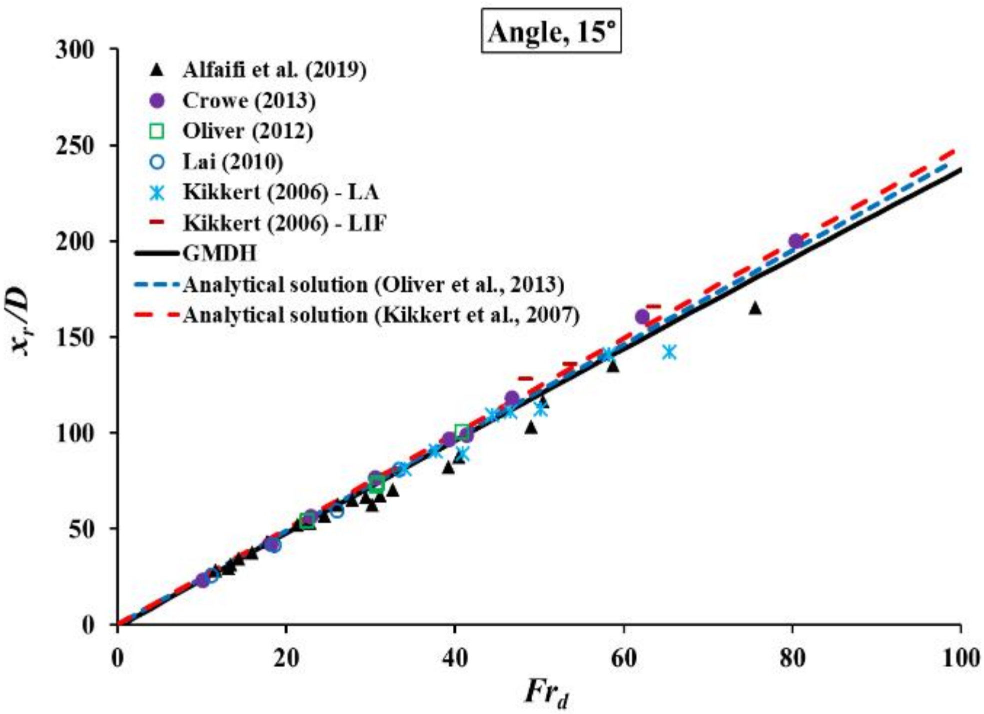

(a)

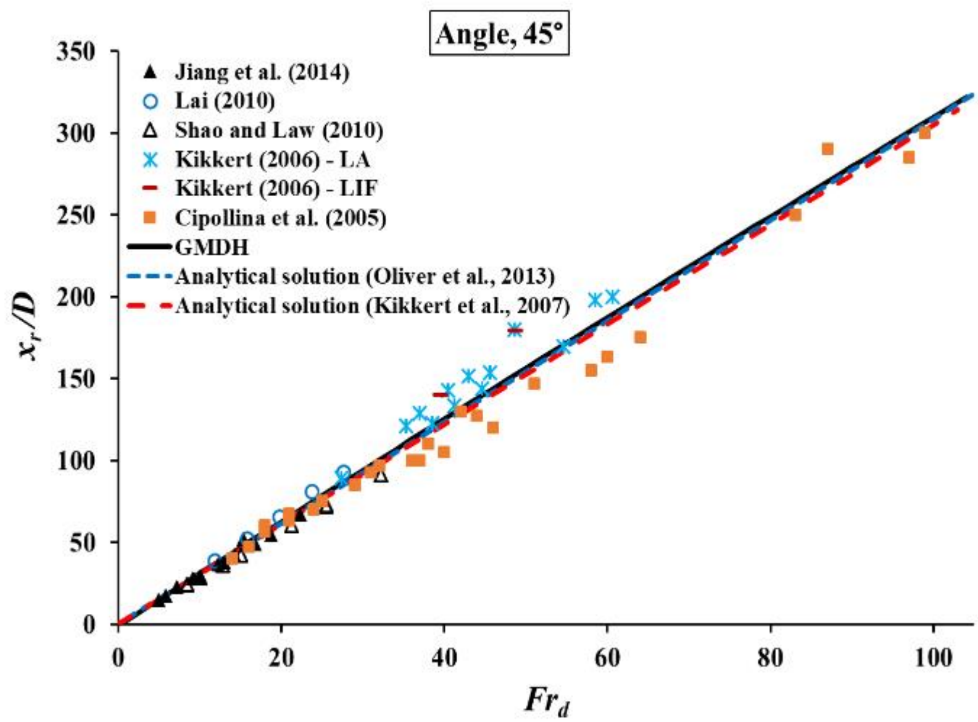
Angle, 45°
Jiang et al. (2014)
Lai (2010)
Shao and Law (2010)
Kikkert (2006) - LA
Kikkert (2006) - LIF
Cipollina et al. (2005)
GMDH
Analytical solution (Oliver et al., 2013)
Analytical solution (Kikkert et al., 2007)
x_r/D
Fr_d

(b)

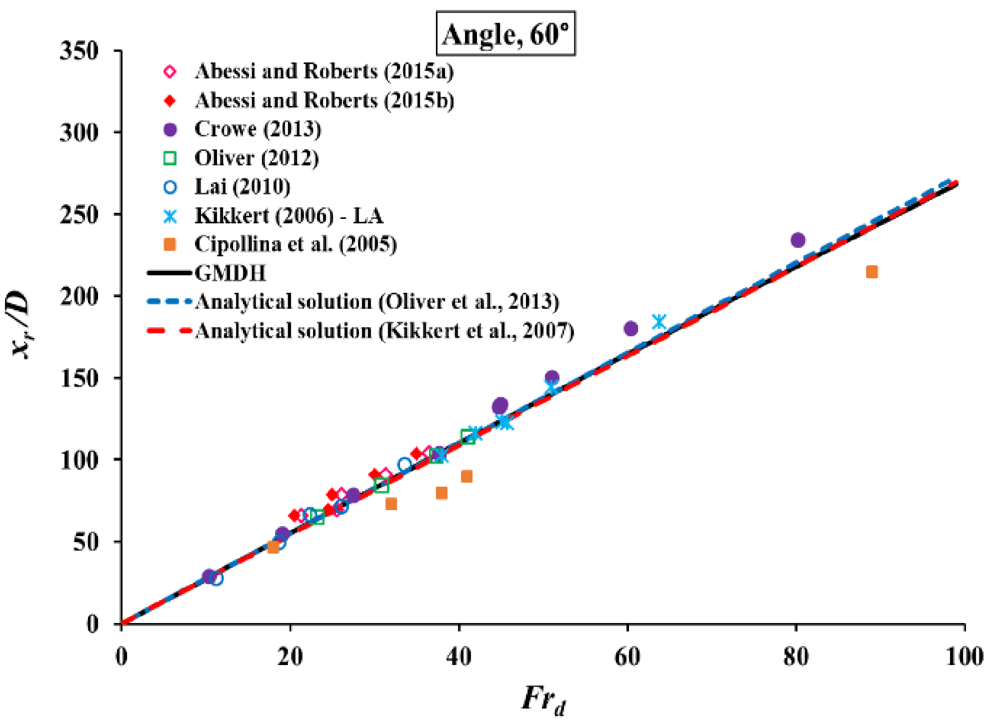
Angle, 60°
Abessi and Roberts (2015a)
Abessi and Roberts (2015b)
Crowe (2013)
Oliver (2012)
Lai (2010)
Kikkert (2006) - LA
Cipollina et al. (2005)
GMDH
Analytical solution (Oliver et al., 2013)
Analytical solution (Kikkert et al., 2007)
x_r/D
Fr_d

(c)

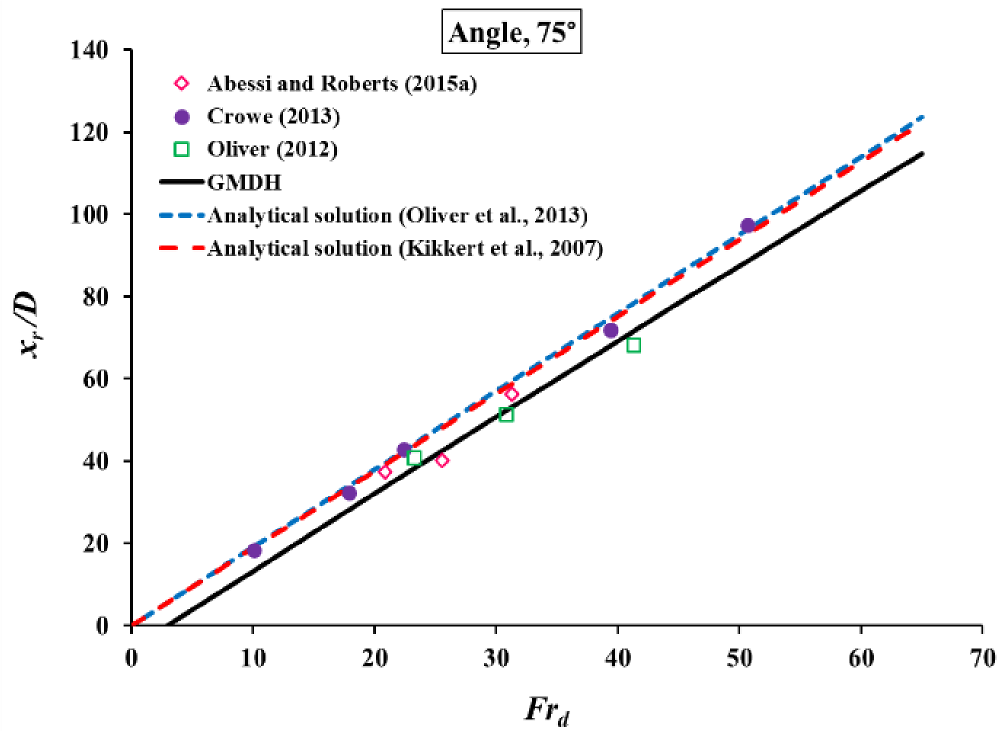

(d)

Figure 4-4: A comparison of GMDH predicted results with previous analytical solutions for x_r/D for angles: (a) 15°, (b) 45°, (c) 60°, and (d) 75°.

Another comparison for the GMDH predicted results for y_t/D is presented in Figures 4-5 a, b, c, d, and e. A fifth angle was added for the y_t/D comparison (i.e., 85°) to test the predictive capability of the proposed model. In these figures, two other models were added to the comparison (i.e., CORJET and VISJET). The proposed model (GMDH) showed a good prediction of all angles. It should be noted that it is in a neutral position for the data scatter. In addition, there is a convergence of the GMDH and VISJET models presented by Lee and Chu (2003) in Figures 4-5b and c. The predicted results of other analytical models (i.e., Kikkert et al., 2007; Oliver et al., 2013) were seen slightly higher than other models as the inclination angle increased, while the predicted results of the CORJET model were lowest in terms of comparing to the actual data and other models.

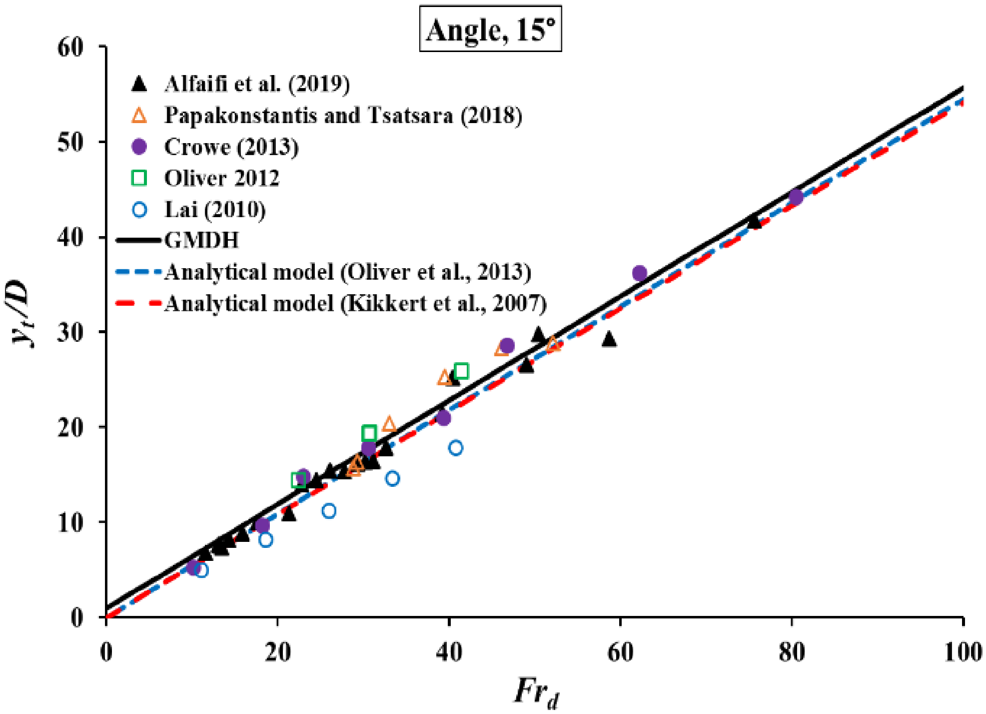
Angle, 15°
Alfaifi et al. (2019)
Papakonstantis and Tsatsara (2018)
Crowe (2013)
Oliver 2012
Lai (2010)
GMDH
Analytical model (Oliver et al., 2013)
Analytical model (Kikkert et al., 2007)
y_t/D
Fr_d
0
10
20
30
40
50
60
0
20
40
60
80
100

(a)

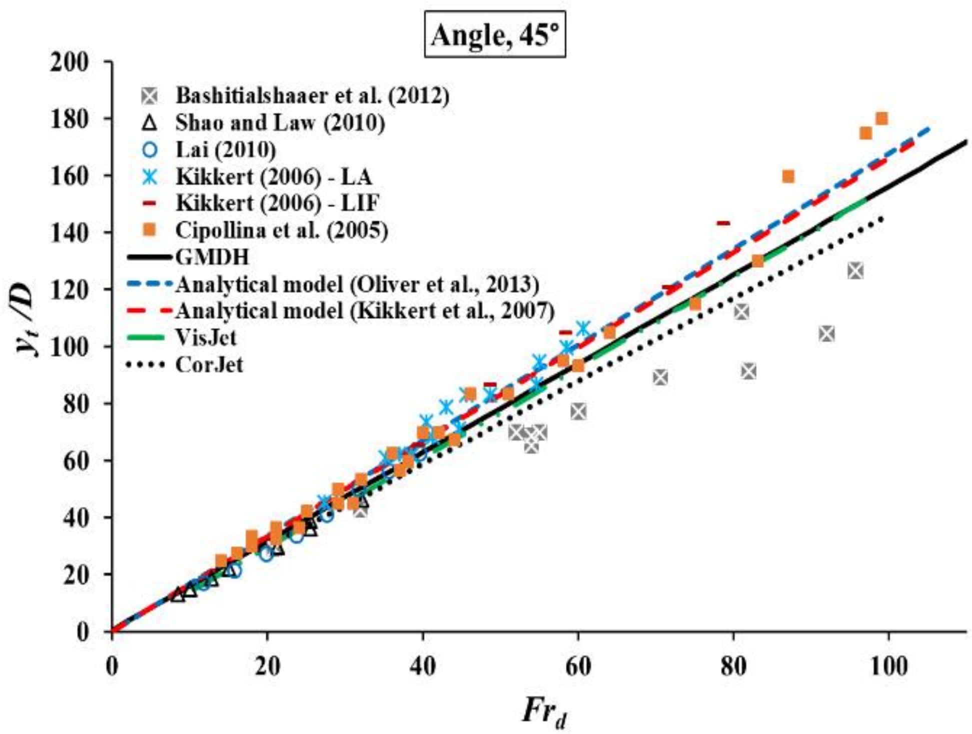
Angle, 45°
Bashitialshaaer et al. (2012)
Shao and Law (2010)
Lai (2010)
Kikkert (2006) - LA
Kikkert (2006) - LIF
Cipollina et al. (2005)
GMDH
Analytical model (Oliver et al., 2013)
Analytical model (Kikkert et al., 2007)
VisJet
CorJet
y_t/D
Fr_d
0
20
40
60
80
100
120
140
160
180
200
0
20
40
60
80
100

(b)

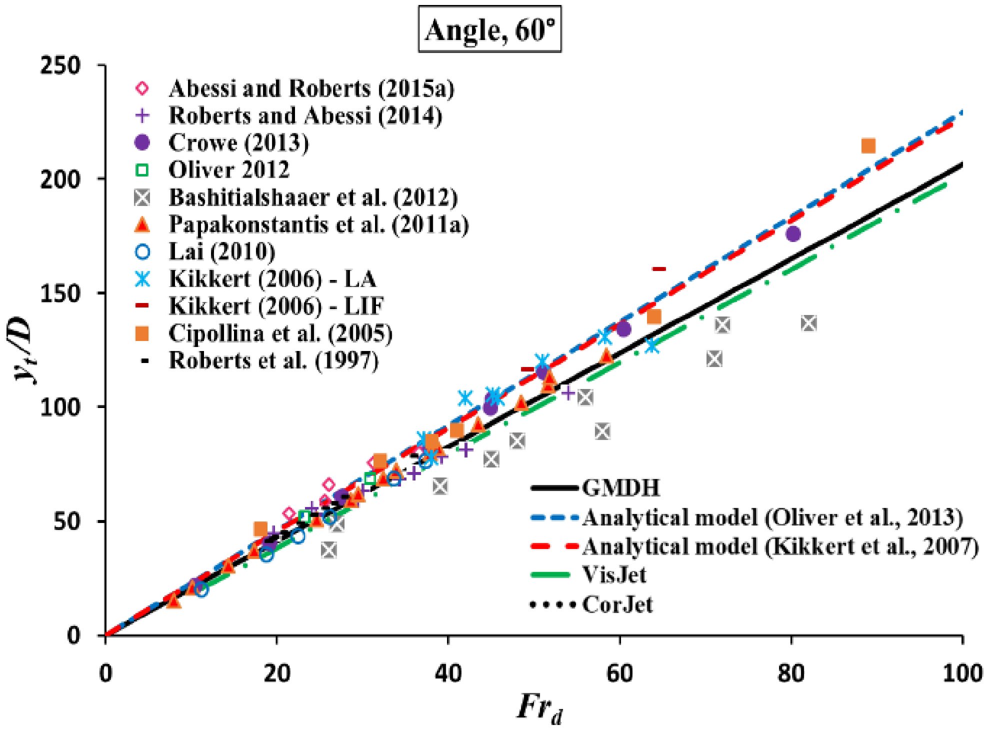
Angle, 60°
Abessi and Roberts (2015a)
Roberts and Abessi (2014)
Crowe (2013)
Oliver 2012
Bashitialshaaer et al. (2012)
Papakonstantis et al. (2011a)
Lai (2010)
Kikkert (2006) - LA
Kikkert (2006) - LIF
Cipollina et al. (2005)
Roberts et al. (1997)
GMDH
Analytical model (Oliver et al., 2013)
Analytical model (Kikkert et al., 2007)
VisJet
CorJet
y_t/D
Fr_d
0
50
100
150
200
250
0
20
40
60
80
100

(c)

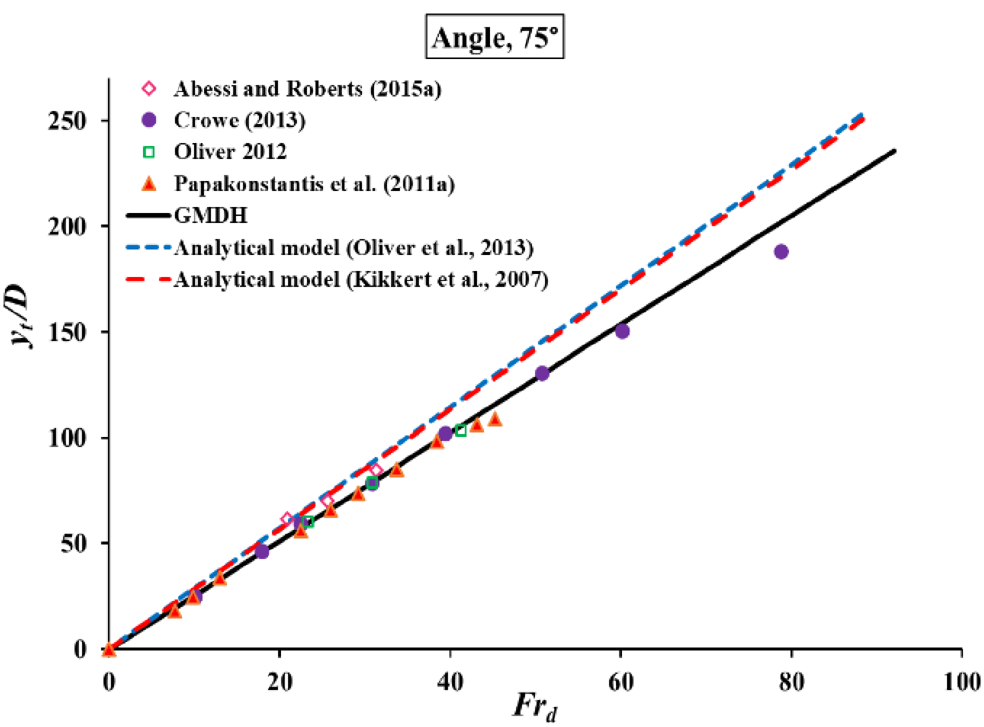
Angle, 75°
Abessi and Roberts (2015a)
Crowe (2013)
Oliver 2012
Papakonstantis et al. (2011a)
GMDH
Analytical model (Oliver et al., 2013)
Analytical model (Kikkert et al., 2007)
y_t/D
Fr_d
0
50
100
150
200
250
0
20
40
60
80
100

(d)

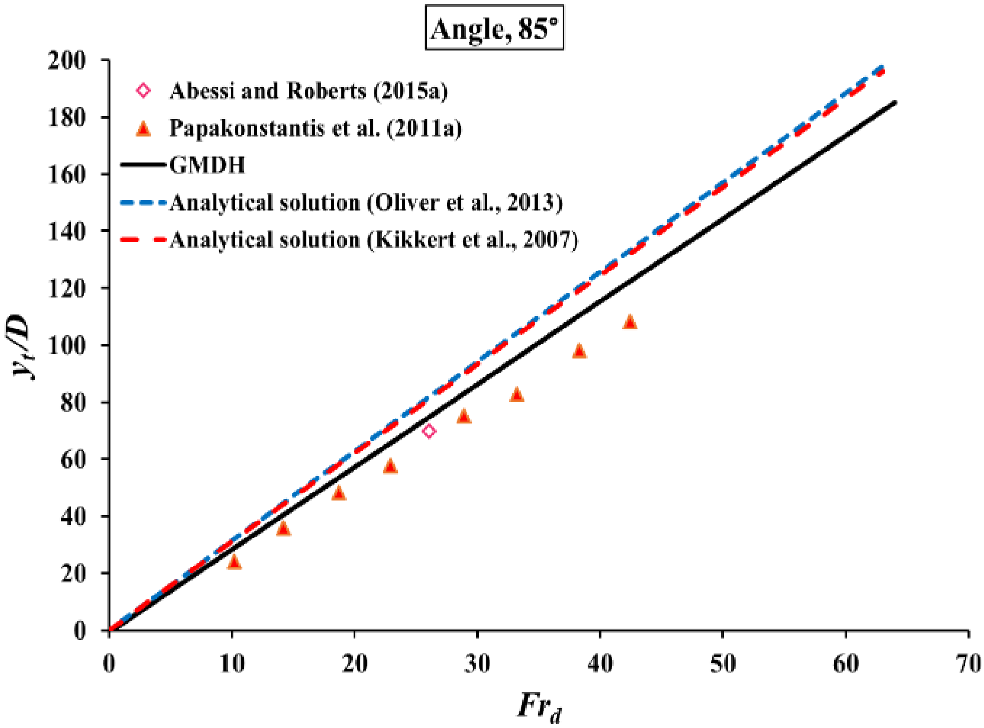

(e)

Figure 4-5: A comparison of GMDH predicted results with previous analytical solutions for y_t/D for angles: (a) 15°, (b) 45°, (c) 60°, (d) 75° and (e) 85°.

To quantify the variations of the results obtained from these models (proposed and previous models) with the actual data, the statistical index equation called Standard Error of the Estimate (SEE) can be used to see which model is preferred and gave a more precise prediction of the actual data. The low value of the SEE, the more accurate of the model. The SEE equation is defined as follows:

$$SEE = \sqrt{\frac{1}{n}\sum(\hat{y} - y)^2} \qquad (4\text{-}11)$$

The results of the model predictions for geometrical parameters for all angles are summarized in Table 4-3. The results of the standard error show that the GMDH model performed better and is much more accurate than other models. All results of the SEE for the GMDH model were the lowest values for all angles for both geometrical parameters except for angle 45° for x_r/D where the result of Oliver et al.'s model was the lowest. Therefore, the SEE results illustrate that all fitting lines of the GMDH model performed well for all geometrical parameter predictions, as the scattered data are closely located around the fitting lines with approximately 10% error around the lines. As a result, the GMDH model is the most accurate model among those tested.

Table 4-3: Results of the standard error of the estimate for all models.

Geometrical parameter	Angle	GMDH model	CORJET	VISJET	Kikkert et al. (2007)	Oliver et al. (2013)
x_r/D	15°	6.39	-	-	7.94	6.86
	45°	10.82	-	-	11.72	10.77
	60°	9.42	-	-	12.29	9.51
	75°	4.35	-	-	20.80	4.99
y_t/D	15°	3.35	-	-	3.72	3.66
	45°	11.13	12.16	11.31	15.71	12.44
	60°	9.81	12.17	10.96	18.72	12.31
	75°	3.93	-	-	12.00	12.95
	85°	9.06	-	-	15.53	16.39

Accordingly, this provides evidence that the GMDH model is considered a reliable model for predicting the geometrical parameters of the near-field mixing zone of the inclined dense jets. Figures 4-6a and b shows the results of the constant values for the normalized forms (x_r/DFr_d) and (y_t/DFr_d) for the GMDH model plotted against the initial discharge angle along with the data reported in previous studies. Third-order polynomial fittings were obtained for all models in both figures. Despite the large dispersion in the actual data, the fitting curve of the proposed model is considered the best prediction compared to the other models in terms of being close to most of the actual data. Moreover, the results obtained from the GMDH model are consistent with what was previously stated by Abessi and Roberts (2015b), which shows that the horizontal distance of the return point increases with an increasing angle up to approximately 40° and then the distance begins to decrease. For Figure 4-6b, the results show that the terminal rise height gradually increases as the angle of the jet increases until reaching approximately angle 85°, at which point the fitting curve stays almost constant without any change. In this figure, the GMDH model was in good agreement with the observed data. Generally, it can be seen that the GMDH predictive model shows better results with the observed data than the other models.

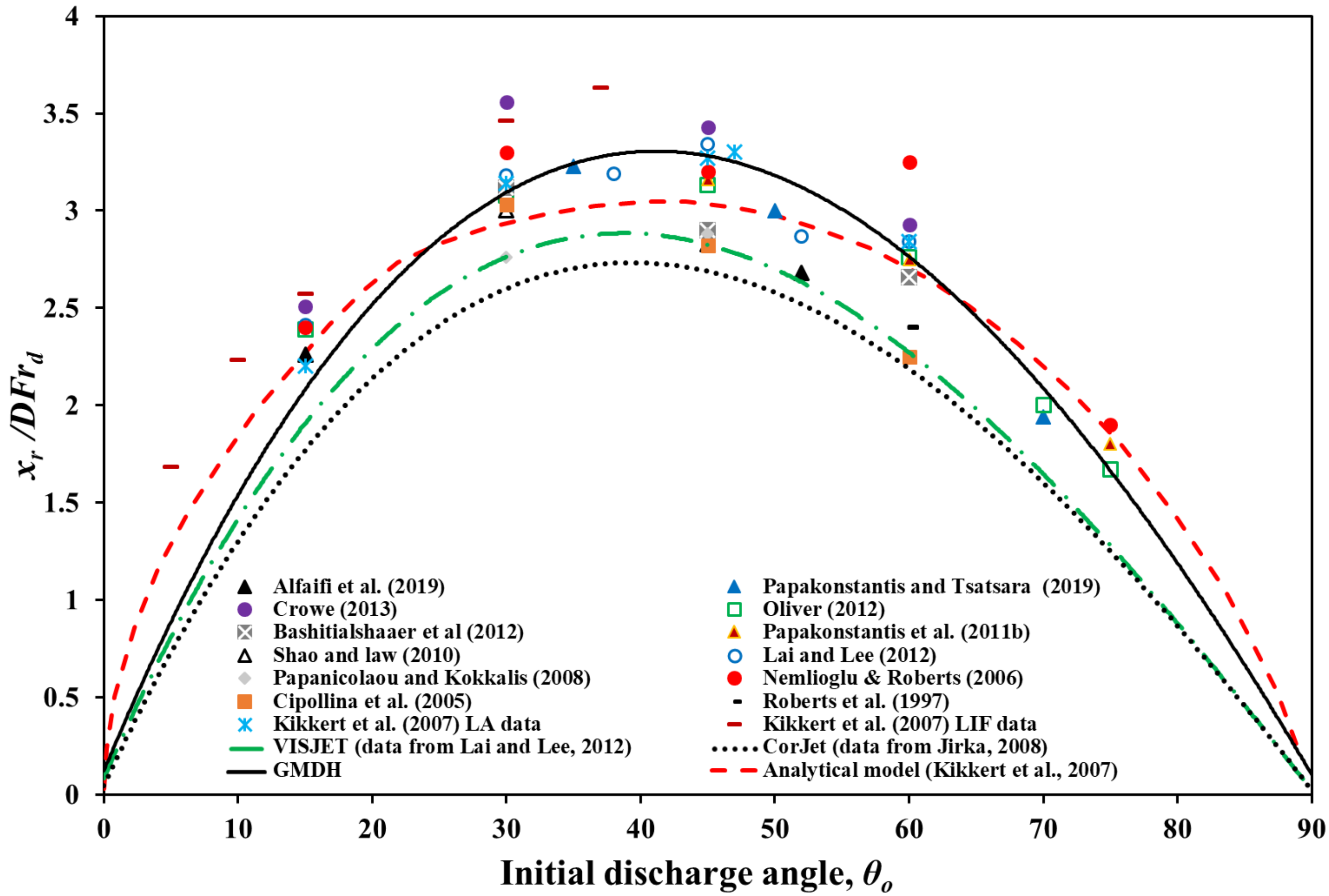

4
3.5
3
2.5
2
1.5
1
0.5
0
x_r/DFr_d
0
10
20
30
40
50
60
70
80
90
Initial discharge angle, θ_o
Alfaifi et al. (2019)
Crowe (2013)
Bashitialshaaer et al (2012)
Shao and law (2010)
Papanicolaou and Kokkalis (2008)
Cipollina et al. (2005)
Kikkert et al. (2007) LA data
VISJET (data from Lai and Lee, 2012)
GMDH
Papakonstantis and Tsatsara (2019)
Oliver (2012)
Papakonstantis et al. (2011b)
Lai and Lee (2012)
Nemlioglu & Roberts (2006)
Roberts et al. (1997)
Kikkert et al. (2007) LIF data
CorJet (data from Jirka, 2008)
Analytical model (Kikkert et al., 2007)

(a)

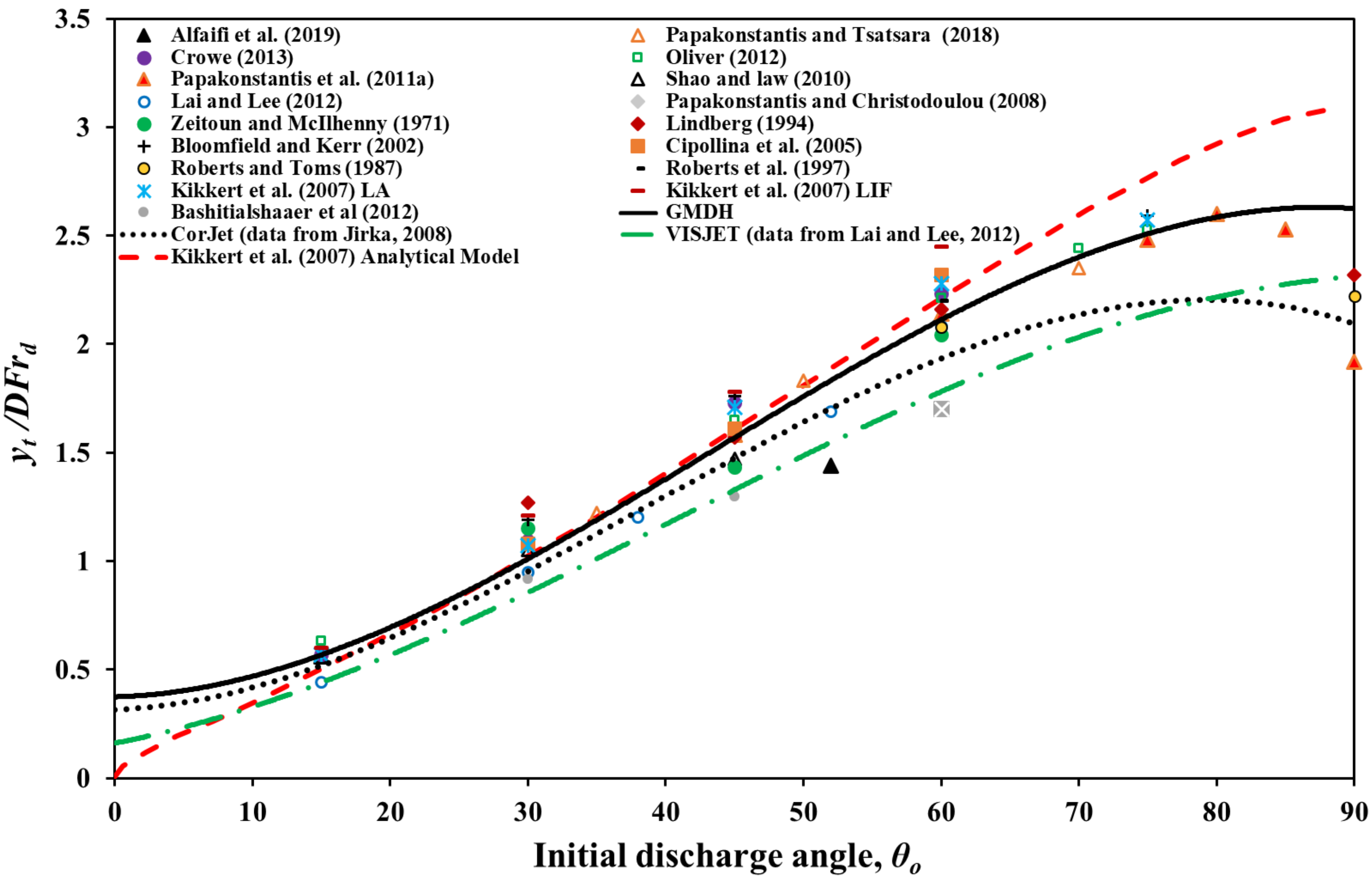

(b)

Figure 4-6: Results of various nozzle angles compared with previous observed data and analytical models for: (a) horizontal distance of return point; (b) Terminal rise height.

4.4. Conclusions

Discharge of the brine water produced from desalination plants back into the coastal ocean using a submerged pipe is a common method widely used in engineering practices. Therefore, studying the mixing behavior of this discharge in the near-field zone has become a research priority to reduce the impact of this water on the marine environment. The discharged water can be formed as an inclined negatively-buoyant jet when its density is higher than the density of the receiving water. Therefore, predicting the geometrical characteristics of this jet is crucial important for improving the understanding of the mixing behavior of this type of discharging and its dilution. In this study, the geometrical characteristics of the inclined negatively-buoyant jet for angles ranging from 15° to 85° was modeled and predicted using a type of artificial neural network (ANN) called group method of data handling (GMDH). Results of this model were evaluated statistically and comparatively with several of other analytical models studied previously. The results show that this model, while being efficient, is more accurate and is better able to accurately predict the geometrical characteristics of the negatively-buoyant jet compared to the others.

Chapter 5. Conclusions and future work

5.1.Conclusions

This study has improved the understanding of jet flow behavior in the near-field zones of outfall systems when the jets' densities differ from those of the receiving environments, as well as the understanding of the mixing of both positively and negatively buoyant jets. In addition, it provides numerical simulation results to predict those processes.

In the first part of this study, these aspects were accomplished:

- A comparative experimental study for thermal and nonthermal buoyant offset jets discharged into fresh and saline ambient waters was conducted. The effect of the receiving water conditions on the offset buoyant jet behavior was also investigated.
- Various characteristics of the jet flow, such as the centerline jet trajectory, jet growth rate, and jet velocity decay, were measured using a PIV system.
- All comparative experiments were conducted using the same densimetric Froude numbers and density differences.
- The results show that jet flows behave differently if discharged into ambient water with different conditions, even if the densimetric Froude number is the same, and that the trajectories of thermal jets are not the same as those of nonthermal jets, as the thermal jets traveled farther than the nonthermal jets.
- Three RANS turbulence models were applied to predict the behavior of these jets, which included the standard $\boldsymbol{k}$-$\boldsymbol{\varepsilon}$, realizable $\boldsymbol{k}$-$\boldsymbol{\varepsilon}$, and buoyancy-modified $\boldsymbol{k}$-$\boldsymbol{\varepsilon}$.
- To assess the accuracy of the simulations, the numerical results were compared with the experimental results obtained in the present study.
- The best prediction of the centerline jet trajectory for all experimental data was obtained from the realizable $\boldsymbol{k}$-$\boldsymbol{\varepsilon}$. However, the buoyancy-modified $\boldsymbol{k}$-$\boldsymbol{\varepsilon}$ model predicted the jet trajectory better than the standard $\boldsymbol{k}$-$\boldsymbol{\varepsilon}$ model, especially in the nonthermal cases.

- This study demonstrates that ambient water conditions can significantly affect jet characteristics and behaviors. Also, the obtained results reveal that the source of buoyancy (salinity versus temperature for the same values of $\boldsymbol{Fr_d}$ and same$\Delta\boldsymbol{\rho}$) affects the trajectory and mixing properties of the jet.

In the second part of this study, these aspects were accomplished:

- The main geometrical characteristics of an inclined negatively-buoyant jet discharged into stagnant water were experimentally investigated using a high-resolution digital camera. Two jet discharge angles (15° and 52°) were used in this study. Two advantages of this study were the wide range of densimetric Froude numbers used, ranging from 11 to 75; and to provide more experimental data to be used for developing and evaluating the performance of the proposed model.
- Three different densities ranging from 1011 to 1030.7 kg/m^3 were used to obtain more diversity in the source of the discharged water and thus to investigate how the geometrical characteristics of the jet were affected by changes in density.
- A comparison of the geometrical characteristics of both angles with previous reported data was also presented. The results showed a good agreement with most of the previous data for all geometrical parameters, especially for the angle of 15°, while the 52° angle results were slightly different from the compared data, and this variation may be attributed to the limitations of the existing data for the 52° angle.
- The experimental results of angles 15° and 52° obtained in this study were useful as a database for training and testing of the artificial neural network (GMDH) model used in this study in order to estimate the observed data on the behavior of negatively-buoyant dense jets.
- Based on the R^2 results, the obtained results showed that the GMDH model has high prediction accuracy and an excellent agreement with all observed experimental data. Also, the statistical results of the mean absolute percentage error (MAPE), ranging between 2.6 to 8.4%, indicate that the GMDH model performed with good accuracy.
- More assessment of the accuracy of the GMDH model was conducted by comparing its results with two analytical solutions reported in previous studies. The results of the GMDH method showed excellent predictions for both angles, compared with those of analytical solutions for all geometrical characteristics, where the scattered of the

experimental data are closely located around the GMDH fitting lines showing better prediction than those of analytical solutions.

In the third part of this study, these aspects were accomplished:

- A comprehensive study for predicting the geometrical characteristics of inclined negatively buoyant jets discharged were studied numerically using the artificial neural network called group method of data handling (GMDH). A wide range of jet inclination angles, raining from 15° to 85° were covered in this study.
- Two evaluation methods (statistically and comparatively with previous reported data) were employed on the proposed model (GMDH) and presented in this study.
- The previous reported data were used for training and testing the model with the training of approximately 70% to 80% of the data.
- The obtained results of the statistical indices are also provided, which showed a high accuracy of the proposed model with values of the coefficient of determination (R^2) 0.9719 and 0.9513 for training and testing for the x_r/D parameter, and 0.9454 and 0.9565 for training and testing for y_t/D.
- Then, comparisons of the results of the present model for the geometrical characteristics with four previous analytical models were also presented. The results revealed the superiority of the proposed model in predicting the geometrical characteristics of the inclined dense jet for all tested angles.
- Moreover, the standard error of estimate (SEE) was applied to demonstrate which model performed the best in terms of getting closer to the actual data. The results indicated that all fitting lines of the GMDH model performed very well for all geometrical parameter predictions and was the best model with approximately 10% error, which was the lowest value of error among the models.
- In conclusion, this study confirms the ability to use the GMDH model to predict the geometrical properties of the inclined negatively buoyant jet with high performance and accuracy.

5.2.Future work

This research study highlighted benefits of the first detailed study into the effect of receiving water conditions (thermal and nonthermal) on offset positively buoyant jets behavior as well as the first use of the artificial neural network introduced by the GMDH method for negatively-buoyant jets. Therefore, the following recommendations are suggested for future work on the positively and negatively buoyant jet discharged into deep stagnant ambient water:

- The effect of two parameters (densimetric Froude number and density) have been applied in the first part of this thesis with employing three RANS turbulence models (the standard $\boldsymbol{k}$-$\boldsymbol{\varepsilon}$, realizable $\boldsymbol{k}$-$\boldsymbol{\varepsilon}$, and buoyancy-modified $\boldsymbol{k}$-$\boldsymbol{\varepsilon}$). One more parameter would be interesting to be added to the previous parameters (i.e.$\boldsymbol{Re}$) to be compared with those of parameters tested and see if there is any influence occurred.
- Regarding the numerical aspect, another numerical approach would be interesting using Large Eddy Simulations (LES) model and related schemes such as Detached Eddy Simulation (DES) along with one Reynolds Stress model (e.g., LRR) and compare the results obtained from these models with what obtained previously. The reason for selecting these models are the positive results obtained comparing to others.
- For the second part, several experiments have been conducted for the angles considered herein. However, it would be useful to conduct more experiments using a high-resolution apparatus, such as PIV and LIF, for more angles that have not been tested before. In addition, it can also be beneficial to apply the previous suggested models for predicting the geometrical characteristics of the negatively buoyant jets and make a comparison with the performance of the GMDH model.
- Moreover, another approach related to the artificial neural network based on the multigene genetic-programming (MGGP) technique would be a good idea for research to be employed in the mixing behavior of the near-field zone. Also, two other approaches based on Genetic Algorithm-based regression methods namely the Genetic Algorithm Artificial neural network (GAA) and the Genetic Programming (GP), are interesting to be tested in this field as well.

References:

Abessi, O., 2018. Brine Disposal and Management-Planning, Design, and Implementation. In: Sustainable Desalination Handbook: Plant Selection, Design and Implementation. Elsevier Inc., pp. 259–303.

Abessi, O., Roberts, P.J.W., 2014. Multiport Diffusers for Dense Discharges. J. Hydraul. Eng. 140, 04014032.

Abessi, O., Roberts, P.J.W., 2015a. Effect of Nozzle Orientation on Dense Jets in Stagnant Environments. J. Hydraul. Eng. 141, 06015009.

Abessi, O., Roberts, P.J.W., 2015b. Dense Jet Discharges in Shallow Water. J. Hydraul. Eng. 142, 04015033.

Abessi, O., Saeedi, M., Bleninger, T., Davidson, M., 2012. Surface discharge of negatively buoyant effluent in unstratified stagnant water. J. Hydro-Environment Res. 6, 181–193.

Agelin-Chaab, M., Tachie, M.F., 2011. Characteristics of Turbulent Three-Dimensional Offset Jets. J. Fluids Eng. 133, 1–9.

Ahmad, M., 2002. Environmental Effects of Multi-Stage Flash (Msf) Desalination Plant At Al-Jubail, Saudi Arabia. Master thesis, Faculty of Engineering and Applied Science, Memorial University of Newfoundland, Newfoundland, Canada.

Ahmad, N., Baddour, R.E., 2014. A review of sources, effects, disposal methods, and regulations of brine into marine environments. Ocean Coast. Manag. 87, 1–7.

Alfaifi, H., Mohammadian, A., Bonakdari, H., 2019a. Experimental and empirical study of geometrical characteristics of 15° and 52° inclined negatively buoyant jets. J. Coast. Res. (To Appear.

Alfaifi, H., Mohammadian, A., Gildeh, H.K., Gharavi, A., 2019b. Experimental and numerical study of the characteristics of thermal and nonthermal offset buoyant jets discharged into stagnant water. Desalin. Water Treat. 141, 171–186.

Alitaleshi, F., Daghbandan, A., 2019. Using a multi-objective optimal design of GMDH type neural networks to evaluate the quality of treated water in a water treatment plant. Desalin. Water Treat. 139, 123–132.

Anderson, J. 1995. Computational Fluid Dynamics, the Basics with Applications. McGraw-Hill, US.

Assoudi, A., Habli, S., Mahjoub Saïd, N., Bournot, H., Le Palec, G., 2016. Three-dimensional study of turbulent flow characteristics of an offset plane jet with variable density. Heat Mass Transf. 52, 2327–2343.

Assoudi, A., Habli, S., Saïd, N.M., Bournot, H., Palec, G. Le, 2015. Experimental and numerical study of an offset jet with different velocity and offset ratios. Eng. Appl. Comput. Fluid Mech. 9, 490–512.

Azimi, H., Bonakdari, H., Ebtehaj, I., 2017. A Highly Efficient Gene Expression Programming Model for Predicting the Discharge Coefficient in a Side Weir along a Trapezoidal Canal. Irrig. Drain. 66, 655–666.

Bashitialshaaer, R., Larson, M., Persson, K.M., 2012. An experimental investigation on inclined negatively buoyant jets. Water (Switzerland) 4, 720–738.

Berberović, E., Van Hinsberg, N.P., Jakirlić, S., Roisman, I. V., Tropea, C., 2009. Drop impact onto a liquid layer of finite thickness: Dynamics of the cavity evolution. Phys. Rev. E 79, 036306.

Bleninger, T., Niepelt, A., Jirka, G., 2010. Desalination plant discharge calculator. Desalin. Water Treat. 13, 156–173.

Bleninger, T., Jirka, G.H., 2010. Environmental planning , prediction and management of brine discharges from desalination plants, Middle East Desalination Research Center (MEDRC), Muscat, Sultanate of Oman.

Bloomfield, L.J., Kerr, R.C., 2002. Inclined turbulent fountains. J. Fluid Mech. 451, 283–294.

Bombar, G., Dölgen, D., Alpaslan, M.N., 2016. Environmental impacts and impact mitigation plans for desalination facilities. Desalin. Water Treat. 57, 11528–11539.

Bonakdari, H., Mohammadian, A., 2019. Evolutionary prediction of an inclined dense jet in shallow water. Desalin. Water Treat. 151, 1–16.

Bosanquet, C.H., Horn, G., Thring, M.W., 1961. The Effect of Density Differences on the Path of Jets. Proc. R. Soc. London, Ser. A, Math. Phys. Sci. 263, 340–352.

Cambridge, M.L., Kendrick, G.A., Mondon, J., Zavala-Perez, A., Cawthray, G.R., 2017. Effects of high salinity from desalination brine on growth, photosynthesis, water relations and osmolyte concentrations of seagrass Posidonia australis. Mar. Pollut. Bull. 115, 252–260.

Cipollina, A., Brucato, A., Grisafi, F., Nicosia, S., 2005. Bench-Scale Investigation of Inclined Dense Jets. J. Hydraul. Eng. 131, 1017–1022.

Coleman, H.W., Steele, W.G., 1995. Engineering application of experimental uncertainty analysis. AIAA J. 33, 1888 – 1896.

Crowe, A.T., 2013. Inclined negatively buoyant jets and boundary interaction. PhD Thesis, University of Canterbury, Christchurch, New Zealand.

Cuthbertson, A.J.S., Davies, P.A., 2008. Deposition from Particle-Laden, Round, Turbulent, Horizontal, Buoyant Jets in Stationary and Coflowing Receiving Fluids. J. Hydraul. Eng. 134, 390–402.

Daghbandan, A., Khalatbari, S., Abbasi, M.M., 2019. Applying GMDH-type neural network for modeling and prediction of turbidity and free residual aluminium in drinking water. Desalin. Water Treat. 140, 118–131.

Daly, B.J., Harlow, F.H., 1970. Transport equations in turbulence. Phys. Fluids 13, 2634 – 2649.

Ebtehaj, I., Bonakdari, H., Khoshbin, F., Bong, C.H.J., Ab Ghani, A., 2017. Development of group method of data handling based on genetic algorithm to predict incipient motion in rigid rectangular storm water channel. Sci. Iran. 24, 1000–1009.

Ebtehaj, I., Bonakdari, H., Sharifi, A., 2014. Design criteria for sediment transport in sewers based on self-cleansing concept. J. Zhejiang Univ. Sci. A 15, 914–924.

Ebtehaj, I., Bonakdari, H., Zaji, A.H., Azimi, H., Khoshbin, F., 2015. GMDH-type neural network approach for modeling the discharge coefficient of rectangular sharp-crested side weirs. Eng. Sci. Technol. an Int. J. 18, 746–757.

Einav, R., Harussi, K., Perry, D., 2003. The footprint of the desalination processes on the environment. Desalination 152, 141–154.

Eleuch, O., Latrache, N., Frikha, S., Driss, Z., 2018. Experimental Study of the Injection of a Pure Water Jet in Miscible Salt Water. Thermo-Mechanics Appl. Eng. Technol. 223–241.

Findlay, M.J., 1998. Experimental and computational investigation of inclined jets in a crossflow. PhD dissirtation, University of British Columbia, 1998.

Fischer, H.B., List, E.J., Hoe, R.C.Y., Imbercer, J., Brook, N.H., 1979. mixing in inland and coastal waters. Academic Press.

Forliti, D.J., Strykowski, P.J., Debatin, K., 2000. Bias and precision errors of digital particle image velocimetry. Exp. Fluids 28, 436 – 447.

Ghaedi, A.M., Baneshi, M.M., Vafaei, A., Rayegan, A., Nejad, S., Tyagi, I., Kumar, N., Galunin, E., Tkachev, A.G., Agarwal, S., Gupta, V.K., 2018. Comparison of multiple linear regression and group method of data handling models for predicting sunset yellow dye removal onto activated carbon from oak tree wood. Environ. Technol. Innov. 11, 262–275.

Gholami, A., Bonakdari, H., Ebtehaj, I., Shaghaghi, S., Khoshbin, F., 2017. Developing an expert group method of data handling system for predicting the geometry of a stable channel with a gravel bed. Earth Surf. Process. Landforms 42, 1460–1471.

GMDH LLC, 2019. GMDH Shell Ds, version 3.8.9 [WWW Document]. URL https://gmdhsoftware.com/

Greenshields, C.J., 2019. OpenFOAM User Guide; Version 7.0; The OpenFOAM Foundation: London, UK, 2019.

Gu, R., 1996. Modeling Two-Dimensional Turbulent Offset Jets. J. Hydraul. Eng. 122, 617–624.

Hashim, A., Hajjaj, M., 2005. Impact of desalination plants fluid effluents on the integrity of seawater, with the Arabian Gulf in perspective. Desalination 182, 373–393.

Hoch, J., Jiji, L., 1981. Two-dimensional turbulent offset jet-boundary interaction. J. Fluids Eng. 103, 154–161.

Ivakhnenko, A.G., 1971. Polynomial Theory of Complex Systems. IEEE Trans. Syst. Man. Cybern. 4, 364–378.

Jiang, B., Law, A.W.-K., Lee, J.H.-W., 2014. Mixing of 30° and 45° Inclined Dense Jets in Shallow Coastal Waters. J. Hydraul. Eng. 140, 241–253.

Jirka, G.H., 2004. Integral Model for Turbulent Buoyant Jets in Unbounded Stratified Flows. Part I: Single Round Jet. Environ. Fluid Mech. 4, 1–56.

Jirka, G.H., 2008. Improved Discharge Configurations for Brine Effluents from Desalination Plants. J. Hydraul. Eng. 134, 116–120.

Kanna, P.R., Das, M.K., 2005. Numerical simulation of two-dimensional laminar incompressible offset jet flows. Int. J. Numer. Methods Fluids 49, 439–464.

Ketsetzi, A., Stathoulopoulou, A., Demadis, K.D., 2008. Being “ green ” in chemical water treatment technologies : issues , challenges and developments 223, 506–512.

Kheirkhah Gildeh, H., Mohammadian, A., Nistor, I., Qiblawey, H., 2014. Numerical Modeling of Turbulent Buoyant Wall Jets in Stationary Ambient Water. J. Hydraul. Eng. 140, 04014012.

Kheirkhah Gildeh, H., Mohammadian, A., Nistor, I., Qiblawey, H., 2015a. Numerical modeling of 30 and 45 inclined dense turbulent jets in stationary ambient. Environ. Fluid Mech. 15,

537–562.
Kheirkhah Gildeh, H., Mohammadian, A., Nistor, I., Qiblawey, H., Yan, X., 2015b. CFD modeling and analysis of the behavior of 30° and 45° inclined dense jets – new numerical insights. J. Appl. Water Eng. Res. 4, 112–127.
Kikkert, G.A., 2006. Buoyant jets with two and three-dimensional trajectories. PhD Thesis, University of Canterbury, Christchurch, New Zealand.
Kikkert, G.A., Davidson, M.J., Nokes, R.I., 2007. Inclined Negatively Buoyant Discharges. J. Hydraul. Eng. 133, 545–554.
Lai, C.C., 2010. Mixing of inclined dense jets. M.Phil. thesis, Dept of Civil Engineering, the University of Hong Kong, Hong Kong.
Lai, C.C.K., Lee, J.H.W., 2012. Mixing of inclined dense jets in stationary ambient. J. Hydro-Environment Res. 6, 9–28.
Lattemann, S., Höpner, T., 2008. Environmental impact and impact assessment of seawater desalination. Desalination 220, 1–15.
Launder, B.E., Spalding, D.B., 1974. The Numerical Computation of Turbulent Flows. Comput. Methods Appl. Mech. Eng. 3, 269 – 289.
Lee, J.H.W., Cheung, V., 1990. Generalized lagrangian model for buoyant jets in current. J. Environ. Eng. (United States) 116, 1085–1106.
Lee, J.H.W., Chu, V.H.., 2003. Turbulent Jets and Plumes: A Lagrangian Approach. Kluwer Academic Publishers, The Netherlands., Dordrecht, The Netherlands.
Lindberg, W.R., 1994. Experiments on Negatively Buoyant Jets, with and without Cross-Flow. In: Davies P.A., Neves M.J.V. (Eds) Recent Research Advances in the Fluid Mechanics of Turbulent Jets and Plumes. NATO ASI Series (Series E: Applied Sciences). Springer, Dordrecht, pp. 131–145.
Liu, P., Lam, K.M., 2015. Large-eddy simulation of horizontally discharging sediment-laden jets. J. Hydro-Environment Res. 9, 388–403.
Mabrook, B., 1994. Environmental impact of waste brine disposal of desalination plants, Red Sea, Egypt. Desalination 97, 453–465.
Madandoust, R., Bungey, J.H., Ghavidel, R., 2012. Prediction of the concrete compressive strength by means of core testing using GMDH-type neural network and ANFIS models. Comput. Mater. Sci.

Manera, A., Bardet, P., Petrov, V., 2018. High-resolution time-resolved experiments on mixing and entrainment of buoyant jets in stratified environments (No. 14-6552), Doe Osti.Gov.

Mehri, Y., Soltani, J., Khashehchi, M., 2019. Predicting the coefficient of discharge for piano key side weirs using GMDH and DGMDH techniques. Flow Meas. Instrum. 65, 1–6.

Michas, S.N., Papanicolaou, P.N., 2009. Horizontal round heated jets into calm uniform ambient. Desalination 248, 803–815.

Milione, M., Zeng, C., 2008. The effects of temperature and salinity on population growth and egg hatching success of the tropical calanoid copepod, Acartia sinjiensis. Aquaculture 275, 116–123.

Millero, F.J., Huang, F., 2009. The density of seawater as a function of salinity (5 to 70 g kg−1) and temperature (273.15 to 363.15 K). Ocean Sci. 5, 91–100.

Millero, F.J., Poisson, A., 1981. International one-atmosphere equation of state of seawater. Deep Sea Res. Part A, Oceanogr. Res. Pap. 28, 625–629.

Moayed, R.Z., Kordnaeij, A., Mola-Abasi, H., 2017. Compressibility indices of saturated clays by group method of data handling and genetic algorithms. Neural Comput. Appl. 28, 551–564.

Naeini, S.A., Moayed, R.Z., Kordnaeij, A., Mola-abasi, H., 2018. Elasticity modulus of clayey deposits estimation using Group Method of Data Handling type neural network. Measurement 121, 335–343.

Najafzadeh, M., Barani, G., Hessami-Kermani, M.R., 2013. Group method of data handling to predict scour depth around vertical piles under regular waves. Sci. Iran. 20, 406–413.

Nasr, A., Lai, J.C.S., 1998. A turbulent plane offset jet with small offset ratio. Exp. Fluids 24, 47–57.

Nemlioglu, S., Roberts, P.J.W., 2006. Experiments on dense jets using three-dimensional laser-induced fluorescence (3DLIF). In: MWWD 2006 - the 4th International Conference on Marine Waste Water Disposal and Marine Environment. Antalya, Turkey.

Oliver, C.J., 2012. Near Field Mixing of Negatively Buoyant Jets. PhD Thesis, University of Canterbury, Christchurch, New Zealand.

Oliver, C.J., Davidson, M.J., Nokes, R.I., 2013a. Predicting the near-field mixing of desalination discharges in a stationary environment. Desalination 309, 148–155.

Oliver, C.J., Davidson, M.J., Nokes, R.I., 2013b. Removing the boundary influence on negatively buoyant jets. Environ. Fluid Mech. 13, 625–648.

Papakonstantis, I.G., Christodoulou, G.C., 2008. Discussion of “Inclined NegativelyBuoyant Discharges” by G. A. Kikkert,M. J. Davidson, and R. I. Nokes. J. Hydraul. Eng. 134, 1782–1784.

Papakonstantis, I.G., Christodoulou, G.C., Papanicolaou, P.N., 2011a. Inclined negatively buoyant jets 1: Geometrical characteristics. J. Hydraul. Res. 49, 3–12.

Papakonstantis, I.G., Christodoulou, G.C., Papanicolaou, P.N., 2011b. Inclined negatively buoyant jets 2: Concentration measurements. J. Hydraul. Res. 49, 13–22.

Papakonstantis, I.G., Tsatsara, E.I., 2018. Trajectory Characteristics of Inclined Turbulent Dense Jets. Environ. Process. 5, 539–554.

Papakonstantis, I.G., Tsatsara, E.I., 2019. Mixing Characteristics of inclined turbulent dense jets. Environ. Process. 1–17.

Papanicolaou, P.N., Kokkalis, T.J., 2008. Vertical buoyancy preserving and non-preserving fountains, in a homogeneous calm ambient. Int. J. Heat Mass Transf.

Parsaie, A., Azamathulla, H.M., Haghiabi, A.H., 2018. Prediction of discharge coefficient of cylindrical weir–gate using GMDH-PSO. ISH J. Hydraul. Eng. 24, 116–123.

Parsaie, A., Haghiabi, A.H., 2017. Improving modelling of discharge coefficient of triangular labyrinth lateral weirs using SVM, GMDH and MARS techniques. Irrig. Drain. 66, 636–654.

Petersen, K.L., Heck, N., Reguero, B.G., Potts, D., Hovagimian, A., Paytan, A., 2019. Biological and physical effects of brine discharge from the Carlsbad Desalination plant and implications for future desalination plant constructions. Water (Switzerland) 11.

Petersen, K.L., Paytan, A., Rahav, E., Levy, O., Silverman, J., Barzel, O., Potts, D., Bar-Zeev, E., 2018. Impact of brine and antiscalants on reef-building corals in the Gulf of Aqaba – Potential effects from desalination plants. Water Res. 144, 183–191.

Picow, M., 2009. Saudi Arabia Opens World’s Largest Desalination Plant | Green Prophet [WWW Document]. Green Tech Gadgets. URL https://www.greenprophet.com/2009/05/saudi-arabia-desalination/ (accessed 4.6.19).

Prins, G., 2016. Cape Beachgoers Concerned Over Sewage Outfalls [WWW Document]. URL https://www.capetownmagazine.com/news-beachgoers-concerned-about-sewage-outfalls (accessed 4.6.19).

Poungkrajorn, T., 2015. Assuring Asset Integrity Through Improving the Accuracy of Leakage Source Identification of a Permanently Installed Subsea Leak Detection System using Artificial Neural Networks. Master’s thesis.

Raffel, M., Willert, C.E., Wereley, S.T., Kompenhans, J., 2007. Particle image velocimetry, a practical guide, Second Edi. ed. Springer.

Rathore, S.K., Das, M.K., 2015. A comparative study of heat transfer characteristics of wall-bounded jets using different turbulence models. Int. J. Therm. Sci. 89, 337–356.

Roberts, D.A., Johnston, E.L., Knott, N.A., 2010. Impacts of desalination plant discharges on the marine environment: A critical review of published studies. Water Res. 44, 5117–5128.

Roberts, P.J.W., Ferrier, A., Daviero, G., 1997. Mixing in Inclined Dense Jets. J. Hydraul. Eng. 123, 693–699.

Roberts, P.J.W., Toms, G., 1987. Inclined Dense Jets in Flowing Current. J. Hydraul. Eng. 113, 323–340.

Rostami, A., Hemmati-sarapardeh, A., Karkevandi-talkhooncheh, A., Husein, M.M., Shamshirband, S., Rabczuk, T., 2019. Modeling heat capacity of ionic liquids using group method of data handling : A hybrid and structure-based approach. Int. J. Heat Mass Transf. 129, 7–17.

Sadi, M., Shahrabadi, A., 2018. Evolving robust intelligent model based on group method of data handling technique optimized by genetic algorithm to predict asphaltene precipitation. J. Pet. Sci. Eng. 171, 1211–1222.

Shaghaghi, S., Bonakdari, H., Gholami, A., Ebtehaj, I., Zeinolabedini, M., 2017. Comparative analysis of GMDH neural network based on genetic algorithm and particle swarm optimization in stable channel design. Appl. Math. Comput. 313, 271–286.

Shao, D., Law, A.W.-K., 2009. Turbulent mass and momentum transport of a circular offset dense jet. J. Turbul. 10, 1–24.

Shao, D., Law, A.W.K., 2010. Mixing and boundary interactions of 30° and 45° inclined dense jets. Environ. Fluid Mech. 10, 521–553.

Shao, D., Law, A.W.K., 2011. Boundary impingement and attachment of horizontal offset dense jets. J. Hydro-Environment Res. 5, 15–24.

Shih, T.H., Zhu, J., Lumley, J.L., 1995. A new Reynolds stress algebraic equation model. Comput. Methods Appl. Mech. Eng. 125, 287–302.

Sultanate of Oman (2005): Ministerial Decision No: 159/2005, Promulgating the bylaws to discharge liquid waste in the marine environment, Ministry of Regional Municipalities, Environment and Water Resources.

US EPA (2006): National Recommended Water Quality Criteria, National Center for Environmental Publications and Information, 11029 Kenwood Road, Cincinnati, Ohio 45242, USA. Available at http://www.epa.gov/waterscience/criteria/wqctable/nrwqc-2006.pdf

Wec (2002): Perth metropolitan desalination proposal. Environmental protection statement, prepared by Welker Environmental Consultancy for Water Cooperation.

World Bank Group (1998): Thermal Power: Guidelines for New Plants, from the Pollution Prevention and Abatement Handbook. Download from: http://www.ifc.org/ifcext/enviro.nsf/Content/EnvironmentalGuidelines

World Bank Group (2007b): Environmental, Health, and Safety General Guidelines (EHS Guidelines).Download from http://www.ifc.org/ifcext/enviro.nsf/Content/EnvironmentalGuidelines

Yan, X., Mohammadian, A., 2017. Numerical modeling of vertical buoyant jets subjected to lateral confinement. J. Hydraul. Eng. 143, 04017016.

Yan, X., Mohammadian, A., 2019. Multigene Genetic-Programming-Based Models for Initial Dilution of Laterally Confined Vertical Buoyant Jets. J. Mar. Sci. Eng. 7, 246.

Zaji, A.H., Bonakdari, H., 2019. Robustness lake water level prediction using the search heuristic-based artificial intelligence methods. ISH J. Hydraul. Eng. 25, 316–324.

Zeitoun, M.A., McIlhenny, W.F., 1971. Conceptual Designs Of Outfall Systems For Desalination Plants. In: Offshore Technology Conference, 19-21 April, Houston, Texas.

Zhang, S., Jiang, B., Law, A.W.K., Zhao, B., 2016. Large eddy simulations of 45° inclined dense jets. Environ. Fluid Mech. 16, 101–121.

Appendix A

A.1 PIV system and measurement procedure

In the present study, a particle image velocimetry (PIV) system is employed to visualize and quantify the velocity field. Two-dimensional (planar) was used to measure the velocity distributions with two components. This device is manufactured, by Lavision, and the results were extracted using the Davis software provided by Lavision. The PIV system includes four main components: a laser box unit (an Nd:YAG laser with a frequency of 100 mJ per pulse at a wavelength of 532nm), a 2560×1600-pixel high-speed camera (sCMOS) that achieves a 40Hz frame rate at full resolution, a computer with the Davis software, and a synchronizer/timing box. A single field of view experiment (i.e., with one camera) was performed, as the resolution of the camera was high enough for the whole domain.

The main function of the PIV system is to photographically record the movement of tracer particles in fluid. Thereafter, the motion of the particles is determined using image processing methods, and the flow velocity is obtained from the photographic records. The optic system includes a laser unit. In this system, two spherical lenses are combined to focus the original laser beam, and the third (planar concave) lens is used to form a light sheet which is aligned to the jet, as shown in Figure A-1. In most applications, small tracer particles are added to the discharge flow in order to follow the fluid path. In the present study, hollow glass particles with a diameter of 20 μm and a specific gravity of 1.1 were used as the seeding particles. The seeding particles were added to both the ambient water and the jet flow. The data acquisition rate was 40Hz using the single camera with 2D2C (two dimensions, i.e., x and y, and two components, i.e., u and v). The stereo PIV was used to extract the velocity vector distribution with a frequency of 40*Hz*.

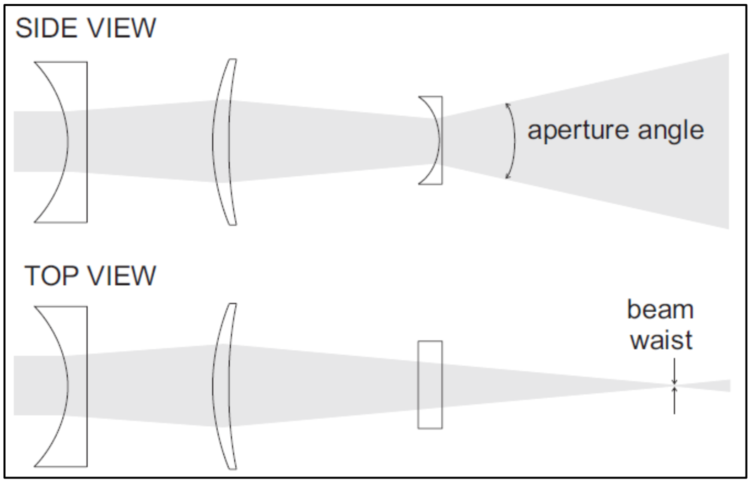

Figure A-1. Components of the optical system of the laser unit (from Manera et al., 2018).

The 30 cm × 30 cm calibration target which was used for all experiments is shown in Figure A-2. The window size selected after calibration for the final interrogation was 25 × 20 pixels^2, with an overlap of 75%. In order to achieve good turbulent statistics, more than 2000 images were taken. Calibration for the recorded images was done two-dimensionally by using dots at the front and real planes.

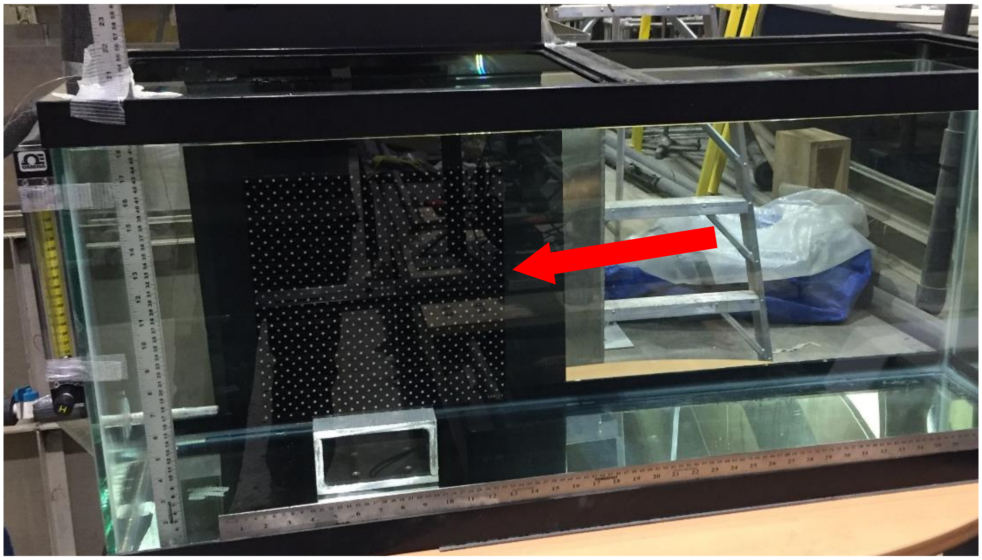

Figure A-2. Calibration target.

The high-speed camera was placed at a cross-section of the tank that was illuminated by a laser sheet in order to capture the illuminated tracer particles in the fluid flow. An optical filter was placed in front of the camera lens which were scattered by the particles, to pass. The main components of the experimental setup are shown in Figure A-3. These components are: A) the laser box, B) laser delivery arm, C) laser lenses, D) high-speed camera (sCMOS), E) nozzle for the discharged water, F) flow meter (rotameter), and G) thermometer.

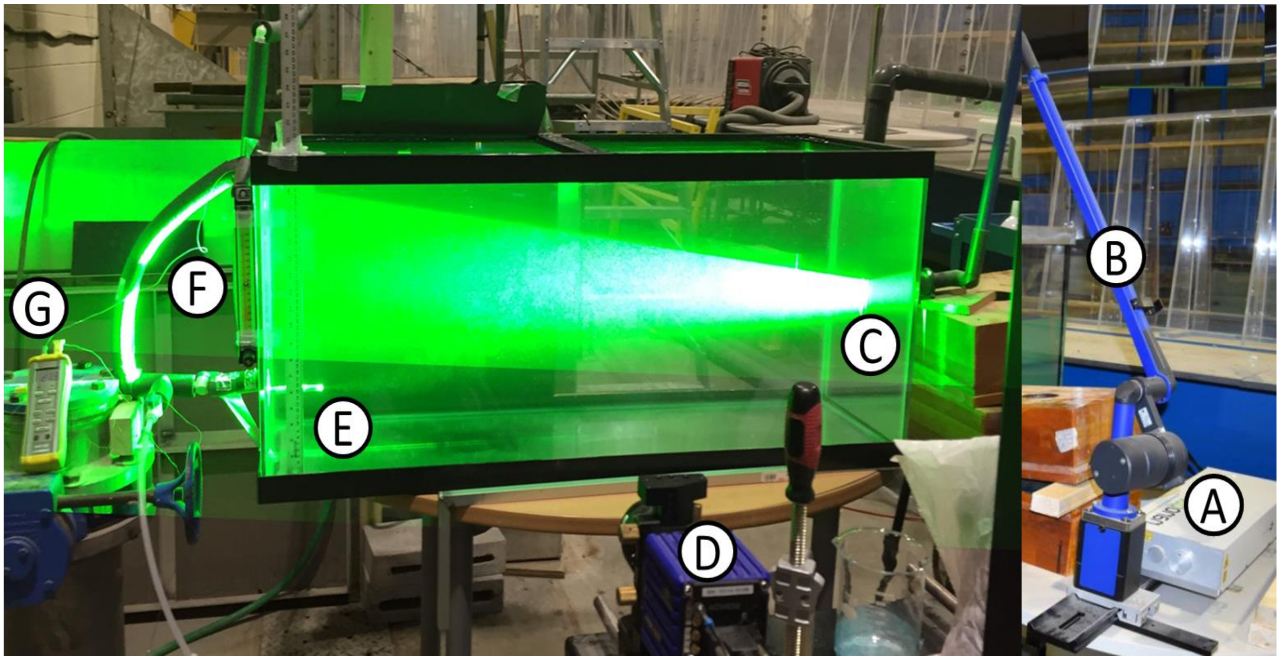

Figure A-3: Experimental setup components with the PIV system.

Images were recorded in the dual-frame sCMOS camera mode (i.e., the Δt between two frames is be different than the Δt between data acquisition), and from the images, the instantaneous velocity field was calculated by cross-correlation calculations between the two frames. During the laser illumination, the camera captured two frames (one frame for each pulse of the pulse pair) separated by a very small time interval (Δt between each frame was 0.002 s, i.e., 2000 μs). The Δt of the data acquisition between each velocity fields were 0.025 s. Figure A-4 shows the method used for extracting the images. The obtained images were then transferred to the processor for the cross-correlation computations (Raffel et al., 2007), then the images from the dual frames are used for the velocity calculation. The time interval of 0.002s was chosen as the best quality by trial and error based on the partial velocity being small, while the 0.025s Δt (equivalent to 40Hz) was chosen based on the best capacity of our system for the desired resolution.

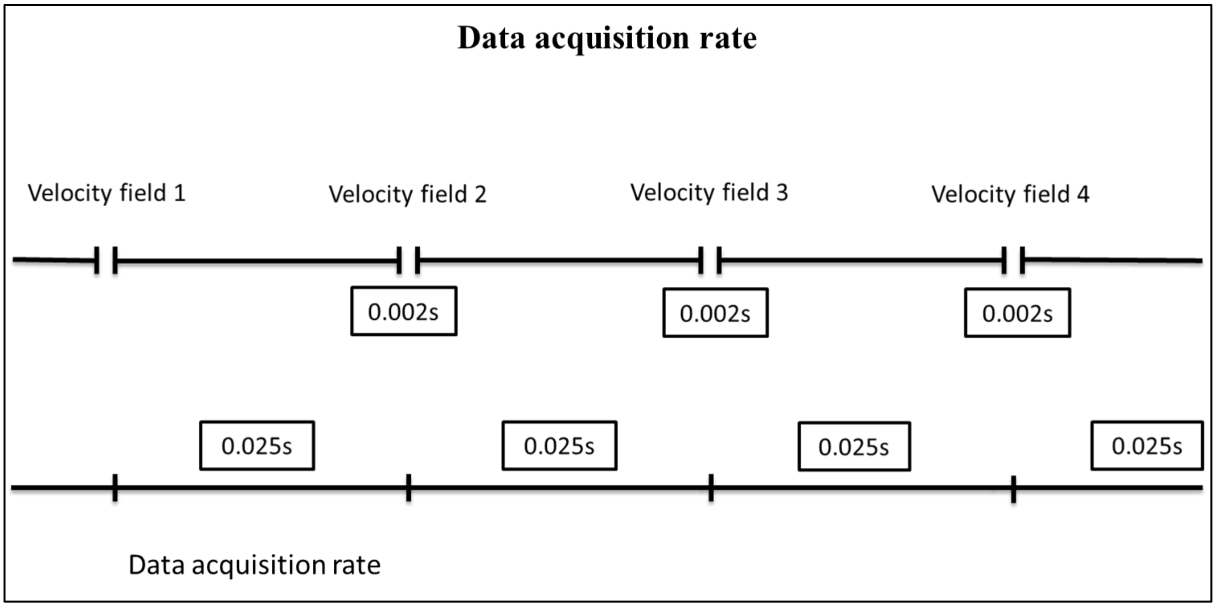

Figure A-4: Method used for computing the data acquisition rate.

A.1.1 Turbulent kinetic energy

In this study, turbulent statistics analysis was conducted by calculating the turbulent kinetic energy for the thermal and nonthermal jets. For brevity, the results of two cases (T1 and S1) for the two types of jet are presented in Figure A-5. As can be seen from Figure A-5a (thermal jet), the jet's kinetic energy at the beginning is very low due to the velocity being lower at the beginning, while in Figure A-5b (nonthermal jet), the jet's kinetic energy at the beginning is high, which was expected because the shear and the velocity is higher at the beginning. Therefore, the jet leading to higher shear thus higher kinetic energy in the nonthermal jet.

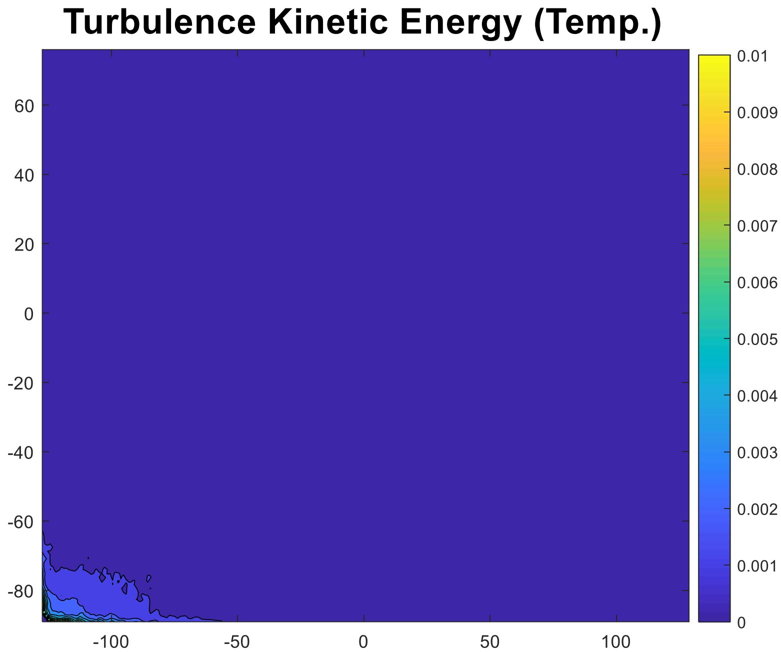

(a)

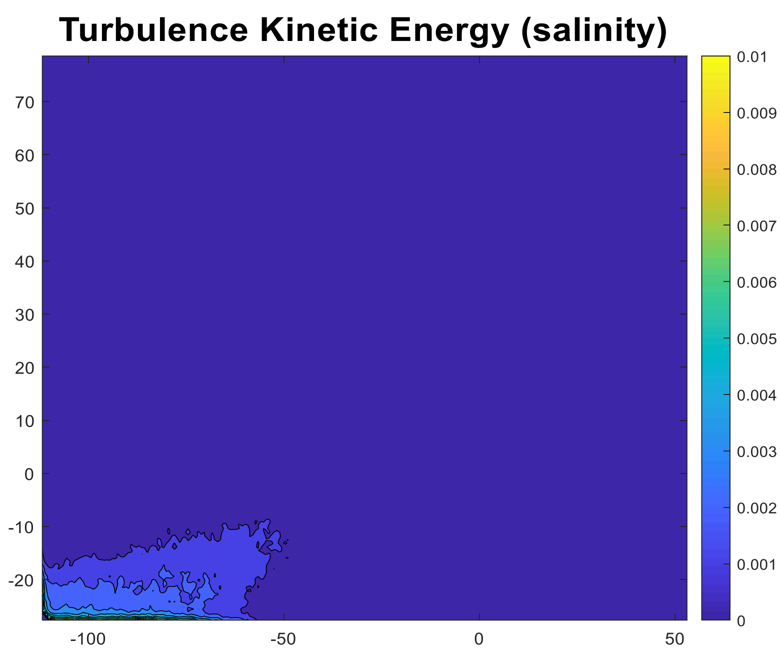

(b)

Figure A-5: Kinetic energy obtained from PIV system for: (a) thermal jet and (b) nonthermal jet.

Appendix B

B.1 Computational approach

Using numerical simulation to predict the jet trajectory of positively buoyant offset jet is one of the objectives of this research. The data obtained from the experimental part will be used to validate the outcome of the numerical simulations.

In this part, the governing equations used in the computations are presented, including the conservation of mass, momentum, and energy for incompressible flows of a Newtonian fluid with constant properties. Fluid flow and heat transfer phenomena can be described using fundamental physical principle describing the conservation of mass, momentum, and energy (Findlay, 1998):

$$\nabla . U = 0 \tag{B-1}$$

$$\rho \frac{DU}{Dt} = -\nabla P + \nabla . (\mu \nabla U) \tag{B-2}$$

$$\rho c_p \frac{DT}{Dt} = \nabla . (k \nabla T) \tag{B-3}$$

B.1.1 Governing equations

The conservation of mass and momentum laws are used to describe the flow by using three-dimensional Reynolds-averaged Navier-Stokes equations in the x, y and z directions as the governing equations for incompressible fluids, as shown in the following:

Continuity Equations:

$$\frac{\partial u_x}{\partial x} + \frac{\partial u_y}{\partial y} + \frac{\partial u_z}{\partial z} = 0 \tag{B-4}$$

Momentum Equations:

$$\frac{\partial u_x}{\partial t}+\frac{u_x\partial u_x}{\partial x}+\frac{u_y\partial u_x}{\partial y}+\frac{u_z\partial u_x}{\partial z}=\frac{\partial}{\partial x}\left[v_e\left(\frac{\partial u_x}{\partial x}\right)\right]+\frac{\partial}{\partial y}\left[v_e\left(\frac{\partial u_x}{\partial y}\right)\right]+\frac{\partial}{\partial z}\left[v_e\left(\frac{\partial u_x}{\partial z}\right)\right]-\frac{1}{\rho_0}\frac{\partial P}{\partial x} \quad \text{(B-5)}$$

$$\frac{\partial u_y}{\partial t}+\frac{u_x\partial u_y}{\partial x}+\frac{u_y\partial u_y}{\partial y}+\frac{u_z\partial u_y}{\partial z}=\frac{\partial}{\partial x}\left[v_e\left(\frac{\partial u_y}{\partial x}\right)\right]+\frac{\partial}{\partial y}\left[v_e\left(\frac{\partial u_y}{\partial y}\right)\right]+\frac{\partial}{\partial z}\left[v_e\left(\frac{\partial u_y}{\partial z}\right)\right]-\frac{1}{\rho_0}\frac{\partial P}{\partial y}-g' \quad \text{(B-6)}$$

$$\frac{\partial u_z}{\partial t}+\frac{u_x\partial u_z}{\partial x}+\frac{u_y\partial u_z}{\partial y}+\frac{u_z\partial u_z}{\partial z}=\frac{\partial}{\partial x}\left[v_e\left(\frac{\partial u_z}{\partial x}\right)\right]+\frac{\partial}{\partial y}\left[v_e\left(\frac{\partial u_z}{\partial y}\right)\right]+\frac{\partial}{\partial z}\left[v_e\left(\frac{\partial u_z}{\partial z}\right)\right]-\frac{1}{\rho_0}\frac{\partial P}{\partial z} \quad \text{(B-7)}$$

where u_x, u_y and u_z are the components of the mean velocity in the Cartesian coordinates; P is the fluid pressure; t is the time; v_e is the effective kinematic viscosity of water ($v_e = v_t + v$); v_t is the turbulent kinematic viscosity; and v is the kinematic viscosity. The effect of variable density (buoyancy) in the vertical direction (y-coordinate) is considered and added in equation (B-6)

Temperature and Salinity equations:

$$\frac{\partial T}{\partial t}+\frac{u_x\partial T}{\partial x}+\frac{u_yT}{\partial y}+\frac{u_zT}{\partial z}=k_e\frac{\partial}{\partial x}\left[\frac{\partial T}{\partial x}\right]+\frac{\partial}{\partial y}\left[\frac{\partial T}{\partial y}\right]+\frac{\partial}{\partial z}\left[\frac{\partial T}{\partial z}\right] \quad \text{(B-8)}$$

$$\frac{\partial S}{\partial t}+\frac{u_x\partial S}{\partial x}+\frac{u_yS}{\partial y}+\frac{u_zS}{\partial z}=k_e\frac{\partial}{\partial x}\left[\frac{\partial S}{\partial x}\right]+\frac{\partial}{\partial y}\left[\frac{\partial S}{\partial y}\right]+\frac{\partial}{\partial z}\left[\frac{\partial S}{\partial z}\right] \quad \text{(B-9)}$$

where:

$$k_e=\frac{v_t}{Pr_t}+\frac{v}{Pr} \quad \text{(B-10)}$$

in which k_e is the heat transfer coefficient, Pr is the Prandtl number, and Pr_t is the turbulent Prandtl number. The common ranges of both Pr and Pr_t are 0.6-1.0; both parameters were chosen as 1.0 based on Kheirkhah Gildeh et al. (2015a, 2015b and 2014). For brevity, the details of the buoyancy-modified k-ε turbulence model are not described here, but can be found in Yan and Mohammadian (2017).

The fluid properties were assumed to be constant except for density, which depends on changes in temperature and salinity. The method used for calculating the density will be discussed in the following section.

B.1.2 Density calculation

The density can be calculated based on the equation of state. Millero and Poisson's equation (Millero and Poisson, 1981) is one of the most widely used formulas for calculating density as a function of temperature and salinity. This formula is referred to as the equation of state of seawater and is used in this study for calculating the density:

$$\rho = \rho_0 + AS + BS^{3/2} + CS \tag{B-11}$$

where ρ_0 is the density, and is defined as follows:

$$\rho_0 = 999.842594 + 6.793952 \times 10^{-2}T - 9.095290 \times 10^{-3}T^2 + 1.001685 \times 10^{-4}T^3 - 1.120083 \times 10^{-6}T^4 + 6.536336 \times 10^{-9}T^5 \tag{B-12}$$

while *A*, *B*, and *C* are defined as follows:

$$A = 8.24493 \times 10^{-1} - 4.0899 \times 10^{-3}T + 7.6438 \times 10^{-5}T^2 - 8.2467 \times 10^{-7}T^3 + 5.3875 \times 10^{-9}T^4 \tag{B-12}$$

$$B = -5.72466 \times 10^{-3} + 1.0227 \times 10^{-4}T - 1.6546 \times 10^{-6}T^2 \tag{B-13}$$

$$C = 4.8314 \times 10^{-4} \tag{B-14}$$

The limits of temperature and salinity in this equation are $0 < T < 40$, and $0.5 < S < 43$. Later, Millero and Huang (Millero and Huang, 2009) conducted new seawater density measurements to modify Millero and Poisson's equation of state with the aim of expanding its limits to a wider range of temperature (0-90 °C) and absolute salinity S_A (0-70 kg/m^3) values and found that the results obtained were consistent, with the standard error being 0.0063 kg/m^3.

B.1.3 Discretization approaches

The main reason for deriving the numerical model is to solve it in a way appropriate for computer calculations, and the first step in this process involves equation discretization. The approach to this discretization mainly depends on providing a set of discrete algebraic equations, with one equation for every node. The value in the node should be in relation with the ones in the neighboring node. Then, by satisfying all the equations in the set, the numerical solution can be found. The following is a discussion of the process used for discretization in the present study (Anderson, 1995).

B.1.3.1 Finite Volume Method (FVM)

In this study, the software OpenFOAM was used for simulating the positively buoyant offset jet is based on the finite volume method (FVM), which works with the integral form of the conservation equations. The finite volume method is an appropriate and common method for discretization of governing equation in fluid mechanics, and it is suitable for the simulation of a wide range of fluid mechanics problems arising from laws regarding conservation of principle. Using structured or unstructured grid points, it is applicable for different domains and geometries. An attractive feature of this method is that numerical flux can be conserved from one cell to a neighboring cell. This feature makes it useful for fluid mechanics purposes.

Generally, domains are divided into finite volumes in which the centroids represent the node for calculation, and the grid merely defines the boundaries between the different volumes and does not need to be related to the metrics used. Variable surface values, in terms of nodal values, are expressed through interpolation. As long as the surface integrals for volumes with a shared face are equal for both volumes, this method is considered conservative. One drawback of FVM compared to Finite Difference Method (FDM) is that creating higher than second-order schemes for the purposes of 3D simulation is considerably more challenging because of the three levels of approximation required, which are integration, differentiation and interpolation. However, because it is easy to implement and understand and due to its very physical approach, FVM is the approach that is the most widely used method in fluid mechanics.

B.1.3.2 Computational domain and boundary conditions

In the present study, only half of the buoyant offset jet domain is considered because of the symmetrical nature of the problem. Figures B-1a and b illustrate the computational domain with the mesh system. The dimensions of the computational domain (Figure B-1a) were chosen to simulate the present experiments, and a refined mesh is considered in the near-field zone of the offset jet for all simulations in order to better capture the velocity and temperature characteristics, as shown in Figure B-1b. It is also worthy of note that mesh independency tests (sensitivity analysis) were performed to get the best density for the mesh grid for more than five levels. In all cases, a refined mesh was used for the simulations in order to get enough resolution, and the optimal number of cells was set at 1.6 million. The parameters used herein are similar to those used in the experiments (see Table 2-1). The nozzle boundary conditions were chosen based on Kheirkhah Gildeh et al. (2015a and 2015b), as follows: $u_x = U_0$, $u_y = u_z = 0$, $T = T_0$, $k = 0.06u^2$, and $\varepsilon = 0.06u^3/D$. A zero gradient boundary condition perpendicular to the outlet plane is defined for u_x, u_y, u_z, k, ε, T, and S for the flow at the outlet boundary section. For the walls, boundary conditions defined as z and $u_z = 0$ and a no-slip condition were applied in this study. Thus, k and ε are assumed to follow standard wall functions at the wall for both thermal and nonthermal buoyant jets. Moreover, a second-order solution scheme was used (i.e., Gauss Limited Linear) to better capture the variables (U, S, T, k, and ε), with accurate results. Finally, the symmetry boundary was modeled using a symmetry plane condition.

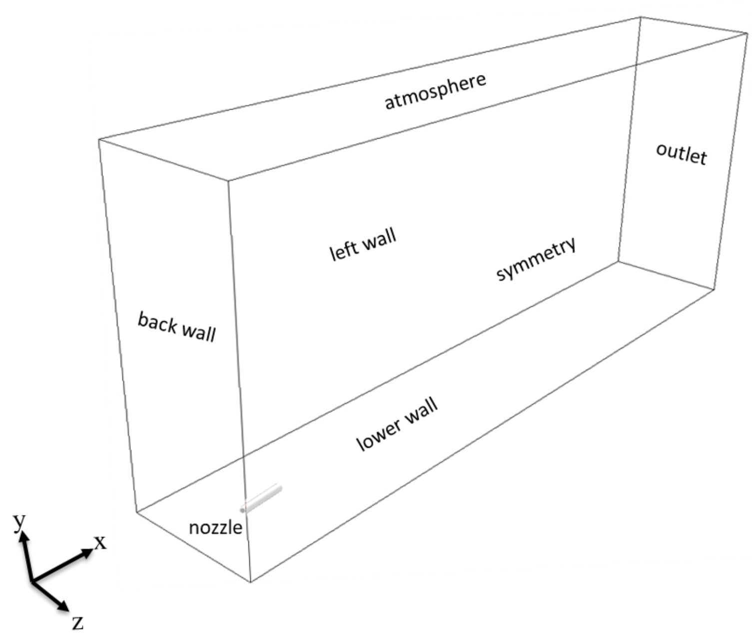

(a)

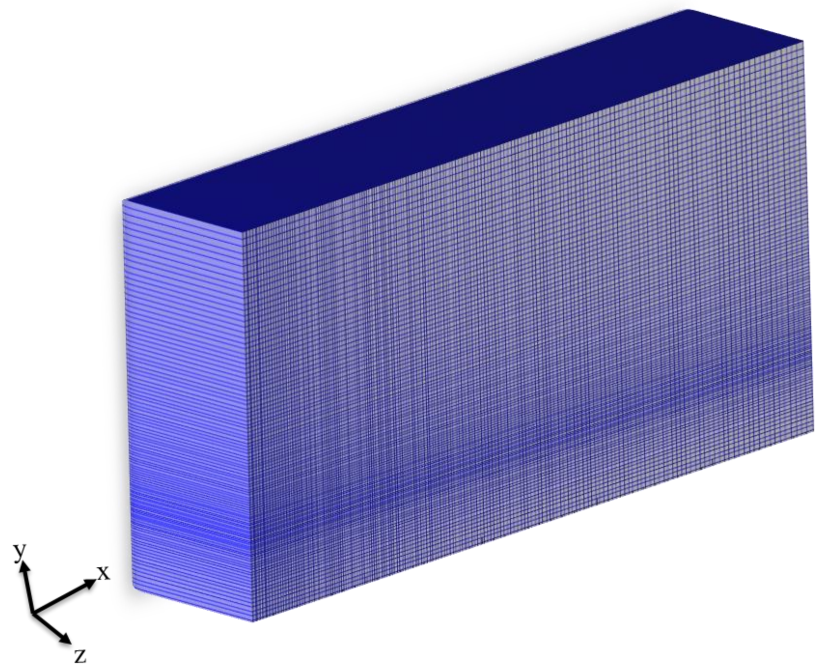

(b)

Figure B-1: Computational domain: (a) The numerical model domain and boundary definitions; and (b) the structured grid of the domain with a refined mesh near the nozzle.

B.2 Computational fluid dynamic (CFD) model

B.2.1 OpenFoam

An open-source CFD software OpenFOAM (Open Source Field Operation And Manipulation) with a structured grid was used in this study to simulate the buoyant offset jet discharge. The OpenFOAM model (a free open-source package) is widely used for modeling and solving several physical phenomena in fluid mechanics, including positively and negatively-buoyant jets. The model solves a set of partial differential equations (PDEs) using the finite volume method (FVM). The OpenFOAM platform has a wide array of libraries, solvers, and utilities, and it is useful for a wide range of problems. Another advantage is that it can be modified and to develop new problems, applications, boundary conditions and solvers. Among several solvers, the "pisoFoam" solver is used in the present study. The base of this solver for incompressible fluids was developed by implementing the advection-diffusion equation for salinity and temperature in order to calculate the transport and dispersion of those parameters. This solver is also able to reproduce hydraulic interaction problems.

B.2.1.1 Model Preparation

As noted, with some knowledge of the underlying method, OpenFOAM users can create new utilities and solvers, which is just one strength of this software. The OpenFOAM pre- and post-processing environments are illustrated in Figure B-2. Since the interface for the pre- and post-processing is a standard one in OpenFOAM, therefore consistent data handling is ensured. OpenFOAM's overall structure is shown in Figure B-3. This section clarifies the use of OpenFOAM applications for simulating jet behaviors in stagnant ambient water.

The following directories are included in the case directory for each problem (Hjertager, 2009). The case structure is also shown in Figure B-3.

- Constant file: this controls the turbulence and material properties and the mesh characteristics corresponding to each problem.
- System file: this defines the solution controls, time step size, and number of iterations.
- Zero file: this determines the boundary conditions and initial flow fields.

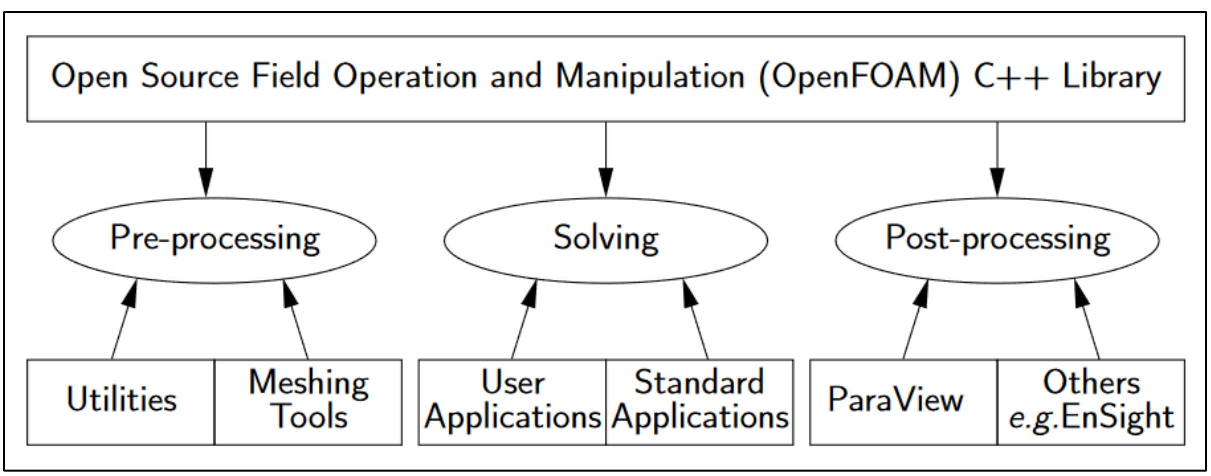

Figure B-2: Overview structure of OpenFOAM (Greenshields, 2019).

As noted previously, a number of solvers in OpenFOAM can be chosen depending on which problems one wishes to solve (Poungkrajorn, 2015). In this research, the pisoFoam solver was chosen for the experimental problem. The pisoFoam is a transient solver for incompressible flows, and was used for all the models examined.

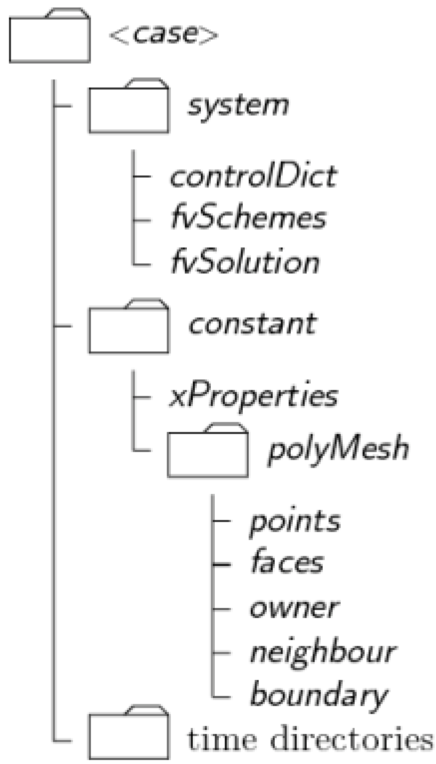

Figure B-3: Case directory structure (Greenshields, 2019).

B.2.1.2 Implementation of the Solvers

B.2.1.2.1 pisoFoam Solver

The pisoFoam solver is useful for both turbulent and laminar conditions, with the PISO (Pressure Implicit with Splitting of Operators) algorithm being its base. Essentially, pisoFoam involves pressure-velocity calculations which include a predictor step and two corrector steps. To solve intermediate pressure fields, momentum equations are used in the predictor step, and this is the idea behind the SIMPLE algorithm. Ensuring the relevant parameters in addition to the correcting is accomplished by the corrector steps so that the continuity and momentum equations are satisfied

(Versteeg and Malalasekera, 2007). So, by adding corrector steps to ensure the values calculated, pisoFoam can also be considered an extension of the SIMPLE algorithm (Poungkrajorn, 2015).

B.2.1.3 Courant number and time step control

A self-adapting time step has been used in order to ensure proper stability of the calculations, and the time step is adjusted according to pre-determined upper limit values for the Courant number (Co_{max}) and time step (Δt_{max}). The Courant number is determined by:

$$Co = \frac{|U_f . S_f|}{d . S_f} \Delta t \qquad \text{(B-14)}$$

where d is a vector between the faces of two adjacent control volumes. The values for U_f and Δt in equation B-15 are determined from the previous time step, and based on these values, the new time step can be determined (Berberović et al., 2009), as follows:

$$\Delta t^n = min\left[\frac{Co_{max}}{Co^0}, \left(1 + \lambda_1 \frac{Co_{max}}{Co^0}\right) \Delta t^0, \lambda_2 \Delta t^0, \Delta t_{max}\right] \qquad \text{(B-15)}$$

where Co^0 represents the maximum value of the local Courant number. Berberović et al. (2009) stated that the maximum Courant number value should not be greater than 0.2. The values for the damping factor, λ_1=0.1 and λ_2=1.2, are intended prevent instability due to fluctuations in the time step. Provided that the maximum value of a local Courant number does not go beyond its limit, the stability of a given time step should be ensured. However, it must be noted that an intermediate time step (Δt^*_{ini}) should be specified at the beginning of the simulation in order to determine the initial time step value, i.e.:

$$\Delta t^*_{ini} = min\left(\frac{Co_{max}}{Co^0} \Delta t_{ini}, \Delta t_{max}\right) \qquad \text{(B-16)}$$

The intermediate value in equation B-16, Δt^0, provides reasonable values for the maximum local Courant numbers and the subsequent new time steps.

B.3 Turbulence Modelling

A wide array of turbulence models are available in the literature, and the choice of which one is most appropriate is dependent on the nature of the problem. For example, obtaining the turbulent flow parameters can be done either by applying Direct Navier-Stokes (DNS) equations directly, or they can be obtained in temporally averaged form by using Reynolds-Averaged Navier-Stokes equations (RANS). In this study, different RANS models are applied as turbulence models, and their capability in terms of simulating the turbulence accurately is compared. These models are explained in detail in the following sections.

B.3.1 Standard k-ε Turbulence Model

The most extensively used model for turbulence modeling is standard k-ε turbulence model, which was developed and proposed by Launder and Spalding (1974). Its extensive use can be attributed to its good balance between accuracy and efficiency. It is a two-equation model, where the turbulence kinetic energy k and its dissipation rate ε are calculated from their respective transport equations. In this model, the turbulent kinetic energy (k) transport equation is derived from momentum equations; however, the turbulent energy dissipation (ε) transport equation is determined by using physical reasoning to be similar to the transport equation for k, which is derived mathematically. In this model, the turbulent kinetic energy and its dissipation rate are obtained through the following equations:

$$\frac{\partial k}{\partial t}+\frac{\partial k u_i}{\partial x_i}=\frac{\partial}{\partial x_i}\left(Dk_{eff}\frac{\partial k}{\partial x_i}\right)+G_k-\varepsilon \qquad \text{(B-17)}$$

$$\frac{\partial \varepsilon}{\partial t}+\frac{\partial \varepsilon u_i}{\partial x_i}=\frac{\partial}{\partial x_i}\left(D\varepsilon_{eff}\frac{\partial \varepsilon}{\partial x_i}\right)+C_{1\varepsilon}\frac{\varepsilon}{k}G_k-C_{2\varepsilon}\frac{\varepsilon^2}{k} \qquad \text{(B-18)}$$

where G_ε represents the turbulent kinetic energy generation due to the mean velocity gradients, and Dk_{eff} and $D\varepsilon_{eff}$ represent the effective diffusivity for k and ε, respectively. The values for Dk_{eff} and $D\varepsilon_{eff}$ are calculated by:

$$Dk_{eff} = \nu + \frac{\nu_t}{\sigma_k} \tag{B-19}$$

$$D\varepsilon_{eff} = \nu + \frac{\nu_t}{\sigma_\varepsilon} \tag{B-20}$$

The turbulent kinematic viscosity for each point relates to the local values of the turbulent kinetic energy and its dissipation rate, and is determined by:

$$\nu_t = C_\mu \frac{k^2}{\varepsilon} \tag{B-21}$$

where σ_ε represents the turbulent Prandtl number for ε, $C_{1\varepsilon}$, $C_{2\varepsilon}$, C_μ and σ_k are constants which were experimentally determined and were given the following values:

$$C_{1\varepsilon} = 1.44,\ \ C_{2\varepsilon} = 1.92,\ \ C_\mu = 0.09,\ \ \sigma_k = 1.0,\ \ \sigma_\varepsilon = 1.3$$

The production term of the turbulent kinetic energy G_k is seen in most turbulence models, and is determined by:

$$G_k = -\overline{u_i' u_j'} \frac{\partial u_j}{\partial x_i} \tag{B-22}$$

This equation can also be written as follows:

$$G_k = 2\nu_t S_{ij}^2 \tag{B-23}$$

where

$$S_{ij} = 0.5(\frac{\partial u_j}{\partial x_i} + \frac{\partial u_i}{\partial x_j}) \tag{B-24}$$

where u_i', u_j' and S_{ij} are the fluctuating velocity and strain-rate tensor terms respectively.

B.3.2 Realizable k-ε Turbulence Model

The Realizable k-ε Turbulence Model was developed by Shih et al. (1995), and is one of the most recent k-ε turbulence models. This model differs from the standard k-ε model in two aspects. First, it uses a new turbulent viscosity equation, and second, the equation for the dissipation rate transport is obtained from the mean-squared vorticity fluctuation transport equation. The eddy viscosity equations are determined based on realizability constraints; i.e., normal Reynolds stress positivity and Schwarz's turbulent shear stress inequality. These conditions are not met by the standard k-ε which makes the realizable model more precise in simulating such phenomena as separated flows and flows that have complex secondary features.

Reflecting the improvements by Shih et al. (1995), the transport equations are then written as:

$$\frac{\partial k}{\partial t}+\frac{\partial k u_i}{\partial x_i}=\frac{\partial}{\partial x_i}\left(Dk_{eff}\frac{\partial k}{\partial x_i}\right)+G_k-\varepsilon \tag{B-25}$$

$$\frac{\partial \varepsilon}{\partial t}+\frac{\partial \varepsilon u_i}{\partial x_i}=\frac{\partial}{\partial x_i}\left(D\varepsilon_{eff}\frac{\partial \varepsilon}{\partial x_i}\right)+\sqrt{2}C_{1\varepsilon}S_{ij}\varepsilon-C_{2\varepsilon}\frac{\varepsilon^2}{k+\sqrt{\nu\varepsilon}} \tag{B-26}$$

Similar to prior versions of k-ε models, turbulent viscosity is obtained by:

$$\nu_t=C_\mu\frac{k^2}{\varepsilon} \tag{B-27}$$

where C_μ is calculated from:

$$C_\mu=\frac{1}{A_0+A_sU^*\frac{k}{\varepsilon}} \tag{B-28}$$

$$U^*=\sqrt{S_{ij}S_{ij}+\widetilde{\Omega}_{ij}\widetilde{\Omega}_{ij}} \tag{B-29}$$

$$\widetilde{\Omega}_{ij}=\Omega_{ij}-2\varepsilon_{ijk}\omega_k \tag{B-30}$$

$$\Omega_{ij}=\overline{\Omega}_{ij}-\varepsilon_{ijk}\omega_k \tag{B-31}$$

where $\overline{\Omega}_{ij}$ is the rotation tensor mean rate as viewed in a rotating reference frame with the angular velocity ω_k. Constants values of A_0 and A_s are determined by:

$$A_0=4,\ A_s=\sqrt{6}\,cos\varphi \tag{B-32}$$

$$\varphi = \frac{1}{3} Arc\ \cos(\min(\max(\sqrt{6}W, -1), 1) \tag{B-33}$$

$$W = \frac{S_{ij}S_{jk}S_{ki}}{\tilde{S}^2} \tag{B-34}$$

It can be seen that C_μ is a function of the angular velocity, rotational rates, and mean strain of the rotating system. The value of $C_\mu = 0.09$ was determined to be the solution of equation (B-28) for an inertial sub-layer in the equilibrium boundary layer. $C_{1\varepsilon}$ is also not constant in this model, and can be determined by:

$$C_{1\varepsilon} = max\left(\frac{\eta}{5+\eta}, 0.43\right) \tag{B-35}$$

The constants C_2, σ_k and σ_ε were determined by Shih et al. (1995), and are:

$$C_{2\varepsilon} = 1.9,\ \ \sigma_k = 1.0,\ \ \sigma_\varepsilon = 1.2$$

B.3.3 Buoyancy-modified k-ε Model

Buoyancy-modified k-ε model (also referred as k-ε GGDH turbulence model) is basically the standard k-ε model accomplished by adding new terms of buoyancy source to the k and ε equations. These terms are indeed based on the generalized gradient diffusion hypothesis (GGDH) (Daly and Harlow, 1970). The modified model is as follows (Yan and Mohammadian, 2017):

$$\frac{\partial k}{\partial t} + \frac{\partial k u_i}{\partial x_i} = \frac{\partial}{\partial x_i}\left(Dk_{eff}\frac{\partial k}{\partial x_i}\right) + G_k + \hat{B} - \varepsilon \tag{B-36}$$

$$\frac{\partial \varepsilon}{\partial t} + \frac{\partial \varepsilon u_i}{\partial x_i} = \frac{\partial}{\partial x_i}\left(D\varepsilon_{eff}\frac{\partial \varepsilon}{\partial x_i}\right) + C_{1\varepsilon}\frac{\varepsilon}{k}G_k + C_{1\varepsilon}(1 - C_{3\varepsilon})\frac{\varepsilon}{k}\hat{B} - C_{2\varepsilon}\frac{\varepsilon^2}{k} \tag{B-37}$$

where

$$\hat{B} = -\frac{3}{2}\frac{\nu_t}{\sigma_t \rho k}\left(\overline{u_i' u_j'}\frac{\partial \rho}{\partial x_j}\right)\left(\frac{\partial P}{\partial x_i} + \rho_0 g_i\right) \tag{B-38}$$

$$G = \nu_t\left(\frac{\partial U_i}{\partial x_j} + \frac{\partial U_j}{\partial x_i}\right)\frac{\partial U_i}{\partial x_j} \tag{B-39}$$

$$\nu_t = C_\mu \frac{k^2}{\varepsilon} \qquad \text{(B-27)}$$

where U_i is the velocity component in x_i direction, $\hat{B}$ is the production of turbulence due to the buoyancy effect, $\overline{u_i' u_j'}$ is the velocity fluctuation, and G_k is the production of turbulence due to shear. The constant values of the model (i.e., $C_{1\varepsilon}$, $C_{2\varepsilon}$, σ_k, and σ_ε) are similar to the standard k-ε constant values given previously. The values of the coefficients $C_{3\varepsilon}$ and σ_t are set to 0.8 and 1.0, respectively.

Appendix C

C.1 Uncertainty analysis

Uncertainty analysis was performed to analyze the predictive accuracy of the equations presented throughout the thesis. Uncertainty analysis is crucial to assess the confidence in the results obtained and evaluate the proposed GMDH models. Therefore, to measure the uncertainty of the prediction of the geometrical characteristics obtained from the GMDH models, several explicit statistics were employed such as, the prediction error (E_i), Mean Prediction Error (MPE), Standard Deviation (s_d), and Width of Uncertainty Band (WUB). These parameters are calculated for the whole dataset employed in this study. The negative and positive values of the MPE demonstrate that the models are underestimating or overestimating the observed values, respectively. These parameters are as follows (Bonakdari and Mohammadian, 2019):

$$E_i = Prediction_i - Actual_i \quad \text{(C-1)}$$

$$\bar{E} = \sum_{i=1}^{n} E_i/n \quad \text{(C-2)}$$

$$MPE = \frac{\sum_{i=1}^{n}(Prediction - Actual)}{n} \quad \text{(C-3)}$$

$$s_d = \frac{\sqrt{\sum_{i=1}^{n}(E_i - \bar{E})^2}}{(n-1)} \quad \text{(C-4)}$$

$$WUB = 1.96\frac{s_d}{\sqrt{n}} \quad \text{(C-5)}$$

where n is the sample size. Moreover, a confidence band was defined around the prediction error values for MPE and s_d by using Wilson score method without a continuity correction. The difference between the low and high uncertainty bands is defined as the WUB. The model can be considered highly accurate when the value of the WUB is smaller. Therefore, a confidence band of 95% was achieved using ±1.96 $s_d/\sqrt{n}$ values (Shaghaghi et al., 2017).

Results of the uncertainty analysis obtained for the GMDH models predictions of the x_m/D, x_r/D, y_m/D , and y_t/D are presented in Table C-1 along with the mean prediction errors, the width of uncertainty band and 95% Prediction Error Interval (PEI).

Table C-1: Uncertainty analysis for GMDH prediction models of the geometrical characteristics.

GMDH model for the geometrical characteristic	Number of sample size	MPE	s_d	WUB	95% PEI
x_m/D	309	$+0.29$	8.58	± 0.96	-0.66 to $+1.25$
x_r/D	305	-0.11	9.29	± 1.04	-1.15 to $+0.93$
y_m/D	341	-0.10	6.11	± 0.65	-0.75 to $+0.55$
y_t/D	420	-0.03	8.25	± 0.79	-0.82 to $+0.76$

Based on the results shown in the Table C-1, the lowest values for the mean prediction error was for the non-dimensional y_t/D, while the lowest value of the s_d, WUB, and 95% PEI is obtained for the y_m/D which indicates that it is the most accurate model compared to other models. On the other hand, the least accurate predicted model in this study was found to be for the non-dimensional geometrical parameters of x_m/D and x_r/D with the higher values of the s_d, WUB, and 95% PEI, respectively. For the MPE, it can be seen that the largest value was for the x_m/D, i.e., $+0.29$. Although both x_r/D and y_m/D had almost the same value of the MPE, but considering the WUB and 95% PEI values the predicted model of y_m/D is more accurate. The larger value of the WUB was noted for the x_r/D where was ranging from -1.04 to $+1.04$, which is inaccurate compared to other predicted models. As a result, the non-dimensional values of the geometrical characteristic y_m/D predicted by the model showed the lowest values of the mean prediction error, smallest uncertainty band width, and confidence band of 95% prediction error interval, therefore, validating the accuracy of this GMDH methodology.